27 May 2011 | $10

Science

AAAS

EDITORIAL

1009 Innovation Needs Novel Thinking
Alan I. Leshner

NEWS OF THE WEEK

1016 A roundup of the week's top stories

NEWS & ANALYSIS

1019 Texas's $3 Billion Fund Lures Scientific Heavyweights

1020 Regulatory T Cells Get Their Chance to Shine

1023 India's Earth-Observing System Comes Under Fire

NEWS FOCUS

1024 The Prion Heretic

1028 Manta Machines
>> Science *Podcast*

1030 Biology of Genomes Meeting
DNA Circles Cause Cow Coat Color Changes
On the Trail of Brain Domestication Genes
Disease Risk Links to Gene Regulation

LETTERS

1032 Springtime for Science in Egypt
M. Aglan

CT Risks Dwarfed by Diagnostic Benefits
L. Bodenstein

Value of Small Forest Fragments to Amphibians
F. R. Da Silva et al.

1033 CORRECTIONS AND CLARIFICATIONS

1033 TECHNICAL COMMENT ABSTRACTS

BOOKS *ET AL.*

1034 Soul Dust
N. Humphrey, reviewed by M. J. Proulx

1035 Dirt
K. Ford et al., *curators;*
Dirt
R. Cox et al.

POLICY FORUM

1036 Mitigating Local Causes of Ocean Acidification with Existing Laws
R. P. Kelly et al.

PERSPECTIVES

1038 Limb Cells Don't Tell Time
S. Mackem and M. Lewandoski
>> *Reports pp. 1083 and 1086*

1039 A Logical Use for Atoms
A. Heinrich and S. Loth
>> *Report p. 1062*

1040 Chameleon Magnets
I. Žutić and J. Cernë
>> *Report p. 1065*

1041 Explaining Human Behavioral Diversity
A. Norenzayan
>> *Report p. 1100*

1043 KSR Plays CRAF-ty
F. Shi and M. A. Lemmon

1044 Assessing the Status of Alaska's Glaciers
A. A. Arendt

SCIENCE PRIZE ESSAY

1046 The Periodic Table of Videos
B. Haran and M. Poliakoff

CONTENTS continued >>

page 1024

page 1035

COVER

A 1-year-old child will spend more time looking at a visual display of moving objects when what he sees is not what he expects. How young children incorporate prior probabilities with current dynamic cues to make predictions about future events can be explained by modeling the child as a Bayesian observer. See the Research Article by Téglás *et al.* on page 1054.

Photo: Ryan McVay/Getty Images

DEPARTMENTS

1005 This Week in *Science*
1011 Editors' Choice
1014 *Science* Staff
1048 AAAS News & Notes
1105 New Products
1106 *Science* Careers

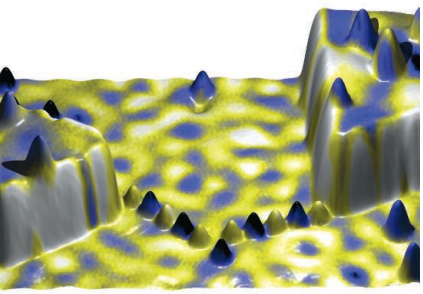

pages 1039 & 1062

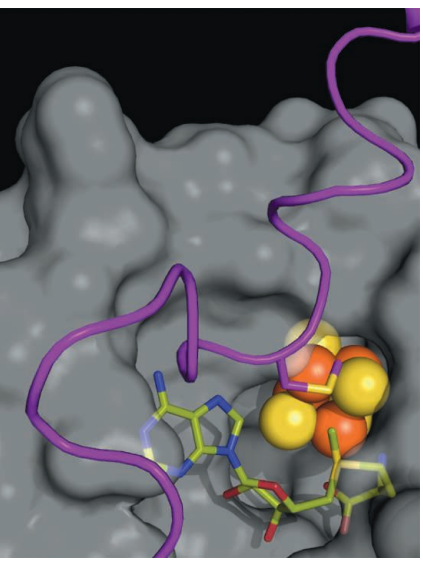

page 1089

REVIEW

1049 Dyscalculia: From Brain to Education
B. Butterworth et al.

RESEARCH ARTICLE

1054 Pure Reasoning in 12-Month-Old Infants as Probabilistic Inference
E. Téglás et al.
Twelve-month-old infants employ Bayesian statistics.

REPORTS

1059 Experimental Repetitive Quantum Error Correction
P. Schindler et al.
An error correction algorithm is applied multiple times to a small quantum system.

1062 Realizing All-Spin–Based Logic Operations Atom by Atom
A. A. Khajetoorians et al.
Scanning tunneling microscopy is used to assemble and read out signals from a device based on atomic spins.
>> Perspective p. 1039

1065 Electrically Induced Ferromagnetism at Room Temperature in Cobalt-Doped Titanium Dioxide
Y. Yamada et al.
The magnetic properties of a magnetic insulator can be controlled by an electric field at room temperature.
>> Perspective p. 1040

1068 Seismic Imaging of Transition Zone Discontinuities Suggests Hot Mantle West of Hawaii
Q. Cao et al.
Hot material upwelling from deep below Hawaii may pool up far below and to the west of the islands.

1071 Computational Design of Virus-Like Protein Assemblies on Carbon Nanotube Surfaces
G. Grigoryan et al.
Proteins are designed to bind to specific surfaces while also presenting a programmed surface superstructure.

1076 Impact of Antarctic Circumpolar Current Development on Late Paleogene Ocean Structure
M. E. Katz et al.
The modern four-layered ocean structure developed during the early Oligocene, when Antarctica developed permanent ice cover.

1079 Early Warnings of Regime Shifts: A Whole-Ecosystem Experiment
S. R. Carpenter et al.
High-frequency monitoring of manipulated and reference lakes enabled early detection of subsequent catastrophic regime shift.

1083 Initiation of Proximal-Distal Patterning in the Vertebrate Limb by Signals and Growth
K. L. Cooper et al.
Growth of limb cells in culture conditions with subsequent in vivo transplantation allows the dissection of limb patterning.

1086 Diffusible Signals, Not Autonomous Mechanisms, Determine the Main Proximodistal Limb Subdivision
A. Roselló-Díez et al.
Cells compare proximal and distal signals to set their identity along the vertebrate limb.
>> Perspective p. 1038

1089 Structural Basis for Methyl Transfer by a Radical SAM Enzyme
A. K. Boal et al.
An enzyme harnesses methyl donation and reductive cleavage of its cofactor within a single active site to methylate RNA.

1093 Human Cytomegalovirus Directly Induces the Antiviral Protein Viperin to Enhance Infectivity
J.-Y. Seo et al.
Human cytomegalovirus uses a host-encoded antiviral protein to its own advantage.

1097 Deciphering the Rhizosphere Microbiome for Disease-Suppressive Bacteria
R. Mendes et al.
A common plant pathogen induces the growth of disease-suppressive microbes in local soil communities.

1100 Differences Between Tight and Loose Cultures: A 33-Nation Study
M. J. Gelfand et al.
The differences across cultures in the enforcement of conformity may reflect their specific histories.
>> Perspective p. 1041; Science *Podcast*

Published by AAAS

SCIENCEONLINE

SCIENCEXPRESS
www.sciencexpress.org

High Pre-Eruptive Water Contents Preserved in Lunar Melt Inclusions
E. H. Hauri et al.
Primitive magmatic melt inclusions from the Moon contain as much water as some terrestrial mid-ocean ridge magmas.
10.1126/science.1204626

Selective Attention from Voluntary Control of Neurons in Prefrontal Cortex
R. J. Schafer and T. Moore
The activity of neurons with both visual and motor properties in the frontal eye field can be controlled voluntarily.
10.1126/science.1199892

TFEB Links Autophagy to Lysosomal Biogenesis
C. Settembre et al.
Starvation activates a transcriptional program controlling autophagosome formation, lysosome fusion, and substrate degradation.
10.1126/science.1204592

Phosphorylation of the Autophagy Receptor Optineurin Restricts *Salmonella* Growth
P. Wild et al.
Phosphorylation of an autophagy receptor restricts pathogenic cytosolic bacterial growth.
10.1126/science.1205405

TECHNICALCOMMENTS

Comment on "A Persistent Oxygen Anomaly Reveals the Fate of Spilled Methane in the Deep Gulf of Mexico"
S. B. Joye et al.
Full text at www.sciencemag.org/cgi/content/full/332/6033/1033-c

Response to Comment on "A Persistent Oxygen Anomaly Reveals the Fate of Spilled Methane in the Deep Gulf of Mexico"
J. D. Kessler et al.
Full text at www.sciencemag.org/cgi/content/full/322/6033/1033-d

SCIENCENOW
www.sciencenow.org
Highlights From Our Daily News Coverage

Lousy Flies Explain Weird Evolution of Pigeon Pests
Hitchhiking on flies could help explain why some lice species evolve more closely with their host than others.
http://scim.ag/lousy-flies

Stars With Multiple Planets Abound
The Kepler space telescope spies well more than a hundred of them.
http://scim.ag/multiple-planets

Brains on Jazz Feel the Music
Empathy helps listening musicians judge whether music is improvised or rehearsed.
http://scim.ag/jazz-brains

SCIENCESIGNALING
www.sciencesignaling.org
The Signal Transduction Knowledge Environment
24 May issue: http://scim.ag/ss052411

RESEARCH ARTICLE: α-Catenin Is a Tumor Suppressor That Controls Cell Accumulation by Regulating the Localization and Activity of the Transcriptional Coactivator Yap1
M. R. Silvis et al.

PODCAST
J. F. Martin et al.
A cell-cell adhesion protein suppresses skin carcinoma development by attenuating the signaling of a transcriptional coactivator in the Hippo pathway.

RESEARCH ARTICLE: p38α Signaling Induces Anoikis and Lumen Formation During Mammary Morphogenesis
H.-C. Wen et al.
The kinase p38α may suppress breast cancer by promoting formation of the proper architecture of mammary glands.

MEETING REPORT: Progress in the Function and Regulation of ADP-Ribosylation
M. O. Hottiger et al.
Scientists gathered in Zurich, Switzerland, to discuss new insights into cell, structural, and developmental biology of ADP-ribosylation.

SCIENCETRANSLATIONAL MEDICINE
www.sciencetranslationalmedicine.org
Integrating Medicine and Science
25 May issue: http://scim.ag/stm052511

COMMENTARY: Quality Versus Quantity—Assessing Individual Research Performance
J.-A. Sahel
Bibliometrics could potentially improve objective evaluation of individual researchers, if qualitative measurements are included.

RESEARCH ARTICLE: A Therapeutic Antibody Targeting BACE1 Inhibits Amyloid-β Production in Vivo
J. K. Atwal et al.

RESEARCH ARTICLE: Boosting Brain Uptake of a Therapeutic Antibody by Reducing Its Affinity for a Transcytosis Target
Y. J. Yu et al.

PERSPECTIVE: Therapeutic Antibodies for Brain Disorders
S. M. Paul

PODCAST
S. M. Paul and O. M. Smith
An enzyme implicated in Alzheimer's disease can be inhibited using a human monoclonal antibody that can cross the blood-brain barrier.

RESEARCH ARTICLE: Indocyanine Green Enables Near-Infrared Fluorescence Imaging of Lipid-Rich, Inflamed Atherosclerotic Plaques
C. Vinegoni et al.
An FDA-approved fluorescence imaging agent can detect lipid-rich, inflammatory plaques in arteries.

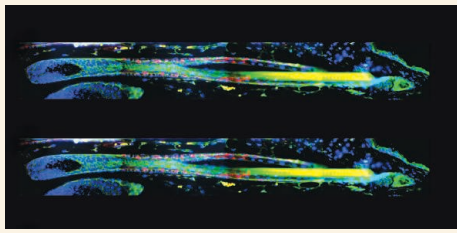

SCIENCESIGNALING
Hair follicles, a site of stem cells.

SCIENCECAREERS
www.sciencecareers.org/career_magazine
Free Career Resources for Scientists

Experimental Error: Fetus Don't Fail Me Now
A. Ruben
With his daughter still in the embryonic stage, our columnist wonders whether it is too early to steer her toward a career in science.
http://scim.ag/ee_fetus

Focus on Aging: Understanding Brain Plasticity
E. Pain
Neuroscientist Sara Burke investigates how aging affects the plasticity of neuronal networks and, ultimately, behavior.
http://scim.ag/pain_plasticity

SCIENCEPODCAST
www.sciencemag.org/multimedia/podcast
Free Weekly Show
On the 27 May *Science* Podcast: explaining cultural diversity, robots that mimic manta rays, your Letters to *Science*, and more.

SCIENCEINSIDER
news.sciencemag.org/scienceinsider
Science Policy News and Analysis

SCIENCE (ISSN 0036-8075) is published weekly on Friday, except the last week in December, by the American Association for the Advancement of Science, 1200 New York Avenue, NW, Washington, DC 20005. Periodicals Mail postage (publication No. 484460) paid at Washington, DC, and additional mailing offices. Domestic individual membership and subscription (51 issues): $149 ($74 allocated to subscription). Domestic institutional subscription (51 issues): $990; Foreign postage extra: Mexico, Caribbean (surface mail) $55; other countries (air assist delivery) $85. First class, airmail, student, and emeritus rates on request. Canadian rates with GST available upon request, GST #1254 88122. Publications Mail Agreement Number 1069624. **Printed in the U.S.A.**

Change of address: Allow 4 weeks, giving old and new addresses and 8-digit account number. **Postmaster:** Send change of address to AAAS, P.O. Box 96178, Washington, DC 20090–6178. **Single-copy sales:** $10.00 current issue, $15.00 back issue prepaid includes surface postage; bulk rates on request.

AAAS
ADVANCING SCIENCE, SERVING SOCIETY

CREDIT: BRIDGET T. KREGER/DIVISION OF HUMAN BIOLOGY/FRED HUTCHINSON CANCER RESEARCH CENTER

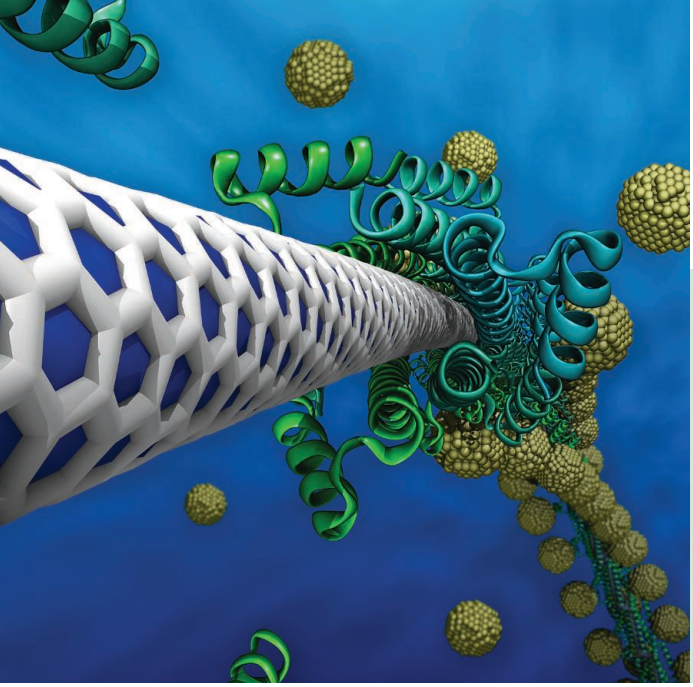

<< All Wrapped Up

Proteins can be used to bind selectively to specific surfaces, but can proteins be designed to form a superstructure on the bound surface? **Grigoryan *et al.*** (p. 1071) describe an algorithm for generating specific protein sequences that would allow for the wrapping of carbon nanotubes with specific helicities. The design was accomplished by first parameterizing the geometry of the nanotube wrappings and then matching the geometry to known protein backbones. Then a combination of chemical intuition, conservation, and computational design was used to determine the peptide sequences. The designs were verified by a variety of biophysical measurements, including a crystal structure of a peptide dimer (without the nanotube) and 2D photoluminescence of suspended nanotubes stabilized by the peptides.

Understanding Dyscalculia

For some people, understanding mathematics comes so easily that it seems as if the world is written in numbers. For those with dyscalculia, a disorder that reflects impaired math skills, all the effort and studying possible still leaves math a mystery. The effects of dyscalculia echo through a person's life, lessening school progress and employment opportunities. **Butterworth *et al.*** (p. 1049) review what is known about dyscalculia, what genetic and developmental factors may contribute to the disorder, and what sorts of educational interventions may help.

Baby Einsteins

Having complete information with which to make predictions is a rarity and is often achieved only in theoretical studies with paper and pencil. **Téglás *et al.*** (p. 1054) now find that when 12-month-old infants view complex displays of multiple moving objects, they can form rational probabilistic expectations about future events by integrating dynamic spatiotemporal cues present in a scene, weighting these information sources as predicted by a Bayesian ideal observer model.

Repeated Corrections

Quantum computation involves having to work with fragile quantum states that have a tendency to decay on a rather short time scale. While techniques abound for mitigating the losses and improving the robustness of the systems, errors are unavoidable and so quantum error correction algorithms will be required for the implementation of large-scale quantum systems. **Schindler *et al.*** (p. 1059) describe a multiple correction algorithm applied to a three-qubit (3 atoms) system where the loss of information encoded on the atoms is protected against. Multiple correction algorithms are likely to become a necessary component for scaling up to practical systems.

Binary Logic on an Island

Scanning tunneling microscopes with magnetic tips have enabled precise manipulation and spin readout of surface-adsorbed atoms. By placing atoms at just the right distance from each other, it is possible to control their spin states based on the distance-dependent Ruderman-Kittel-Kasuya-Yosida interaction, making these systems an attractive candidate for spin-based computation. **Khajetoorians *et al.*** (p. 1062, published online 5 May; see the Perspective by **Heinrich and Loth**) now describe a device consisting of two atomic spin chains, each attached to a magnetic island whose magnetizations can be manipulated independently. An output atom placed in the vicinity of the ends of the two spin chains was able to perform a binary logic OR operation with the help of an external magnetic field.

Electrically Switched Magnetism

Magnetic memory is a robust, cheap, and widely used medium for information storage. Controlling the magnetic behavior with an electric field would provide further functionality and lower power consumption of devices. While such control has been demonstrated in dilute magnetic semiconducting materials, it has been limited to very-low-temperature operation. Using an electrolyte double-layer gate structure, **Yamada *et al.*** (p. 1065; see the Perspective by **Žutić and Cerně**) were able to modulate the carrier density and the magnetic properties of cobalt doped TiO_2 at room temperature. The findings should help in the development of practical spintronic devices.

Hawaii's Deep Plume—Ponded

Hotspots in Earth's crust are often considered to be the products of vertical plumes of hot material upwelling from great depths to form surface structures. The Hawaiian islands are perhaps the most commonly cited example, but efforts to image a plume using a range of seismological techniques have provided often contradictory results. Another method is to look at the temperature-dependent depth of mineral phase transitions—which result in seismic discontinuities—throughout the region where a plume purportedly exists. **Cao *et al.*** (p. 1068) interpreted inverse scattering of *SS* waves to create a topographic view of these discontinuities beneath near Hawaii. Instead of a narrow vertical structure, the results show a broad thermal anomaly west of the islands at the depth of one of the seismic discontinuities. Hotspot volcanism in Hawaii may thus be derived from a deep pond of hot material that gets carried by the flowing mantle up to the surface.

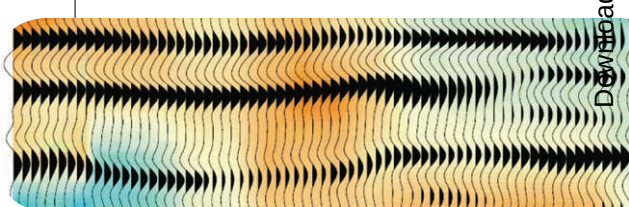

Continued on page 1007

CREDITS (TOP TO BOTTOM): ROBERT A. JOHNSON; CAO *ET AL.*

Continued from page 1005

The Ocean's Layers

A long interval of continental-scale Antarctic glaciation began about 34 million years ago at the beginning of the Oligocene, after 25 million years of global cooling following the peak warmth of the early Eocene, an event that had great influence on global climate and ecosystems. **Katz *et al.*** (p. 1076) compared the carbon- and oxygen-isotopic compositions of benthic foraminifera from shallower waters from the western North Atlantic continental slope and those of the deep Southern Ocean. The findings revealed a large difference between water masses developed in the early Oligocene, probably as the result of the development of Antarctic Intermediate Water. At the same time, the densest water, formed around Antarctica, was confined by a strengthening Antarctic Circumpolar Current to higher latitudes, forming a bottom layer generating a four-layered ocean like the one that exists today.

Predicting Ecosystem Change

Rapid transitions, or phase shifts, have been observed in diverse types of ecosystem, and often result from the loss or addition of top predators. **Carpenter *et al.*** (p. 1079, published online 28 April) show that it can be possible to detect an impending phase shift before it actually occurs. The populations of large predator fish in a northern American lake ecosystem were manipulated, and the effects of population change on other components of the food web were compared with an adjacent control lake. Subtle, but distinct, changes were observed in the manipulated lake at least a year before the transition of the food web to a new structure occurred.

CREDIT: ALBERTO ROSELLÓ, CNIC

Plasticity in Limb Development

The development of limbs has long been a model for understanding vertebrate development. As the buds grow, the different parts of the limb proximal-distal (PD) axis are laid down from the shoulders to digit tips in a temporal sequence. Prior work has invoked a clock-like mechanism, one that is insensitive to instructive signals. Two papers now provide an alternate view of PD patterning (see the Perspective by **Mackem and Lewandoski**). **Cooper *et al.*** (p. 1083) grew chick limb mesenchyme in tissue culture conditions where the signaling environment could be controlled and then grafted the cells onto the flank of a chick embryo, where they formed recognizable limb structures. The findings suggest that the set of signals seen by the early limb bud both keep the mesenchyme undifferentiated and also maintain its potential to form all three major limb segments. As the limb bud grows, PD regionalization results from the balance between proximal and distal signals. **Roselló-Díez *et al.*** (p. 1086) reach a similar conclusion, transplanting recombinant and normal chicken limb buds to host embryos.

Hostile Takeover

One of the hallmarks of the host's response to viral infection is the production of interferon cytokines, which trigger the induction of a broad array of antiviral genes. Viperin is an interferon-inducible gene whose expression is induced in response to infection with human cytomegalovirus (HCMV). **Seo *et al.*** (p. 1093, published online 28 April) now show that HCMV co-opts viperin to its advantage. vMIA, a virus-encoded protein, interacted with viperin and induced viperin relocalization from the endoplasmic reticulum to the mitochondria in response to infection. Mitochondria-localized viperin inhibited ATP generation in the mitochondria, which resulted in disruption of the actin cytoskeleton and enhanced viral replication.

Microbes Beat Disease

Most soil communities limit plant-pathogen activity to some degree by virtue of competition by resident microorganisms. But some naturally occurring soils develop an ability to suppress specific pathogens, often after a disease outbreak, suggesting that a specific microbial community has been selected. **Mendes *et al.*** (p. 1097, published online 5 May) investigated a soil that had developed resistance to the widespread fungal pathogen and saprophyte, *Rhizoctonia solani*. Strains of pseudomonad bacteria were isolated from the suppressive soil that were most efficient at inhibiting the pathogen in bioassays. Subsequent mutagenesis and functional studies revealed these bacteria were using nonribosomal peptide synthetase to synthesize an antifungal chlorinated lipopeptide resembling syringomycin.

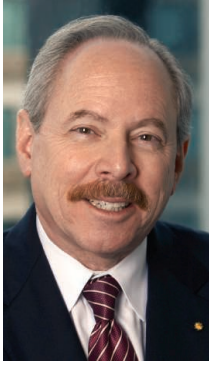

Alan I. Leshner is the chief executive officer of the American Association for the Advancement of Science and executive publisher of *Science*.

Innovation Needs Novel Thinking

SCIENCE, TECHNOLOGY, AND INNOVATION ARE CRITICAL DRIVERS OF ECONOMIC GROWTH AND national well-being. As a result, investing in them has become a source of hope for many countries, both rich and poor. But innovation demands that novel ideas be pursued, and the science and technology (S&T) enterprise may not be well structured, in the United States and elsewhere, to attract, recognize, and exploit new ideas. Some long-held traditions and modes of operation need to be reexamined to ensure that the system is optimized as an engine for advancing society's goals.

Peer review is widely recognized as the best system for choosing among research projects to fund and deciding which papers to publish. However, peer review can be somewhat conservative, particularly when grant support is limited, resulting in the support of "safer" projects over more risky ones that are based on scant pilot evidence. Urging peer reviewers and funders to support more high-risk but also potentially high-payoff or transformative research, which can revolutionize fields, has not worked well, at least in the United States, as pointed out in 2007 by the U.S. National Science Board.* What is needed are more programs like the U.S. National Institutes of Health's (NIH's) Pioneer Awards or the U.S. Department of Energy's ARPA-E program, in which funds are set aside for research that pushes the frontiers in groundbreaking ways. Projects are reviewed by committees charged with evaluating the projects' potential to be transformative, as well as their overall quality.

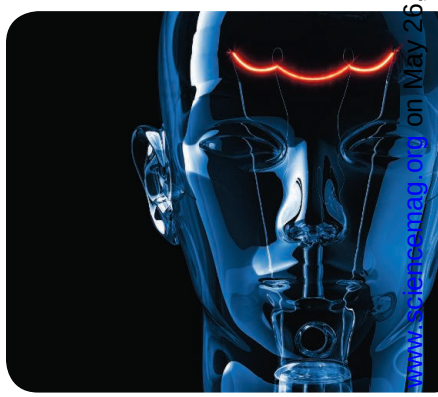

Research institutions pursuing high-risk research may have to rethink evaluation timelines and the criteria for judging and rewarding performance. Achieving the goals of a transformative research program can take longer than those of an incremental program designed in a more linear way; transformative research can have many false starts and thus a reduced publication rate. This factor must also be considered by funders, who may likewise need to rethink their criteria for support and for evaluating progress.

Fostering innovation will also benefit from increases in both the number of young scientists and the diversity of the pool of researchers. One of the best arguments for funding more young investigators is that scientists should be enabled to pursue their most creative ideas, which many people believe come earlier in one's career. There need to be more programs like the European Research Council's Starting Independent Researcher Grants, NIH's New Innovator Awards, and the U.S. National Science Foundation's CAREER grants.

In addition, innovation often comes from nontraditional thinking, and many new ideas will come from new participants in science and engineering who often are less tied to traditional ways. That argues for increasing the diversity of the scientific human resource pool, adding more women, minority, and disabled scientists, as well as researchers from smaller and less-well-known institutions. The benefits of increasing diversity for fostering innovation and economic success have been argued well elsewhere.** Both research institutions and funders need to attend more to these sources of novel thinking and may have to refine recruitment, reward, and funding systems accordingly.

These kinds of systemic adjustments in the major S&T-performing and -funding institutions will be hard to make, particularly in the face of severe budget cutbacks that threaten ongoing research programs in many parts of the world. Making these changes will require leadership and courage at the highest levels of S&T institutions. But if the S&T community is going to continue to deliver on its part of the promise that has led to the belief that science, technology, and innovation will be the source of future well-being, changes will have to be made.

– Alan I. Leshner

10.1126/science.1208330

*www.nsf.gov/nsb/documents/2007/tr_report.pdf. **S. E. Page, *The Difference: How the Power of Diversity Creates Better Groups, Firms, Schools and Societies* (Princeton Univ. Press, Princeton, NJ, 2007).

Published by AAAS

ECOLOGY

Diversity Takes Time

Like many groups of organisms in the Amazonian tropical rainforest, hylid tree frogs show very high diversity. Moreover, there is strong variation in local diversity, with some localities and regions having much higher density of species than others. Wiens *et al*. take a phylogenetic approach to the question of the cause of this local variation. Their analysis indicates that there is little or no relationship between variation in local species richness and climate variables such as temperature and precipitation. Nor are the rates of diversification or morphological variation correlated with local richness. Instead, diversity is related to the length of time that hylids have occupied a region. Even though diversification rates slow down when multiple clades occupy a region, species nonetheless continue to accumulate with the length of time that the region has been occupied: The highest diversity occurs where the largest number of clades have coexisted for longest. — AMS

Ecol. Lett. **14**, 10.1111/j.1461-0248.2011.01625.x (2011).

CHEMISTRY

Being in Touch

Cellular communication in three-dimensional (3D) tissues often requires contacts between neighboring cells. These events are mediated by the surrounding extracellular matrix, which influences cell positioning and signal transmission and receipt. Although techniques exist for creating 3D cell constructions, they often depend on artificial scaffolds or the manipulation of individual cells via external forces or tools. Dutta *et al.* use liposomes that incorporate cationic lipids to fuse orthogonal functional groups, in the form of ketone and oxyamine molecules, to cell membranes of different populations of cells, which can subsequently be coupled through selective oxime ligation. Techniques have previously been developed to generate protein tags on a cell's surface, but these tags have tended to be large and bulky, and thus interfered with other glycans and biomolecules or with the biochemical pathways or functioning of the cells. The authors explored a wide range of applications for their methodology, including the delivery of reagents to cell surfaces, formation of spheroid assemblies of cells with controlled interconnectivity, and patterning of multilayered cell tissues. When multilayers of human mesenchymal stem cells and fibroblasts were assembled together, differentiation led to tissue structures resembling adipocytes and fibroblasts. Liposome fusion could be performed on the same cells several times; thus, there is scope for giving cells multiple surface functionalities or for increasing the concentration of the functional groups at the surface. — MSL

J. Am. Chem. Soc. **133**, 10.1021/ja2022569 (2011).

CELL BIOLOGY

Sickle Cells Protect

The genetic mutation that causes sickle cell anemia is a double-edged sword. Individuals who carry one copy of the mutant hemoglobin allele do not develop sickle cell disease but can show greater resistance to malaria. This may be because despite not developing full-blown disease, their blood still carries some consequences of the mutated allele. Ferreira *et al*. have now analyzed the chain of events that connect the pathology of one copy of mutant hemoglobin with defense against malaria. Mice that express a sickle variant of the human hemoglobin gene were less likely to develop cerebral malaria than normal mice, despite similar parasite loads. The protective effect was attributed to heme oxygenase-1 (HO-1), which metabolizes free heme, generating carbon monoxide as one of the derivatives. In mice with the sickle cell allele, there was a greater tendency for release of free heme, leading to increased induction of HO-1 to remove the heme, which generated more carbon monoxide, which in turn bound to and stabilized hemoglobin, with the overall effect being reduced immune pathology and oxidative stress. Unlike many defense strategies that reduce pathogen burden, this strategy allows the host to be more tolerant of the infection. — PJH

Cell **145**, 398 (2011).

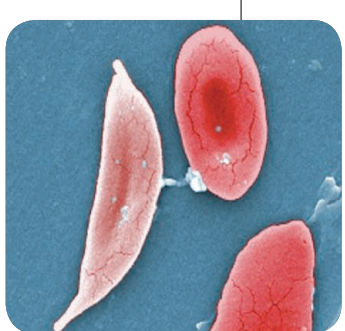

CREDIT (TOP TO BOTTOM): DAN MOEN; JANICE HANEY CARR/CDC

GEOPHYSICS

Cool, Sink, and Thicken

The oceanic lithosphere, which includes the crust and some of the brittle underlying mantle, forms at mid-ocean ridges. As this material is pushed further away from a ridge, it slowly cools over millions of years and sinks, creating deep ocean basins with measurable depths. The evolution of lithosphere thickness with age or distance from the ridge, however, is more difficult to quantify, because seismic methods often fail to resolve its lower limits (over 100 km) across an oceanic plate. Using a method based on waveform modeling of seismic wave precursors, Rychert and Shearer mapped

Continued on page 1013

Continued from page 1011

the seismic discontinuity that defines the bottom of the lithosphere across the Pacific Ocean. Like depth, lithosphere thickness increases with distance from the ridge, in the direction that the convecting mantle below pulls it away. Moreover, the boundary layer is defined by a sharp velocity drop, signifying that the depth of the discontinuity is at least in part controlled by thermal variations between the lithosphere and the underlying viscous asthenosphere. Water or melting may also contribute to the sharpness of the discontinuity. — NW

J. Geophys. Res. **116**, 10.1029/2010JB008070 (2011).

MOLECULAR BIOLOGY

Demethylation DNA Dynamics

The methylation of DNA on cytosine (C) bases, most often at CpG sites, plays an important role in the epigenetic regulation of genomic imprinting, suppression of transposons and other parasitic DNA sequences, and X chromosome inactivation. Addition and removal of DNA methylation can be highly dynamic, but the means by which the methyl mark is removed in animals is unclear. One possible route involves the oxidation of 5-methylcytosine (5mC) to 5-hydroxymethylcytosine (5hmC) by the ten-eleven translocation (Tet) enzyme family.

Xu *et al*. map the binding of Tet1 across the genome of mouse embryonic stem cells and, along with Pastor *et al*., map the genome-wide occurrence of 5hmC. Tet1 bound to unmodified CpG, to 5mCpG, and to 5hmCpG. Tet1 was enriched at promoters and in gene bodies, and its binding correlated with high CpG levels. Besides being enriched in gene bodies (and particularly exons), 5hmC was found at transcription start sites and at silenced promoters and at poised (but inactive) promoters in particular. Its occurrence at some enhancers further reinforces the idea that the presence of 5hmC might prime some quiescent loci for rapid activation. — GR

Mol. Cell **42**, 1 (2011); *Nature* 10.1038/nature10102 (2011).

CELL BIOLOGY

Pass the Calcium, Please

The prostate gets a lot of bad press as a source of problems for aging men, but now a new study suggests that it plays a key role in preparing sperm for successful fertilization. Prostate cells release prostasomes, vesicles that fuse with sperm cells during ejaculation. Park *et al*. found that fusion with prostasomes transfers a molecular "tool kit" to sperm that enables the dynamic calcium signaling events in sperm required for optimal motility and subsequent fertilization. In vitro analysis showed that sperm that had fused with prostasomes received components of the calcium signal transduction machinery, including progesterone receptors (which respond to progesterone released by cells surrounding the egg), ryanodine receptors (which are calcium-permeable channels), and an enzyme that produces cyclic adenosine diphosphoribose (which acts to open ryanodine receptor channels). The transfer of these various elements enhanced calcium signaling in the sperm, sperm motility, and fertilization efficiency in vitro. Thus, despite being stripped-down cells with little cytoplasm and few organelles, sperm are able to use a sophisticated calcium signaling mechanisms, thanks to the bits passed to them from the prostate. — LBR

Sci. Signal. **4**, ra31 (2011).

MATERIALS SCIENCE

A Bumpy Road to the Surface

Nanoparticles formed from mixtures of proteins and synthetic polymers are of interest for applications such as protein delivery. Ge *et al*. examined the surface evolution of particles comprising conjugates of bovine serum albumin (BSA) and poly(methyl methacrylate) (PMMA). They first added 51 acryloyl groups to each denatured BSA molecule and then initiated radical polymerization at each site. Nanoparticles varying in BSA content from 4 to 82% by

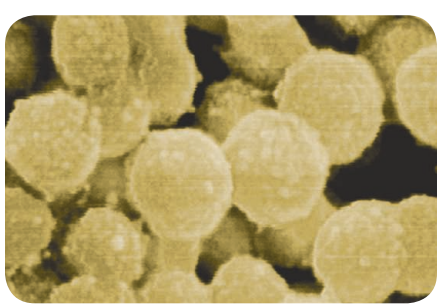

weight resulted from injection of an acetonitrile solution of these conjugates into phosphate-buffered saline. At the highest BSA content, the nanoparticles were well dispersed but the otherwise uniform surface of PMMA was covered with islands of BSA (as shown above). These islands grew over 2 weeks' time from surface patches to surface bumps in the buffered saline, but were unchanged if the nanoparticles remained in acetonitrile. The authors present a model in which PMMA, which is better solvated in acetonitrile, forms the main shell at the outset; over time in the aqueous medium, the more hydrophilic BSA then migrates to the surface. — PDS

Nano. Lett. **11**, 10.1021/nl201303q (2011).

CREDIT: GE *ET AL.*, *NANO. LETT.* **11**, 10.1021/NL201303Q (2011)

www.sciencemag.org

Science

1200 New York Avenue, NW
Washington, DC 20005
Editorial: 202-326-6550, FAX 202-289-7562
News: 202-326-6581, FAX 202-371-9227
Bateman House, 82-88 Hills Road
Cambridge, UK CB2 1LQ
+44 (0) 1223 326500, FAX +44 (0) 1223 326501

Subscription Services For change of address, missing issues, new orders and renewals, and payment questions: 866-434-AAAS (2227) or 202-326-6417, FAX 202-842-1065. Mailing addresses: AAAS, P.O. Box 96178, Washington, DC 20090-6178 or AAAS Member Services, 1200 New York Avenue, NW, Washington, DC 20005

Institutional Site Licenses please call 202-326-6755 for any questions or information

Reprints: Author Inquiries 800-635-7181
Commercial Inquiries 803-359-4578

Permissions 202-326-7074, FAX 202-682-0816

Member Benefits AAAS/Barnes&Noble.com bookstore www.aaas.org/bn; AAAS Online Store www.apisource.com/aaas/ code MKB6; AAAS Travels: Betchart Expeditions 800-252-4910; Apple Store www.apple.com/eppstore/aaas; Bank of America MasterCard 1-800-833-6262 priority code FAA3YU; Cold Spring Harbor Laboratory Press Publications www.cshlpress.com/affiliates/aaas.htm; GEICO Auto Insurance www.geico.com/landingpage/go51.htm?logo=17624; Hertz 800-654-2200 CDP#343457; Office Depot https://bsd.officedepot.com/portalLogin.do; Seabury & Smith Life Insurance 800-424-9883; Subaru VIP Program 202-326-6417; VIP Moving Services www.vipmayflower.com/domestic/index.html; Other Benefits: AAAS Member Services 202-326-6417 or www.aaasmember.org.

science_editors@aaas.org	(for general editorial queries)
science_letters@aaas.org	(for queries about letters)
science_reviews@aaas.org	(for returning manuscript reviews)
science_bookrevs@aaas.org	(for book review queries)

Published by the American Association for the Advancement of Science (AAAS), *Science* serves its readers as a forum for the presentation and discussion of important issues related to the advancement of science, including the presentation of minority or conflicting points of view, rather than by publishing only material on which a consensus has been reached. Accordingly, all articles published in *Science*—including editorials, news and comment, and book reviews—are signed and reflect the individual views of the authors and not official points of view adopted by AAAS or the institutions with which the authors are affiliated.

AAAS was founded in 1848 and incorporated in 1874. Its mission is to advance science, engineering, and innovation throughout the world for the benefit of all people. The goals of the association are to: enhance communication among scientists, engineers, and the public; promote and defend the integrity of science and its use; strengthen support for the science and technology enterprise; provide a voice for science on societal issues; promote the responsible use of science in public policy; strengthen and diversify the science and technology workforce; foster education in science and technology for everyone; increase public engagement with science and technology; and advance international cooperation in science.

Information for Authors
See pages 784 and 785 of the 11 February 2011 issue or access www.sciencemag.org/about/authors

AROUND THE WORLD

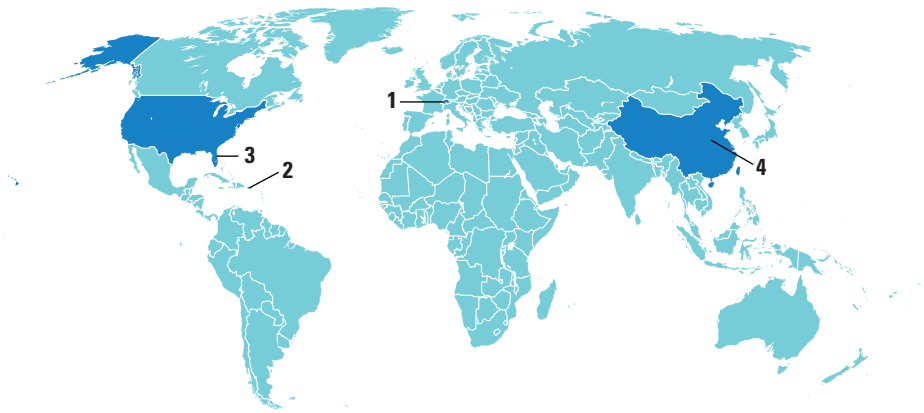

Geneva, Switzerland **1**

Smallpox Virus Wins 3-Year Reprieve

The smallpox virus, on death row for decades, will live to see another day. On 24 May, the World Health Assembly (WHA) decided not to set a deadline for the destruction of the last samples of the virus, called variola, and to revisit the issue in 2014.

Smallpox was eradicated in the 1970s, but the planned destruction of the two remaining repositories has been postponed because their holders, the United States and Russia, argue that they need more time to develop new vaccines, treatments, and diagnostics. In recent years, however, pressure has built to set a deadline for destruction (*Science*, 28 January, p. 389).

Yet in the run-up to the WHA, "a lot of arm-twisting" by the United States had brought many developing countries over to the U.S.-Russian camp, says Jonathan Tucker, a biosecurity specialist at the Federation of American Scientists in Washington, D.C. The European Union was in favor of retaining the virus as well, but a group of at least 20 countries, many in the Middle East, remained firmly opposed. The 3-year extension that emerged as a compromise is "regrettable," says Donald Henderson of the University of Pittsburgh in Pennsylvania, who spearheaded the smallpox eradication campaign and is a leading advocate of destruction. **http://scim.ag/smallpox-stays**

Arecibo, Puerto Rico **2**

Famous Observatory Changes Hands

After 4 decades under the direction of Cornell University, Arecibo Observatory in Puerto Rico, home to the largest radio telescope in the world, will have a new manager. The National Science Foundation (NSF) has decided to award a 5-year contract to a consortium comprising SRI International, the Universities Space Research Association, Universidad Metropolitana, and other institutions. Aided by money from NASA, NSF last year agreed to a level of funding that will keep Arecibo open at least through 2016. It also launched a competition to run the facility; a Cornell-led consortium and the SRI-led partnership were the only bidders. An Arecibo researcher who confirmed the decision notes that SRI had circulated a memo among staff members indicating that the new management would do its best to maintain current salaries and staffing. The status of observatory employees on Cornell's campus is uncertain, as is the fate of some Arecibo-related technology development projects at Cornell. **http://scim.ag/_arecibo**

Kennedy Space Center, Florida **3**

Cosmic Ray Detector Up and Running

The largest and most expensive particle detector ever to be flown in space was safely bolted onto the International Space Station on 19 May during the space shuttle Endeavour's last mission and is already recording celestial hits.

The nearly 7-ton, $2 billion Alpha Magnetic Spectrometer (AMS), detects charged cosmic rays, particles that whizz through space at high speeds. Logging 10,000 cosmic rays per minute, AMS should be able to measure the flux of particles far more precisely than balloon-borne experiments. Its creators hope to solve one of astrophysics' most enduring mysteries: What cosmic event launches the particles off into space at nearly the speed of light? The researchers also hope to catch particles from theorized antimatter galaxies, and even elusive dark matter, in the bargain.

After the 3-hour transfer operation, involving both the shuttle's and the station's robot arms, physics Nobelist Samuel Ting, who masterminded AMS, thanked the astronauts for "a great ride and a safe delivery," adding, "You made a great contribution to our understanding of the universe."

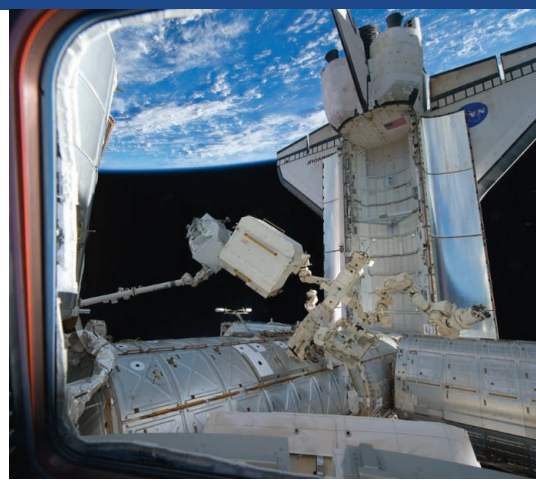

A robot arm brings AMS aboard the International Space Station from the space shuttle Endeavour.

China **4**

AIDS Deaths Plummet With Government's About-Face

Encouraging new results from China's recent campaign against HIV reflect a dramatic change in the country's attitude toward the disease.

In 2002, China introduced antiretroviral (ARV) drugs to treat HIV-infected people. Over the next 7 years, mortality from the disease dropped by 60%, according to a new report from the Chinese Center for Disease Control and Prevention (CDC). The results, published online 19 May in *The Lancet Infectious Diseases*, highlight China's evolution from a country in denial about its epidemic to one that has now mounted a serious response.

The Chinese CDC estimates that the country has 740,000 HIV-infected people and that slightly under half of them know their status. As of the end of 2009, China—with the help of more than $500 million in

CREDITS (TOP TO BOTTOM): NASA; CDC/ DR. FRED MURPHY

Published by AAAS

grants from the Global Fund to Fight AIDS, Tuberculosis and Malaria—provided ARVs to 82,450 HIV-infected people, which the report authors note is a "remarkable" 63.4% of those identified as infected and in immediate need of the drugs.

China's response still falls far short of what's needed, the CDC report says. It calls for scaling up HIV testing to detect more infections, increasing efforts to start ARVs earlier, and more aggressively monitoring for drug resistance. Yet the government has not committed new money to these efforts and, in a sobering turn of events, the Global Fund last week halted payments to China because of concerns about how the country manages its grants.

NEWSMAKERS

Man With a Mission

At a scientific forum this week in Boston, former congressman **Patrick Kennedy** kicked off an ambitious new campaign to raise $5 billion for basic brain research over the next 10 years. The effort, called One Mind for Research, was developed with the help of prominent neuroscientists and hopes to draw money from a combination of government, corporate, and philanthropic sources to spur research on genetics, epigenetics, brain circuit mapping, stem cells, and other areas that could provide insights into neuropsychiatric disorders.

In an interview with *Science*, Kennedy drew a parallel to the rallying cry to send a man to the moon made by his uncle, President John F. Kennedy, 50 years ago this week. He says that it's a national obligation to find treatments for soldiers returning from Iraq and Afghanistan with traumatic brain injuries and post-traumatic stress disorder, and to mitigate the overall social and financial burden caused by brain disorders. "The goal is to address the largest moral, economic and political crisis we're facing as a nation," he says.

Kennedy says he hopes to unite researchers and advocates working on specific diseases around the common goal of better basic science. "We've started by trying to break down the silos, by reminding everyone at this conference this week that we share the same highway of basic neuroscience that will get us to our respective off-ramps." The effort's 10-year research plan is available online at www.1mind4research.org.

FINDINGS

A Remarkable Recovery

A college athlete paralyzed in a hit and run accident has regained the ability to stand for a few minutes and to perform some voluntary movements, thanks to electrodes doctors fixed onto his spinal cord.

After his injury, Rob Summers couldn't move his trunk or legs, even after 2 years of intensive physical therapy. In December 2009, surgeons at the University of Louisville in Kentucky placed a strip of electrodes on top of his spinal cord. Following a few therapy sessions in which researchers pulsed electric current through the electrodes, Summers was able to maintain a standing position with some assistance. Seven months later, he was able to stand unassisted for several minutes and could move his toes, feet, and legs on command while lying in bed. He also reports improved bladder control and sexual function, according to a 20 May case report in *The Lancet.*

Other researchers say Summers's recovery is remarkable, perhaps even unprecedented. But they caution that the procedure is far from a complete cure and may not work as well for patients who are older or whose injuries are more severe.
http://scim.ag/_recovery

Long-Lost Tree Rat Reappears

A rare arboreal rat wandered up to an eco-lodge in Colombia earlier this month, dumbfounding researchers who had previously searched for it in vain. "It's almost Disney-esque," says conservation biologist Paul Salaman of the World Land Trust-US, which had conducted the search. "It found us. "

The red-crested tree rat (*Santamartamys rufodorsalis*) was last seen in 1898, when a collector shot one in northern Colombia near what is now the El Dorado Nature Reserve. Six years ago, mammalogist Louise Emmons of the Smithsonian Institution's National Museum of Natural History studied the two known specimens and concluded that they represented a new genus. That inspired Salaman and others to >>

A Home for Curiosity?

Scientists who next year will be searching for signs of ancient life on Mars using NASA's Curiosity rover (a.k.a. Mars Science Laboratory) spent last week in a 3-day-long huddle near the Jet Propulsion Laboratory in Pasadena, California, trying to decide where to land their rover. The workshop of about 120 scientists ended 19 May without producing a clear favorite, but NASA Associate Administrator Edward Weiler, with advice from Curiosity project leaders, will make a final decision by early July. One of four finalists is Gale Crater, constructed here from Mars imaging and other data. The target in Gale would be its 5-kilometer-high pile of sediments—or rather the bottom layers, laden with both clays and sulfates that may record the loss of an early, life-friendly environment on Mars. For images of the three other potential landing spots, visit http://scim.ag/land_mars.

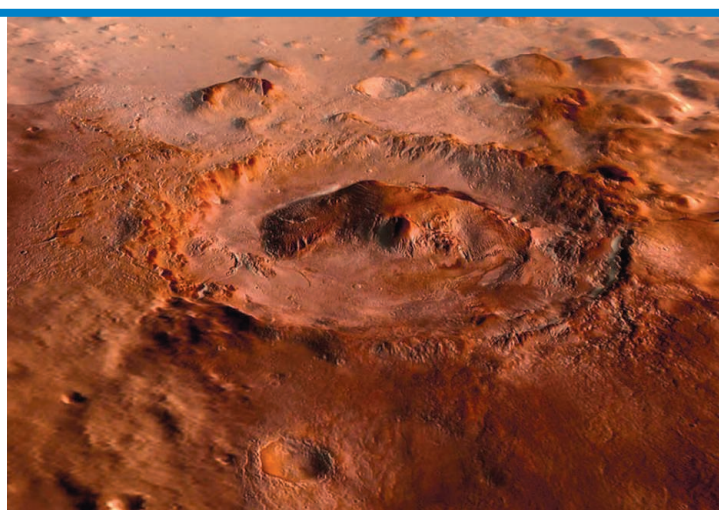

CREDITS (TOP TO BOTTOM): STEVEN SENNE/AP PHOTO; LIZZIE NOBLE/PROAVES; STEVEN HOBBS/NASA, JET PROPULSION LABORATORY

Published by AAAS

BY THE NUMBERS

50% The reduction in greenhouse gas emissions below 1990 levels that the United Kingdom is obligated to reach by 2025, according to the country's new targets.

$25 million Amount donated by energy baron and philanthropist George Mitchell to the proposed Giant Magellan Telescope, one of two massive, ground-based telescope projects competing for National Science Foundation funding.

$1.7 million Amount for which a California woman allegedly tried to sell what she claimed was a moon rock to NASA investigators during a sting operation last week.

Random Sample

A Bright Mind Shines Again

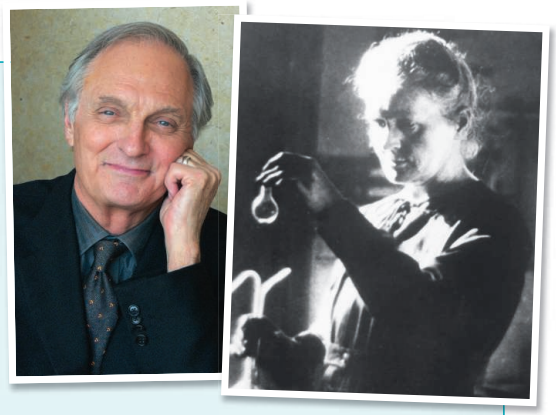

True to empirical tradition, while writing his new play on Marie Curie, actor Alan Alda once hurried through the streets of Paris from the Sorbonne to a certain apartment on Rue du Banquier. The goal: to see how breathless the physicist would have been upon arriving at trysts with her lover. On 1 June, a reading of *Radiance: The Passion of Marie Curie*, with Maggie Gyllenhall reading the part of Curie, will kick off the World Science Festival in New York City.

The play covers the interval between Curie's two Nobel prizes, during which she was reviled for "what people thought were transgressions in her personal life," Alda says. The Nobel committee grudgingly included her with husband Pierre and Henri Becquerel for the physics prize in 1903 but demanded that she sit in the audience at the award ceremony "as if she was Pierre's assistant," Alda says. "It was misogyny." Because of an illicit romance after Pierre's death, in 1911 she was almost denied her second Nobel, in chemistry, for her work in radioactivity. "There's an arc to her character," Alda says of those 8 years. "You see her gather her forces against tremendous obstacles."

Alda himself faced hindrances. Curie's letters are still radioactive, so he tracked down a rare French copy of her diaries. During a visit to her lab, his guide held a Geiger counter up to a notebook entry from the day she discovered radium. Says Alda, "The page clicked like a tap dancer."

>>FINDINGS

mount a search in 2007 for the species in the reserve. They had no luck. But on the evening of 4 May, two volunteer field assistants were climbing the stairs to the reserve's ecolodge when a juvenile tree rat hopped onto the hand rail, where it curled up for 2 hours. The volunteers sent photographs to Salaman, who immediately identified it.

Lost species of mammals are rediscovered every decade or so in South America, says Emmons. Salaman worries that feral cats may find such a tame animal an easy meal; he is sending traps to help remove the predators from the 809-hectare reserve.

Raising a Planetary Runt

With a mass 11% that of Earth, Mars is decidedly undersized. But planetary dynamicists following their standard recipes for making planets have always cooked up a Mars the size of Earth or Venus. Now it appears Mars failed to grow into an Earth-size planet because it escaped prematurely from its nurturing womb of dust and rubble.

This week in *Nature*, geochemists Nicolas Dauphas of the University of Chicago and his former postdoc Ali Pourmand report that Mars reached its current size lightning fast compared to our planet. Based on the steady decay of radioactive hafnium to tungsten recorded in martian meteorites, Mars stopped growing after only 2 million to 4 million years, not the tens of millions of years that Earth would have taken to agglomerate from moon- to Mars-size planetary "embryos."

So why did Mars grow no further? Two studies presented at March's Lunar and Planetary Science Conference in Houston, Texas, suggest that the best way to arrest Mars's development was to starve it of building material. One has Mars popping out of its rock-filled birthing grounds into such thinly populated space that it stopped growing. The other proposes that Jupiter drifted inward, carving out a gap where Mars starved, then drifted back out. **http://scim.ag/mars-runt**

From Humble Beginnings

Llama wool and meat have long been staples among people of the central Andes. A new study suggests that a much humbler llama byproduct—dung—may have helped maize farming in the region take off, fueling the rise of ancient Andean society.

Paleoecologist Alex Chepstow-Lusty of the Institut Français d'Études Andines in Lima took sediment cores from a lakebed some 65 kilometers northwest of Cuzco. While he was radiocarbon-dating the core's organic material and analyzing pollen trapped in the layers, he noticed the remains of small, soil-dwelling invertebrates. They were oribatid mites, which dine on dung and other detritus.

Maize pollen first appeared in the core some 2700 years ago, at the same point that mite numbers began spiking, indicating that growing numbers of llamas and possibly alpacas were supplying manure that could be used to fertilize maize fields, Chepstow-Lusty says. As they expanded their cornfields with the help of fertilizer, the people in the Cuzco Basin amassed greater surpluses of food, allowing them to feed a large standing army and work on infrastructure such as new road networks.

"Maize soon strips the fertility from the soils and this needs to be replenished by fertilizers," says Chepstow-Lusty. Dung was an obvious choice to keep the farms running, he notes, and maybe that in turn helped make a more complex society possible. **http://scim.ag/llama-dung**

CREDITS (TOP TO BOTTOM): COURTESY OF ALAN ALDA; RADIUM INSTITUTE, COURTESY AIP EMILIO SEGRÈ VISUAL ARCHIVES; NASA (3)

Published by AAAS

CANCER RESEARCH

Texas's $3 Billion Fund Lures Scientific Heavyweights

Last September when a shift toward industrial research in their adopted Singapore persuaded mouse geneticists Neal Copeland and Nancy Jenkins to return to the United States, they soon realized it wouldn't be easy. The two had spent most of their careers at the U.S. National Cancer Institute (NCI), which funded their costly mouse research program. The setup was similar at Singapore's Institute of Molecular and Cell Biology. But at most academic institutions in the United States, they would need to apply for grants at a time when the chances of winning funding from the budget-strapped NCI are at a record low. "It wasn't a pretty picture," Copeland says.

Then they got an enticing offer from The Methodist Hospital Research Institute (TMHRI) in Houston, Texas. With help from a $3 billion state cancer research fund, the institute came up with a 5-year, $29 million package that includes the two scientists' salaries, research costs, and ample space in a new research building for their hundreds of mice. "Texas is the only place right now to get that kind of money," Copeland says.

The power couple aren't the only big fish that the state is reeling in with help from the Cancer Prevention and Research Institute of Texas (CPRIT), approved by voters through a ballot initiative in 2007. The institute, which received $450 million for its first 2 years, expects to announce three more "superstar" recruits this year. That comes on top of 18 junior and midcareer scientists brought in over the past 2 years, scores of grants for researchers already in Texas, and a new clinical trials network. "Things are going spectacularly," says Alfred Gilman, chief scientific officer of CPRIT, which bills itself as the largest cancer research fund in the country besides the $5 billion NCI.

Cancer geneticist Ronald DePinho of the Dana-Farber Cancer Institute in Boston, who was tapped this month to head MD Anderson Cancer Center in Houston, says CPRIT was one of several factors that persuaded him to leave Boston for the Lone Star state. "It's an important element," DePinho says. "It's a very positive shot in the arm for Texas research in general."

Texas cancer research advocates and legislators crafted the plan to sell $3 billion in bonds over 10 years for CPRIT 4 years ago, inspired by California's $3 billion stem cell research fund. Although some worried that politics would override scientific merit in awarding grants, concerns faded when Gilman, a Nobel Prize–winning biochemist then at the University of Texas (UT) Southwestern Medical Center at Dallas, joined CPRIT (*Science*, 15 May 2009, p. 868). Peer review of grant applications, all done by non-Texans, is "going extremely well," largely due to Gilman's "strong scientific taste and backbone," says William Kaelin of Dana-Farber, a member of CPRIT's scientific review council, which is chaired by biologist Phillip Sharp of the Massachusetts Institute of Technology.

Most of the money has gone to academic researchers in Texas—a mix of individual and multi-investigator projects, training grants, and other awards (see chart). (Institutions must come up with funds for a 50% match.) Although some projects overlap with what NCI already supports, "we will accept a lot more risk to fund things with real impact," Gilman says. And CPRIT grants aren't particularly easy to get: The success rate for newly submitted research grants has ranged from 8% to 18%, which is comparable to NCI success rates, Gilman says.

Another chunk of funds has gone into recruiting researchers from outside Texas. "Rising star" Joshua Mendell, who will move his microRNA lab from Johns Hopkins University to UT Southwestern this summer, says he wasn't looking to leave Baltimore. "They were able to convince me that I would be able to expand my research in new directions" that might be considered too risky by National Institutes of Health reviewers, he says. Mendell's wife, Kathryn O'Donnell, who is winding up a postdoc at Johns Hopkins, will start her first lab at UT Southwestern with CPRIT support.

Copeland and Jenkins, who mutate DNA in mice to find new potential cancer genes and model human cancers, will use their technique to develop cancer treatments. "Their role is perfect for us," says Mauro Ferrari, president of TMHRI, which is expanding after forming 7 years ago. Meanwhile, Sean Morrison of the University of Michigan, Ann Arbor, who studies how adult stem cells can give rise to birth defects and cancer, is moving to UT Southwestern, where he will head a pediatric research initiative. He will "bring cancer stem cell research in a large way to Texas," says UT Southwestern developmental biologist Luis Parada, who helped recruit him.

Rice University in Houston has used CPRIT funds to woo physicists José Onuchic and Herbert Levine, who head a U.S. National Science Foundation–funded center for integrating physics and biology at the University of California, San Diego. The two have been looking to apply their work on how proteins fold and cells move to the growth and spread of cancer cells, and the CPRIT

An offer they couldn't refuse. Cancer geneticists Nancy Jenkins and Neal Copeland are two of the "superstars" relocating to Texas.

CREDIT: COURTESY OF NEAL COPELAND AND NANCY JENKINS

> *"People are asking, 'How can you move from San Diego to Texas?' The answer is that science comes first at the end of the day; weather comes second."*
>
> —HERBERT LEVINE, UCSD

Published by AAAS

award will provide "a springboard," says Onuchic. Quips Levine: "People are asking, 'How can you move from San Diego to Texas?' The answer is that science comes first at the end of the day; weather comes second." (The five "superstar" recruitments won't be official until CPRIT's board approves them in July, Gilman says.)

Now that CPRIT has proved itself, Gilman expects the legislature to approve the full $600 million for the next 2 years. One question is whether the state will reach a "saturation" point where all Texas labs with worthy proposals have won a grant, Kaelin says. But Gilman says another 10 to 20 recruits each year will help keep up the demand for grants. In addition, the fund will soon begin supporting clinical trials through CTNeT, a state clinical trials network that aims to avoid problems with NCI's creaky cooperative groups. "It will be streamlined from the get-go," with genetic analysis of tumors and high-quality tissue banking, says network steering committee chair and UT Southwestern oncologist David Johnson, whom CPRIT recruited from Vanderbilt University last year.

Gilman says CPRIT has plenty left to do: "It's tough to figure out exactly where the steady state will be, but I think it will work out pretty well."

–JOCELYN KAISER

CPRIT's First 2 Years

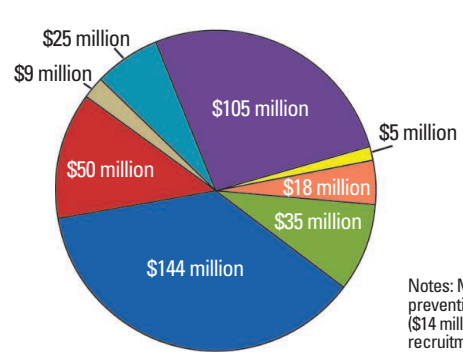

Notes: Multiyear awards. Does not include prevention ($45 million), administration ($14 million), or full obligations for July 2011 recruitments.

Spreading the wealth. CPRIT is spending its first $450 million on a variety of programs.

IMMUNOLOGY

Regulatory T Cells Get Their Chance to Shine

Like a heavily recruited high school basketball star, regulatory T cells (T regs) carry a hefty burden of expectations. The cells naturally rein in immune attacks, and infusing T regs into mice curbs the rejection of transplanted organs and halts, or even reverses, the progression of autoimmune diseases. Whether T regs can duplicate such feats in people is now the question.

Researchers are encouraged by results from initial T reg safety trials, in which the cells were given to patients vulnerable to graft-versus-host disease (GVHD), a sometimes lethal complication of transplants of bone marrow and blood-making stem cells that occurs when mature immune cells in the transplant turn on their new host. The first clinical trial to pit T regs against an autoimmune disease, type 1 diabetes, has also recently begun. And European scientists are starting a study of the cells' ability to forestall rejection of transplanted kidneys. "It's a terrific, exciting time in the field," says immunologist Alexander Rudensky of the Memorial Sloan-Kettering Cancer Center in New York City.

Once known as suppressor T cells before they fell out of favor decades ago, T regs have made a comeback over the past 15 years as researchers have found better ways to identify and study these cells (*Science*, 6 August 2004, p. 772). Still, immunologist Ethan Shevach of the National Institute of Allergy and Infectious Diseases in Bethesda, Maryland, and other scientists caution that most of the practical questions about the cells—which varieties of T regs to use in a treatment, how many to transfer, how long their effects last—remain unanswered. And as three papers (http://scim.ag/human-treg, http://scim.ag/funtional-treg, and http://scim.ag/exvivo-treg) published last week in *Science Translational Medicine* (*STM*) reveal, researchers are still hunting for the best method to obtain clinically useful quantities of the rare, hard-to-grow cells.

Leading the way on T regs are scientists searching for new ways to forestall GVHD. For example, transplant immunologist Bruce Blazar of the University of Minnesota, Twin Cities, and colleagues recently conducted a phase 1 trial in which they transferred T regs into 23 leukemia and lymphoma patients who had just undergone transplants of cord blood, which contains blood-generating stem cells. Almost simultaneously, a group led by hematologist Mauro Di Ianni of the University of L'Aquila in Italy was administering T regs to 28 lymphoma and leukemia patients who had gotten replacement blood-forming stem cells.

> *"It's a terrific, exciting time in the field."*
>
> —ALEXANDER RUDENSKY, MEMORIAL SLOAN-KETTERING CANCER CENTER

Neither team has found any obvious safety concerns. A potential hazard was that the added T regs would scupper immune defenses against microbes, but Blazar and colleagues reported online in October in *Blood* that the cancer patients receiving T regs and cord blood didn't suffer more infections, compared with historical controls, suggesting that the cells didn't impair overall immunity. The results also hinted that T regs didn't affect how long the patients

Regulatory T Cells Enter the Clinic

Target	Source of T regs	Type of trial	Status
Graft-versus-host disease (GVHD)	Cord blood	Phase I	Completed
GVHD	Peripheral blood	Phase I	Completed
Type 1 diabetes	Autologous	Phase I	Recruiting patients
Kidney transplant rejection	Autologous	Phase I	Received funding
GVHD	Induced in patient by interleukin-2	Phase II	Recruiting patients

GRAPH SOURCE: CANCER PREVENTION AND RESEARCH INSTITUTE OF TEXAS

award will provide "a springboard," says Onuchic. Quips Levine: "People are asking, 'How can you move from San Diego to Texas?' The answer is that science comes first at the end of the day; weather comes second." (The five "superstar" recruitments won't be official until CPRIT's board approves them in July, Gilman says.)

Now that CPRIT has proved itself, Gilman expects the legislature to approve the full $600 million for the next 2 years. One question is whether the state will reach a "saturation" point where all Texas labs with worthy proposals have won a grant, Kaelin says. But Gilman says another 10 to 20 recruits each year will help keep up the demand for grants. In addition, the fund will soon begin supporting clinical trials through CTNeT, a state clinical trials network that aims to avoid problems with NCI's creaky cooperative groups. "It will be streamlined from the get-go," with genetic analysis of tumors and high-quality tissue banking, says network steering committee chair and UT Southwestern oncologist David Johnson, whom CPRIT recruited from Vanderbilt University last year.

Gilman says CPRIT has plenty left to do: "It's tough to figure out exactly where the steady state will be, but I think it will work out pretty well."

–JOCELYN KAISER

CPRIT's First 2 Years

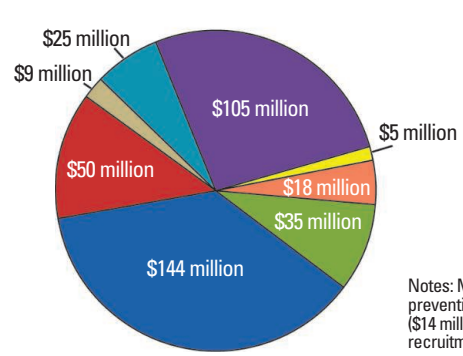

Notes: Multiyear awards. Does not include prevention ($45 million), administration ($14 million), or full obligations for July 2011 recruitments.

Spreading the wealth. CPRIT is spending its first $450 million on a variety of programs.

IMMUNOLOGY

Regulatory T Cells Get Their Chance to Shine

Like a heavily recruited high school basketball star, regulatory T cells (T regs) carry a hefty burden of expectations. The cells naturally rein in immune attacks, and infusing T regs into mice curbs the rejection of transplanted organs and halts, or even reverses, the progression of autoimmune diseases. Whether T regs can duplicate such feats in people is now the question.

Researchers are encouraged by results from initial T reg safety trials, in which the cells were given to patients vulnerable to graft-versus-host disease (GVHD), a sometimes lethal complication of transplants of bone marrow and blood-making stem cells that occurs when mature immune cells in the transplant turn on their new host. The first clinical trial to pit T regs against an autoimmune disease, type 1 diabetes, has also recently begun. And European scientists are starting a study of the cells' ability to forestall rejection of transplanted kidneys. "It's a terrific, exciting time in the field," says immunologist Alexander Rudensky of the Memorial Sloan-Kettering Cancer Center in New York City.

Once known as suppressor T cells before they fell out of favor decades ago, T regs have made a comeback over the past 15 years as researchers have found better ways to identify and study these cells (*Science*, 6 August 2004, p. 772). Still, immunologist Ethan Shevach of the National Institute of Allergy and Infectious Diseases in Bethesda, Maryland, and other scientists caution that most of the practical questions about the cells—which varieties of T regs to use in a treatment, how many to transfer, how long their effects last—remain unanswered. And as three papers (http://scim.ag/human-treg, http://scim.ag/funtional-treg, and http://scim.ag/exvivo-treg) published last week in *Science Translational Medicine* (*STM*) reveal, researchers are still hunting for the best method to obtain clinically useful quantities of the rare, hard-to-grow cells.

Leading the way on T regs are scientists searching for new ways to forestall GVHD. For example, transplant immunologist Bruce Blazar of the University of Minnesota, Twin Cities, and colleagues recently conducted a phase 1 trial in which they transferred T regs into 23 leukemia and lymphoma patients who had just undergone transplants of cord blood, which contains blood-generating stem cells. Almost simultaneously, a group led by hematologist Mauro Di Ianni of the University of L'Aquila in Italy was administering T regs to 28 lymphoma and leukemia patients who had gotten replacement blood-forming stem cells.

> *"It's a terrific, exciting time in the field."*
>
> —ALEXANDER RUDENSKY, MEMORIAL SLOAN-KETTERING CANCER CENTER

Neither team has found any obvious safety concerns. A potential hazard was that the added T regs would scupper immune defenses against microbes, but Blazar and colleagues reported online in October in *Blood* that the cancer patients receiving T regs and cord blood didn't suffer more infections, compared with historical controls, suggesting that the cells didn't impair overall immunity. The results also hinted that T regs didn't affect how long the patients

Regulatory T Cells Enter the Clinic

Target	Source of T regs	Type of trial	Status
Graft-versus-host disease (GVHD)	Cord blood	Phase I	Completed
GVHD	Peripheral blood	Phase I	Completed
Type 1 diabetes	Autologous	Phase I	Recruiting patients
Kidney transplant rejection	Autologous	Phase I	Received funding
GVHD	Induced in patient by interleukin-2	Phase II	Recruiting patients

GRAPH SOURCE: CANCER PREVENTION AND RESEARCH INSTITUTE OF TEXAS

remained alive and free of cancer.

Although the studies primarily addressed the safety of the treatment, both found evidence that it hinders GVHD. (Di Ianni's team reported its findings online in February in *Blood*.) For example, Blazar's team documented that just 43% of the T reg recipients developed the acute form of GVHD, which usually strikes in the first 3 months after the procedure. Typically, 61% of patients suffer from the complication. Blazar suggests that his group might have seen an even stronger protective effect if they'd been able to isolate more T regs to infuse: The researchers describe a new technique for cultivating large numbers of T regs in one of the *STM* papers.

The T regs in these GVHD studies share a drawback: They are third-party cells, meaning they didn't come from the intended recipients or from the same source as the bone marrow or stem cells being transplanted. (Blazar's group isolated T regs from umbilical cord blood, the other group from freshly donated blood.) The immune system could treat third-party T regs as invaders, unleashing an attack that could annihilate the cells or sicken the recipients. So in a recently launched diabetes trial, immunologist Jeffrey Bluestone of the University of California, San Francisco (UCSF), and colleagues instead plan to isolate T regs from each participant's blood, expand their numbers in the lab, and return them to that patient. The initial target population for this so-called autologous T reg therapy consists of young adults newly diagnosed with type 1 diabetes, in which the immune system devastates the insulin-making beta cells in the pancreas.

By the time people learn they that have type 1 diabetes, they typically retain only 15% to 40% of their beta cells, says pediatric endocrinologist Stephen Gitelman of UCSF, who is working with Bluestone on the trial. But even at this stage, they can usually keep their blood glucose under control with insulin doses and other measures. The ultimate goal, Gitelman says, is to determine whether T regs can "preserve the honeymoon," allowing people with manageable diabetes to remain at this stage by curbing the loss of beta cells.

Organ transplant recipients, who now require lifelong courses of drugs that knock down the immune system to prevent rejection of the transplant, are also about to receive T regs. Six European institutions are collaborating on the ONE Study, a 5-year project to test whether T regs can prevent rejection of kidney transplants. "There's a huge need to improve immunosuppression in [organ] transplants," says Andrew Bushell, a transplant immunologist at the University of Oxford in the United Kingdom, which is part of the project.

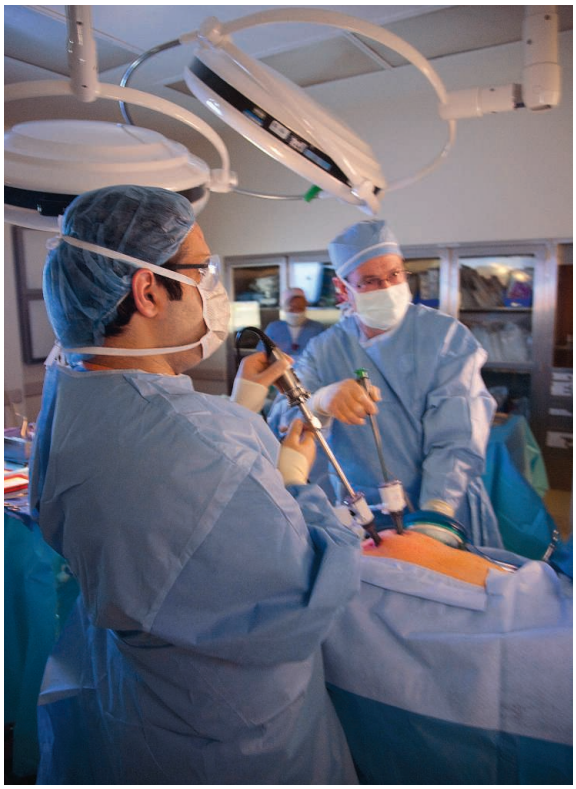

CREDIT: B. SLAVEN MD / CUSTOM MEDICAL STOCK PHOTO

Cellular help. Kidneys are often rejected by a recipient after a transplant operation (*above*), but administering regulatory T cells may prevent this.

The ONE Study and Bluestone's type 1 diabetes trial will dose patients with polyclonal T regs, which turn down immune responses relatively broadly. The alternative is so-called antigen-specific T regs, which block attacks by other T cells that target a particular antigen, such as a characteristic protein on the cells in a transplanted organ. In theory, antigen-specific T regs shouldn't provoke general immune suppression that might undermine antipathogen defenses and even lead to cancer. "We really believe that antigen specificity is the future of any successful T reg therapy," says transplant immunologist and ONE Study collaborator Giovanna Lombardi of King's College London. Bluestone says that future diabetes trials will also probably switch to antigen-specific T cells.

> *"Yes, we are going to see these cells in the clinic."*
>
> —ANDREW BUSHELL, UNIVERSITY OF OXFORD

Researchers can obtain antigen-specific human T regs that suppress immune responses to, say, a skin graft by exposing the T regs to cells from the graft's donor. But generating specific T regs to treat type 1 diabetes is tricky, Bluestone says, because researchers don't know which antigen they should protect in order to spare beta cells. Another limitation is that the techniques for producing antigen-specific T regs are less efficient than those for making the polyclonal variety. Two of the *STM* papers published last week address this problem. Bushell and colleagues showed that a drug prescribed for vascular inflammation could spur generalist human T cells to specialize into T regs that, when injected into mice, prevented rejection of human artery grafts. Meanwhile, Lombardi and her group found that they could hike the yield of antigen-specific human T regs in culture by sorting the cells based on two surface proteins that mark activated T regs.

Although the initial GVHD trials revealed no obvious safety risks, immunologist Christophe Benoist of Harvard Medical School in Boston notes that it remains a contentious issue whether T regs can convert into cells that attack rather than suppress. "In that case, antigen-specific T regs could be harmful," he says, because the treatment might introduce a large number of potentially destructive cells into the body.

Therapies that involve growing T regs in the lab face some big challenges. For one thing, Rudensky says, they are expensive. Blazar says that his cord-blood treatment cost nearly $40,000 per patient. Lombardi puts the cost of generating polyclonal T regs for the ONE Study at $32,000 to $48,000 per recipient.

Because of the technical challenges of producing ample T regs and the related high costs, some immunologists favor alternative approaches, such as identifying drugs that spur T regs to multiply within the body. For example, researchers at Baylor College of Medicine in Houston, Texas, and colleagues have begun a clinical trial to test whether injections of interleukin-2, an immune system messenger, boost T reg numbers and prevent GVHD. Still, other researchers are confident that transplanted T regs will have a medical role. "Yes, we are going to see these cells in the clinic," Bushell predicts. **–MITCH LESLIE**

Published by AAAS

REMOTE SENSING

India's Earth-Observing System Comes Under Fire

NEW DELHI—India's space officials were expecting a friendly get-together with the prime minister on 9 May to review images from a new satellite, but instead they got probing questions. The normally soft-spoken head of state, Manmohan Singh, demanded to know why satellites of the Indian Space Research Organisation (ISRO) were of no use in locating a recent air crash. On 30 April, a helicopter carrying Dorjee Khandu, chief minister of the eastern state of Arunachal Pradesh, went down near the border with Bhutan. ISRO—whose Earth-imaging operation includes a search-and-rescue function—was unable to find the wreckage. Villagers on foot found it 5 days later; Khandu did not survive.

The reason for the delay, ISRO Chair K. Radhakrishnan told Singh, was that the rainforest site was under heavy cloud cover and couldn't be seen. Nor did India's RISAT-II, an Israeli-made cloud-penetrating radar satellite with a resolution of 1 meter, offer help.

"We worked day and night but failed to identify the crash site," Radhakrishnan acknowledged in an interview with *Science*. He said that ISRO initially was misled by incorrect information from local authorities and by "false signals" caused by steep, mountainous terrain. The incident tarnished ISRO's image. A 5 May banner on *The Times of India* read, "Villagers Succeed Where Hi-Tech Failed."

ISRO was already under fire for the alleged inefficiency of its 10-satellite Earth-observing system, one of the world's largest. Critics say that it is expensive, poorly managed, and saddled with security restrictions that stifle its use by researchers and companies.

Some of these criticisms came to the fore in April when government auditors handed Parliament a scathing 57-page review of the National Remote Sensing Centre (NRSC) in Hyderabad, ISRO's Earth-observing arm. The Comptroller and Auditor General of India (CAG) conducted a "performance audit" of seven remote-sensing satellites over 7 years and found that they had been built without an adequate assessment of need. The system lacked an "appropriate marketing strategy," CAG found. And CAG faulted the network for "delays in data processing."

NRSC was meant to support national remote-sensing projects on food and water security, conversion of wastelands into usable land, and disaster management. But CAG faulted ISRO for poor interagency coordination. For example, CAG noted, the Ministry of Rural Development entrusted NRSC to map the inventory of wasteland using satellites in 1986. It took 14 years to produce the maps. NRSC says the pace was slow in part because it failed to get timely input from the Ministry of Rural Development. The bottom line, according to CAG, is that "inadequate co-ordination contributed to non-reclamation of 86.5 % of the targeted wastelands."

CREDIT: SHIVRAJ/GOVERNMENT OF INDIA

Tarnished image. ISRO Chair K. Radhakrishnan (*left*) and V. K. Dadhwal (*right*), director of the National Remote Sensing Centre, were cross-examined by Prime Minister Manmohan Singh (*center*) when they briefed him on 9 May.

Another vexing issue is the system's low usage rate. CAG found that 89% of all remote-sensing images in the collection are "idling," or lying unused in NRSC archives. V. Jayaraman, who until April was director of NRSC, says weather is partly to blame: "A third of the time, India is cloud-covered during the monsoons, during which time images yield nothing but yet have to be stored."

The CAG report says that between 2002 and 2009, India spent almost $551 million to design and launch the seven satellites it examined; in this period NRSC sold data worth about $39 million, recovering 7% of that expenditure. The CAG report says this was not even enough to "match its yearly operational expenditure." Radhakrishnan acknowledges that CAG's numbers are accurate but says that the system was not meant to pay for itself: "Nowhere [in the world] is remote sensing a commercially viable service."

The biggest headache for companies and nonprofit researchers hoping to use satellite images may be India's 2001 Remote Sensing Data Policy. It gives NRSC a monopoly within India to control access to images with less than 5.8-meter resolution—not just images from Indian satellites but also those from foreign sources. The policy is "primitive," says Arup Dasgupta, managing editor of *Geospatial World*, based here, who spent 35 years at ISRO working on remote sensing. Furthermore, Dasgupta says, the policy is "unimplementable, as it only hampers the policy-abiders, not the policy bypassers." (India does not block Google Earth images on the Internet.)

Thomas Snitch, a consultant to the GeoEye Foundation, a Herndon, Virginia–based remote-sensing nonprofit, agrees that the policy is a major problem. In an e-mail, he wrote that, "If an Indian researcher or student applies to the GeoEye Foundation for free imagery, I must turn them down unless they have an NRSC license." There was a time when India rejected applications by citing the need to protect national security, he notes. But applications are often "summarily denied with little or no justification" and no line of appeal. At the same time, Snitch says, would-be buyers may be contacted by ISRO's commercial arm, the Antrix Corp., and informed that they can buy Antrix imagery. "I know of no other nation that operates in this manner," Snitch says.

Kumar Navulur of DigitalGlobe Inc. in Longmont, Colorado, a company that owns imaging satellites, has a more charitable view. He says India needs to balance defense and commercial interests and weigh each case individually, as "programs are designed to get the right intelligence at the right time."

It is true, Radhakrishnan says, that because of the 2001 policy, ISRO cannot freely disseminate remote-sensing data that has a resolution of less than 5.8 meters. But he indicates that "the remote-sensing policy is being reviewed." **–PALLAVA BAGLA**

Published by AAAS

The Prion Heretic

For 30 years, Laura Manuelidis has rejected the dominant theory that misfolded proteins cause infection. Sticking to a minority view has become a career in itself

NEW HAVEN, CONNECTICUT—Laura Manuelidis has an acrobatic mind. Her train of thought evokes a circus performance. She soars up and drops down, she twirls, she swoops in one direction and swerves back to where she started. She titled her volume of poetry, published in 2007, *Out of Order*. "Isn't that fitting?" she says with a laugh.

Manuelidis has spent her whole adult life here at the Yale School of Medicine, first as one of a half-dozen women in her 1967 graduating class and then as a parser of brain tissue. At 24, she ignored taboo and wed her professor, 48-year-old Elias Manuelidis. Despite naysayers who declared the marriage doomed, it turned out to be a lively and passionate one, lasting until her husband's death from a stroke in 1992. Since then Manuelidis has pursued the work they began together: challenging the now-entrenched view that prions, which are misshapen proteins, transmit disease. Skeptics linger but rarely speak out. Now 68 years old, Manuelidis has become the de facto representative for doubters worldwide.

She knows that the history of science is littered with heretics who reject conventional wisdom, insisting that their experiments reveal the truth while others' do not. Often they turn out to be wrong and either abandon their view when the evidence against it grows overwhelming or go to their grave still believing. Sometimes they're right. Manuelidis, comfortable in the role of dissenter, likes to quote 20th century mathematician and philosopher Bertrand Russell: "Doubt is the essence of science," she says.

Her seeds of doubt—or rather, tall, flourishing plants—germinated years ago. In 1982, Stanley Prusiner, a neurologist at the University of California, San Francisco, gave prions their name. He described them as infectious particles made up mainly of a protein, PrP, that misfolds and goes awry in the brain, causing a cluster of rare, transmissible, and fatal brain diseases. Mad cow disease (officially known as bovine spongiform encephalopathy) is arguably the most famous.

When first proposed, Prusiner's theory was widely dismissed as bizarre. Biology then held that infectious disease was caused by organisms built from DNA, RNA, or both, like viruses and bacteria—something containing a nucleic acid sequence that can replicate and spread through a cell. Proteins lack these sequences. But Prusiner promoted his thesis, snagging millions of dollars in grants and publishing his experiments widely. In 1997, he won the Nobel Prize. Today, Prusiner's view dominates. "It's the dogma," says Adriano Aguzzi, a neuropathologist at the University Hospital of Zurich in Switzerland, who counts himself a believer.

Manuelidis takes an opposing stance that we don't need to rewrite the book on infectious disease to accommodate prions. She regards the protein not as the cause of infection but as a pathological reaction to it and believes mad cow disease and others like it are triggered by viruses. What—and where—those viruses are, Manuelidis isn't sure. No one has found them. Whether that means they don't exist depends on whom you ask.

CREDIT: MICHAEL MARSLAND/YALE UNIVERSITY OFFICE OF PUBLIC AFFAIRS

Published by AAAS

She's not the only prion doubter, but her voice is by far the loudest. In part that's because she's safe. Long a tenured professor at Yale, Manuelidis still commands vast lab space she no longer uses. Her unpopularity among top prion scientists leaves her unfazed. "What can they do to me?" she says. "If I don't say it, nobody's going to say it."

Beginnings

In her youth, Manuelidis aspired to be a poet. She enrolled at Sarah Lawrence College, a small liberal arts school outside New York City known for its strong focus on the arts and literature. Her older brother, with whom she'd always been close, was attending Harvard Medical School at the time. "He said, 'I don't see any want ads in *The New York Times* for poets. … How long are you going to be a parasite on Mom and Dad?' "

Manuelidis considered this problem and settled on medical school as an alternative. "My brother said, 'Why don't you become a nurse?' and I said, 'Why don't *you* become a nurse?' " she remembers. "He wanted a normal sister."

In medical school she knew from the start that she would focus on the brain, hoping to cure schizophrenia. Manuelidis had been deeply affected by college summers spent volunteering at Waltham State Hospital outside Boston, where she says patients were rarely seen by physicians. ("I looked in the charts" to find out.) They were so heavily drugged that they reeked of Thorazine, an antipsychotic drug. "I saw people with frontal lobotomies," she says. "I felt there was a certain arrogance in medicine. It was very good to see before I went to medical school."

Manuelidis embraced pathology, encouraged by a supportive department chair. Another draw was her neuropathologist husband-to-be, a confirmed bachelor when she met him. Their relationship was scandalous, she says. They lived together openly and threw large parties at his house attended by many of her friends.

The two began exploring a class of deadly diseases called transmissible spongiform encephalopathies (TSEs), so named because once symptoms surface, the brain turns into spongy tissue with alarming speed. TSEs in people are rare; the most prevalent, sporadic Creutzfeldt-Jakob disease, strikes about one person in 1 million each year. A curious feature is that TSEs, like viral diseases, can be passed from one animal to another by injecting affected brain tissue. TSEs also have a long latency period in animals. The first guinea pigs Elias Manuelidis exposed to TSE thrived for 500 days before getting sick.

But the virus, if there was one, was elusive. Some experiments indicated that there couldn't be a virus at all. A radiobiologist named Tikvah Alper showed in the 1960s that blasting infected tissue with radiation didn't destroy its ability to infect. And exposing tissue to high heat failed to prevent transmission of a TSE called scrapie, which kills sheep and goats. Strategies that annihilate the usual viruses didn't do much to halt disease.

In the early 1980s, Prusiner began to advocate a different theory to explain where the "transmissible" in TSEs came from. The answer, he argued, was a particle he called a prion, in effect the first infectious protein. The evidence, "one has to admit, was very shaky" to start, Aguzzi says. But the work slowly advanced. Prusiner reported that purifying bits of scrapie-laden brain down to their infectious components always left behind a protein that resisted chemical breakdown, suggesting it might be misfolded. In 1985, the gene that generates the prion protein was cloned, and researchers were shocked to discover that the healthy prion protein, PrP, was naturally abundant in the brain tissue of normal people.

Aguzzi became convinced of the prion hypothesis in the early 1990s, when he was working with prion biologist Charles Weissmann, then at the Institute of Molecular Biology in Zurich, and saw that mice genetically engineered to lack PrP didn't get sick when injected with infected material. This suggested to Aguzzi that the disease is transmitted by a misfolded PrP protein and that it targets healthy PrP in the brain and turns it toxic, killing neurons. "That was really the tipping point" for me, he says.

Another tipping point came when Prusiner won the Nobel Prize in physiology or medicine in 1997 for "his discovery of prions—a new biological principle of infection," the Nobel Committee announced. "Numerous attempts to disprove the prion hypothesis over the past 15 years have failed," Prusiner declared in his Nobel lecture on 8 December of that year, shortly before accepting the prize in Stockholm, Sweden. For him, the case was settled.

Days after the award was announced, Manuelidis shared her blunt assessment with *The New York Times*. "My fear is that debate is going to be stifled," she told a reporter. "That's the problem with Nobel prizes. If people feel everything is decided, you can't possibly risk going against the grain." Manuelidis keeps a yellowed clipping of that article pinned up outside her office door.

Prusiner's Nobel came as fear of TSEs was running high. In 1995, the first person died of what would later be called variant Creutzfeldt-Jakob disease (vCJD): a version of the neurological ailment, transmitted by eating beef from affected cows. Panic ensued, especially in the United Kingdom, where 175 people were eventually diagnosed as having the lethal disease. But uncertainty about its cause hasn't been "an impediment to making sensible public health decisions," says David Asher, chief of the laboratory of Bacterial and TSE Agents at the U.S. Food and Drug Administration (FDA). Governments simply took steps to keep meat from sick cows out of the food supply. Recently, cases of vCJD have dropped, and fear has subsided.

Battle lines

In the years since Prusiner won his Nobel, even some who have wavered on the prion hypothesis say that evidence has mounted steadily in its favor. About 10 years ago, neuroscientist Claudio Soto, who trained in Chile and is now at the University of

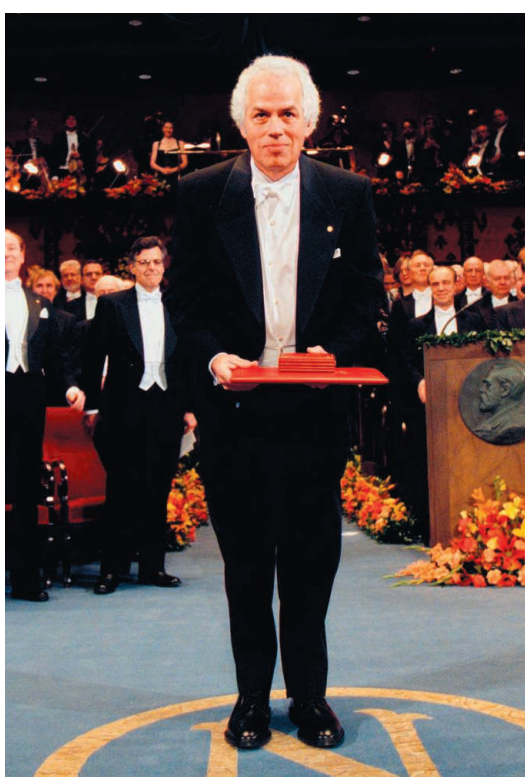

CREDIT: JONAS EKSTROMER/AP

Nobelist. The views of neurologist Stanley Prusiner, at the Nobel Prize ceremony in 1997, are now dogma in the field.

Published by AAAS

Texas Medical School at Houston, developed a new technology called protein misfolding cyclic amplification (PMCA). As its name suggests, PMCA is designed to boost the concentration of prion protein in a sample and eliminate living cells (along with viruses they may contain). To test for infectivity, researchers run samples of brain homogenate through PMCA and inject the concentrated product into mice. Because the mice get sick, many believe this points to prions as the infectious culprit.

The results have been difficult to argue with. Bruce Chesebro, who has long been on the fence about the prion hypothesis, is leaning in its favor. Chief of the Laboratory of Persistent Viral Diseases at the U.S. National Institute of Allergy and Infectious Diseases, based in Montana, Chesebro now says, "PMCA suggests it may not be a virus" that triggers these maladies.

Biochemist Jiyan Ma of Ohio State University in Columbus and his colleagues reported online in *Science* on 28 January 2010 (http://scim.ag/prion_ma) that mixing PrP with various lipid molecules, which force it to misfold, and then injecting the mixture into the brains of healthy mice gave them prion disease. "The data show that prions exist," says Surachai Supattapone of Dartmouth College, who published one of the landmark experiments in a 2007 issue of the *Proceedings of the National Academy of Sciences* (*PNAS*). "That's I think now clear." And, he adds, prions are "not viruses."

This all sounds unambiguous, but even backers of the prion hypothesis admit to some gaps in the evidence. Misfolded PrP is sometimes found in noninfectious tissue, and sometimes it is not found in tissue that can infect other animals. Brain homogenates from people and animals afflicted by prion disease—even prion diseases from the same species—can have wildly different effects when injected into animals, including genetically identical ones. Some develop symptoms after a few months, others not until years later. Prion supporters attribute the variation to different "strains" of PrP, suggesting that the protein can misfold into different chemical conformations that have different levels of toxicity. Not everyone buys it.

Another festering worry, Manuelidis and some others say, is that prion experiments are easily contaminated. Anyone examining the brains of animals with TSEs risks winding up with the infectious agent on their equipment, Chesebro says—on their test-tube racks, their benchtops, the hoods under which they work for protection. Although great care is taken to keep stray bits of brain tissue at bay, there isn't an airtight solution short of switching to a new lab each time. What does this mean, practically speaking? If an unidentified infectious agent exists, it could be a stealthy actor even in the best-controlled experiments.

Family ties. Laura and Elias Manuelidis built their careers together, and their family—here in 1967 with their infant son Manoli.

The Ma study, many argue, has come the closest to definitively proving the prion hypothesis. Researchers synthesized misfolded PrP in the lab, injected it into normal animals, and watched them develop symptoms of TSEs. But no one has replicated this result. Instead, researchers often use genetically engineered mice that overproduce healthy PrP because they develop symptoms faster once infected. This makes for cheaper and easier experiments. Normal mice can take an eternity to show symptoms. It "might take longer than the life span of the mouse," Aguzzi says. "So it helps to have an overexpresser."

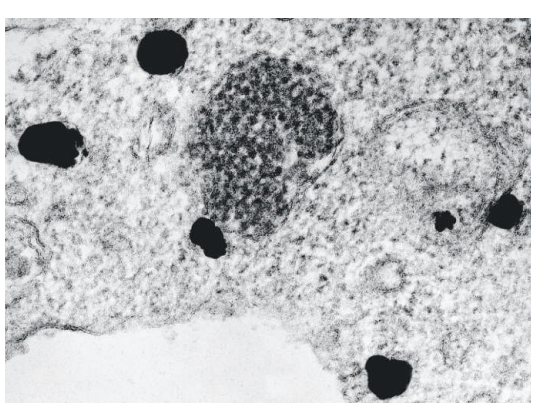

Minority view. Viruslike particles cluster as small circles inside a large bundle, while PrP protein (labeled by large black dots) scatter nearby. Manuelidis discovered the particles and says they're likely causing prion diseases.

Casting a long shadow over the field is Prusiner, who is as tight-lipped in public as Manuelidis is loquacious. He almost never talks to the press and declined, through his correspondence manager, to be interviewed for this article.

Minority views

Asking Manuelidis to elaborate on her prion skepticism can be an exercise in frustration. Encouraging her to talk is not the problem—but grasping her case against prions isn't easy. Manuelidis is aware of this. "I can't think in a straight sentence," she says, soon after parking her low-slung Mazda convertible and sitting down for dinner at a Portuguese restaurant. "My brain goes into literature."

Many prion biologists—even some with questions about the current dogma—are disappointed by the evidence she's turned up. In 2007, Manuelidis published a paper in *PNAS*, describing small viruslike particles in TSE-infected tissue but not in uninfected samples. That's a correlation, however, not proof that the particles are causing disease, Chesebro says. "I'm sympathetic of her battle," he notes. "I wish she were more convincing."

Weissmann, Aguzzi's colleague, who's now at the Scripps Research Institute in Palm Beach, Florida, has been both friend and foil of Manuelidis over the years and was the only one to mention her unprompted in conversation. (More often there is a long pause after her name is brought up.) "The work itself is sound; she's done some interesting work with cell cultures," Weissmann says. "But then she tries to force it into the viral hypothesis," going through "contortions" to interpret the data. His language is nearly identical to Manuelidis's descriptions of the work of the "prion cabal."

Manuelidis and others say she has paid a price for holding so tightly and so publicly to her virus theory. She describes a prominent prion scientist walking out when she took the lectern at a meeting, and another screaming at her in a room full of people. Anonymous reviews of her papers have sometimes been caustic and personal, she says. "She's had a very tough time scientifically, but she also has many friends and allies," says Robert

CREDITS (TOP TO BOTTOM): COURTESY LAURA MANUELIDIS; L. MANUELIDIS ET AL., *PNAS* **104** (6 FEBRUARY 2007)

Published by AAAS

Somerville, who studies TSEs at the Roslin Institute at the University of Edinburgh in the United Kingdom. He's known Manuelidis since 1980 and considers himself a good friend. "The divisions run perhaps deeper in our field than others and are longer lasting. Which is sad, really—it can be difficult to have a useful, constructive discussion."

Like Somerville, Asher of FDA worries about the path prion biology has taken. "I'm still left with this nagging concern that the abnormal protein, important though it may be, has not been demonstrated to be the infectious agent," he says. "The field has been very forgiving of failures of the prion hypothesis to predict things that are found in the laboratory." Asher also complains that prion studies are almost never repeated—scientists just move on to a new one. And, he says, papers that fit the dogma are more readily published than those that do not.

Maurizio Pocchiari, a neurologist at the Istituto Superiore di Sanità in Rome, agrees that siding with the vocal majority can certainly help one's career. "If you are aligned with the prion hypothesis, it is very easy to publish, … [and] it's easier to get a good result" experimentally, he thinks, thanks partly to the genetically modified mice churning out PrP that are so popular.

Pocchiari is another member of the Manuelidis fan club. He disagrees that a conventional virus is lurking behind TSEs, believing it would have been found by now—but he isn't satisfied with the protein-only dogma, either. "We now are pretty aware that when we try to purify infectivity, we purify the pathological prion protein, but we also purify something else," he says. "There is a something else, … [but] we have no idea what we are looking for." Some, like Somerville, wonder about a "virino," a small viral particle that doesn't code for proteins on its own and acts in conjunction with PrP. Virinos fit the bill in part because of their size, which is useful because of long-ago studies suggesting that nothing as large as a virus was hiding in TSE-infected tissue. But virinos are a concept invented to fit the experimental data that haven't been found anywhere else. Then again, many argued before the prion theory took hold that prions shared this feature, too.

Tenacity

If there is a virus behind TSEs, how could it have stayed hidden for so long? Isolating these tiny snippets, Manuelidis argues, is just plain difficult because copies are so scarce, even in brain tissue where disease concentrates. Most people disagree with her, but not everyone. "The fact that we can't detect it is, I would argue, not a statement of what's present or not, but maybe more a statement about our abilities as scientists to discover it," Somerville says. Asher hopes that Manuelidis will continue her work with the viruslike particles she identified in the 2007 *PNAS* paper. "Far too little has been done with it," he says.

Manuelidis perseveres, working near the morgue in the basement of the surgery building, where she's been since the mid-1970s. The labs are old; her husband's office remains largely untouched. Like everywhere else, precautions against infection were an afterthought when they first began this work. "My husband was determined you had to feel the stuff; nobody put on gloves and then [we] ate lunch," Manuelidis says. A guinea pig injected with CJD that mysteriously didn't get sick was christened Harold and lived for 12 years in the lab's biohazard facility. Manuelidis accidentally squirted herself once in the eye with an infectious brain sample and took out a $1 million life insurance policy for 10 years for her two sons. She never developed the disease, reinforcing her view that TSEs are not particularly virulent and may need to be injected or ingested in large quantities for someone to get sick.

In the late 1990s, Manuelidis began downsizing her lab, frustrated by how grueling her struggle for money had become—a shift that began after Prusiner's Nobel, she says. Now she has three recent Yale undergraduates working for her, as they bridge time between college and medical or graduate school. Her students learned the prion gospel in biology class and are fascinated by what, to them, is a new controversy. They're not sure where they stand. As they tell it, Manuelidis doesn't push them. "The data doesn't seem to contradict" the virus theory, says Terry Kipkorir, a thoughtful 2010 graduate who grew up in Kenya and slouches at a desk, a blue stocking cap on his head. Kipkorir and the others are looking for viral particles in infected tissue and trying to determine which components are infectious. But "I don't want to dismiss the prion theory" either, he says. If there's one thing he's realized as he ends an academic year in Manuelidis's lab, it is to prize autonomy. "I don't think I'm going to work under a lot of direction" going forward, he says.

Manuelidis attributes the slow pace of her never-ending virus hunt to technical challenges and a shortage of money. She has the same CJD grant from the National Institutes of Health that she's had for more than 30 years; it now brings in $539,000 a year, nearly $200,000 of which goes to Yale for overhead costs. Multimillion-dollar awards—the kind that allow you to work with hundreds of animals—are not in her future, she thinks.

Should they be? The same researchers who lament how incomplete her work is say no. "To be quite frank, I don't think it's worth funding," Weissmann says. "In the 19th century, there were still people who thought that life could originate from boiled hay. These people just die out—there's always fewer and fewer of them." He believes that Manuelidis will never relinquish a theory to which she's held tight for decades, no matter what story the data tell.

Asked if letting go would be hard for her, Manuelidis is unambiguous. "No, no," she says. "All I know is that my experiments don't show" that prion protein is causing disease. She's hopeful now that she's on the cusp of something new. "I think I can crack this stuff," she says.

–JENNIFER COUZIN-FRANKEL

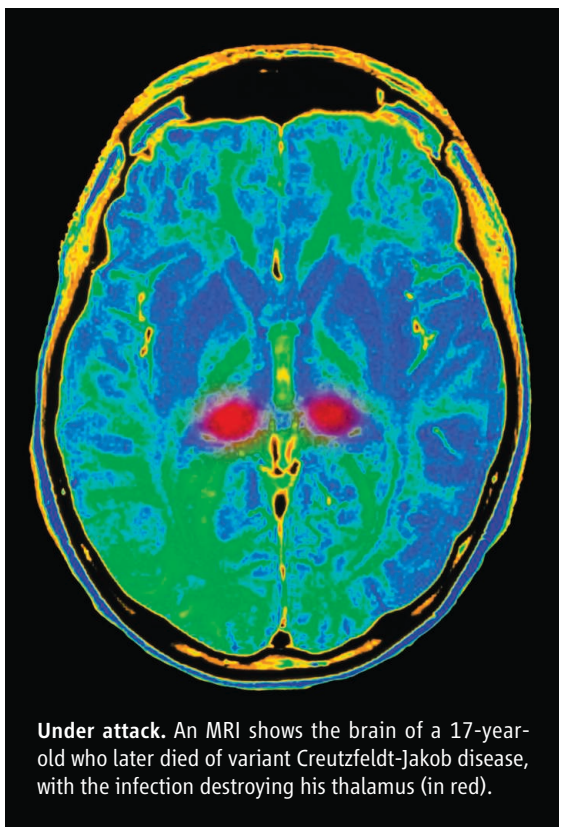

Under attack. An MRI shows the brain of a 17-year-old who later died of variant Creutzfeldt-Jakob disease, with the infection destroying his thalamus (in red).

CREDIT: SIMON FRASER/PHOTO RESEARCHERS INC.

Published by AAAS

BIO-INSPIRED ENGINEERING

Manta Machines

By observing manta rays in the wild, modeling them, and building robots, researchers are learning how these agile animals ply the oceans

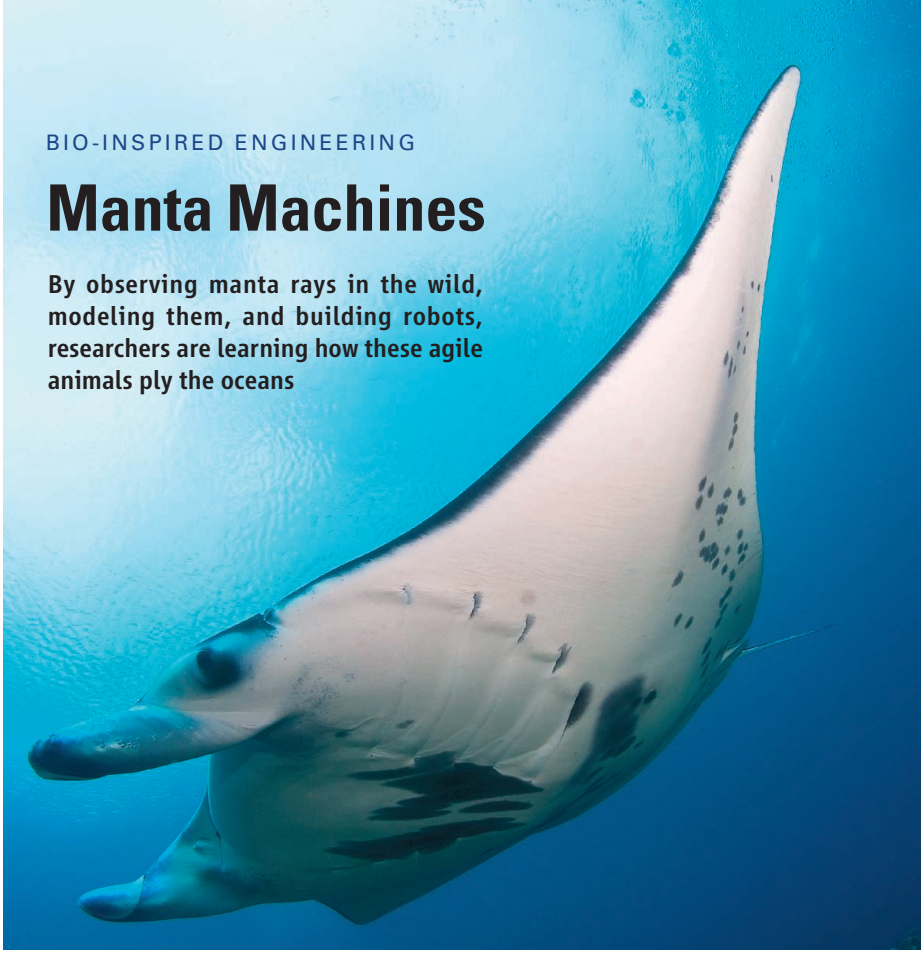

Swimming like butterflies underwater, with mesmerizing ease and grace, manta rays are the envy of engineers seeking more efficient underwater vehicles. For the past 3 years, researchers at Princeton University and the University of Virginia (UVa) have been working to understand how these meters-wide fish are so light on their fins. Now, their students are putting the insights they have gained to the test—in a manta robot competition between the two collaborating universities.

On this April afternoon, Princeton mechanical engineering senior Mohammad Javed is scrambling to show how close his manta robot comes to emulating the animal's dexterity.

"Three minutes left," a judge calls out.

"I'm going to try one more time," Javed responds as he frantically lifts "A Bot Named Sue" out of the water to remove a weight from its back and to screw another weight onto its front. He needs to adjust the buoyancy enough that the robot can dive down a meter, swim under a bar, surface, and swim back over the bar.

Less than 3 weeks ago, his robot was still in pieces. The body of his first iteration leaked, ruining the electronics that moved the fins. By the time he got a replacement, he barely had time to test it.

Earlier in the day, UVa's contender, Manny, had dashed down the length of the pool at twice Sue's speed. But it was not as good at diving or turning as Javed's robot and never succeeded in the "under and over the bar" test. So this was Javed's chance to clinch victory. During his first try on this test, one of the servomotors driving the fins overheated and the robot shut down. This time around, the weights caused it to nosedive to the bottom and flip onto its back so it couldn't come back up.

Javed puts the robot back into the water, and a diver positions it in front of the bar. It dives, but the weights still aren't quite right and the clock runs out.

There's no clear winner—the judges declared a tie—but the onlookers and the contestants are quite pleased. "For the first time out, [both teams] are doing pretty well," says judge Gilbert Lee, a materials scientist at the Carderock Division of the U.S. Naval Surface Warfare Center in West Bethesda, Maryland, where the competition is being held. "They were successful in achieving raylike propulsion," adds Robert Brizzolara, a program officer with the Office of Naval Research (ONR) in Arlington, Virginia.

That was the goal. Mantas are everything one could want in an autonomous underwater vehicle (AUV). "I've thought for a long time that the people who are interested in robotic mimicry were missing the boat in not looking at manta rays," says Adam Summers, a comparative biomechanist at Friday Harbor Laboratories in Washington state. Most fish swing their body from side to side, and "that's not very handy if you are trying to stuff [instruments] inside." The manta body is stiff. Mantas are also quiet, efficient swimmers—AUVs tend to be one or the other. The best AUVs have a turning radius of 0.7 body lengths; the manta needs just 0.27 its body length and maneuvers like a fighter plane. Based on the two robots' performance, "in terms of maneuverability, we're on the right track" in understanding how mantas achieve such grace, says Frank Fish, a functional morphologist at West Chester University in Pennsylvania who is working with UVa and Princeton on the manta project.

Understanding manta rays

The focus on manta rays traces back to a snorkeling trip Alexander Smits took in Australia about a decade ago. "They are such self-possessed, graceful animals," he says. "It was almost mystical," he recalls about his experience swimming among these 2-meter- to 5-meter-wide fish. "I decided I've got to know something about them."

An expert in experimental fluid mechanics at Princeton, Smits persuaded Hilary Bart-Smith, a postdoc at the time designing flexible aircraft wings, to consider instead developing shape-morphing fins for underwater locomotion, based on manta ray swimming. They couldn't get funding at first, so the research didn't get very far. But Bart-Smith took the project with her to UVa and got fellowships to work toward building an artificial structure that could recapitulate the highly maneuverable, seemingly effortless movements of manta rays.

Then 4 years ago, ONR issued Bart-Smith's dream request for proposals: a solicitation for "bio-inspired" sea vehicles. She called Smits and recruited him, Fish, and three other researchers to look at not just mantas but also other rays from biological, engineering, fluid dynamics, and modeling perspectives. In 2008, their proposal was awarded $6.5 million over 5 years. "They've got a challenging problem to solve: to produce a flexible mantalike wing that could have its motion controlled accurately," says George Lauder, a biomechanist at Harvard University.

It fell on Fish, the biologist on the grant, to get the nitty-gritty details of the manta ray's swimming behavior. His first job was to catch the animals in action. For that he headed to

Online
sciencemag.org
Podcast interview with author Elizabeth Pennisi.

CREDIT: MIKE VEITCH/ALAMY

Published by AAAS

Yap, an island in Micronesia where manta rays regularly visit the protected waters inside the island's reefs to be cleaned by tiny fish living there. Fish and his colleagues set up two video cameras in water 24 meters deep to capture manta movements in three dimensions. They came home with 36 hours of video.

Back in Pennsylvania, he and his team have been analyzing the videos through a painstaking process of digitizing key landmarks of the manta's body—the fin tip, eye, and so forth—frame by frame. "We want to define the motion for animals going at a variety of speeds as well as up and down maneuvers," he explains.

Already they have been able to figure out the details of how the winglike fins deform. Two waves are set in motion in the fins as they flap. One travels from front to back of the fin. A second ripple extends out from the base of the fin to the tip. "The motion is far more complicated than what we find from a dolphin or tuna," Fish explains.

To complement the video footage, Fish has used computed tomography (CT) scans to probe the internal structure of the fins of several ray species. UVa biomechanics expert Silvia Blemker used the scans to construct 3D renditions of the underlying cartilage, revealing large differences between the fin skeletons. "It's a very complicated structure, with many elements and many links," Bart-Smith says.

UVa computational hydrodynamicist Hossein Haj-Hariri has created mathematical models based on the underlying cartilage structures to learn how different skeletal configurations contribute to swimming performance. "To mimic [the fin] exactly is incredibly challenging," Bart-Smith says, so she wants to know how much they can simplify the robot's "skeleton" and still have it work well.

What Haj-Hariri does in a computer, Smits tries to do in a tank at Princeton. He and his colleagues have built manta ray fins of flexible plastic and examined water as it flows over them. They are testing how different fin shapes and movements affect thrust and efficiency in steady swimming.

From the videos, the researchers had observed that manta fins both flap up and down and undulate, sending a traveling wave from the front to the rear of the fin. "This undulatory part of the swimming is really the most important part of it," Smits says, based on his measurements. It is four times more important than flapping for propelling the fish forward.

Making mantabots

Over beers one night, Haj-Hariri, Bart-Smith, and Smits decided to recruit undergraduates to the project for a competition in which the students build manta ray robots. "It's a good way to test out a variety of prototypes," Lauder says. "You learn a tremendous amount by trying to build something even before you think you know enough to try."

At UVa, Bart-Smith and Haj-Hariri organized a yearlong senior engineering class whose goal was to build a robot for the competition. The students used a cable-rod matrix—called a tensegrity structure—encased in a soft silicon material as a fin. Tensegrity structures are rigid rods held together by tensioning cables, which creates a stiff, lightweight structure. Pulling on the cables in different combinations bends the tensegrity rods into a curved shape that allows the fin to move up or down.

Manta mimics. Mohammad Javed fixes his manta "bot" (*top*) in hopes of beating out UVa's competing robot (*below*).

The CT scans gave the students a sense of the range of shapes and physical characteristics possible for ray swimming: They decided to follow nature's design fairly closely. Then they had to scale those parameters down from several meters to a robot that was 60 centimeters long from wingtip to wingtip. Whereas the real fish has muscles in the fin itself, the UVa team put their "muscles"—devices called actuators—inside the "body" to reduce the weight of what had to move up and down. The body itself was made with a 3D printer, but because the plastic used was porous, they had to coat it with epoxy.

They studied the videos to decide on their turning strategies. For fast turns, they held one fin steady and flapped the other vigorously; for slow ones, they flapped the inner fin more slowly than the one on the outer edge of the turn.

At Princeton, Smits and his team persuaded Javed to represent them in the competition as the university's sole contender. His robot looks less manta-ish than UVa's. Seen from above, the UVa manta ray fin is triangular, but Princeton's is much more lobular. Javed put a horizontal rudder in the back that moves up and down and helps pitch the manta for diving and surfacing.

His manta's body is a single piece of machined plastic sealed with a lid screwed down like a manhole cover. Instead of containing a tensegrity structure, each fin has four parallel steel cables the diameter of toothpicks that extend from the body core toward the tip. They are arranged with two on top and two on the bottom and connected in the body to a cylinder driven by a servomotor. Pulling on the top cables curves the fin upward; pulling on the bottom causes the fin to flap downward.

Each team had 1 hour to complete five tasks: the over-and-under bar move, diving to the bottom of the tank and resurfacing, making the tightest 360° turn possible, going the fastest for a specified distance, and demonstrating the robot's swimming prowess with a freestyle maneuver. Both teams excelled at flapping the fins, but both had issues with buoyancy and water leaking into the bodies. But that didn't faze Brizzolara. "In any number of technologies that I have been associated with, the first time they put something in the water there are always hiccups and bumps," he says. Just getting to this point of having robots to test was "a step forward in the science."

Bart-Smith hopes to hold another robot competition next year. One of her UVa colleagues has built his own manta ray robot, one that is supposedly waterproof. And a company in Germany has a version whose fins are based on fish tail mechanics. Manta "bots," Summers says, are "getting far enough along that people are learning something about how the animals work by looking at how the robots work." **–ELIZABETH PENNISI**

CREDITS (TOP TO BOTTOM): E. PENNISI/*SCIENCE*; DEVIN PISNER

Published by AAAS

DNA Circles Cause Cow Coat Color Changes

CREDIT: ARNAUD SARTELET

Circles for stripes. Belgian blue cattle got white back stripes from DNA circles moving a gene.

Keith Durkin wasn't trying to figure out why some Belgian Blues, a cattle breed known for its big muscles, have a wide white stripe down their backs. And the young geneticist certainly didn't expect to uncover what seems to be a new way that a cell shuffles its genes around. A postdoc at the University of Liège in Belgium in 2009, Durkin was scanning a database containing the genotypes of 4400 animals to flag duplicated chromosomal regions. One such region, which showed up in nine of the cattle, caught his eye because it included a gene called *KIT* that is involved in coloring animal coats. When he checked on those nine, each animal had the telltale white stripe.

Durkin was a little puzzled at first because the database information suggested the repeated DNA was on chromosome 6. His University of Liège colleague Carole Charlier had been homing in on the mutation for this "color-sided" trait and had seemingly localized it to chromosome 29, not chromosome 6. By using fluorescing tags that home in on specific pieces of DNA, Durkin and his colleagues showed that a copy of a piece of chromosome 6 had at some point jumped to chromosome 29. It seems that when the 480,000-base-long stretch of DNA broke away, *KIT* became separated from some regulatory DNA, and the subsequent misregulation led to the unusual coat color pattern.

But the sequence of the duplicated region on chromosome 29 was also somewhat confusing. The researchers could tell from the chromosome 6 sequence what the beginning and end of the duplicated DNA should be, but these sequences were instead in the middle of the chromosome 29 copy. When the segment jumped out of chromosome 6, Durkin concluded, it must have formed a loop of DNA that then broke apart in a different place before inserting into chromosome 29. Imagine forming a circle out of a sequence of letters, such as A, B, C, D, E, and F, then snipping that loop someplace different from where the ends originally joined. If the break came between C and D, for example, the new linear sequence would be D, E, F, A, B, C.

Durkin's story doesn't end there. In color-sided Brown Swiss cattle, he and his colleagues found that the *KIT*-containing chromosome 29 segment had copied itself into another loop and then hopped back into chromosome 6 next to the original sequence. Durkin also found scrambled duplications of this DNA sequence in other color-sided breeds, including distantly related cattle from Ireland and Ethiopia. That observation suggests that this circularized DNA shuffling must have occurred early in the development of cattle breeds.

Geneticists say they haven't seen genes move between chromosomes in quite this way before. "The circular mechanism is really novel," says Douglas Antczak, a veterinary geneticist at Cornell University. "The mechanism by which fragments of genes go to another place is not well-known," adds Xavier Estivill, a geneticist at the Center for Genomics Regulation in Barcelona, Spain. There is a group of so-called transposable elements called Heliotrons that also seem to jump around the genome as circles of DNA, but the sequences of the circles in these cattle look nothing like these transposable elements, Durkin says. Estivill wonders whether this circle-driven, gene-shuffling mechanism will prove common. "We are now trying to find some examples in humans," he says. **–E.P.**

On the Trail of Brain Domestication Genes

Domesticated animals have far more in common than service to humankind. As Charles Darwin observed, compared with their wild counterparts, dogs, pigs, and cattle tend to be smaller, have finer bones, and sport spotted coats. Domesticated animals generally are also less aggressive, less fearful, and more playful.

Fascinated by these behavioral similarities, Svante Pääbo, Frank Albert, and their colleagues at the Max Planck Institute for Evolutionary Anthropology in Leipzig, Germany, wondered whether these tamed species—and perhaps even some primates, including humans—also share similar patterns of gene expression in their brains. Researchers as far back as Darwin have speculated that humans underwent "self-domestication," and, more recently, Brian Hare of Duke University in Durham, North Carolina, proposed that bonobos evolved domesticated behavior to encourage group living.

To explore this issue, Albert, now at Princeton University, turned to the genes active in the prefrontal cortex, which is responsible for long-term planning and associative thinking. Albert isolated genetic material representing active genes from the prefrontal cortex of a half-dozen dogs and wolves, as well as from the brains of a half-dozen domestic pigs and rabbits and their wild counterparts. He sequenced these genetic fragments to determine the genes from which they derived and then estimated each gene's level of activity by quantifying how often his sequencing highlighted it.

He looked for genes whose activity was increased or decreased in the three domesticated species compared with in the wild ones. He found 60 such genes and then sought confirmation by doing a similar comparison of the domestic guinea pig and its close wild relative, a cavy. About 40 of the 60 genes displayed the same boost or drop,

he reported at the meeting.

With these 40 putative brain domestication genes in hand, Albert compared their expression in humans versus chimps. No clear pattern of human domestication emerged. But the activity of that gene group in bonobos was clearly "domesticated" compared with chimps, Albert reported. "What causes this very dramatic behavior in bonobos is somehow mechanistically similar to what was selected for when the dog and pig were domesticated," Pääbo says.

Hare is delighted with the new study. "These results not only provide exciting support for the self-domestication hypothesis of bonobos but also point to domestication as an exciting model for potentially revealing the evolutionary process by which psychology more generally evolves, including in our own species," he says.

"That the same genes would be involved in domestication in this wide range of species is really cool," adds geneticist Magnus Nordborg of the Gregor Mendel Institute of Molecular Plant Biology in Vienna. Still, he calls for more comprehensive statistical analyses of the gene expression data, which Pääbo says are being done. His team also hopes to pin down the changes in the regulatory DNA that create the domesticated gene profile in the brain. **–E.P.**

Disease Risk Links To Gene Regulation

Two of the hotter areas in genomics research came together last week, sending sparks flying that could boost the search for causes and treatments of common diseases. Over the past 6 years, biomedical researchers have looked for genetic variants associated with particular disorders by scanning the genomes of tens of thousands of people with and without the diseases (*Science*, 11 May 2007, p. 820). Some have called these so-called genome-wide association studies (GWAS) a bust because the variants identified so far typically account for just a small portion of a disease's risk. Moreover, GWAS usually pinpointed just subtle variations in the human genome, known as single-nucleotide polymorphisms, without revealing if the SNPs themselves boosted disease risk or were simply markers for something nearby that did. "You could find associations but not the causal variant," says computational biologist Chris Ponting of the University of Oxford in the United Kingdom.

In another corner of the genomics community, researchers, including those who are part of an international project called ENCODE, have been surveying regions of the human genome to identify functions of DNA outside the protein-coding portions of genes. They have, for example, generated genome-wide maps showing places where gene regulation occurs. Now, two teams at the meeting here report that gene regulatory sites surprisingly often are the spots where GWAS-identified SNPs fall. "We're seeing how pervasive a role gene regulation is playing in disease," says genomicist John Stamatoyannopoulos of the University of Washington, Seattle, who led one of the groups.

A variety of techniques allow researchers to find where along DNA gene regulation occurs, often by pinpointing places where a cell's protein-DNA complex, called chromatin, has been modified to allow a gene to become active. For example, Stamatoyannopoulos uses a method called DNase-seq that depends on an enzyme, DNaseI, to cut DNA wherever chromatin has unwound enough to let regulatory proteins bind to it. Stamatoyannopoulos then sequences the resulting fragments and matches them back up to a finished human genome to pinpoint the locations of these so-called DNaseI hypersensitive sites. He has cataloged such gene regulatory sites in 130 human cell types and developmental stages, including fetal tissues, adult organ tissues, and cancer cell lines. Different cell types have different subsets of hypersensitive sites, depending on their gene expression profiles.

Stamatoyannopoulos reported finding 2.1 million of these sites, taking up well more than 11% of the genome. Some 7500 were identified in all cell types, while about 450,000 were found in just one cell type, suggesting that those latter sites are involved in regulating genes for specific kinds of cells.

GWAS have so far linked 3800 SNPs to 427 diseases and traits, and Stamatoyannopoulos looked at where these markers were located relative to the hypersensitive sites. About 53% "were dead hits," Stamatoyannopoulos reported. In contrast, only about 7% of the SNPs fall in the DNA sequences that actually encode proteins. Stamatoyannopoulos's team has "provided the resolution required to identify the functional variants in a vast number of diseases," Ponting says. By pointing out gene regulatory regions that may influence disease risk, this analysis "gives us particular functional elements that are likely to be biologically important," adds Joel Hirschhorn, a geneticist at the Broad Institute in Cambridge, Massachusetts.

Often the bull's-eyes Stamatoyannopoulos found were in a relevant cell type: SNPs associated with heart disease coincided with DNase hypersensitive sites in developing heart tissue, while those tied to autoimmune disease matched up with gene regulation sites in immune cells, for example. Also, in many cases, the cell types where disease SNPs matched gene regulatory regions tended to be fetal tissue, suggesting that perhaps some of these disorders have roots in development, Stamatoyannopoulos said.

At the meeting, Jason Ernst of the Massachusetts Institute of Technology in Cambridge also reported on combining GWAS data with gene regulatory sites. He and his colleagues took into account nine surveys that revealed in nine cell types, including embryonic stem cells and muscle and lung cells, where along the human genome chromatin had been modified. At these sites, they assessed the type of gene regulation that occurred—such as activation or repression—and what transcription factors were involved. They also discovered that disease-linked SNPs from 10 different studies coincided, in cells appropriate for the given disease, with sites regulating genes already implicated in the particular condition. (Ernst and his colleagues' study also appeared in the 5 May issue of *Nature*.) "We're starting to get to the scale of data where we are starting to see patterns," says Hirschhorn, who thinks many more connections between gene regulation and diseases will be forthcoming.

–ELIZABETH PENNISI

Breakdown of Genome-Wide Association Studies

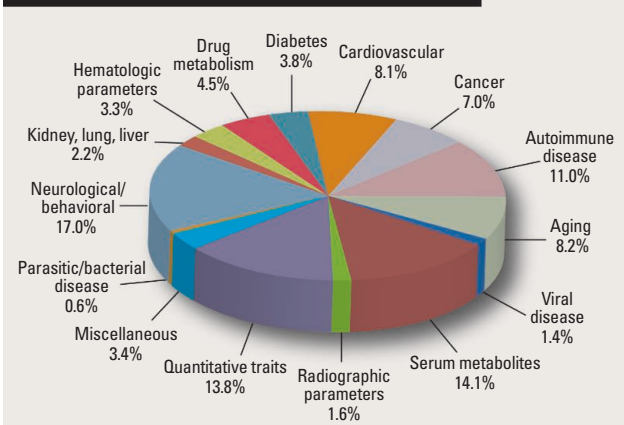

GRAPH: HAO WANG/UNIVERSITY OF WASHINGTON; GRAPH SOURCE: NHGRI GWAS DATABASE

LETTERS

edited by Jennifer Sills

Springtime for Science in Egypt

AS A PROFESSOR OF HUMAN GENETICS AT A RESEARCH INSTITUTE in Egypt, I read with great interest the News & Analysis story "Post-Mubarak era seen as opening for science" (A. Lawler, 25 February, p. 996). I share the optimism that my Egyptian research colleagues expressed in the story, but to ensure that a new attitude toward science takes hold, we must consider several crucial points.

First, advances in scientific research must be supported by political will. The new government should make scientific research a national priority. Second, the Egyptian youths' demand for freedom in Egypt must also be applied to scientific research; researchers must have the freedom to access knowledge and participate in international collaborations and exchanges. The direction of research should not be governed by state security but should be directed only by a national research strategy determined by local needs and modern fields of research. Third, I agree with Ali Douraghy that the bureaucracy needs to be streamlined, but political will and transparent measures will gradually solve this problem. Simplifying the processes for obtaining necessary equipment and creating a cooperative environment between research centers are essential steps toward improving research. Fourth, we must improve the working conditions and financial compensation for researchers.

Researchers in Egypt and abroad must work together to ensure an environment of freedom, transparency, and social interaction in the new modern Egypt.

MONA AGLAN

Department of Clinical Genetics, Human Genetics and Genome Research Division, National Research Centre, Cairo, Egypt. E-mail: drmona_aglan@yahoo.com

CT Risks Dwarfed by Diagnostic Benefits

THE NEWS FOCUS STORY "SECOND THOUGHTS about CT imaging" (L. Schenkman, 25 February, p. 1002) describes the theoretical risk of low-dose radiation from computed tomography (CT), the growing use of CT in medical practice, and its use (and presumed overuse) in the diagnosis of appendicitis, especially in children. The story suggests that without CT, appendicitis can be "diagnosed easily by ultrasound or even observation." This reflects a common misconception. Hands-on familiarity with the clinical problem will quickly dispel this notion and validate the use of CT.

In the era before widespread use of CT, diagnosis almost exclusively relied on clinical criteria and observation. These methods consistently yield a negative appendectomy rate (normal appendix found at surgery) of at least 15% (*1*, *2*). Given more than 250,000 appendectomies in the United States per year, this in turn translates into tens of thousands of unnecessary surgeries per year—most done in otherwise healthy individuals, often children. In contrast, CT evaluation can help drive down the negative appendectomy rate to as low as 2% (*2*, *3*). One must contrast this very large and well-established cost of not imaging (in morbidity and dollars) with the small and theoretical future risk from CT-associated radiation exposure.

Ultrasound is a valuable tool in the diagnosis of appendicitis, but it cannot replace CT. At least 5% of ultrasounds interpreted as positive are false positives (*4*, *5*), and more than one-third are interpreted as equivocal (*5*). If accuracy is defined as the ability to correctly diagnose the presence or absence of appendicitis, the accuracy of ultrasound is a discouraging 60% (*5*). In addition, the ease and safety of ultrasound make it more likely to be used in cases of lower clinical suspicion. This generates a Bayesian nightmare. In this low-incidence population, even a modest false-positive rate will lead to a large number of negative appendectomies. Furthermore, the many equivocal ultrasound scans will prompt many follow-up CT scans for definitive diagnosis. Thus, perversely, aggressive use of ultrasound may increase the number of CT scans performed, specifically in patients without significant pathology.

Sensitive to the radiation concerns, we continue to explore alternative approaches, such as enhanced-ultrasound and magnetic resonance imaging (MRI). Not surprisingly, these strategies have their own issues. For example, MRI is not as readily available, and the longer acquisition time requires sedation in younger children. Until we have accurate, well-vetted

Letters to the Editor

Letters (~300 words) discuss material published in *Science* in the past 3 months or matters of general interest. Letters are not acknowledged upon receipt. Whether published in full or in part, Letters are subject to editing for clarity and space. Letters submitted, published, or posted elsewhere, in print or online, will be disqualified. To submit a Letter, go to www.submit2science.org.

Published by AAAS

Culture:
Loose or tight?
1041

SPORE Prize
Essay
1046

alternatives, it would be an astounding failure of mission and an unconscionable abdication of responsibility to our patients to eschew CT and allow the current radiation scare to return us to the dismal days of uncertain diagnoses, error, and patient misfortune.

LAWRENCE BODENSTEIN

Department of Surgery, Columbia University, New York, NY 10032, USA. E-mail: lb2126@columbia.edu

References

1. R. F. Lewis, J. W. Holcroft, J. Boey, J. E. Dunphy, *Arch. Surg*. **110**, 677 (1975).
2. A. S. Raja *et al.*, *Radiology* **256**, 460 (2010).
3. K. E. Applegate *et al.*, *Radiology* **220**, 103 (2001).
4. S. Kaiser, B. Frenckner, H. K. Jorulf, *Radiology* **223**, 633 (2002).
5. S. Schuh *et al.*, *J. Pediatrics* **158**, 112 (2011).

Value of Small Forest Fragments to Amphibians

MANY IN THE BRAZILIAN SCIENTIFIC COMMUNITY are concerned about the Forest Act revision, the proposed environmental legislation affecting private lands (*1*, *2*). The revision would benefit sectors that hope to expand agricultural frontiers by clear-cutting forests

CREDIT: ALBERTO CESAR/GREENPEACE/AP PHOTO

and savannas. The vote on the law (#1876/99) was put on hold in late 2010 for the presidential elections. It is scheduled to resume in the coming week. We would like to emphasize that, although conservationists typically lobby for protection of large areas of contiguous forests to support biodiversity, even forest fragments have value. Clear-cutting existing forest fragments, which will result if the Forest Act revision is passed, will have serious ramifications for some species, particularly amphibians.

Studies have demonstrated that the presence of small forest fragments of Semidecidual Atlantic Forest (70 to 100 ha) significantly enhances the diversity of amphibians (*3*, *4*). Small forest cover provides amphibians with habitat refuge and dispersal corridors. These limited habitats may also be important for maintaining hydrologic regimes and water quality that are critical for many amphibians' existence. The reduction in forest area remnants can promote the "habitat split" phenomenon (*5*), recognized as a major threat to anuran (frogs with aquatic larvae). This process occurs when the environments that anurans use for foraging and reproduction are disconnected, resulting in a more hostile environment during migration and dispersion. In inland São Paulo state, the expansion of sugarcane crops to produce ethanol has led to the elimination of small forest areas and ponds outside woodlands, threatening the anurans that use the ponds as breeding sites. We join the chorus of the scientific community and nongovernmental environmental organizations in urging Brazil's congressmen to reconsider this revision of the environmental legislation, in view of the damage that it could bring to Brazilian biodiversity.

FERNANDO RODRIGUES DA SILVA,[1]* VITOR HUGO MENDONÇA DO PRADO,[2] DENISE DE CERQUEIRA ROSSA-FERES[1]

[1]Departamento de Zoologia e Botânica, Universidade Estadual Paulista (UNESP), Campus de São José do Rio Preto, CEP 15054-000, São José do Rio Preto, SP, Brazil. [2]Departamento de Zoologia, UNESP, Campus de Rio Claro, CEP 13506-900, Rio Claro, SP, Brazil.

*To whom correspondence should be addressed. E-mail: bigosbio@yahoo.com.br

References

1. J. P. Metzger *et al.*, *Science* **329**, 276 (2010).
2. F. Michalski, D. Norris, C. A. Peres, *Science* **329**, 1282 (2010).
3. C. A. Joly *et al.*, *Science* **328**, 1358 (2010).
4. F. R. Silva, thesis, Universidade Estadual Paulista (2011).
5. C. G. Becker, C. R. Fonseca, C. F. B. Haddad, R. F. Batista, P. I. Prado, *Science* **318,** 1775 (2007).

CORRECTIONS AND CLARIFICATIONS

News & Analysis: "Winds of change leave bioscientists scrambling" by D. Normile (8 April, p. 165). Stephanie Wehner, of the Centre for Quantum Technologies at National University of Singapore, completed her postdoc at California Institute of Technology in Pasadena, not Stanford University. Also, the Agency for Science, Technology, and Research is a statutory board under Singapore's Ministry of Trade and Industry, not a department of the Economic Development Board.

Reports: "Early Pleistocene presence of Acheulian hominins in South India" by S. Pappu *et al*. (25 March, p. 1596). Author affiliation 3 was incorrect in the manuscript. It should read "Centre Européen de Recherche et d'Enseignement de Géosciences de l'Environnement, CEREGE, CNRS and Université Paul Cézanne, BP 80 Europôle Méditerranéen de l'ARBOIS, 13545 Aix en Provence cedex 04, France." Additionally, the following information was omitted from the acknowledgments: "We thank N. Durand, D. Bourlès, the Université Paul Cézanne Aix Marseille, and CNRS for assistance." The ASTER national facility (CEREGE, Aix-en-Provence) is supported by the Université Paul Cézanne Aix-Marseille III.

TECHNICAL COMMENT ABSTRACTS

Comment on "A Persistent Oxygen Anomaly Reveals the Fate of Spilled Methane in the Deep Gulf of Mexico"

Samantha B. Joye, Ira Leifer, Ian R. MacDonald, Jeffery P. Chanton, Christof D. Meile, Andreas P. Teske, Joel E. Kostka, Ludmila Chistoserdova, Richard Coffin, David Hollander, Miriam Kastner, Joseph P. Montoya, Gregor Rehder, Evan Solomon, Tina Treude, Tracy A. Villareal

Kessler *et al*. (Reports, 21 January 2011, p. 312) reported that methane released from the 2010 Deepwater Horizon blowout, approximately 40% of the total hydrocarbon discharge, was consumed quantitatively by methanotrophic bacteria in Gulf of Mexico deepwaters over a 4-month period. We find the evidence explicitly linking observed oxygen anomalies to methane consumption ambiguous and extension of these observations to hydrate-derived methane climate forcing premature.

Full text at www.sciencemag.org/cgi/content/full/332/6033/1033-c

Response to Comment on "A Persistent Oxygen Anomaly Reveals the Fate of Spilled Methane in the Deep Gulf of Mexico"

John D. Kessler, David L. Valentine, Molly C. Redmond, Mengran Du

We hypothesized that methane from the Deepwater Horizon oil spill was quantitatively consumed and presented results from four tests supporting this finding. Subsequent published studies provide further support for our conclusions. We refute the criticisms by Joye *et al*., which are incorrect, internally contradictory, based on flow-rate estimates that exceed consensus values, and overall do not disprove our hypothesis or invalidate its underlying assumptions.

Full text at www.sciencemag.org/cgi/content/full/332/6033/1033-d

Published by AAAS

NEUROSCIENCE

Consciousness: What, How, and Why

Michael J. Proulx

Children love perceptual illusions such as Penrose stairs (see illustration), which appear to always proceed up (or down), or the similar audio experience provided by a Shepard-Risset glissando (*1*). Cognitive scientists, curious and young at heart, do, too. Why do many other adults grow out of this fascination with the ways the brain plays tricks on us? One reason might be that illusions are "magic tricks" and therefore seem irrelevant when it comes to normal experience. After all, stairs and musical notes cannot rise or fall continuously and end up back where they began. Illusions are scientifically interesting, however, precisely because they are directly relevant to daily life and reveal that even perceiving something as simple as this black pigment on a page is an illusion in a sense. The "magic" of consciousness is that we think we are experiencing the world through our eyes and ears, but really everything is seen and heard in the brain.

These facts (and their possible implications for a biological definition of the soul) were the crux of Francis Crick's "astonishing hypothesis" (*2*). Crick focused on research methodology to examine an "easy" aspect of consciousness: that of awareness for simple visual elements such as color. When many people think about what it is to be conscious, however, something much harder comes to mind: one's private, inexplicable feelings that arise from thinking about something. In *Soul Dust*, Nicholas Humphrey begins where Crick and others have left off. He audaciously aims to provide a theoretical basis for understanding the level of consciousness that corresponds with one's personal qualitative experience. Whereas Crick might have focused on the representation of one's awareness of one aspect of the Penrose stairs, Humphrey (a psychologist at the London School of Economics) wants to explain the entirety of one's feeling of what it is like to experience that illusion. As he warns, the book is not an easy read. But his very personal account of his ideas and their development offers engaging "excursions into speculative neuroscience."

Just as the trick that makes an illusion possible takes place in the brain, all conscious experience is created there. Humphrey describes the personal experience of a tomato's redness. That one's experience of redness is personal, private, and constructed in one's brain does not mean that the tomato is an illusion or that it might not really be red. Peripheral sensory receptors (such as cone cells) translate the light reflected from the tomato into electrical signals, and the brain represents the tomato's redness through the activity of neurons. This perception of a discrete color category is an illusion based on a physically continuous spectrum of light. While this category of red is monitored in the brain, that representation may itself be resampled, giving rise to a phenomenological feeling of redness. The personal experience of the color is applied to the tomato even though the feelings of red are all taking place internally. This projection from internal experiences to external object is the spreading of "soul dust" that informs the book's title.

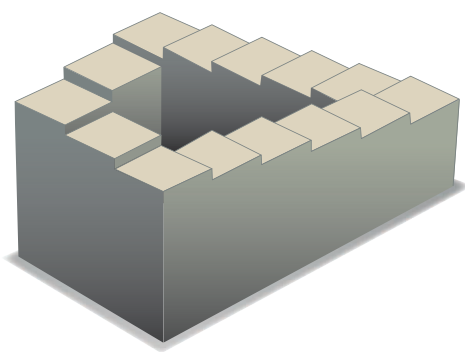

Ever upward to no avail. Penrose stairs always return you to the level at which you started.

For a cognitive scientist who refuses to grow up, this epiphany is empowering. By grounding the hard problem of private, phenomenal consciousness in the easy problem of sensory awareness, Humphrey has laid out a new agenda for consciousness research. Surprisingly, he doubts whether such investigations can be undertaken experimentally at present, and he disparages the approach of looking for consciousness in cognitive studies (such as those examining how we pay attention). He does not, however, entirely write off neuroscience, noting that the presence of primary visual cortex layer 4A in humans (*3*) but not other apes or monkeys might underlie unique features of our sensory-based consciousness. Humphrey's empirical pessimism might have arisen, in part, from his not having delved into the experimental literature as far as Crick did—and thus seeing how far this approach has progressed.

Soul Dust
The Magic of Consciousness
by Nicholas Humphrey
Princeton University Press, Princeton, NJ, 2011. 255 pp. $24.95, £16.95. ISBN 9780691138626.

One approach to researching the phenomenology of sensations is hinted at in Humphrey's quotations from the painter Wassily Kandinsky, who uses musical metaphors to describe color. Kandinsky exhibited synthesia, the neurobiological condition in which stimulation of one sensory pathway gives rise to automatic experiences in another. Synthesia research provides the opportunity to study phenomenal experiences that are not present externally.

Toward the end of the book, Humphrey provides some interesting arguments for why consciousness might be adaptive and could have arisen gradually through natural selection, but his discussion falls short of describing a natural history of consciousness. His conclusion that humans are special and have a unique form of consciousness comes across as species chauvinistic and is not well supported. Nonetheless, he makes the point that this should and can be addressed empirically. Perhaps bigger brains provide more circuits for self-reflective (or reentrant) processing that gives rise to phenomenal experience. And even in the absence of an evolutionary increase in brain volume, the novel compartmental organization of human primary visual cortex might have increased circuitry: more connections could lead to different reentrant information processing that supports unique, conscious experiences.

Humphrey also considers how the human sense of self and spirituality might have arisen from the adaptive nature of consciousness. His discussion provides an important connection between the current scientific approaches to consciousness that he considered in the early chapters and the crucial aspects of the soul as society sees it. Here he again regrets what he sees as the limited scope of contemporary cognitive science, with its focus on attention instead of attitudes and values. Many cognitive scientists are, however, currently examining the relation between values and attention and thus already on the way to closing this gap.

Crick ended *The Astonishing Hypothesis* with a challenge for vision scientists:

The reviewer is in the Biological and Experimental Psychology Group, School of Biological and Chemical Sciences, Queen Mary University of London, Mile End Road, London E1 4NS, UK. E-mail: m.proulx@qmul.ac.uk

CREDIT: ADAPTED FROM FIG. 8 IN *SOUL DUST*

"consciousness now." Humphrey's *Soul Dust* should encourage research into a fuller understanding of phenomenal consciousness and its evolutionary origins: the magic of consciousness now.

References and Notes

1. http://en.wikipedia.org/wiki/Shepard_tone.
2. F. Crick, *The Astonishing Hypothesis: The Scientific Search for the Soul* (Scribner, New York, 1994).
3. T. M. Preuss, G. Q. Coleman, *Cereb. Cortex* **12**, 672 (2002).
4. Thanks to A. de Sousa for discussions about the book.

10.1126/science.1206704

EXHIBITION: ART

"All Bespeckled with Yellow Stains"

Dust for bricks. E. H. Dixon's watercolor (1837) of the Great Dust-Heap at King's Cross, London. The mound, next to Battle Bridge and the Smallpox Hospital, was removed in 1848 "to assist in the rebuilding" of Moscow.

CREDIT: WELLCOME LIBRARY, LONDON

Dirt is inescapable, nor can we escape the ironies it generates. Those who work in laboratories constantly worry about contamination from dirt, but others make a living from organizing dirt or scavenging in our waste tips. Fortunately, the exhibition *Dirt: The Filthy Reality of Everyday Life* is arranged in a perfectly clean room. In case we are worried, there is a broom propped in one corner. This appears to be splattered in paint and quite forgotten, but this is the Wellcome Collection—and sure enough. there is an explanatory plaque that relates to it. The splatters are in fact precious stones embedded in the woodwork by the artist Susan Collis, who likes to challenge our perceptions of the value of the everyday. Thus too, scavengers value everyday dirt that the privileged can afford to discard.

The exhibition offers a grand tour of conceptions of dirt from grit to germs at six locations and periods. We start in 17th-century Delft, where cleanliness was indeed devotional. But one citizen of Delft, Antonie van Leeuwenhoek, inspected life in Delft more closely with his tiny single-lensed microscopes and discovered an unsweepable universe of the minuscule. Blue and white ceramic Delftware portraits of him were quite common, perhaps encouraging the virtuous housewives of Delft to even more strenuous efforts. The engravings of Geertruid Roghman are a testament to the sheer hard labor required of women in their daily efforts to keep Dutch households clean.

Serena Korda, inspired by the commodification of waste in Victorian London, has made a pile of red bricks using dust for their matrix. A list of dust sponsors hangs beside the bricks and includes, suitably, donations from occupants of the London School of Hygiene and Tropical Medicine. Brick was, of course, the primary building material for the Victorians' most magnificent engineering achievement: Joseph William Bazalgette's sewers were built to enclose and divert the stench of the Thames downstream. The huge (and valuable) dustheaps at Gray's Inn Road and King's Cross, from which Victorian brick was made, have long gone; fittingly, a vast medical research center is now under construction in this area. But in 1854 the Thames was London's sewer, and cholera stormed through Soho via the contaminated water of the Broad Street pump. Despite the Medical Council's studious collection of detailed data, John Snow's painstaking work to identify the source of cholera was trashed by the miasmatists who persisted in believing the infection was caused by bad air. Filippo Pacini discovered the cholera vibrio in 1854, but it was not until 30 years later that Robert Koch developed the germ theory of disease, and European slums were cleaned up systematically. Meanwhile, a small flask of grayish liquid offers a disquieting souvenir of the emissions from a choleric London gut.

Another form of dirt took over in Soho during the 20th century in the form of strip clubs and brothels. Vice may be considered dirty, but in India dirt from the doorways of brothels is valuable, as this is the place men shed their virtues. A nugget of this virtuous dirt forms the heart of the statue of the goddess Durga, with the rest of the body being made from Ganges mud. Although the brothel dirt is not a problem, the holy Ganges mud is, making the sculptors ill and their skin erupt into sores.

Dirt being given this degree of intellectual consideration becomes absorbing, even thrilling—particularly when one is made sensitive to its barely controlled ubiquity. It is horrifying, too, to contemplate the ghastly nightmare of lives on the dustheaps of the world's megacity slums. With almost 7 billion people on our planet and despite the best efforts of the good wives of Delft to sweep our dirt away, ultimately there is no place "away," and we must relearn how to value our dirt. This exhibition thus gives us a glimpse into a choice of possible futures: life in a recycled paradise or grim existences eked out on a planetary garbage dump.

–Caroline Ash

10.1126/science.1208190

Dirt
The Filthy Reality of Everyday Life
Kate Forde, James Peto, and Lucy Shanahan, curators
Wellcome Collection, London. Through 31 August 2011. www.wellcomecollection.org/whats-on/exhibitions/dirt.aspx

Dirt
The Filthy Reality of Everyday Life
by Rosie Cox, Rose George, R. H. Horne, Robin Nagle, Elizabeth Pisani, Brian Ralph, and Virginia Smith
Profile, London, 2011. 224 pp. Paper, £20. ISBN 9781846684791.

OCEANS

Mitigating Local Causes of Ocean Acidification with Existing Laws

Even as global and national efforts struggle to mitigate CO_2 emissions, local and state governments have policy tools to address "hot spots" of ocean acidification.

R. P. Kelly,[1*†] M. M. Foley,[1*] W. S. Fisher,[2] R. A. Feely,[3] B. S. Halpern,[4] G. G. Waldbusser,[5] M. R. Caldwell[1]

As the level of atmospheric carbon dioxide (CO_2) continues to rise, so too does the amount of CO_2 in the ocean (*1*, *2*), which increases the ocean's acidity. This affects marine ecosystems on a global scale in ways we are only beginning to understand: for example, impairing the ability of organisms to form shells or skeletons, altering food webs, and negatively affecting economies dependent on services ranging from coral reef tourism to shellfish harvests to salmon fisheries (*3*–*5*). Although increasing anthropogenic inputs drive acidification at global scales, local acidification disproportionately affects coastal ecosystems and the communities that rely on them. We describe policy options by which local and state governments—as opposed to federal and international bodies—can reduce these local and regional "hot spots" of ocean acidification.

Several studies document acidification hot spots, patches of ocean water with significantly depressed pH levels relative to historical baselines occurring at spatial scales of tens to hundreds of square kilometers [e.g., (*6*, *7*)]. These coastal hot spots may be due to nonuniform changes in circulation and biological processes (*6*), and precipitation runoff (*4*, *5*, *8*), in concert with globally increased atmospheric CO_2 (*8*) (see the figure). Local studies in the Kennebec River plume in the Gulf of Maine (*9*), the Chesapeake Bay (*10*), and the Manning River estuary in New South Wales, Australia (*11*), illustrate that freshwater inputs, pollutants, and soil erosion can acidify coastal waters at substantially higher rates than atmospheric CO_2 alone.

These nonatmospheric inputs can have particularly large consequences when they coincide with biotic phenomena [e.g., spawning events (*9*)] or abiotic processes, such as upwelling events that bring low-pH water to nearshore areas (*1*, *2*). Additional local phenomena—such as sulfur dioxide precipitation (*12*), hypoxia (*13*), eutrophication (*10*, *14*), and both emissions and runoff from acidic fertilizers (*15*)—can intensify these localized hot spots. These impacts are likely to be magnified when combined with other stressors in the coastal ocean, including overfishing, habitat destruction, temperature increases, and nonacidifying pollution (*16*).

Policy Recommendations

As global and national efforts to mitigate CO_2 emissions struggle to gain traction, smaller-scale actions become increasingly important. In the United States, for example, local and state governments have both the authority and motive to address many stressors that drive or exacerbate acidification conditions. This runs contrary to the widely held perception that acidification cannot be addressed at the scale of local (e.g., municipal and county) or regional (state, multistate, and territorial) jurisdictions [e.g., (*16*, *17*)]. Although we focus here on U.S. policies, similar legal tools exist elsewhere to guard against non-CO_2 acidification drivers.

U.S. federal environmental laws (e.g., Clean Air Act, Clean Water Act, and Coastal Zone Management Act), state laws, and local ordinances provide multiple layers of protection for coastal waters by controlling emissions, runoff, and land-use patterns through zoning and permitting (table S1). Implementing measures that reduce residential and agricultural runoff, for example, can minimize beach and river contamination and algal blooms, while reducing pollutants that acidify the local coastal ocean. Many states have already passed legislation to limit residential runoff, although these are not specifically aimed at mitigating acidification (*18*).

A recent lawsuit and the resulting U.S. Environmental Protection Agency (EPA) memoranda (*19*, *20*) illustrate states' responsibilities to apply federal environmental laws to combat acidification in state waters. In *Center for Biological Diversity* v. *EPA* (*21*), the Center for Biological Diversity (CBD) challenged Washington State's failure to designate coastal waters as "impaired" because of a decline in pH by 0.2 units from baseline levels, as required under the federal Clean Water Act (*22*). Despite the lack of substantive reform of the National Water Quality Standard for marine pH (*19*, *20*) owing to insufficient data, the EPA highlighted the seriousness of acidification's impacts on ocean life and encouraged states to list pH-impaired waters where data are available (*19*). A focus on data collection could lead to future regulatory revisions that allow state governments to better restrict pollutants in coastal waters (*23*). States may also use existing law to develop biological water quality standards for acidification to assess if a water body is impaired on the basis of biological indicators (e.g., negative impacts on coral species) (*24*). Water quality standards and impairment designations, however, are only ecologically meaningful in light of baseline conditions, vulnerability of ecosystems, and thresholds for ecosystem change, which are often undefined.

Four Approaches

Few jurisdictions have taken steps to mitigate acidification, likely because of the combination of low awareness and a sense that the causes are globally diffuse. Four approaches have particular potential for combating locally intensified acidification. First, the Clean Water Act directs state government agencies to ensure that precipitation runoff and associated pollutants (which can increase acidification) are monitored, limited, and consistent with the sustainable functioning of aquatic ecosystems. Stormwater surge prevention (e.g., holding tanks), coastal and riparian buffers (areas of vegetation near land-water intersections), intact wetlands, and improved onsite water treatment facilities are effective measures to address watershed runoff and associated pollutants. In many cases, federal funding is available to help local governments complete these kinds of projects, and local watershed groups provide a grassroots base for ensuring that states and EPA meet their responsibilities.

Second, controlling coastal erosion is a classic function of local and state governments and one that could markedly benefit

[1]Center for Ocean Solutions, Stanford University, Stanford, CA 94305, USA. [2]Gulf Ecology Division, U.S. Environmental Protection Agency, Gulf Breeze, FL 32561, USA. [3]Pacific Marine Environmental Laboratory, National Oceanic and Atmospheric Administration (NOAA), Seattle, WA 98115, USA. [4]National Center for Ecological Analysis and Synthesis, Santa Barbara, CA 93101, USA. [5]College of Atmospheric and Oceanic Sciences, Oregon State University, Corvallis, OR 97331, USA.

*These authors contributed equally to this work.
†Author for correspondence. E-mail: rpk@stanford.edu

Published by AAAS

coastal ecosystems by reducing nutrient and sediment loading of water and protecting the physical integrity of the habitat itself. Such coastal inputs may be enriched with fertilizers and, if unchecked, can further increase acidification in estuaries and coastal waterways. Independent local actions, such as increasing vegetation cover, may be effective at small scales, but concerted action among multiple local jurisdictions—as would likely be necessary to address erosion within an entire watershed, for example—may require coordination among state or regional governments, adding a layer of regulatory complexity.

Third, land-use change facilitated through local and regional planning, zoning, and permitting policies can reduce direct and indirect (e.g., deforestation) CO_2 emissions, runoff, and other threats (*25*). Antisprawl land-use plans can help reduce vehicle-miles traveled and impermeable surface cover, limiting both emissions and runoff. At least two state laws [Massachusetts (Global Warming Solutions Act) and California (SB 375)] explicitly link land-use development, transportation, and climate change mitigation. These state-level rules are models for state action, but cities and counties can adopt policies and alter zoning provisions and general plans that could help safeguard their own waters—without waiting for state governments to act (*26*).

Finally, simply enforcing existing federal emissions limits for pollutants such as nitrogen oxide and sulfur oxide (for example, from coal-fired power plants) could help ameliorate local drivers of ocean acidification (*13*). Reductions could have immediate local effects, because these pollutants have short atmospheric residence times, falling out of the atmosphere and into the water and/or land near where they were produced (*12*). Reducing pollutants to benefit local environmental conditions increases the likelihood of responsible stewardship by matching political incentives and environmental remediation at the same spatial scale (*27*).

In addition to regulating inputs to the coastal zone, protecting important ecosystem components (such as shell material) provides another potential mechanism to combat locally intensified acidification. Returning crushed shell material to coastal habitats to approximate densities found in healthy clam populations can substantially increase pH and mitigate localized acidification impacts on clams (*10*, *28*).

Tenaciously enforcing existing limits for sediment runoff, erosion, and emissions may alone improve the health of coastal waters and safeguard coastal economies dependent on calcium carbonate–producing organisms, such as shellfish and corals. In the face of declining conditions, however, it is increasingly critical to establish historical and current pH levels to inform future federal or state regulations aimed at protecting against ocean acidification. The potential biological, ecological, and socioeconomic effects of acidification are likely to affect nearshore environments most severely, affecting the delivery of ecosystem services that over half of the world's population depend on and costing billions of dollars in lost product and income (*5*). Minimizing additional stressors on coastal ecosystems can also help to ameliorate threats to coastal resources, thereby maintaining ecosystem resilience and sustainable economic benefits from the ocean.

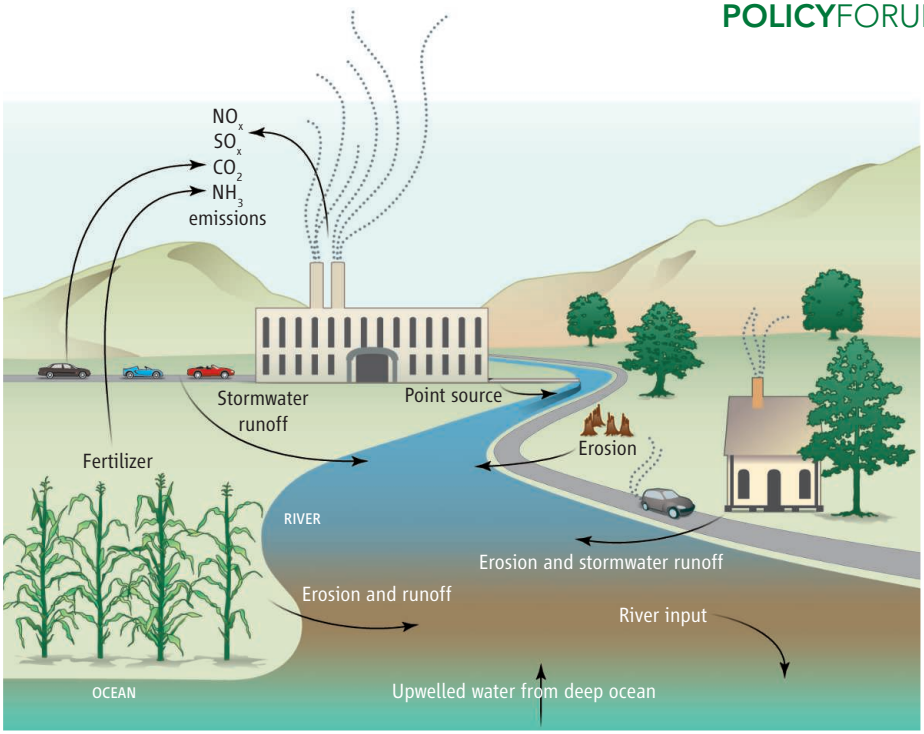

Contributors to ocean acidification. In addition to global atmospheric CO_2, this figure depicts the major local (within 100 km) sources contributing to coastal ocean acidification.

CREDIT: ADAPTED FROM WILL YANG, SHELBY DESIGNS

References and Notes

1. R. A. Feely, S. C. Doney, S. R. Cooley, *Oceanography (Washington, D.C.)* **22** (4), 36 (2009).
2. S. C. Doney, *Science* **328**, 1512 (2010).
3. W. W. L. Cheung *et al.*, *Glob. Change Biol.* **16**, 24 (2010).
4. W. W. L. Cheung *et al.*, *Fish Fish.* **10**, 235 (2009).
5. S. R. Cooley, S. C. Doney, *Environ. Res. Lett.* **4**, 024007 (2009).
6. R. A. Feely *et al.*, *Estuar. Coast. Shelf Sci.* **88**, 442 (2010).
7. R. A. Feely, C. L. Sabine, J. M. Hernandez-Ayon, D. Ianson, B. Hales, *Science* **320**, 1490 (2008).
8. S. C. Doney, V. J. Fabry, R. A. Feely, J. A. Kleypas, *Annu. Rev. Mater. Sci.* **1**, 169 (2009).
9. J. Salisbury, M. Green, C. Hunt, J. Campbell, *Eos Trans. AGU* **89**, 513 (2008).
10. G. Waldbusser, E. Voigt, H. Bergschneider, M. Green, R. Newell, *Estuaries Coasts* **34**, 221 (2011).
11. M. C. Dove, J. Sammut, *J. Shellfish Res.* **26**, 519 (2007).
12. S. C. Doney *et al.*, *Proc. Natl. Acad. Sci. U.S.A.* **104**, 14580 (2007).
13. W. M. Kemp *et al.*, *Mar. Ecol. Prog. Ser.* **303**, 1 (2005).
14. A. V. Borges, N. Gypens, *Limnol. Oceanogr.* **55**, 346 (2010).
15. F. Dentener *et al.*, *Global Biogeochem. Cycles* **20**, GB4003 (2006).
16. B. S. Halpern *et al.*, *Ocean Coast. Manage.* **51**, 203 (2008).
17. L. S. Fore *et al.*, *Science* **322**, 1788 (2008).
18. New Jersey, for example, has both stormwater and water-quality management laws governing runoff. See (*29*).
19. EPA, Integrated Reporting and Listing Decisions Related to Ocean Acidification, memorandum, 15 November 2010.
20. EPA, Decision on Re-evaluation and/or Revision of the Water Quality Criterion for Marine pH for the Protection of Aquatic Life, memorandum, 15 April. 2010.
21. *CBD* vs. *EPA*, No. 2:09-cv-00670-JCC (W.D. Wash. 2009).
22. 33 U.S. Code § 1313(d).
23. 74 *Fed. Regist.* (17484), 15 (2009).
24. P. Bradley, W. S. Fisher, L. S. Fore, W. S. Davis, *Coral Reef Biological Criteria: Using the Clean Water Act to Protect a National Treasure* (Tech. Report No. EPA/600/R-10/054, EPA, Washington, DC, 2010).
25. J. S. Baron *et al.*, *Preliminary Review of Adaptation Options for Climate-Sensitive Ecosystems and Resources* (EPA, Washington, DC, 2008).
26. King County, WA, for example, issued multiple executive orders, requiring county departments to take increasingly aggressive action to mitigate the effects of global climate change. See (*30*).
27. R. Costanza *et al.*, *Science* **281**, 198 (1998).
28. M. A. Green, G. G. Waldbusser, S. L. Reilly, K. Emerson, S. O'Donnell, *Limnol. Oceanogr.* **54**, 1037 (2009).
29. New Jersey Administrative Code 7:8 and 7:15, www.state.nj.us/dep/watershedmgt/rules.htm.
30. King County, Washington, Executive orders governing public utilities: PUT 7-5, 7-7, 7-8, and 7-10-1; www.kingcounty.gov/operations/policies.aspx.

31. The authors thank L. Crowder, N. Baron of Communication Partnership for Science and the Sea (COMPASS), and E. Hartge for helpful comments. Funding was provided by the David and Lucile Packard Foundation. The scientific views, opinions, and conclusions expressed herein are solely those of the authors and do not represent the views, opinions, or conclusions of NOAA, the Department of Commerce, or the EPA.

Supporting Online Material

www.sciencemag.org/cgi/content/full/332/6033/1036/DC1

10.1126/science.1203815

Published by AAAS

DEVELOPMENT

Limb Cells Don't Tell Time

A balance of signals, not a clock, controls proximal-distal fates and maintains progenitors in the developing chick limb.

Susan Mackem and Mark Lewandoski

Although limb development is one of the best models to study pattern formation and morphogenesis, the mechanisms that control its sequential proximal-to-distal, shoulder to finger tip formation have remained controversial (*1*). According to the "progress zone" model, limb progenitor cells become progressively "distalized" in identity via an internal clock mechanism that tracks time spent under the influence of permissive fibroblast growth factor (FGF) signals from the distal limb bud margin, although recent work has challenged this idea (*2*). Alternative models propose that proximal signals could instruct proximal-distal cell fate, obviating the need for a cell-autonomous clock. Two papers in this issue, by Cooper *et al*. (*3*) on page 1083 and Roselló-Díez *et al*. (*4*) on page 1086, support the latter model and show that the dynamic balance between proximal retinoic acid (RA) signaling and distal FGF activity governs the proximal-distal pattern of major limb segments in the chick. Combined signals also maintain the proximal-distal plasticity and progenitor state of limb bud cells. These signaling roles in limb development are reminiscent of events during limb regeneration, suggesting a higher level of parsimony between the two than once thought.

Cooper *et al*. and Roselló-Díez *et al*. reconstituted "recombinant" chick limb buds from dissociated, undifferentiated limb bud cells repacked into an empty limb ectoderm hull. Roselló-Díez *et al*. demonstrate that recombinant limbs made from cells that would otherwise form only distal limb structures can be reprogrammed to include proximal identities if treated with RA, or if grafted near a known embryonic source of the signal. A RA antagonist prevented proximal respecification by embryonic tissue signals, whereas antagonism of FGF receptors enhanced this response. Cooper *et al*. built on recent work showing that FGFs, together with WNTs (another type of secreted signal); signals maintain limb progenitors in an undifferentiated state in cell culture (*5*). They demonstrate that these cultured cells maintain the ability to form limb structures, but specify proximal fates only with continued RA exposure. In vivo, as progenitors are displaced from the RA-producing flank consequent to limb outgrowth, they progressively express more distal-specific markers. Cooper *et al*. mimic this phenomenon in vitro by removing RA from the culture for different time periods. In the emerging model, a temporal dynamic between relative RA and FGF activities regulates proximal-distal identity during outgrowth as the progenitor pool maintained by distal WNT and FGF signals is displaced from proximal RA influence (see the figure).

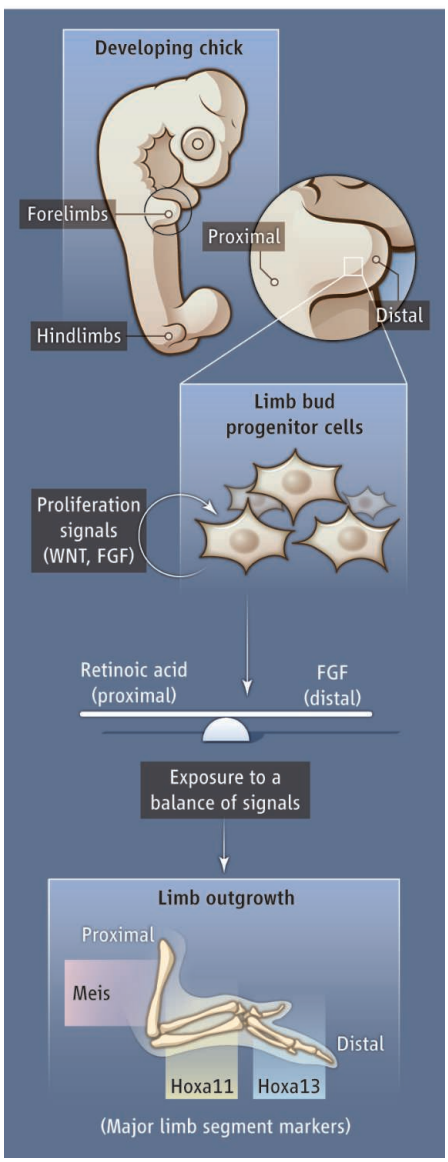

A balance of signals. WNT and FGF signals maintain the undifferentiated, proliferative state of limb bud progenitor cells in the chick. Dependent on the balance of exposure to proximal retinoic acid and distal FGF signals that diverge during outgrowth, progenitors give rise to the different major limb segments. As progenitors become specified to generate each segment, they selectively express the specific markers shown.

One caveat to this instructive model comes from recent genetic studies in the mouse challenging the view that RA plays any role in proximal-distal limb patterning. Mutant mice lacking certain biosynthetic enzymes produce little RA and form no limb buds. Low-level dietary RA provided maternally rescues limb development, but does not activate RA-responsive genes in the vicinity of the limb bud (*6*). This suggests that RA is needed only remotely and is not required locally to pattern the limb bud (assuming that trace amounts of RA, undetected by responsive genes, are not instructing proximal fates). Possibly chick limbs use RA whereas mouse limbs do not, but this is unappealing from a parsimony perspective—though equally surprising developmental differences do exist between these two species (*7*). Alternatively, RA and its antagonists might mimic the activity of, or act in conjunction with, elusive endogenous factors, thereby confounding data. More directly comparable experiments in both species will be necessary to resolve this issue. Although mouse limb progenitors cannot develop in the chick recombinant system, their gene expression profiles and response to signals in cell culture could be similarly evaluated. The cell culture approach might be used to compare RA target genes in limb progenitors of both species.

In addition to resolving the role of RA in mammals, another question concerns the role of FGF in proximal-distal patterning. Because two signals are involved, the data are compatible with either a permissive or an instructive FGF role. The dynamic RA-FGF balance proposed by Roselló-Díez *et al*. suggests a more instructive role, also consistent with a recent analysis of compound FGF mutants in the mouse (*8*).

The extent to which proximal-distal specification of the developing limb resembles the events occurring during amphibian limb regeneration has been debated. However, the studies of Cooper *et al*. and Roselló-Díez *et al*. point to intriguing similarities in the role of RA, WNT, and FGF in both processes. In regenerating limbs, RA is critical for setting the proximal extent of regenerated segments

Cancer and Developmental Biology Laboratory, Center for Cancer Research, National Cancer Institute, Frederick, MD 21702, USA. E-mail: mackems@mail.nih.gov, lewandom@mail.nih.gov

Published by AAAS

formed; excess RA can reprogram a "distal" amputation blastema (the site of progenitors for regeneration) to produce more proximal in addition to distal structures (*9*). Signaling by WNT and FGF plays an essential role in appendage regeneration in several different systems (*10*, *11*), and WNTs may prolong regeneration in species that normally lose this capacity at metamorphosis (*10*). Whether this occurs through the maintenance of progenitors by WNT and FGF, as seen in the chick limb bud, remains to be seen. The finding that embryonic limb progenitor cells can be manipulated to maintain or extend their plasticity opens a new door to analyzing how these progenitors become committed to particular fates, whether and to what extent this process can be reversed, and the degree to which such programming is shared between limb development and regeneration.

References

1. C. Tabin, L. Wolpert, *Genes Dev.* **21**, 1433 (2007).
2. J. L. Galloway *et al.*, *Nature* **460**, 400 (2009).
3. K. L. Cooper *et al.*, *Science* **332**, 1083 (2011).
4. A. Roselló-Díez *et al.*, *Science* **332**, 1086 (2011).
5. D. ten Berge *et al.*, *Development* **135**, 3247 (2008).
6. X. Zhao *et al.*, *Curr. Biol.* **19**, 1050 (2009).
7. J. Schlueter, T. Brand, *Cytogenet. Genome Res.* **117**, 256 (2007).
8. F. V. Mariani *et al.*, *Nature* **453**, 401 (2008).
9. M. Maden, *Nature* **295**, 672 (1982).
10. Y. Kawakami *et al.*, *Genes Dev.* **20**, 3232 (2006).
11. G. Lin, J. M. Slack, *Dev. Biol.* **316**, 323 (2008).

10.1126/science.1207554

PHYSICS

A Logical Use for Atoms

The coupled spins of individual atoms can be used to demonstrate basic logic function.

Andreas Heinrich and Sebastian Loth

It is increasingly more difficult and costly to continue to shrink silicon chip components. Moore's law, which describes such progress, is running into serious trouble. Technologists have been seeking out alternative architectures for computation. Some have even pondered the possibility of shrinking the components to the ultimate end of any roadmap—to the scale of atoms. On page 1062 of this issue, Khajetoorians *et al*. present such a radical leap forward (*1*) by demonstrating spin-based logic operation in chains of magnetic atoms on a surface.

Spintronics promises to add functionality to semiconductor devices by making use of the spin—the magnetic degree of freedom—of electrons that are flowing through devices. But can logic operations be performed without pushing electrons (spin-polarized or not) through wires? Indeed, several schemes have been proposed to do just that. One example is magnetic domain wall logic (*2*). Another relies on the dipolar coupling between magnetic nanodots. Cascades of such dots can meet at intersections where it was shown that logic operations could be performed (*3*, *4*).

About 10 years ago (*5*), it was shown that computation of an arbitrary logic operation on the scale of atoms is possible by using the controlled motion of molecules on a surface. In practice, however, that scheme made the scanning tunneling microscope (STM) an integral part of the logic circuit because repeated operation required precise reassembly of the nanostructure.

In what constitutes a major breakthrough, Khajetoorians *et al*. demonstrate repeatable atomic-scale logic operations with spins of individual atoms. The spin of atoms can be likened to compass needles. Compass needles can in principle carry information from permanent bar magnets (the inputs) to an interaction region (see the figure, panel A). Khajetoorians *et al*. took the bold step of implementing such functionality on a length scale that is seven orders of magnitude smaller. Magnetic atoms were placed on a metallic surface and positioned in precisely defined locations by atom manipulation (*6*). They then used a spin-polarized STM to read the magnetic state of each atom. Relatively large magnetic islands were used as inputs, and chains of magnetic atoms were then coupled to these input bits with a magnetic exchange interaction. In this fashion, the magnetic state of the input island could be transferred to the end of such a chain. Later, a second chain was attached to another input island and both chains were assembled to meet at a central point: the gate, where logic operations were demonstrated.

Khajetoorians *et al*. were able to use an external magnetic field to controllably switch the magnetic state of the input islands independently, by selecting islands of different sizes and hence different switching fields. In their setup, the presence of the STM tip is not required for the gate operation, only for readout of the output state. In essence, they were able to park the STM tip at the output of the gate, switch the state of the two input islands through the four distinct combinations, and watch the output of the logic gate. For certain input configurations (such as the one shown in the figure, panel B), the output of the gate is in a frustrated magnetic state; that is, it is equally likely to point up or down. Khajetoorians *et al*. broke this frustration with a small biasing magnetic field, which allowed them to switch the type of the spin gate from AND to OR. This is a beautiful demonstration of the power of atomically precise manipulation applied to spin systems on surfaces.

These features—independently controllable inputs, signal propagation from one

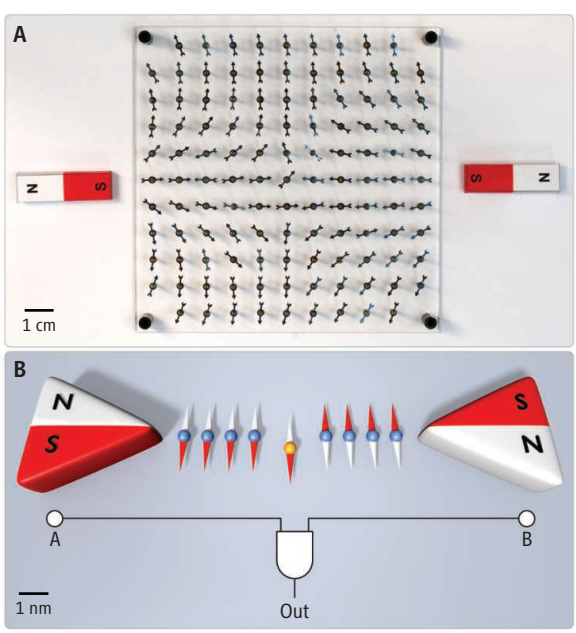

Shrinking logic. (**A**) An array of compass needles responding to the magnetic field of two bar magnets. (**B**) Coupled magnetic atoms performing a logic operation. Nearest-neighbor exchange interactions transfer the magnetic state of the input islands to the center atom. An equivalent logic circuit with inputs A and B is sketched below.

Almaden Research Center, IBM Research Division, 650 Harry Road, San Jose, CA 95120, USA. E-mail: heinrich@almaden.ibm.com

point to another, and gate operation with threshold behavior—constitute most of the components needed to enable arbitrary binary logic. So what is preventing the wiring up of an atomic-scale calculator? Aside from practical issues such as room-temperature operation, a conceptual challenge is the implementation of energy gain: Does the binary signal decay in longer chains? Can the output of the logic gate drive one or more successive gates? It is likely that in order to achieve this goal, energy must be put into the system at certain stages. Borrowing ideas from nanodot logic, one possibility might be to elevate the spins into metastable states at a clock frequency (*3*, *4*). If a successful technology could be built from such spins, it promises low energy consumption.

So when will we reach the end of Moore's law? It is clear that the ultimate size limit is the scale of atoms, and this work takes a decisive step toward a real demonstration of spin-based computation at this limit. Given that there is currently about a factor of 1000 difference in areal density between silicon chip technology and the demonstration by Khajetoorians *et al*., there is still sufficient time to tackle the intriguing questions opened up by this work.

References

1. A. A. Khajetoorians, J. Wiebe, B. Chilian, R. Wiesendanger, *Science* **332**, 1062 (2011); 10.1126/science.1201725.
2. D. A. Allwood *et al*., *Science* **309**, 1688 (2005).
3. A. Imre *et al*., *Science* **311**, 205 (2006).
4. L. Gross *et al*., *Nanotechnology* **21**, 325301 (2010).
5. A. J. Heinrich *et al*., *Science* **298**, 1381 (2002); 10.1126/science.1076768.
6. D. M. Eigler, E. K. Schweizer, *Nature* **344**, 524 (1990).

10.1126/science.1206086

PHYSICS

Chameleon Magnets

An external voltage can switch ferromagnetism on and off in a material at room temperature, which may add new functionality to electronics.

Igor Žutić and John Cerně

The spin of an electron can serve as a magnetic messenger. Permanent magnetism, or ferromagnetism, comes from the spontaneous alignment of the electron spins and their associated magnetic moments in metals such as iron and cobalt, which results in their or magnetization. Ferromagnetism plays an important role in information storage, not only to keep refrigerator magnets in place (and notes held by them) but to store data in computer hard drives (*1*, *2*). A more common effect is paramagnetism—a material becomes magnetic only when an external magnetic field causes its spins to align. Silicon is paramagnetic, but its semiconductor properties, not its magnetism, make silicon useful in logic circuits. On page 1065 of this issue, Yamada *et al*. (*3*) report a breakthrough that brings together these two different worlds of ferromagnetic metals and paramagnetic semiconductors and may better integrate logic and memory. By adding cobalt impurities to nonmetallic and nonmagnetic titanium dioxide, they created an intriguing material $(Ti,Co)O_2$, which, like a chameleon, can reversibly transform from a paramagnet to a ferromagnet at room temperature.

Electrically controlled material properties are at the heart of modern microelectronics, which rely on devices such as silicon field-effect transistors (FETs). An applied electric field changes the number of current carriers in a semiconductor (an effect called doping) and can switch the current flowing through the FET on and off. This reversible effect differs from chemical doping (adding impurities), where the number of charge carriers is permanently changed. The FET approach allows an electric field to dope the same sample reversibly and even transform it from insulating to metallic (*4*, *5*). Yamada *et al*. start with chemical doping. They replace approximately 10% of Ti^{4+} ions in TiO_2 with Co^{2+} ions, which introduces three aligned spins for each Co^{2+}. The Co^{2+} ions and their spins (depicted by thick arrows in the figure) are localized, and their random orientations do not align in any particular way from Co^{2+} ion to Co^{2+} ion, a characteristic of a paramagnet (see the figure, panels A and B).

With applied positive voltage (depicted in the figure, panel C), extra electrons and their associated spins are added to $(Ti,Co)O_2$. These electrons are mobile and convey information about electron spin alignment between different Co^{2+} ions. The Co^{2+} ions adopt a ferromagnetic alignment and also transfer this spin alignment to the mobile electrons (see the figure, panel D).

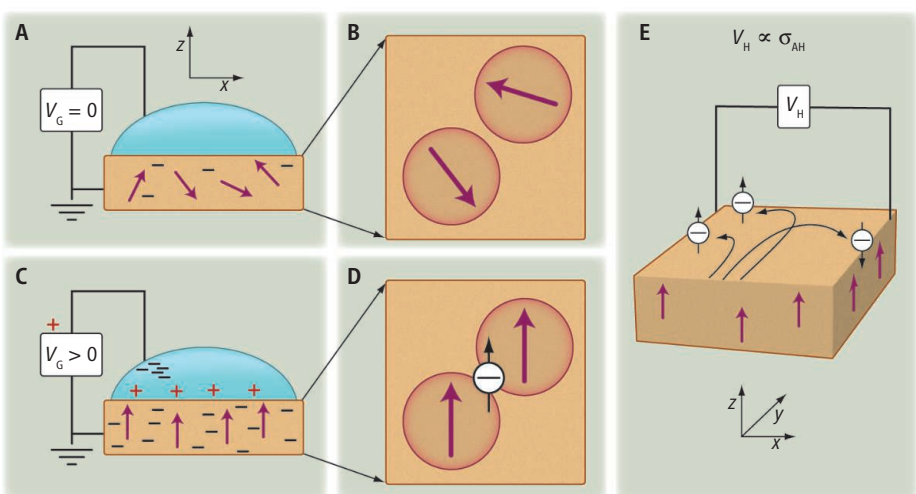

Tunable ferromagnetism. Cobalt-doped titanium dioxide, $(Ti,Co)O_2$, is paramagnetic. Yamada *et al*. show that applying a voltage to this material in an electrolytic cell causes it to become a ferromagnet. (**A** and **B**) With no applied gate voltage V_G between the electrolytic top contact and the $(Ti,Co)O_2$, the carrier density (electrons, e^-) is low, and the Co^{2+} spins (violet arrows) interact weakly and are not aligned. (**C** and **D**) For V_G at 3.8 V, the carrier density increases by nearly a factor of 10 and the electrons act as magnetic messengers, aligning the Co^{2+} spins. (**E**) Magnetization can be detected because it creates an imbalance in the electron spin populations. For an electron current flowing in the *y* direction, the spin-up electrons will tend to scatter to the left (–*x* direction) and the spin-down electrons to the right (+*x* direction). With more spin-up electrons, there will be a net accumulation of electrons on the left side of the sample, which in turn can be measured as an anomalous Hall voltage V_H or Hall conductivity σ_{AH}. Reversing V_G to zero transforms the ferromagnet back into a paramagnet.

Department of Physics, State University of New York at Buffalo, Buffalo, NY 14260, USA. E-mail: zigor@buffalo.edu; jcerne@buffalo.edu

Similar chameleon magnets were initially demonstrated by Ohno *et al*. (*6*), but they operated at cryogenic temperatures (about 25 K) and required very large applied voltages (±125 V). What allowed Yamada *et al*. to produce magnetic order at room temperature (300 K) and require only a few volts to turn the ferromagnetism on and off was a clever twist on the standard FET principle (*3*, *5*, *7*). Very large electric fields can irreparably damage materials—they act like a lightning strike. The maximum carrier density that can be reversibly induced in a material occurs at a field strength known as the breakdown electric field. Yamada *et al*. incorporated an electrochemical cell into a FET and effectively increased both the breakdown field and the maximum carrier density that can be added to a semiconductor by a factor of 10. The more carriers, the more their spin can promote a robust ferromagnetic alignment that can persist at higher temperatures.

With ferromagnetic alignment in place, the challenge remains to detect it. For example, tiny magnetic nanoclusters may form and give a spurious magnetization (*1*, *8*) that is not tunable with an electric field and lacks chameleon features. The authors measured the anomalous Hall effect (AHE), first reported in 1880 (*9*), which yields a voltage (V_{AH}), or equivalently conductivity (σ_{AH}), in the direction transverse to the charge flowing through the material. With imbalance in the electron spin populations, the AHE arises from the coupling of spin and orbital properties of the carriers, which produces asymmetry of the scattering: Carriers of opposite spins ("up" or "down") are deflected in opposite directions, transverse to the charge current (see the figure, panel E). By carefully comparing AHE for samples with carrier density altered by chemical or electric field doping, the authors provide strong support for the idea that the magnetization comes from mobile magnetic messengers (*10*).

What are the next steps, and can we expect further surprises? Unlike in chameleon magnets, ferromagnetism in semiconductors can have different origins and can be independent of electric fields (*11*). To simplify quests for other chameleon magnets, complementary measurement techniques could overcome challenges associated with constant-current measurements, in which genuine material properties can become obscured if the current flows nonuniformly along an atypical path. One possible approach is to perform higher-frequency (infrared) AHE measurements (*12*), which could reduce these difficulties and directly probe how the carriers in the host semiconductor are altered with the addition of magnetic ions.

It would also be important to understand how changing the carrier density modifies the maximum temperature for the onset of ferromagnetism. The elegant spin alignment in ferromagnets tends to be fragile at elevated temperatures. Heat ruins the order of nicely aligned spins in the same way that it ruins the order in a snowflake by melting. However, with chameleon magnets, the reverse may be possible. Heating semiconductors creates extra carriers, which could strengthen their role as magnetic messengers and could conceivably overcome the usual role of heat as the main foe of ferromagnetism (*13*, *14*).

Chameleon magnets could also help us make more versatile transistors and bring us closer to the seamless integration of memory and logic by providing smart hardware that can be dynamically reprogrammed for optimal performance of a specific task (*1*, *15*). Large applied magnetic fields can enforce the spin alignment in semiconductor transistors (*16*). With chameleon magnets, such alignment would be tunable and would require no magnetic field and could revolutionize the role ferromagnets play in technology.

References

1. I. Žutić *et al*., *Rev. Mod. Phys.* **76**, 323 (2004).
2. S. Maekawa, Ed., *Concepts in Spin Electronics* (Oxford Univ. Press, Oxford, 2006).
3. Y. Yamada *et al*., *Science* **332**, 1065 (2011).
4. C. H. Ahn *et al*., *Rev. Mod. Phys.* **78**, 1185 (2006).
5. K. Ueno *et al*., *Nat. Mater.* **7**, 855 (2008).
6. H. Ohno *et al*., *Nature* **408**, 944 (2000).
7. M. Endo *et al*., *Appl. Phys. Lett.* **96**, 022515 (2010).
8. S. R. Shinde *et al*., *Phys. Rev. Lett.* **92**, 166601 (2004).
9. M. I. Dyakonov, Ed., *Spin Physics in Semiconductors* (Springer, Berlin, 2008).
10. H. S. Hsu *et al*., *Appl. Phys. Lett.* **96**, 242507 (2010).
11. M. Venkatesan *et al*., *Nature* **430**, 630 (2004).
12. G. Acbas *et al*., *Phys. Rev. Lett.* **103**, 137201 (2009).
13. A. G. Petukhov *et al*., *Phys. Rev. Lett.* **99**, 257202 (2007).
14. M. J. Calderón, S. Das Sarma, *Phys. Rev. B* **75**, 235203 (2007).
15. H. Dery *et al*., http://arxiv.org/abs/1101.1497 (2011).
16. N. Rangaraju *et al*., *Phys. Rev. Lett.* **105**, 117202 (2010).

10.1126/science.1205775

BEHAVIOR

Explaining Human Behavioral Diversity

Ara Norenzayan

A study of 33 nations explores the ecological, historical, and cultural foundations of behavioral differences.

People have been captivated and puzzled by human diversity since ancient times. In today's globalized world, many of the key challenges facing humanity, such as reversing climate change, coordinating economic policies, and averting war, entail unprecedented cooperation between cultural groups on a global scale. Success depends on bridging cultural divides over social norms, habits of thinking, deeply held beliefs, and values deemed sacred. If we ignore, underestimate, or misunderstand behavioral differences, we do so at everyone's peril.

When it comes to understanding these differences, getting the science right is more important than ever. Ironically, one reason that the scientific study of human thought and behavior is so daunting, fascinating, and often controversial is precisely because, more than any other species, so much of human behavior is subject to considerable population variability. To better understand both this variability and humanity's shared characteristics, in recent years researchers in the social, behavioral, cognitive, and biological sciences have been using a variety of methods (including ethnographic and historical studies, experiments, and surveys) to deepen and extend our knowledge of cultural differences. These research programs are producing quantifiable, falsifiable, and replicable results. On page 1100 of this issue, for example, Gelfand *et al*. (*1*) report on an ambitious 33-nation study that compares the degree to which societies regulate social behavior and sanction deviant behavior. It highlights differences between "tight" cultures with strong norms and high sanctioning, and "loose" cultures with weak norms and low sanctioning.

Gelfand *et al*. surveyed 6823 people in the 33 nations, asking them to rate the appropriateness of 12 behaviors (such as eating or crying) in 15 situations (such as being in a

Department of Psychology, University of British Columbia, Vancouver, BC V6T1Z4, Canada. E-mail: ara@psych.ubc.ca

bank or at a party). Then, they compared the responses to an array of ecological and historical factors. Overall, they found that societies exposed to contemporary or historical threats, such as territorial conflict, resource scarcity, or exposure to high levels of pathogens, more strictly regulate social behavior and punish deviance. These societies are also more likely to have evolved institutions that strictly regulate social norms. At the psychological level, individuals in tightly regulated societies report higher levels of self-monitoring, more intolerant attitudes toward outsiders, and paying stricter attention to time. In this multilevel analysis, ecological, historical, institutional, and psychological variables comprise a loosely integrated system that defines a culture.

These findings complement a growing literature that reveals the power of the comparative approach in explaining critically important features of human behavior. For example, research suggests that the substantial variation in religious involvement among nations can be explained, in large part, by perceived levels of security. Religion thrives when existential threats to human security, such as war or natural disaster, are rampant, and declines considerably in societies with high levels of economic development, low income inequality and infant mortality, and greater access to social safety nets (*2*). Another recent investigation (*3*) suggested that past agricultural practices—specifically the adoption of the plow or the hoe by farmers—can have long-term effects on contemporary gender-related social norms and behaviors. It found that, all else being equal, societies that adopted the plow at an earlier historical period tended to have greater contemporary gender inequality (such as lower levels of women's participation in the labor market and lower percentages of women in government). In contrast, societies that adopted the hoe tend to have greater gender equality today. Gelfand *et al*.'s findings are consistent with other research suggesting that population variability seeps deep into the workings of human minds, affecting, for example, seemingly basic processes such as perception, reasoning, self-concept, distinct motivation, and cooperative strategies in economic games (*4*).

As more investigations enrich the cross-cultural database, two complex but critical questions open up for investigation. The first is: What are the causal pathways between variables (such as ecological, historical, and psychological variables), and how do they interact? Typically, for instance, researchers give causal precedence to chronologically earlier events and ecological factors, such as resource scarcity or pathogen levels, because they predate institutions, social practices, and individuals. In most cases, however, we know relatively little about the direction of causality. Do institutional structures socialize individuals to have certain values and preferences? Or do values and preferences lead to the creation of certain types of institutions? Or both? Knowledge of these pathways could shed light on a related question: How do sociocultural systems stabilize or change over time (*5*)?

Differences. Researchers are exploring the origins of the vast behavioral diversity across human population.

The second question, which researchers are just beginning to be tackle, involves the precise origins of the underlying population variation in thought and behavior, such as the differences in conformity, prosocial emotions, and intolerance of outsiders measured by Gelfand *et al*. Current evolutionary models suggest at least three distinct but compatible possibilities. The first posits that the human species is a cultural species, whose behavioral repertoire depends not only on genetic transmission but also on a sophisticated cultural inheritance system (*6*, *7*). This system causes rapid, cumulative, and divergent cultural evolution, the result of which is persistent intergroup variation in behavior, even when populations live in similar environments (*5*, *6*). The second model holds that many population differences are likely the result of different environments and represent noncultural phenotypic plasticity (*8*). Such a process could be reflected in the relationship between pathogen levels and stricter social norms reported by Gelfand *et al*. It remains to be seen, however, whether this plasticity is developmental—triggering locally adapted behavioral patterns early in an individual's life that then persist (an ontogenetic trajectory)—or whether it is "facultative," triggering locally adapted behaviors that are more flexible, and shift over an individual's lifetime in response to variation in ecological conditions. A third possibility is that some population variability originates from a process known as gene-culture coevolution (*9*). Although challenging to demonstrate conclusively, a growing research field is showing that human cultural practices directly alter parts of the human genome; the domestication of large milk-producing mammals, for instance, appears to have led to changes in gene frequencies coding for adult lactose absorption. A similar coevolutionary process may lurk behind some psychological differences, and this is an intriguing possible subject for future research. The relative contribution of these and other possible mechanisms, such as epigenetic (nongenetic) inheritance to behavioral diversity, is being actively debated (*10*).

Progress on these questions will be easier if researchers overcome two immediate obstacles facing the behavioral sciences. One is the extremely narrow cultural database that characterizes the experimental branches of psychology, economics, and the cognitive sciences, including cognitive neuroscience. Recent surveys indicate that the overwhelming majority of research participants are convenience samples selected from Western, educated, industrialized, rich, democratic (sometimes known as WEIRD) societies that often occupy one end of the broad spectrum of human behavior (*4*). Second, traditional disciplinary approaches typically focus on one level of analysis, ignoring others. As Gelfand *et al*.'s efforts illustrate, broad sampling and multiple approaches and methods are needed to investigate these different levels and their interrelations. Diverse samples, and collaborative teams that cross disciplinary boundaries (*11*), will open up new horizons in the behavioral sciences.

References and Notes

1. M. J. Gelfand *et al*., *Science* **332**, 1100 (2011).
2. P. Norris, R. Inglehart, *Sacred and Secular: Religion and Politics Worldwide* (Cambridge Univ. Press, Cambridge, 2004).
3. A. Alesina *et al*., NBER Working paper; www.economics.harvard.edu/faculty/nunn/files/Plough.pdf.
4. J. Henrich, S. J. Heine, A. Norenzayan, *Behav. Brain Sci.* **33**, 61, discussion 83 (2010).
5. D. Cohen, *Psychol. Bull.* **127**, 451 (2001).
6. J. Richerson, R. Boyd, *Not by Genes Alone: How Culture Transformed Human Evolution* (Univ. of Chicago Press, Chicago, 2005).
7. D. Sperber, *Explaining Culture: A Naturalistic Approach* (Blackwell, Cambridge, MA, 1996).
8. S. W. Gangestad *et al*., *Psychol. Inq.* **17**, 75 (2006).
9. K. N. Laland *et al*., *Nat. Rev. Genet.* **11**, 137 (2010).
10. G. R. Brown, T. E. Dickins, R. Sear, K. N. Leland, *Phil. Trans. Roy. Soc. B* **366**, 313 (2011).
11. M. Bang, D. L. Medin, S. Atran, *Proc. Natl. Acad. Sci. U.S.A.* **104**, 13868 (2007).

12. I acknowledge support by a Social Sciences and Humanities Research Council grant (410-2010-0297).

10.1126/science.1207050

BIOCHEMISTRY

KSR Plays CRAF-ty

A scaffold protein has enzymatic activity that controls a major cell signaling pathway.

Fumin Shi and Mark A. Lemmon

Organization of the bewildering array of known cell signaling proteins into coherent networks is facilitated by "scaffold" proteins that guide local information flow by binding multiple signaling molecules (*1*). Recent studies on one such scaffold protein called kinase suppressor of RAS (KSR), however, blur distinctions between the scaffold and the "scaffolded" by indicating that KSR itself has enzymatic activity that controls the signaling pathway assembled upon it (*2*–*4*).

KSR spatially coordinates the protein kinases RAF, mitogen-activated protein kinase (MAPK) kinase (MEK), and extracellular signal–regulated kinase (ERK; also called MAPK) (*5*–*7*), which constitute the classical ERK pathway. This cascade normally transmits signals from the small guanosine triphosphatase RAS (which is activated by cell surface receptors) to the nucleus, controlling the expression of genes that drive proliferation, differentiation, and other cellular processes. The ERK pathway is aberrantly activated in many human cancers, and small-molecule kinase inhibitors, notably those that target the BRAF isoform (ARAF and CRAF are other isoforms), are proving valuable in some clinical situations (*8*, *9*). To scaffold ERK signaling, KSR contains multiple binding sites that bring RAF, MEK, and ERK together at the plasma membrane (see the figure) (*6*, *10*). Recruitment of RAF and MEK requires the kinase-like domain of KSR, which is highly homologous to typical protein kinases, but (in mammals) lacks a catalytically crucial lysine residue. Although controversial, biochemical and genetic studies indicate that KSR's kinase domain is not active (*6*, *10*), placing it among the "pseudokinases" (*11*). Pseudokinases constitute ~10% of all protein kinase domains encoded by the human genome. Rather than functioning enzymatically, pseudokinases are thought either to allosterically regulate other kinases or to function as scaffolds—perhaps regulated by the same mechanisms that control canonical protein kinases (*11*). Both functions have been suggested for KSR (*7*, *10*).

RAF directly phosphorylates (and hence activates) MEK, with KSR acting as scaffold to bring them together. However, recent studies (*2*–*4*, *12*) argue that KSR is not just a scaffold and has much more in common with RAF than previously anticipated. Brennan *et al*. (*2*) and Hu *et al*. (*3*) show that, like RAF, KSR can and does (respectively) function as a protein kinase. In addition, earlier inhibitor studies unveiled a kinase-independent ("pseudokinase-like") function for BRAF (*13*). In cells with activated RAS, selective BRAF inhibitors stabilize BRAF-CRAF heterodimers in which BRAF allosterically activates CRAF to signal through the ERK pathway (*9*, *13*). Structural features crucial for this heterodimerization are retained in KSR's pseudokinase domain, which, like inhibitor-bound BRAF, can also allosterically activate RAF isoforms in KSR-RAF heterodimers (*12*). If this mode of RAF activation is a key function of KSR, then it is one that BRAF shares in the context of inhibitor-induced BRAF-CRAF heterodimers.

McKay *et al*. (*4*) report that BRAF inhibitors promote heterodimerization of BRAF with KSR. The pseudokinase domain of KSR is sufficient for this interaction, but neither RAS activation nor BRAF kinase activity is required. The authors suggest that KSR competes with CRAF for binding to inhibitor-bound BRAF. This competition reduces the degree of ERK activation induced by BRAF inhibitors, indicating that KSR expression should be considered in predicting cellular effects of BRAF-targeted drugs.

How might KSR be affected when it replaces CRAF in heterodimers with BRAF? Brennan *et al*. show that BRAF allosterically activates KSR (as it does CRAF). A crystal structure of the KSR2 kinase domain (bound to MEK1) shows adenosine 5′-triphosphate (ATP) in the KSR active site, and key catalytic residues arranged as in known kinases, suggesting enzymatic capacity. Using an ele-

Department of Biochemistry and Biophysics, and Graduate Group in Biochemistry and Molecular Biophysics, University of Pennsylvania School of Medicine, 422 Curie Boulevard, Philadelphia, PA 19104–6059, USA. E-mail: mlemmon@mail.med.upenn.edu

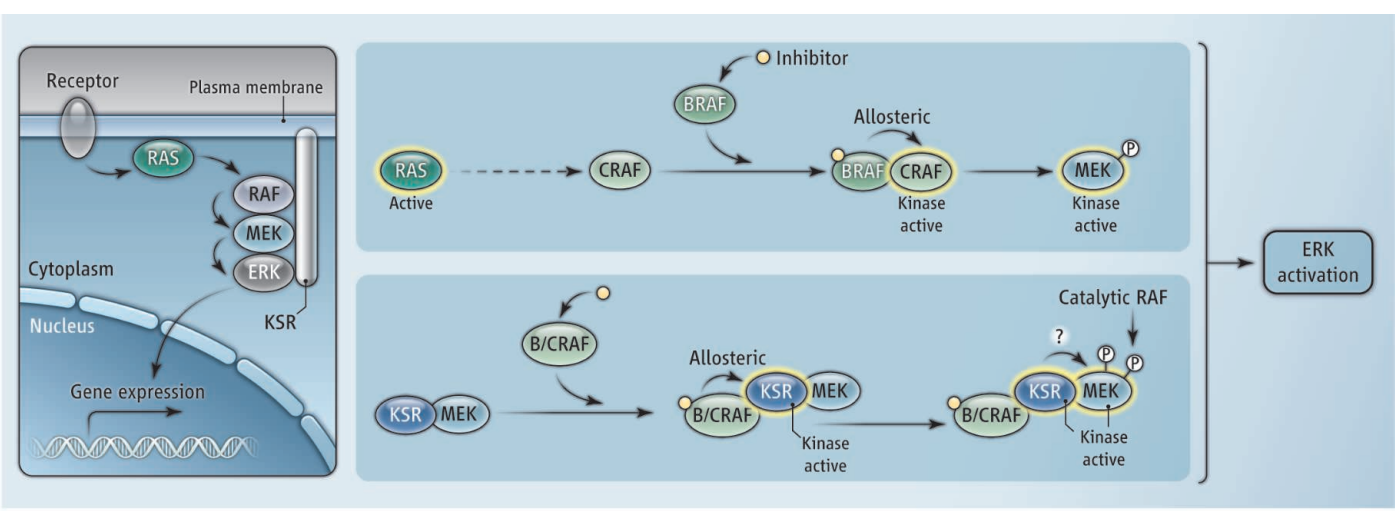

CREDIT: Y. HAMMOND/*SCIENCE*

A not so "pseudo" kinase. (**Left**) KSR is a scaffold for the ERK signaling pathway. (**Right**) In cells with activated RAS, inhibitor-bound BRAF allosterically activates CRAF, which then phosphorylates MEK. Inhibitor-bound BRAF or CRAF also binds to KSR in a KSR-MEK complex, and allosterically enhances KSR's kinase activity. The resulting conformational changes expose sites on MEK for phosphorylation by other catalytic RAF dimers. KSR may also phosphorylate MEK directly.

Published by AAAS

gant chemical genetics approach, Brennan *et al*. show that KSR2 phosphorylates MEK1 in vitro. The kinase activity is very weak, but the structure also reveals that the crucial αC helix in KSR's kinase domain is displaced to yield an inactive-like conformation. Intriguingly, adding BRAF substantially increased KSR's kinase activity under conditions in which BRAF-KSR-MEK complexes form. Compelling structural arguments suggest that BRAF binding shifts KSR's crucial αC helix into an active-like configuration. Biochemical assays bear this out and suggest that BRAF promotes KSR's kinase activity in the same way as it activates CRAF.

Hu *et al*. also describe inhibitor-promoted RAF-KSR interactions in mammalian cells (by studying overexpressed proteins) and detect KSR kinase activity that depends on interaction with inhibitor-bound RAF (in this case, CRAF). Contrary to McKay *et al*., they find that KSR is required for RAF inhibitors to activate ERK in RAS-transformed cells (rather than reducing the effect). This discrepancy may reflect the different specific inhibitors used, but it is also well documented that KSR can exert either positive or negative effects on the ERK signaling pathway depending on its expression level (*6*).

Hu *et al*. devised a clever mutational strategy to determine whether KSR primarily uses its kinase or RAF-interaction (scaffolding) ability to promote ERK activation. Introducing a bulky phenylalanine at a strategic position in KSR's ATP-binding site abolished ATP binding (and kinase activity), but retained scaffolding function (likely mimicking the kinase's ATP-bound, active-like, conformation). This mutated KSR still bound RAF, but no longer augmented ERK activation and did not support RAS transformation of KSR-deficient cells. KSR's scaffolding function is therefore not sufficient. Together with the work of Brennan *et al*., these studies strongly suggest that KSR functions as a kinase.

The studies by Brennan *et al*., Hu *et al*., and McKay *et al*. paint a picture of KSR action in the ERK pathway that is startlingly similar to that of CRAF. KSR competes with CRAF for binding to inhibited BRAF and, like CRAF, is allosterically activated as a result. But numerous questions remain to be answered. The physiological substrates phosphorylated by KSR, as well as the precise nature and stoichiometry of the complexes responsible for the RAF-KSR "collaboration," are unclear. These new findings add further complexity to a once-simple view of ERK pathway control. Moreover, they identify KSR kinase activity as a potential drug target. The studies of Brennan *et al*. and Hu *et al*. should also prompt analogous work to investigate the possibility of allosterically activated kinase activity in the other 40 to 50 presumed pseudokinases that have been ignored therapeutically, some of which clearly retain catalytic activity (*14*, *15*).

References

1. M. C. Good, J. G. Zalatan, W. A. Lim, *Science* **332**, 680 (2011).
2. D. F. Brennan *et al*., *Nature* **472**, 366 (2011).
3. J. Hu *et al*., *Proc. Natl. Acad. Sci. U.S.A.* **108**, 6067 (2011).
4. M. M. McKay, D. A. Ritt, D. K. Morrison, *Curr. Biol.* **21**, 563 (2011).
5. W. Kolch, *Nat. Rev. Mol. Cell Biol.* **6**, 827 (2005).
6. D. K. Morrison, *J. Cell Sci.* **114**, 1609 (2001).
7. M. M. McKay, D. A. Ritt, D. K. Morrison, *Proc. Natl. Acad. Sci. U.S.A.* **106**, 11022 (2009).
8. G. Bollag *et al*., *Nature* **467**, 596 (2010).
9. P. I. Poulikakos, N. Rosen, *Cancer Cell* **19**, 11 (2011).
10. C. M. Udell, T. Rajakulendran, F. Sicheri, M. Therrien, *Cell. Mol. Life Sci.* **68**, 553 (2011).
11. E. Zeqiraj, D. M. van Aalten, *Curr. Opin. Struct. Biol.* **20**, 772 (2010).
12. T. Rajakulendran, M. Sahmi, M. Lefrançois, F. Sicheri, M. Therrien, *Nature* **461**, 542 (2009).
13. K. Cichowski, P. A. Jänne, *Nature* **464**, 358 (2010).
14. K. Mukherjee *et al*., *Cell* **133**, 328 (2008).
15. F. Shi, S. E. Telesco, Y. Liu, R. Radhakrishnan, M. A. Lemmon, *Proc. Natl. Acad. Sci. U.S.A.* **107**, 7692 (2010).

10.1126/science.1208063

GEOPHYSICS

Assessing the Status of Alaska's Glaciers

New methods are providing an increasingly complex picture of a key contributor to global sea level.

Anthony A. Arendt

The glaciers of Alaska and northwestern Canada have long been considered important contributors to global sea level, but their remoteness has complicated efforts to quantify how their mass is changing. Nearly 30 years ago, the first regional assessment—based on data from only three glaciers and a largely intuitive regional extrapolation scheme—suggested that Alaska's glaciers accounted for more than one-third of the total sea-level contribution from glaciers and ice caps (excluding ice sheets) (*1*). Recently, global maps of water-mass variations, developed using satellite measurements of Earth's gravitational field (gravimetry), confirm with remarkable clarity the large role Alaska glaciers play in the global sea-level budget (see the figure). Far from solving the puzzle, however, these and other new observation technologies are revealing unexpected complexities in the magnitude and rate at which Alaska glaciers respond to climate.

Alaska's unique climatic and geologic environment set the stage for complex patterns of glacier change. Five mountain ranges rise up from the Gulf of Alaska to create enormous gradients in snow accumulation and air temperature that drive rapid exchanges of mass between the atmosphere and glacier surfaces. Much of the ice formed at high elevations is discharged at sea level through tidewater glaciers, which can advance and retreat over time scales that are often independent of climate. Further inland, glaciers experience drier conditions and more extreme fluctuations in temperature than their coastal counterparts, resulting in different sensitivities of these glaciers to climate. Glacier surges, volcanic events, and rapid rates of erosion alter the dynamics and geometry of ice in ways that are difficult to predict.

Given these complexities, how have glaciologists arrived at regional estimates of Alaska glacier change? Field measurements of mass accumulation and ablation provide the most direct information, but are logistically difficult to acquire in Alaska. Fortunately, researchers have monitored the Gulkana and Wolverine glaciers biannually since 1965, and these records show unique responses of glaciers to interior and maritime climate conditions (*2*). During the mid-1970s, the Wolverine Glacier gained mass due to an increase in precipitation concurrent with widespread warming across Alaska, while Gulkana Glacier lost mass. Since the early 1990s, both glaciers have been steadily losing mass, and temperature has become the

Geophysical Institute, University of Alaska, Fairbanks, Fairbanks, AK 99775, USA. E-mail: anthony.arendt@gi.alaska.edu

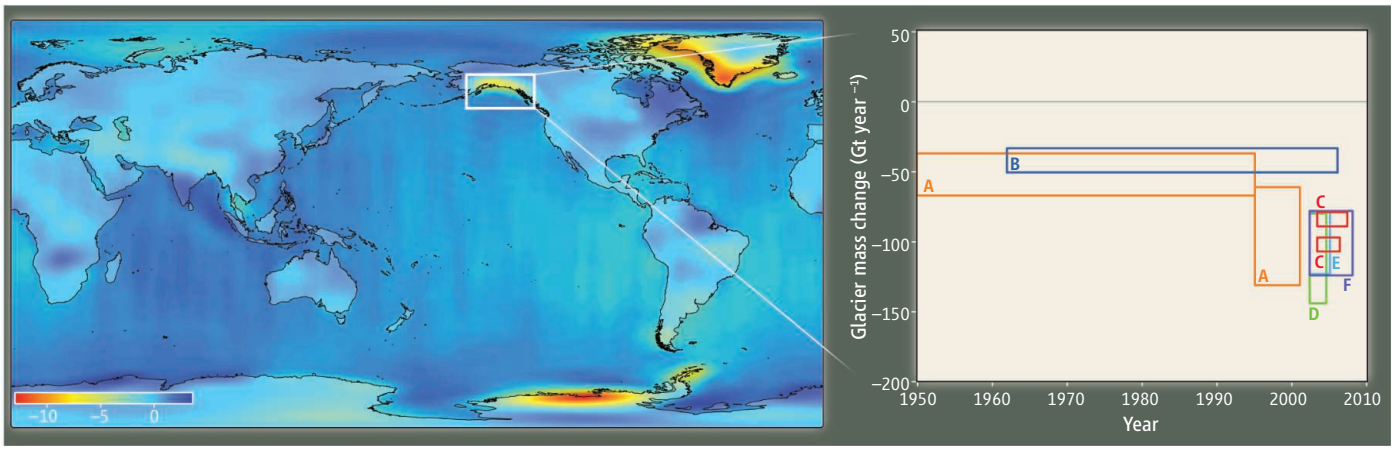

Effects of glaciers on Earth's gravity field. Changes in mass, expressed as centimeters equivalent water height, determined from July 2003 to July 2010 by data from GRACE satellites (*13*). Changes due to terrestrial hydrology and glacial isostatic adjustments have been removed. Inset shows long-term trend in Alaska glacier mass from (A) aircraft altimetry (*8*); (B) digital elevation model differencing (*7*); and (C to F) GRACE data (*9*–*12*).

dominant driver of change for both glaciers. These records are key tools in understanding the response of glaciers to climate, but are limited in spatial coverage.

To expand the scope of ground observations, researchers have turned to remote-sensing methods that provide measurements of glacier elevations through time. In the early 1990s, the University of Alaska, Fairbanks, glaciology group began flying a small aircraft equipped with GPS (Global Positioning System) and LIDAR (light detection and ranging) along the centerline of more than 100 glaciers, comparing elevations with those derived from maps, or from an earlier altimetry measurement (*3*). These measurements continue today as part of NASA's Operation IceBridge, a global airborne glacier-monitoring effort. In addition, measurements of surface elevation from satellite laser and radar altimetry, and stereo photogrammetry, have provided maps of glacier surface-elevation change that cover entire glacier regions (*4*–*7*).

These elevation measurements provided regional estimates of Alaska glacier changes that broadly agreed with field data, including a rapid acceleration in mass loss that began in the mid-1990s (*8*). Moreover, maps of elevation change allowed us to observe the disproportionately large contribution of tidewater glaciers to regional volume loss, the asynchronous behavior of neighboring glacier systems, and the timing of recent surge events. For instance, repeat airborne altimetry showed that the Guyot Glacier in Icy Bay thinned by over 100 m at its terminus between 2007 and 2009, while the nearby Yahtse Glacier terminus thickened by 80 m over the same period. The conclusion from these assessments is that, to account for the complex dynamics of individual glacier systems, nearly every glacier needed to be measured at least once.

In 2003, NASA and the German Aerospace Center launched the Gravity Recovery and Climate Experiment (GRACE), which not only measures all glaciers, but does so at a remarkably high temporal resolution. GRACE uses two satellites to provide a direct measure of Earth's mass variations, reconstructed from analysis of satellite orbital variations. Although much work remains to validate and refine GRACE data, so far the observations strongly support earlier field and remote-mapping estimates of glacier loss (*9*–*12*). GRACE observations also show us just how quickly Alaska glaciers can change from year to year. In 2004, they lost 0.40 ± 0.06 mm/year sea-level equivalent (SLE) in response to extremely high summer temperatures; 3 years later, high winter snow accumulations reduced losses to 0.13 ± 0.06 mm/year SLE (*9*). Such interannual variability suggests that researchers should be cautious about extrapolating future behavior from short time series, and highlights the need for long-term records.

GRACE has proven to be extremely useful for assessing multiannual trends in glacier mass, but researchers have not yet fully exploited high-resolution GRACE data that detail changes over time. In the wet maritime climate of southeast Alaska, huge seasonal variations in glacier mass force the Earth's lithosphere (the crust and upper portion of the mantle) to flex elastically, producing centimeter-scale vertical crustal displacements. To further pinpoint the sources of Alaska glacier changes, researchers are measuring these displacements using precise GPS ground stations and combining these observations with GRACE data and simulation models.

Nearly three decades after Alaska glaciers were first identified as key players in the global sea-level budget, glaciologists have an expanded range of new tools to quantify glacier changes. Recent observations show that, on average, Alaska glaciers have been losing mass more rapidly since the mid-1990s than they were several decades earlier. Understanding whether this trend continues will require an integration of observations across disciplines, as well as the development of robust glacier simulation models. These models must account for the direct effects of changing climate on glacier mass balances, as well as complex nonlinear dynamics of tidewater glaciers. Continuing field, airborne, and satellite observations is essential to provide calibration data for modeling efforts aimed at assessing the future response of glaciers to changing climate.

References and Notes

1. M. F. Meier, *Science* **226**, 1418 (1984).
2. A. Van Beusekom, S. O'Neel, R. March, L. Sass, L. Cox. "Re-analysis of Alaskan benchmark glacier mass balance data using the index method" (U.S. Geol. Surv. Sci. Inv. Rep. 2010-5247, 2010).
3. K. Echelmeyer *et al.*, *J. Glaciol.* **42**, 538 (1996).
4. C. Larsen, R. J. Motyka, A. A. Arendt, K. A. Echelmeyer, P. E. Geissler, *J. Geophys. Res.* **112** (F1), F01007 (2007).
5. J. VanLooy, R. Forster, A. Ford, *Geophys. Res. Lett.* **33**, L21307 (2006).
6. E. Schiefer, B. Menounos, R. Wheate, *Geophys. Res. Lett.* **34**, L16503 (2007).
7. E. Berthier, E. Schiefer, G. Clarke, B. Menounos, F. Rémy, *Nat. Geosci.* **3**, 92 (2010).
8. A. A. Arendt *et al.*, *Science* **297**, 382 (2002).
9. S. B. Luthcke *et al.*, *J. Glaciol.* **54**, 767 (2008).
10. M. E. Tamisiea, E. W. Leuliette, J. L. Davis, J. X. Mitrovica, *Geophys. Res. Lett.* **32**, L20501 (2005).
11. J. L. Chen *et al.*, *Earth Planet. Sci. Lett.* **248**, 353 (2006).
12. X. Wu *et al.*, *Nat. Geosci.* **3**, 642 (2010).
13. S. B. Luthcke *et al.*, *Geophys. Res. Lett.* **33**, L02402 (2006).
14. GRACE data provided by S. Luthcke. We acknowledge NASA Grant NNH07ZDA001N-CRYO.

10.1126/science.1204400

SPORE* SERIES WINNER

The Periodic Table of Videos

A YouTube project, started on impulse, has become a chemistry resource in daily use in classrooms and homes worldwide.

Brady Haran and Martyn Poliakoff†

"I know nothing about hassium. Shall we make something up?" A somewhat unusual opening, but what else can one say when trying to film separate videos about each element in the periodic table?

Our project was devised by Brady Haran, a BBC-trained video journalist, who had spent a year filming University of Nottingham scientists at work (*1*). Inspired by his time working with chemistry researchers, he suggested making a periodic table of videos (PTOV, www.periodicvideos.com), and within days, filming had begun.

The approach was unconventional: no scripts or storyboards, but a passionate desire to appeal to a general audience. An effective format rapidly evolved: Haran interviewed "The Professor" (Martyn Poliakoff) or lanthanide and actinide chemist Stephen Liddle in their offices, with separately filmed laboratory experiments carried out by chemists Peter Licence or Deborah Kays. More ambitious experiments were performed outdoors with the help of long-suffering and usually silent technician Neil Barnes. A key decision was made to avoid collaboration between the participants; each person filmed sections alone with Haran, and no vetting took place before "publication." The first time anyone saw the finished videos was when they had been edited and uploaded to the video-sharing Web site YouTube (*2*).

The result of this unusual process was a collection of videos (*3*) with spontaneity and freshness—a feeling of "live" chemistry. Collaborating with trained journalist Haran resulted in professional production values and editorial standards. Even before all 118 elements had been finished, PTOV's approach had caught the popular imagination. Stories appeared in the UK national media and on blogs worldwide (*4*, *5*). By the end of 5 weeks, when all 118 videos were finished, PTOV already had a strong subscriber base (*6*). The surprise was the breadth of the audience, which ranged from Nobel laureates to a 6-year-old boy in Nova Scotia. Also, our audience clearly expected more. As one viewer said, "I don't care what they do, as long as they keep making videos!" A spontaneous project was to become an ongoing enterprise. So, how to continue?

At the site of hassium's synthesis. Haran and "The Professor" shoot the updated hassium video at the GSI (Gesellschaft fuer Schwerionenforschung), Darmstadt, Germany, where element 108 was first synthesized.

An obvious route was to update some of the more hastily produced videos with more experiments, new information, and, in the case of hassium, a visit to Darmstadt, where the element was synthesized (see the photo, above). Subtitles were added to the element videos to make them easier to understand for non-native speakers of English, and an additional opportunity was identified: linking chemistry to topical events. Themed videos were produced about the 2008 Olympic Games (gold, silver, and bronze); the announcement of Nobel Prizes; and, more lightheartedly, the chemistry of pumpkins for Halloween. Soon PTOV had almost become a chemical news channel, covering events such as giving the name copernicium to element 112 or the *Science* paper in which helium was disguised as $H^{4.1}$ (*7*).

As of May 2011, the site boasted 320 videos with content covering molecules as well as elements, and each new video attracted several thousand views within hours of publication. The PTOV team had grown to include 10 presenters, all professional chemists, with Haran still handling all of the filming, editing, and production. The videos had been viewed more than 15 million times, and the YouTube channel had over 44,700 subscribers in more than 200 countries and territories, surpassing even the channel of Britain's royal family (*8*), until the recent wedding. PTOV now has followers on Twitter, Flickr, Facebook, and other social media sites (*9*).

PTOV has also spawned a successful "sister channel," Sixty Symbols (*10*, *11*), in which physics and astronomy are presented by Nottingham scientists; it already has 29,600 subscribers and 138 videos, all filmed and produced in a format similar to PTOV's.

Overall, 26 of the individual PTOV videos have had more than 100,000 views, and a further 45 have had more than 50,000. The most-viewed video, in which a cheeseburger

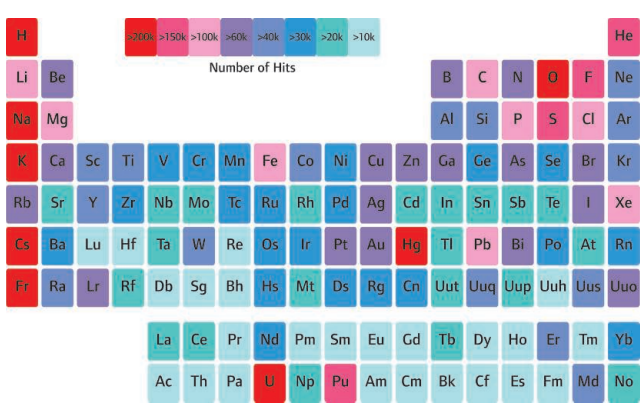

Success by the numbers. The periodic table (*14*) colored according to the number of views of each element as recorded on YouTube, 14 and 15 February 2011.

The School of Chemistry, The University of Nottingham, Nottingham NG7 2RD, UK.

*SPORE, *Science* Prize for Online Resources in Education; www.sciencemag.org/site/special/spore/.

†Author for correspondence. E-mail: martyn.poliakoff@nottingham.ac.uk

Published by AAAS

was plunged into hydrochloric acid, has attracted nearly 458,000 views. The number of views of each element's video is presented graphically in the figure (p. 1046). The most popular videos, such as Caesium and Oxygen, are of reactive elements, and surprisingly, even a synthetic element like hassium has attracted 32,000 views. Even the least popular, protactinium, has garnered over 12,000 views.

We think the impact of PTOV is best judged qualitatively from the many thousands of comments and unsolicited e-mails received from viewers (*12*). A substantial proportion of these suggests that PTOV has made a real difference to aspiring scientists. For example: "My name is David. I am a senior in High school. I have been watching your videos for quite some time. The videos are so interesting and have inspired me to be a Chemistry Major in college. Because of the inspiration you and your team created through the videos, many kids from around my area have also decided to take the interesting and complex journey to becoming chemists as well."

From the other side, we receive messages from teachers who use the videos. "I wanted to write to you to personally thank you for the wonderful work that you and your students have done. My colleagues and I, in Visalia, CA, use them in the classroom with our chemistry students. They are short and to the point. Our students enjoy watching them."

Some of the viewers see us as friends, turning to us for advice in times of need. "I'm very depressed. I love chemistry and I would like to study in Faculty of Pharmaceutical Sciences. Sadly, I failed the admission examination. It's such a very hard examination! What should I do?"

Undoubtedly, part of PTOV's appeal is that of a soap opera or reality TV (*6*). Each presenter attracts a personal following, whether it is the technician's apparent nonchalance or the professor's eccentric hairstyle and endless selection of chemistry-themed neckties. The viewers come to trust the presenters, who know their subject and tackle even the most obscure topics in creative ways. PTOV does not hesitate to show scientists as human, sharing their moments of happiness and grief with the viewers. When demonstrations fail, they still appear in the videos, especially if they are amusing. Shortcomings are never glossed over or edited out, which ensures that the team is seen as honest—they are not "selling" anything apart from a shared love of chemistry.

YouTube remains an ultracompetitive environment, as thousands of videos are uploaded every hour. However, there are several factors that probably help PTOV to stand out from the competition. The videos look professional because they are produced with broadcast-quality equipment used by Haran, yet they deliberately retain an amateur flavor and raw appearance. Like the TV news, PTOV can work fast when necessary, sometimes with a 3-hour turnaround time from filming to uploading. This can be crucial when responding to breaking news, such as our explanation of the recent nuclear crisis in Japan (*13*).

Viewers feel they are watching a "true record" of life in the chemistry department. The presenters are real scientists who are often caught off guard, forced to answer unexpected questions from the interviewer. Their hesitations and occasional admissions of ignorance reinforce the bond with the viewers.

Editorial control has been ceded to the nonscientist Haran, which ensures that interviews are conducted from the perspective of our layperson viewers. In effect, the viewers accompany Haran on his exploration of chemistry, sharing his wonder while being spared the bits he finds boring. All of this probably works because the participating scientists have done something that is increasingly unusual—they have trusted a journalist to tell their stories.

We have also been lucky. With the right team and the right approach, we have been able to exploit YouTube to the benefit of chemists and chemistry students across the world. However, there are new opportunities on the Internet. Undoubtedly, some of these tools could also be adapted to deliver science to the public in new ways. Try to imagine how you could use these technologies, as well as other innovations that will shortly be going live, to communicate your passion for science to the world. There is an audience out there waiting for you.

About the Authors

Brady Haran (fourth from left) is a video journalist specializing in science communication. He previously worked in newspapers and for the BBC. Born in Adelaide, Australia, he has lived in the UK for the past 9 years. **Martyn Poliakoff** (fourth from right) is a research professor in chemistry at the University of Nottingham. His research interests focus on "green" chemistry at the interface of chemistry and engineering, particularly the application of supercritical fluids. He is a Fellow of the Royal Society and, currently, a Council Member of the Institution of Chemical Engineers, IChemE. Shown here with supporting cast of PTOV.

CREDIT: L. GILLIGAN-LEE

References and Notes

1. Test Tube: Videos behind the scenes in the world of science; www.test-tube.org.uk.
2. PTOV on YouTube, www.youtube.com/periodicvideos.
3. PTOV on iTunes, www.nottingham.ac.uk/itunesu/index.aspx.
4. "Fizz-bang-whoosh…., " *Daily Mail* Online, 18 July 2008; www.dailymail.co.uk/sciencetech/article-1036279/Fizz-bang-whoosh---British-scientists-turn-Periodic-Table-internet-hit.html.
5. M. Moore, *Telegraph*, 15 July 2008; www.telegraph.co.uk/science/science-news/3347317/YouTube-periodic-table-Explosive-video-guides.html.
6. S. K. Ritter, *Chem. Eng. News* **86**, 42 (2008).
7. D. G. Fleming *et al.*, *Science* **331**, 448 (2011).
8. The Royal Channel, www.youtube.com/theroyalchannel.
9. Links to social media are accessible from the PTOV home page, www.periodicvideos.com.
10. Sixty Symbols: Videos about the symbols of physics and astronomy, www.sixtysymbols.com.
11. P. Ball, *Chem. World* **7**, 40 (2010).
12. B. Haran, M. Poliakoff, *Nat. Chem.* **3**, 180 (2011).
13. Nuclear reactors in Japan—Periodic Table of Videos, www.youtube.com/watch?v=-bcrLiATLq0.
14. Where there have been updates (e.g., Cs), the views of all versions of a video have been aggregated.

15. We thank P. License, N. Barnes, D. Kays, A. Khlobystov, S. Liddle, J. Moses, R. Stockman, S. Tang, and D. Walsh for their enthusiastic participation in PTOV and J. Gamble, M. Healy, C. Johnson, B. Nerlich, and C. Rudd for their help. We are grateful for funding from the Engineering and Physical Sciences Research Council, COST (www.cost.esf.org), the DICE project (Driving Innovation in Chemistry and Engineering), the Anamax Charitable Foundation, Briggs of Burton PLC, and the University of Nottingham.

10.1126/science.1196980

Published by AAAS

SCIENCE POLICY

Leaders Urge "Political Will" to Support U.S. Innovation Culture

Robert Atkinson is an influential expert on innovation, and in a presentation at the AAAS Forum on Science and Technology Policy, he detailed a troubling pattern that has emerged from the fields of global competition.

Across the world, more nations are becoming tough competitors, said the president of the nonpartisan Information Technology & Innovation Foundation (ITIF). They're adopting rigorous innovation strategies. They're dramatically increasing their investment in research and development and forming government agencies to guide the efforts. The United States, meanwhile, is only now developing a comprehensive innovation strategy. Its R&D investments between 1987 and 2008 were just a little bit better than stagnant.

The result? According to an ITIF study, "The Atlantic Century," the United States in 2009 ranked sixth in research-based competitiveness among 40 nations and regions. When the study ranked which nations made the most progress between 1999 and 2008, the United States placed last.

"All these other countries are continuing to make these investments," Atkinson said. "But we've decided that we can slack off and not continue to ramp up."

The assessment was blunt, but it reflected the clear consensus among science and policy leaders who spoke at the Forum. They described a nation suffering not only from a weak economy and depressed federal and state budgets, but also from an uneven commitment to innovation and the policies needed to compete.

Charles M. Vest, president of the National Academy of Engineering, warned of a "national nightmare" should the country fail to renew its culture of innovation. "We know what the problems are," Vest said. "We know how to solve them. [But] we must develop the political will to do so."

It's the sort of unvarnished insight for which the Forum has become well known. This year, the 36th annual event convened nearly 500 U.S. and foreign leaders from government, education, and business in Washington, D.C., to hear top policy experts analyze critical issues. The Forum, held 5 to 6 May, was organized by AAAS Science and Policy Programs.

To be sure, there was good news. Anthony Fauci, director of the National Institute of Allergy and Infectious Diseases, described how political support from President Ronald Reagan and every U.S. president since has driven vast, life-saving progress in the fight against HIV/AIDS. Meanwhile, some states and regions—the old industrial city of Cleveland, for example—are using innovation initiatives to drive economic growth.

White House science and technology adviser John P. Holdren detailed how key science agencies had mostly been spared from the deepest cuts imposed in other areas by the 2011 budget agreement. Under President Barack Obama's 2012 spending plan, funding for basic and applied research would rise 11%, to $66.1 billion. But Holdren warned that budget and political pressures—next year and beyond—could create "enormous" challenges for S&T initiatives.

A telling example came from David Pomerantz, director of the Democrats' staff on the House Appropriations Committee. Funding for the Advanced Research Projects Agency-Energy hit $400 million in 2010. In 2011, the appropriation fell to $180 million. Obama is proposing $550 million for 2012. But, said Pomerantz, "there's an element, especially in the House, that is repelled by the notion of clean energy or climate research."

Other presentations at the Forum charted big-picture progress for innovation. Most of the trend lines were flat, or falling.

The tax code discourages research partnerships between industry and universities, speakers said, and the R&D tax credit is no longer competitive with similar tax policy in some other nations. Visa policies enacted after 9/11 remain an obstacle to talented foreign students and researchers who could make vital contributions to U.S. innovation.

Any long-term solution requires a focus on education, but there, too, speakers saw worrisome trends. Education was a central focus in the National Academies' landmark 2005 "Rising Above the Gathering Storm" report, but Vest, a member of the committee that wrote the report, said the highest priority recommendations—on K-12 science-related education and improvement of the teacher corps—"have not yet been substantively addressed."

Time is running short, a number of speakers concluded, and they urged the public and political leaders to invest in innovation for long-term national strength.

"The United States used to be full of people who believed in endless possibility," Vest said. "But pessimism is now holding us back…It is time to regain our optimism and our 'can do' spirit in order to remain a great nation and meet the challenges of our times."

See Forum presentation materials at www.aaas.org/spp/rd/forum.

–Katherine Zambon and Bob Roehr contributed to this report.

COMMUNICATION

Screeners Needed for Journalism Awards

Volunteer scientists are needed to review entries in the prestigious AAAS Kavli Science Journalism Awards competition. Scientists residing in the Washington, D.C. area, or who will be in the area in mid-August to mid-September, are invited to help screen print, online, radio, and television reports for scientific accuracy. If interested, please contact Angela Bradley (202-326-6408; abradley@aaas.org) in the AAAS Office of Public Programs.

Published by AAAS

Dyscalculia: From Brain to Education

Brian Butterworth,[1]* Sashank Varma,[2] Diana Laurillard[3]

Recent research in cognitive and developmental neuroscience is providing a new approach to the understanding of dyscalculia that emphasizes a core deficit in understanding sets and their numerosities, which is fundamental to all aspects of elementary school mathematics. The neural bases of numerosity processing have been investigated in structural and functional neuroimaging studies of adults and children, and neural markers of its impairment in dyscalculia have been identified. New interventions to strengthen numerosity processing, including adaptive software, promise effective evidence-based education for dyscalculic learners.

Developmental dyscalculia is a mathematical disorder, with an estimated prevalence of about 5 to 7% (*1*), which is roughly the same prevalence as developmental dyslexia (*2*). A major report by the UK government concludes, "Developmental dyscalculia is currently the poor relation of dyslexia, with a much lower public profile. But the consequences of dyscalculia are at least as severe as those for dyslexia" [(*3*), p. 1060]. The relative poverty of dyscalculia funding is clear from the figures: Since 2000, NIH has spent $107.2 million funding dyslexia research but only $2.3 million on dyscalculia (*4*).

The classical understanding of dyscalculia as a clinical syndrome uses low achievement on mathematical achievement tests as the criterion without identifying the underlying cognitive phenotype (*5*–*7*). It has therefore been unable to inform pathways to remediation, whether in focused interventions or in the larger, more complex context of the math classroom.

Why Is Mathematical Disability Important?

Low numeracy is a substantial cost to nations, and improving standards could dramatically improve economic performance. In a recent analysis, the Organisation for Economic Co-operation and Development (OECD) demonstrated that an improvement of "one-half standard deviation in mathematics and science performance at the individual level implies, by historical experience, an increase in annual growth rates of GDP per capita of 0.87%" [(*8*), p. 17]. Time-lagged correlations show that improvements in educational performance contribute to increased GDP growth. A substantial long-term improvement in GDP growth (an added 0.68% per annum for all OECD countries) could be achieved just by raising the standard of the lowest-attaining students to the Programme for International Student Assessment (PISA) minimum level (Box 1).

In the United States, for example, this would mean bringing the lowest 19.4% up to the minimum level, with a corresponding 0.74% increase in GDP growth.

Besides reduced GDP growth, low numeracy is a substantial financial cost to governments and personal cost to individuals. A large UK cohort study found that low numeracy was more of a handicap for an individual's life chances than low literacy: They earn less, spend less, are more likely to be sick, are more likely to be in trouble with the law, and need more help in school (*9*). It has been estimated that the annual cost to the UK of low numeracy is £2.4 billion (*10*).

What Is Dyscalculia?

Recent neurobehavioral and genetic research suggests that dyscalculia is a coherent syndrome that reflects a single core deficit. Although the literature is riddled with different terminologies, all seem to refer to the existence of a severe disability in learning arithmetic. The disability can be highly selective, affecting learners with normal intelligence and normal working memory (*11*), although it co-occurs with other developmental disorders, including reading disorders (*5*) and attention deficit hyperactivity disorder (ADHD) (*12*) more often than would be expected by chance. There are high-functioning adults who are severely dyscalculic but very good at geometry, using statistics packages, and doing degree-level computer programming (*13*).

There is evidence that mathematical abilities have high specific heritability. A multivariate genetic analysis of a sample of 1500 pairs of monozygotic and 1375 pairs of dizygotic 7-year-old twins found that about 30% of the genetic variance was specific to mathematics (*14*). Although there is a significant co-occurrence of dyscalculia with dyslexia, a study of first-degree relatives of dyslexic probands revealed that numerical abilities constituted a separate factor, with reading-related and naming-related abilities being the two other principal components (*15*). These findings imply that arithmetical learning is at least partly based on a cognitive system that is distinct from those underpinning scholastic attainment more generally.

This genetic research is supported by neurobehavioral research that identifies the representation of numerosities—the number of objects in a

Box 1: PISA question example

At Level 1, students can answer questions involving familiar contexts in which all relevant information is present and the questions are clearly defined. They are able to identify information and carry out routine procedures according to direct instructions in explicit situations. They can perform actions that are obvious and follow immediately from the given stimuli. For example:

Mei-Ling found out that the exchange rate between Singapore dollars and South African rand was 1 SGD = 4.2 ZAR

Mei-Ling changed 3000 Singapore dollars into South African rand at this exchange rate.

How much money in South African rand did Mei-Ling get?

79% of 15-year-olds were able to answer this correctly.

Box 2: Dyscalculia observed

Examples of common indicators of dyscalculia are (i) carrying out simple number comparison and addition tasks by counting, often using fingers, well beyond the age when it is normal, and (ii) finding approximate estimation tasks difficult. Individuals identified as dyscalculic behave differently from their mainstream peers. For example:

To say which is the larger of two playing cards showing 5 and 8, they count all the symbols on each card.

To place a playing card of 8 in sequence between a 3 and a 9, they count up spaces between the two to identify where the 8 should be placed.

To count down from 10, they count up from 1 to 10, then 1 to 9, etc.

To count up from 70 in tens, they say "70, 80, 90, 100, 200, 300…"

They estimate the height of a normal room as "200 feet?"

[1]Centre for Educational Neuroscience and Institute of Cognitive Neuroscience, University College London, Psychological Sciences, Melbourne University, Melbourne VIC 3010, Australia. [2]Department of Educational Psychology, University of Minnesota, Minneapolis, MN 55455, USA. [3]Centre for Educational Neuroscience and London Knowledge Lab, Institute of Education, University of London, London WC1N 3QS, UK.

*To whom correspondence should be addressed. E-mail: b.butterworth@ucl.ac.uk

set—as a foundational capacity in the development of arithmetic (*16*). This capacity is impaired in dyscalculic learners even in tasks as simple as enumerating small sets of objects (*11*) or comparing the numerosities of two arrays of dots (*17*). The ability to compare dot arrays has been correlated with more general arithmetical abilities both in children (*18*) and across the age range (*17*, *19*). This core deficit in processing numerosities is analogous to the core deficit in phonological awareness in dyslexia (Box 2) (*2*).

Although there is little longitudinal evidence, it seems that dyscalculia persists into adulthood (*20*), even among individuals who are able in other cognitive domains (*13*). The effects of early and appropriate intervention with dyscalculia have yet to be investigated. This also leaves open the question as to whether there is a form of dyscalculia that is a delay, rather than a deficit, that will resolve, perhaps with appropriate educational support.

Converging evidence of dyscalculia as a distinct deficit comes from studies of impairments in the mental and neural representation of fingers. It has been known for many years that fingers are used in acquiring arithmetical competence (*21*). This involves understanding the mapping between the set of fingers and the set of objects to be enumerated. If the mental representation of fingers is weak, or if there is a deficit in understanding the numerosity of sets, then the child's cognitive development may fail to establish the link between fingers and numerosities. In fact, developmental weakness in finger representation ("finger agnosia") is a predictor of arithmetical ability (*22*). Gerstmann's Syndrome, whose symptoms include dyscalculia and finger agnosia, is due to an abnormality in the parietal lobe and, in its developmental form, is also associated with poor arithmetical attainment (*23*).

Numbers do not seem to be meaningful for dyscalculics—at least, not meaningful in the way that they are for typically developing learners. They do not intuitively grasp the size of a number and its value relative to other numbers. This basic understanding underpins all work with numbers and their relationships to one another.

What Do We Know About the Brain and Mathematics?

The neural basis of arithmetical abilities in the parietal lobes, which is separate from language and domain-general cognitive capacities, has been broadly understood for nearly 100 years from research on neurological patients (*24*). One particularly interesting finding is that arithmetical concepts and laws can be preserved even when facts have been lost (*25*), and conversely, facts can be preserved even when an understanding of concepts and laws has been lost (*26*).

Neuroimaging experiments confirm this picture and show links from the parietal lobes to the left frontal lobe for more complex tasks (*27*, *28*). One important new finding is that the neural organization of arithmetic is dynamic, shifting from one subnetwork to another during the process of learning. Thus, learning new arithmetical facts primarily involves the frontal lobes and the intraparietal sulci (IPS), but using previously learned facts involves the left angular gyrus, which is also implicated in retrieving facts from memory (*29*). Some of the principal links are summarized in Fig. 1. Even prodigious calculators use this network, although supplementing it with additional brain areas (*30*) that appear to extend the capacity of working memory (*31*).

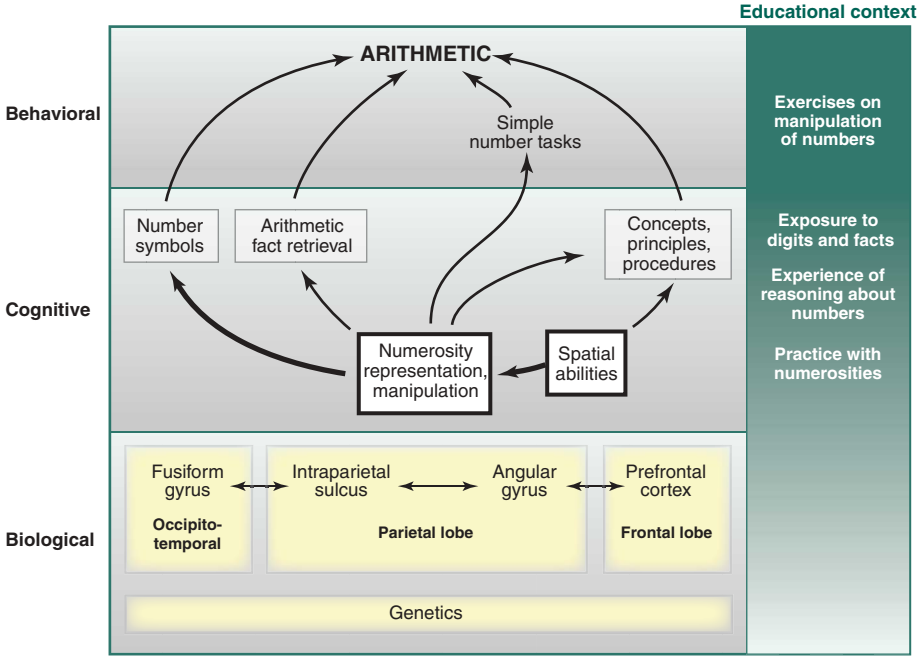

Fig. 1. Causal model of possible inter-relations between biological, cognitive, and simple behavioral levels. Here, the only environmental factors we address are educational. If parietal areas, especially the IPS, fail to develop normally, there will be an impairment at the cognitive level in numerosity representation and consequential impairments for other relevant cognitive systems revealed in behavioral abnormalities. The link between the occipitotemporal and parietal cortex is required for mapping number symbols (digits and number words) to numerosity representations. Prefrontal cortex supports learning new facts and procedures. The multiple levels of the theory suggest the instructional interventions on which educational scientists should focus.

There is now extensive evidence that the IPS supports the representation of the magnitude of symbolic numbers (*32*, *33*), either as analog magnitudes or as a discrete representation that codes cardinality, as evidenced by IPS activation when processing the numerosity of arrays of objects (*34*). Moreover, when IPS functioning is disturbed by magnetic stimulation, the ability to estimate discrete magnitudes is affected (*35*, *36*). The critical point is that almost all arithmetical and numerical processes implicate the parietal lobes, especially the IPS, suggesting that these are at the core of mathematical capacities.

Patterns of brain activity in 4-year-olds and adults show overlapping areas in the parietal lobes bilaterally when responding to changes in numerosity (*37*). Nevertheless, there is a developmental trajectory in the organization of more complex arithmetical abilities. First, the organization of routine numerical activity changes with age, shifting from frontal areas (which are associated with executive function and working memory) and medial temporal areas (which are associated with declarative memory) to parietal areas (which are associated with magnitude processing and arithmetic fact retrieval) and occipito-temporal areas (which are associated with processing symbolic form) (*38*). These changes allow the brain to process numbers more efficiently and automatically, which enables it to carry out the more complex processing of arithmetical calculations. As A. N. Whitehead observed, an understanding of symbolic notation relieves "the brain of all unnecessary work … and sets it free to concentrate on more advanced problems" (*39*).

This suggests the possibility that the neural specialization for arithmetical processing may arise, at least in part, from a developmental interaction between the brain and experience (*40*, *41*). Thus, one way of thinking about dyscalculia is that the typical school environment does not provide the right kind of experiences to enable the dyscalculic brain to develop normally to learn arithmetic.

Of course, mathematics is more than just simple number processing and retrieval of previously learned facts. In a numerate society, we have to

learn more complex mathematical concepts, such as place value, and more complex procedures, such as "long" addition, subtraction, multiplication, and division. Recent research has revealed the neural correlates of learning to solve complex, multidigit arithmetic problems (*24*). Again, this research shows that solving new problems requires more activation in the inferior frontal gyrus for reasoning and working memory and the IPS for representing the magnitudes of the numbers involved, as compared with retrieval of previously learned facts (*42*).

The striking result in all of these studies is the crucial role of the parietal lobes. That the IPS is implicated in both simple and complex calculations suggests that the basic representations of magnitude are always activated, even in the retrieval of well-learned single-digit addition and multiplication facts (*43*). This is consistent with the well-established "problem-size effect," in which single-digit problems take longer to solve the larger the operands, even when they are well known (*44*). It seems that the typically developing individual, even when retrieving math facts from memory, cannot help but activate the meaning of the component numbers at the same time. If that link has not been established, calculation is necessarily impaired.

What Do We Know About the Brain and Dyscalculia?

The clinical approach has identified behavioral deficits in dyscalculic learners typically by performance on standardized tests of arithmetic. However, even in primary school (K1 to 5), arithmetical competence involves a wide range of cognitive skills, impairments in any of which may affect performance, including reasoning, working memory, language understanding, and spatial cognition (*45*). Neural differences in structure or functioning may reflect differences in any of these cognitive skills. However, if dyscalculia is a core deficit in processing numerosities, then abnormalities should be found in the parietal network that supports the enumeration of small sets of objects (*11*) and the comparison of numerosities of arrays of dots (*17*).

The existence of a core deficit in processing numerosities is consistent with recent discoveries about dyscalculic brains: (i) Reduced activation has been observed in children with dyscalculia during comparison of numerosities (*46*, *47*), comparison of number symbols (*46*), and arithmetic (*48*)—these children are not using the IPS so much during these tasks. (ii) Reduced gray matter in dyscalculic learners has been observed in areas known to be involved in basic numerical processing, including the left IPS (*49*), the right IPS (*50*), and the IPS bilaterally (*51*)—these learners have not developed these brain areas as much as typical learners (Fig. 2). And (iii) differences in connectivity among the relevant parietal regions, and between these parietal regions and occipitotemporal regions associated with processing symbolic number form (Fig. 2), are revealed through diffusion tensor imaging tractography (*51*)—dyscalculic learners have not sufficiently developed the structures needed to coordinate the components needed for calculation.

Figure 1 suggests that the IPS is just one component in a large-scale cortical network that subserves mathematical cognition. This network may break down in multiple ways, leading to different dyscalculia patterns of presenting symptoms when the core deficit is combined with other cognitive deficits, including working memory, reasoning, or language (*52*).

Moreover, the same presenting symptom could reflect different impairments in the network. For example, abnormal comparison of symbolic numbers (*53*, *54*) could arise from an impairment in the fusiform gyrus associated with visual processing of number symbols, an impairment in IPS associated with the magnitude referents, analog or numerosity, of the number symbols, or reduced connectivity between fusiform gyrus and IPS.

How Is This Relevant to Maths Education?

There have been many attempts to raise the performance of children with low-numeracy, although not specifically dyscalculia. In the United States, evidence-based approaches have focused on children from deprived backgrounds, usually low socioeconomic status (*46*, *47*). The current National Strategy in the United Kingdom gives special attention to children with low numeracy by (i) diagnosing each child's conceptual gaps in understanding and (ii) giving the child more individual support in working through visual, verbal, and physical activities designed to bridge each gap. Unfortunately, there is still little quantitative evaluation of the effectiveness of the strategy since it was first piloted in 2003: "the evaluations used very diverse measures; and most did not include ratio gains or effect sizes or data from which these could be obtained" [(*55*), p. 13].

It has not been possible to tell, therefore, whether identifying and filling an individual's conceptual gaps with a more individualized version of the same teaching is effective. A further problem is that these interventions are effective when there has been specialist training for teaching assistants, but not all schools can provide this (*55*).

These standardized approaches depend on curriculum-based definitions of typical arithmetical development, and how children with low numeracy differ from the typical trajectory. In contrast, neuroscience research suggests that rather than address isolated conceptual gaps, remediation should build the foundational number concepts first. It offers a clear cognitive target for assessment and intervention that is largely independent of the learners' social and educational circumstances. In the assessment of individual cognitive capacities, set enumeration and comparison can supplement performance on curriculum-based standardized tests of arithmetic to differentiate dyscalculia from other causes of low numeracy (*11*, *56*, *57*).

In intervention, strengthening the meaningfulness of numbers, especially the link between the math facts and their component meanings, is crucial. As noted above, typical retrieval of simple arithmetical facts from memory elicits activation of the numerical value of the component numbers.

Without specialized intervention, most dyscalculic learners are still struggling with basic arithmetic in secondary school (*20*). Effective early intervention may help to reduce the later impact on poor numeracy skills, as it does in dyslexia (*58*). Although very expensive, it promises to repay 12 to 19 times the investment (*10*).

What Can Be Done?

Although the neuroscience may suggest what should be taught, it does not specify how it should be taught. Concrete manipulation activities have been used for many decades in math remediation because they provide tasks that make number concepts meaningful (*59*), providing an intrinsic

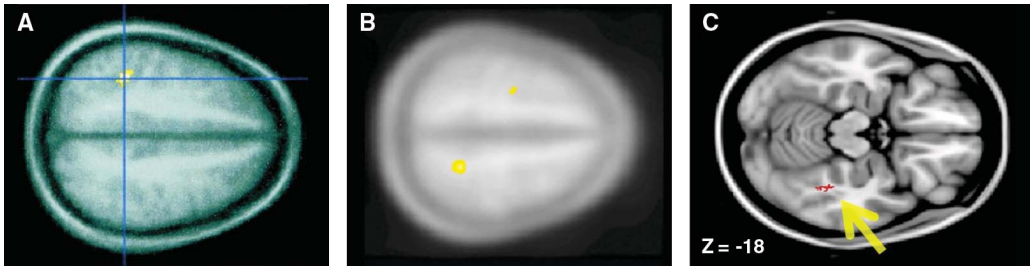

Fig. 2. Structural abnormalities in young dyscalculic brains suggesting the critical role for the IPS. Here, we show areas where the dyscalculic brain is different from that of typically developing controls. Both left and right IPS are implicated, possibly with a greater impairment for left IPS in older learners. (**A**) There is a small region of reduced gray-matter density in left IPS in adolescent dyscalculics (*41*). (**B**) There is right IPS reduced gray-matter density (yellow area) in 9-year-olds (*42*). (**C**) There is reduced probability of connections from right fusiform gyrus to other parts of the brain, including the parietal lobes (*43*).

relationship between a goal, the learner's action, and the informational feedback on the action (*60*). Educators recognize that informational feedback provides intrinsic motivation in a task, and that is of greater value to the learner than the extrinsic motives and rewards provided by a supervising teacher (*61*–*63*).

Experienced special educational needs (SEN) teachers use these activities in the form of games with physical manipulables (such as Cuisenaire rods, number tracks, and playing cards) to give learners experience of the meaning of number. Through playing these games, learners can discover from their manipulations, for example, which rod fits with an 8-rod to match a 10-rod. However, these methods require specially trained teachers working with a single learner or a small group of learners (*64*–*66*) and are allotted only limited time periods in the school schedule.

A promising approach, therefore, is to construct adaptive software informed by the neuroscience findings on the core deficit in dyscalculia. Such software has the potential to reduce the demand on specially trained teachers and to transcend the limits of the school schedule. There have been two examples of adaptive games based on neuroscience findings.

The *Number Race* (*67*) targets the inherited approximate numerosity system in the IPS (*68*) that may support early arithmetic (*18*). In dyscalculics, this system is less precise (*17*), and the training is designed to improve its precision. The task is to select the larger of two arrays of dots, and the software adapts to the learner, making the difference between the arrays smaller as their performance improves, and provides informational feedback as to which is correct.

Another adaptive game, *Graphogame-Maths*, targets the inherited system for representing and manipulating sets in the IPS, which is impaired in dyscalculia (*45*). Again, the basis of the game is the comparison of visual arrays of objects, but here the sets are small and can be counted, and the progressive tasks are to identify the link between the number of objects in the sets and their verbal numerical label, with informational feedback showing which is correct.

The effectiveness of the two games was compared in a carefully controlled study of kindergarten children (aged 6 to 7 years) who were identified by their teachers as needing special support in early maths. After 10 to 15 min of play per school day for 3 weeks, there was a significant improvement in the task practiced in both games—namely, number comparison—but the effect did not generalize to counting or arithmetic. *Graphogame-Maths* appeared to lead to slightly better and longer-lasting improvement in number comparison (*69*).

Although the *Number Race* and *Graphogame-Maths* are adaptive games based on neuroscience findings, neither requires learners to manipulate numerical quantities. Manipulation is critical for providing an intrinsic relationship between task goals, a learner's actions, and informational feedback on those actions (*60*). When a learning environment provides informational feedback, it enables the learner to work out how to adjust their actions in relation to the goal, and they can be their own "critic," not relying on the teacher to guide (*61*–*63*). This is analogous to the "actor-critic" model of unsupervised reinforcement learning in neuroscience, which proposes a critic element internal to the learning mechanism—not a guide that is external to it—which evaluates the informational feedback in order to construct the next action (*70*).

A different approach, one that emulates the manipulative tasks used by SEN teachers, has been taken in adaptive software that, driven by the neuroscience research on dyscalculia, focuses on numerosity processing (Fig. 3) (*56*). The informational feedback here is not an external critic showing the correct answer. Rather, the visual representation of two rods that match a given distance, or not, enables the learner to interpret for themselves what the improved action should be—and can serve as their own internal critic.

An additional advantage of adaptive software is that learners can do more practice per unit time than with a teacher. It was found that for "SEN learners (12-year-olds) using the Number Bonds game [illustrated in Fig. 3], 4–11 trials per minute were completed, while in an SEN class of three supervised learners only 1.4 trials per minute were completed during a 10-min observation" [(*56*), p. 535]. In another SEN group of 11 year olds, the game elicited on average 173 learner manipulations in 13 min (where a perfect performance, in which every answer is correct, is 88 in 5 min because the software adapts the timing according to the response). In this way, neuroscience research is informing what should be targeted in the next generation of adaptive software.

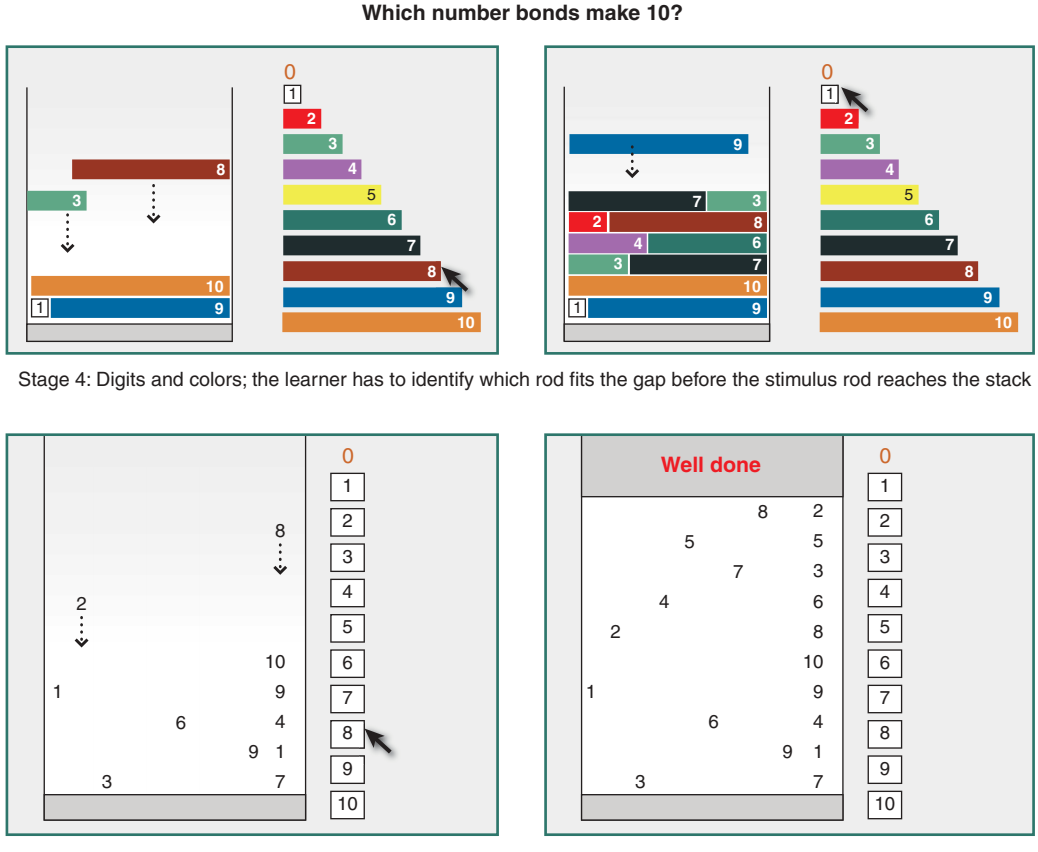

Stage 4: Digits and colors; the learner has to identify which rod fits the gap before the stimulus rod reaches the stack

Stage 6: Digits only; the learner has to identify which digit makes 10 before the stimulus number reaches the stack

Fig. 3. Remediation using learning technology. The images are taken from an example of an interactive, adaptive game designed to help the learner make the link between digits and their meaning. The timed version of the number bonds game elicits many learner actions with informational feedback, and scaffolds abstraction, through stages 1, 5 colors + lengths, evens; 2, 5 colors + lengths, odds; 3, all 10 colors + lengths; 4, digits + colors + lengths; 5, digits + lengths; and 6, digits only. Each rod falls at a pace adapted to the learner's performance, and the learner has to click the corresponding rod or number to make 10 before it reaches the stack (initially 3 s); if there is a gap, or overlap, or they are too slow, the rods dissolve. When a stack is complete, the game moves to the next stage. The game is available from www.number-sense.co.uk/numberbonds/.

At present, it is not yet clear whether early and appropriately targeted interventions can turn a dyscalculic into a typical calculator. Dyscalculia may be like dyslexia in that early intervention can improve practical effectiveness without making the cognitive processing like that of the typically developing.

What Is the Outlook?

Recent research by cognitive and developmental scientists is providing a scientific characterization of dyscalculia as reduced ability for understanding numerosities and mapping number symbols to number magnitudes. Personalized learning applications developed by educational scientists can be targeted to remediate these deficits and can be implemented on handheld devices for independent learning. Because there are also individual differences in numerosity processing in the normal range (*17*, *19*, *71*), the same programs can assist beginning mainstream learners, so one can envisage a future in which all learners will benefit from these developments.

Although much progress has been made, a number of open questions remain.

(i) The possible existence of a variety of dyscalculia behavioral patterns of impairment raises the interesting question of whether one deficit—numerosity estimation—is a necessary or sufficient for a diagnosis of dyscalculia. This is critical because it has implications for whether a single diagnostic assessment based on numerosity is sufficient, or whether multiple assessments are required. It also has implications for whether numerosity should be the focus of remediation, or whether other (perhaps more symbolic) activities must also be targeted.

(ii) Does the sensitivity of neuroscience measures make it possible to identify learners at risk for dyscalculia earlier than is possible with behavioral assessments, as is the case with dyslexia (*72*)?

(iii) Further research is needed on the neural consequences of intervention. Even where intervention improves performance, it may not be clear whether the learner's cognitive and neural functioning has become more typical or whether compensatory mechanisms have developed. This would require more extensive research, as in the case of dyslexia, in which functional neuroimaging has revealed the effects of successful behavioral interventions on patterns of neural function (*2*).

(iv) Personalized learning applications enable fine-grain evaluation of theory-based instructional interventions. For example, the value of active manipulation versus associative learning on one hand, and of intrinsic versus extrinsic motivation and feedback on the other, can be assessed by orthogonally manipulating these features of learning environments. Their effects can be assessed behaviorally in terms of performance on the tasks by target learners. Their effects can also be assessed by investigating neural changes over time in target learners, through structural and functional neuroimaging. Classroom-based but theory-based testing holds great potential for the development of educational theory and could contribute in turn to testing hypotheses in neuroscience.

(v) At the moment, dyscalculia is not widely recognized by teachers or educational authorities nor, it would seem, by research-funding agencies. Recognition is likely to be the basis for improved prospects for dyscalculic sufferers.

There is an urgent societal need to help failing learners achieve a level of numeracy at which they can function adequately in the modern workplace. Contemporary research on dyscalculia promises a productive way forward, but it is still a "poor relation" in terms of funding (*4*), which means there is a serious lack of evidence-based approaches to dyscalculia intervention. An understanding of how the brain processes underlying number and arithmetic concepts will help focus teaching interventions on critical conceptual activities and will help focus neuroscience research on tracking the structural and functional changes that follow intervention. Learning more about how to help these learners is driving, and will continue to drive, where the science should go next.

References

1. R. S. Shalev, in *Why Is Math So Hard for Some Children? The Nature and Origins of Mathematical Learning Difficulties and Disabilities*, D. B. Berch, M. M. M. Mazzocco, Eds. (Paul H. Brookes Publishing, Baltimore, MD, 2007), pp. 49–60.
2. J. D. E. Gabrieli, *Science* **325**, 280 (2009).
3. J. Beddington *et al.*, *Nature* **455**, 1057 (2008).
4. D. V. M. Bishop, *PLoS ONE* **5**, e15112 (2010).
5. V. Gross-Tsur, O. Manor, R. S. Shalev, *Dev. Med. Child Neurol.* **38**, 25 (1996).
6. L. Kosc, *J. Learn. Disabil.* **7**, 164 (1974).
7. R. S. Shalev, V. Gross-Tsur, *Pediatr. Neurol.* **24**, 337 (2001).
8. OECD, *The High Cost of Low Educational Performance: The Long-Run Economic Impact of Improving Educational Outcomes* (OECD, Paris, 2010).
9. S. Parsons, J. Bynner, *Does Numeracy Matter More?* (National Research and Development Centre for Adult Literacy and Numeracy, Institute of Education, London, 2005).
10. J. Gross, C. Hudson, D. Price, *The Long Term Costs of Numeracy Difficulties* (Every Child a Chance Trust and KPMG, London, 2009).
11. K. Landerl, A. Bevan, B. Butterworth, *Cognition* **93**, 99 (2004).
12. M. C. Monuteaux, S. V. Faraone, K. Herzig, N. Navsaria, J. Biederman, *J. Learn. Disabil.* **38**, 86 (2005).
13. B. Butterworth, *The Mathematical Brain* (Macmillan, London, 1999).
14. Y. Kovas, C. Haworth, P. Dale, R. Plomin, *Monogr. Soc. Res. Child Dev.* **72**, 1 (2007).
15. G. Schulte-Körne *et al.*, *Ann. Hum. Genet.* **71**, 160 (2007).
16. B. Butterworth, *Trends Cogn. Sci.* **14**, 534 (2010).
17. M. Piazza *et al.*, *Cognition* **116**, 33 (2010).
18. C. K. Gilmore, S. E. McCarthy, E. S. Spelke, *Cognition* **115**, 394 (2010).
19. J. Halberda, M. M. M. Mazzocco, L. Feigenson, *Nature* **455**, 665 (2008).
20. R. S. Shalev, O. Manor, V. Gross-Tsur, *Dev. Med. Child Neurol.* **47**, 121 (2005).
21. K. C. Fuson, *Children's Counting and Concepts of Number* (Springer Verlag, New York, 1988).
22. M.-P. Noël, *Child Neuropsychol.* **11**, 413 (2005).
23. M. Kinsbourne, E. K. Warrington, *Brain* **85**, 47 (1962).
24. L. Cipolotti, N. van Harskamp, in *Handbook of Neuropsychology*, R. S. Berndt, Ed. (Elsevier Science, Amsterdam, 2001), vol. 3, pp. 305–334.
25. M. Hittmair-Delazer, C. Semenza, G. Denes, *Brain* **117**, 715 (1994).
26. M. Delazer, T. Benke, *Cortex* **33**, 697 (1997).
27. A. Nieder, S. Dehaene, *Annu. Rev. Neurosci.* **32**, 185 (2009).
28. L. Zamarian, A. Ischebeck, M. Delazer, *Neurosci. Biobehav. Rev.* **33**, 909 (2009).
29. A. Ischebeck, L. Zamarian, M. Schocke, M. Delazer, *Neuroimage* **44**, 1103 (2009).
30. M. Pesenti *et al.*, *Nat. Neurosci.* **4**, 103 (2001).
31. B. Butterworth, in *Cambridge Handbook of Expertise and Expert Performance.*, K. A. Ericsson, N. Charness, P. J. Feltovich, R. R. Hoffmann, Eds. (Cambridge Univ. Press, Cambridge, 2006), pp. 553–568.
32. S. Dehaene, M. Piazza, P. Pinel, L. Cohen, *Cogn. Neuropsychol.* **20**, 487 (2003).
33. P. Pinel, S. Dehaene, D. Rivière, D. LeBihan, *Neuroimage* **14**, 1013 (2001).
34. F. Castelli, D. E. Glaser, B. Butterworth, *Proc. Natl. Acad. Sci. U.S.A.* **103**, 4693 (2006).
35. M. Cappelletti, H. Barth, F. Fregni, E. S. Spelke, A. Pascual-Leone, *Exp. Brain Res.* **179**, 631 (2007).
36. R. Cohen Kadosh *et al.*, *Curr. Biol.* **17**, 1 (2007).
37. J. F. Cantlon, E. M. Brannon, E. J. Carter, K. A. Pelphrey, *PLoS Biol.* **4**, e125 (2006).
38. D. Ansari, *Nat. Rev. Neurosci.* **9**, 278 (2008).
39. A. N. Whitehead, *An Introduction to Mathematics* (Oxford Univ. Press, London, 1948).
40. D. Ansari, A. Karmiloff-Smith, *Trends Cogn. Sci.* **6**, 511 (2002).
41. M. H. Johnson, *Nat. Rev. Neurosci.* **2**, 475 (2001).
42. M. Delazer *et al.*, *Neuroimage* **25**, 838 (2005).
43. X. Zhou *et al.*, *Neuroimage* **35**, 871 (2007).
44. N. J. Zbrodoff, G. D. Logan, in *Handbook of Mathematical Cognition,* J. I. D. Campbell, Ed. (Psychology Press, Hove, UK, 2005), pp. 331–345.
45. B. Butterworth, in *Handbook of Mathematical Cognition,* J. I. D. Campbell, Ed. (Psychology Press, Hove, UK, 2005), pp. 455–467.
46. C. Mussolin *et al.*, *J. Cogn. Neurosci.* **22**, 860 (2009).
47. G. R. Price, I. Holloway, P. Räsänen, M. Vesterinen, D. Ansari, *Curr. Biol.* **17**, R1042 (2007).
48. K. Kucian *et al.*, *Behav. Brain Funct.* **2**, 31 (2006).
49. E. B. Isaacs, C. J. Edmonds, A. Lucas, D. G. Gadian, *Brain* **124**, 1701 (2001).
50. S. Rotzer *et al.*, *Neuroimage* **39**, 417 (2008).
51. E. Rykhlevskaia, L. Q. Uddin, L. Kondos, V. Menon, *Front. Hum. Neurosci.* **3**, 1 (2009).
52. O. Rubinsten, A. Henik, *Trends Cogn. Sci.* **13**, 92 (2009).
53. I. D. Holloway, D. Ansari, *J. Exp. Child Psychol.* **103**, 17 (2009).
54. L. Rousselle, M.-P. Noël, *Cognition* **102**, 361 (2007).
55. A. Dowker, "What works for children with mathematical difficulties? The effectiveness of intervention schemes" (Department for Children, Schools and Families, 2009); available at http://nationalstrategies.standards.dcsf.gov.uk/node/174504.
56. B. Butterworth, D. Laurillard, *ZDM Math. Educ.* **42**, 527 (2010).
57. K. Landerl, B. Fussenegger, K. Moll, E. Willburger, *J. Exp. Child Psychol.* **103**, 309 (2009).
58. U. C. Goswami, *Nat. Rev. Neurosci.* **7**, 406 (2006).
59. A. Anning, A. Edwards, *Promoting Children's Learning from Birth to Five: Developing the New Early Years Professional* (Open Univ. Press, Maidenhead, UK, 1999).
60. S. Papert, *Mindstorms: Children, Computers, and Powerful Ideas* (Harvester Press, Brighton, UK, 1980).
61. J. S. Bruner, *Harv. Educ. Rev.* **31**, 21 (1961).
62. E. L. Deci, R. Koestner, R. M. Ryan, *Rev. Educ. Res.* **71**, 1 (2001).
63. J. Dewey, *Experience and Education* (Kappa Delta Pi, New York, 1938).
64. R. Bird, *The Dyscalculia Toolkit* (Paul Chapman Publishing, London, 2007).
65. B. Butterworth, D. Yeo, *Dyscalculia Guidance* (nferNelson, London, 2004).
66. D. Yeo, in *The Dyslexia Handbook*, M. Johnson, L. Peer, Eds. (British Dyslexia Association, Reading, UK, 2003).
67. A. Wilson, S. Revkin, D. Cohen, L. Cohen, S. Dehaene, *Behav. Brain Funct.* **2**, 1 (2006).
68. L. Feigenson, S. Dehaene, E. Spelke, *Trends Cogn. Sci.* **8**, 307 (2004).
69. P. Räsänen, J. Salminen, A. J. Wilson, P. Aunioa, S. Dehaene, *Cogn. Dev.* **24**, 450 (2009).
70. P. Dayan, L. Abbott, *Theoretical Neuroscience: Computational and Mathematical Modeling of Neural Systems* (MIT Press, Cambridge, MA, 2001).
71. C. K. Gilmore, S. E. McCarthy, E. S. Spelke, *Nature* **447**, 589 (2007).
72. H. Lyytinen *et al.*, *Dev. Neuropsychol.* **20**, 535 (2001).

10.1126/science.1201536

Pure Reasoning in 12-Month-Old Infants as Probabilistic Inference

Ernő Téglás,[1,2]* Edward Vul,[3]* Vittorio Girotto,[4,5] Michel Gonzalez,[5] Joshua B. Tenenbaum,[6]† Luca L. Bonatti[7]†

Many organisms can predict future events from the statistics of past experience, but humans also excel at making predictions by pure reasoning: integrating multiple sources of information, guided by abstract knowledge, to form rational expectations about novel situations, never directly experienced. Here, we show that this reasoning is surprisingly rich, powerful, and coherent even in preverbal infants. When 12-month-old infants view complex displays of multiple moving objects, they form time-varying expectations about future events that are a systematic and rational function of several stimulus variables. Infants' looking times are consistent with a Bayesian ideal observer embodying abstract principles of object motion. The model explains infants' statistical expectations and classic qualitative findings about object cognition in younger babies, not originally viewed as probabilistic inferences.

Exploiting statistical regularities of the environment predictively, to adapt behavior to future events, is a basic strategy in biology. Humans, even in infancy, use observed frequencies to learn words (*1*, *2*), spatiotemporal patterns (*3*, *4*), and visual object features (*5*). Adults can make rational statistical judgments on the basis of frequencies of previously experienced events or summaries of event frequencies (*6*, *7*). Even nonhuman mammals and many other organisms use experienced statistical regularities to modify their behavior (*8*, *9*).

However, humans also excel at reasoning about novel situations, flexibly combining abstract knowledge and perceptual information from disparate sources in "one-shot" intuitions to predict outcomes of events they have never before directly experienced. We call this ability "pure reasoning" to distinguish it from more data-driven means of forming expectations on the basis of statistical learning or finding patterns from repeated exposures. To see more clearly the difference between these two prediction modes and the one-shot nature of pure reasoning, consider several configurations of colored blocks arranged on a table (Fig. 1) and the following judgment: If the table is bumped so that one block falls off, is it more likely to be red or yellow? If the blocks are all close to the edges but there are twice as many red blocks (Fig. 1A), you will probably respond "red." However, if the yellow blocks are precariously stacked and located near the edge (Fig. 1B), you will likely respond "yellow." If the red blocks are located closer to the edge (Fig. 1C), you may again respond "red," although with less confidence, but you may revert to yellow if the precarious yellow stack in the center is doubled in height (Fig. 1D). People can make these judgments the first time they see these displays and make such common-sense predictions in a near-infinite variety of real-world situations, confidently and quickly. To do so by using only basic statistical learning mechanisms, recording over many such scenes all the ways any number of objects can be arranged and all the ways they tend to fall, would be almost impossible. Pure reasoning provides a more powerful and flexible approach (*10*). Considering the number of blocks of each color and their locations, together with intuitive knowledge of physical factors determining how they will move, a reasoner can construct a sample of ways that each configuration of blocks might fall if the table is bumped and then observe, purely within the imagined likely possibilities, which outcome appears most probable. This ability to flexibly combine multiple sources of information and knowledge to predict how a complex situation will unfold is at the core of human intelligence and is one of the biggest missing links in building artificial intelligence systems with humanlike "common sense."

Our goal is to probe the roots of this remarkable ability in human infants. Infants' reasoning abilities are typically studied by measuring their looking times to visually presented events as an index of surprise: Longer looking indicates greater violation of infants' expectations relative to their prior knowledge or greater novelty relative to their interpretation of habituation stimuli. Looking-time studies suggest that preverbal infants can reason about novel events depending on certain physical outcomes (*11*, *12*); object numerosities (*13*); other agents' beliefs, goals and behaviors (*14*–*16*); and the likely outcomes of simple random processes (*17*, *18*).

However, the richness, power, and coherence of infants' reasoning about future events remain unclear. Is it anything like the ability of adults to extrapolate likely future states for scenes such as those in Fig. 1? When presented with a complex dynamic environment with multiple objects that move and may be hidden from view as they move for several seconds, do infants form appropriate expectations about where different objects are likely to be observed at future times? Do their expectations about the future vary in systematic and rational ways over different initial configurations of objects in space and different temporal intervals for prediction?

We addressed these questions by using a combination of novel experiments and computational models (*19*). Our experiments independently varied several features of dynamic displays, such that forming appropriate expectations required infants to quantitatively integrate multiple sources of perceptual evidence with optimal weights that vary over time. Across these manipulations, we kept test events fixed and equal in salience so that infants' looking times had the potential to show variations in degrees of belief (or conversely, degrees of surprise) as their expectations changed.

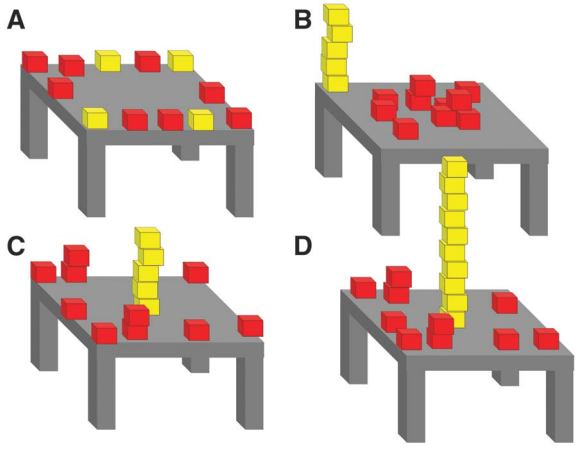

Fig. 1. Examples of common-sense predictions based on pure reasoning. If the table in this scene is bumped so that one block falls off the table onto the floor, is it more likely to be a red or a yellow block? Intuitions will vary according to the number of blocks of each type (**A**), their arrangement into more- or less-precarious stacks and their locations on the table (**B**), and interactions between all these factors (**C** and **D**).

[1]Cognitive Development Centre, Central European University, H-1015 Budapest, Hungary. [2]Hungarian Academy of Sciences, H-1015 Budapest, Hungary. [3]University of California, San Diego, La Jolla, CA 92093, USA. [4]University IUAV of Venice, 30135 Venice, Italy. [5]CNRS and Aix-Marseille University, 13331 Marseille, France. [6]Department of Brain and Cognitive Sciences, Massachusetts Institute of Technology, Cambridge, MA 02139, USA. [7]ICREA (Institució Catalana de Recerca i Estudis Avançats) and Universitat Pompeu Fabra, 08018 Barcelona, Spain.

*These authors contributed equally to this work.
†To whom correspondence should be addressed. E-mail: lucabonatti@mac.com (L.L.B.); jbt@mit.edu (J.B.T.)

We describe a Bayesian ideal observer model that predicts infants' looking times in our studies and extends to other aspects of infants' reasoning about the physical world, giving a unifying explanation of several classic results in infant cognition. This model shows how powerful pure reasoning capacities could derive from the operation of probabilistic inference mechanisms constrained by abstract principles of how objects act and interact over time.

Pure reasoning at 12 months. We probed preverbal infants' expectations about unknown future events when they witness dynamic scenes that contain multiple potentially relevant–but also potentially conflicting–sources of information, similar to (but simpler than) the examples in Fig. 1. Infants viewed movies in which four objects of two types, identified by different shapes and colors, bounced randomly inside a container with an opening on its lower side (movies S1 to S5). After several seconds of observed motion, an occluder covered the container's contents from view for some duration between 0 and 2 s. Finally, one object visibly exited through the bottom opening, and the occluder faded out. Monitoring infants' looking time to this final outcome allowed us to assess how surprised infants were to see an object of either type exit first.

Twelve kinds of movies were generated by manipulating three factors relevant to predicting these outcomes: the number of objects of each type in the scene (three instances of one type and one of the other type), their physical arrangement (objects of one type were always closer to the exit before occlusion than objects of the other type), and the duration of occlusion (0, 1, or 2 s). Forming correct expectations here requires the ability to integrate these three information sources, guided by abstract knowledge about how objects move: at a minimum, qualitative knowledge about solidity (objects are unlikely to pass through walls) and spatiotemporal continuity (objects tend to move short distances over brief time intervals). Infants appear to be sensitive to each of these information sources and knowledge systems individually (*11*, *20*). We asked whether they can also integrate them rationally to predict single future events.

A rational prediction of which object type will exit first should depend on both the number and the physical arrangement of the object types, but the relative importance of these factors should vary with occlusion duration. After a very brief occlusion, the objects' locations before occlusion are most predictive of which object type will exit first; however, when the occlusion is prolonged, proximity to the exit matters less because the objects continue moving in the container. Eventually, after a sufficiently long occlusion, only the number of each object type should be predictive.

In each of three experiments, infants saw four displays varying in whether the object that exited first belonged to the type with one or three instances and whether that type was near or far from the exit before occlusion. Occlusion duration was varied across experiments (Fig. 2A). Mean looking times (M) across all 12 displays showed exactly the rational pattern of predictions described above (Fig. 2, B to D). In experiment 1, with longest occlusion times (2 s), infants looked longer when the single unique object exited the container first [($M_{3\text{-instances}}$) = 11.9 s, $M_{1\text{-instance}}$ = 15.6 s; $F(1, 19)$ = 5.66, P = 0.028 under a repeated measures analysis of variance (ANOVA)], but distance from the exit had no effect [M_{Near} = 13.5 s, M_{Far} = 14.2 s; $F(1, 19)$ = 0.69, P = 0.42]. In experiment 2, with intermediate occlusion times (1 s), infants considered both factors, looking longer at the unique object outcome [$M_{3\text{-instances}}$ = 11.8 s, $M_{1\text{-instance}}$ = 15.0 s; $F(1, 19)$ = 4.65, P = 0.04] and also when an object located far from the opening before occlusion exited first [M_{Near} = 11.6 s, M_{Far} = 15.1 s; $F(1, 19)$ = 5.22, P = 0.03]. In experiment 3 with occlusion time of 0.04 s, looking times were insensitive to type numerosity [$M_{3\text{-instances}}$ = 14.0 s, $M_{1\text{-instance}}$ = 12.4 s; $F(1, 19)$ = 0.65, P = 0.43] but were significantly longer when an object far from the exit left the container first [M_{Near} = 10.2 s, M_{Far} = 15.7 s; $F(1, 19)$ = 16.5, P = 0.0007]. Numerosity and distance did not interact in any experiment [$F(1, 15)$ = 0.007, P = 0.93; $F(1, 17)$ = 2.09, P = 0.17; $F(1, 13)$ = 1.2, P = 0.29, respectively], suggesting that infants tended to consider both cues additively.

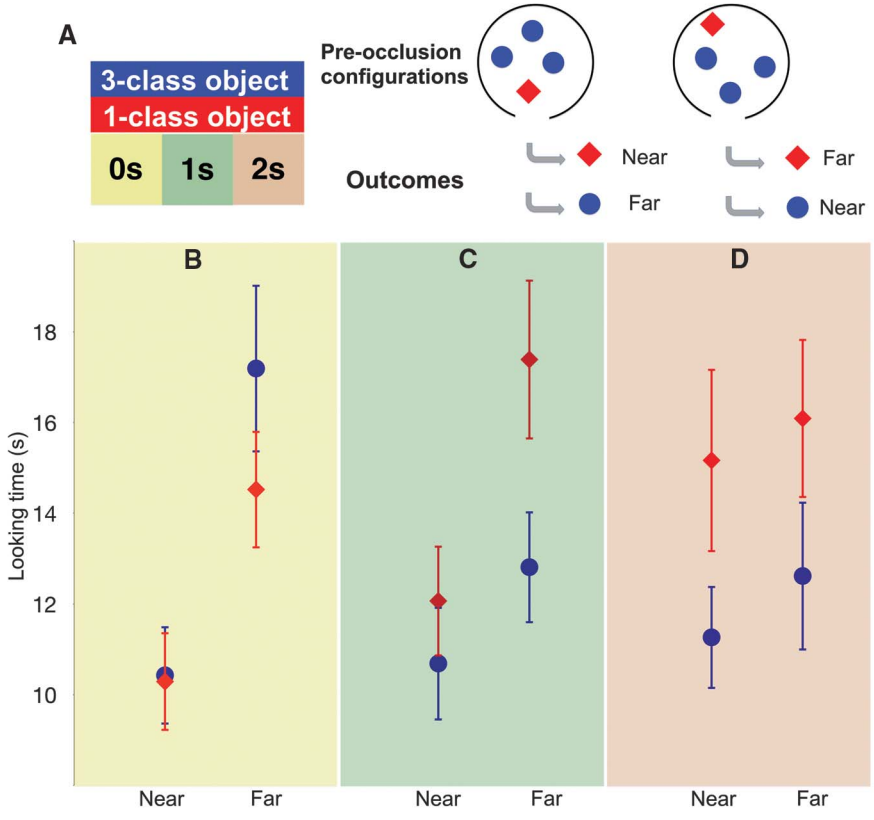

Fig. 2. Experiments probing infants' expectations in dynamic physical scenes. (**A**) Infants saw three objects of one type and one object of another type bouncing randomly inside a container. After some time, an occluder masked the objects, and one of four outcomes occurred: An object exited the container through the bottom opening that was either the common object kind or the unique object, with a position before occlusion that was either far from or near to the exit. The graph reports mean looking time (s, with SEM) of three experiments varying the duration of occlusion before the outcome. (**B**) After a short (0.04 s) occlusion, infants considered only the physical distance in forming their expectations, disregarding the number of objects of each type. (**C**) When occlusion duration was increased to 1 s, infants' looking times reflected both the number of objects of each type and their distance from the exit. (**D**) When the occlusion was longer still (2 s), infants' looking times reflected only the numerosities of each object type, regardless of their preocclusion distance from the exit.

A Bayesian model of infants' pure reasoning. These experiments show that infants possess surprisingly sophisticated abilities to integrate multiple information sources and abstract knowledge in reasoning about future outcomes. We now analyze infants' expectations more quantitatively by comparing them with those of a Bayesian ideal observer equipped with only minimal computational resources and the minimal abstract knowledge about physical objects that, according to classic research, young infants possess.

The observer's knowledge of object dynamics is expressed in the form of a probabilistic model embodying the principles of solidity and spatiotemporal continuity described above. These principles can be formalized as a prior $P(S_t|S_{t-1})$ on how the state S_t of the world at time t depends

probabilistically on the state at time $t-1$, which for simplicity we express as constrained Brownian motion: Objects move by accumulating small independent random spatial perturbations over time, subject to the constraint that they cannot pass through solid barriers (fig. S1).

The observer must also be equipped with some mechanism of inference and some notion of computational resources. Following state-of-the-art approaches in artificial intelligence and Bayesian models of adult cognition (*21*–*24*), we assume that predictions are computed approximately by Monte Carlo sampling. This process corresponds to a kind of hypothetical reasoning: Given a particular observed scenario, the observer has the capacity to consider possible future states of the world as they may unfold according to the observer's probabilistic model. A similar intuition for grounding probabilistic reasoning in representations of possible worlds was the basis for classic "mental models" accounts of adult cognition (*25*), although our treatment differs in explicitly formalizing probabilistic principles of knowledge representation and inference. Formally, the probability of a final outcome D_F given the observed data $D_0,\ldots,_{F-1}$ is approximated as a sum of the scores of K hypothetical trajectories (sequences of states $S_0,\ldots,_F$),

$$P(D_F|D_{0,\ldots,F-1}) \propto \sum_{k=1}^{K} P(D_F|S_F^k) \times \prod_{t=1}^{F} P(D_{t-1}|S_{t-1}^k) P(S_t^k|S_{t-1}^k) \quad (1)$$

where the score is a product over time steps t of how well the kth hypothesis fits the observed data $P(D_t|S_t^k)$ and how probable it is under the prior on object dynamics $P(S_t^k|S_{t-1}^k)$. Intuitively, an observed outcome is expected insofar as many predicted future trajectories are consistent with it or unexpected if it is consistent with few predicted trajectories.

In this analysis, computational resources correspond to the number of hypothetical trajectories (the samples) that an observer can construct. In the limit of infinite samples, these Monte Carlo predictions correspond exactly to the posterior beliefs of the ideal Bayesian observer. This ideal observer forms expectations about which object will emerge first that are very similar to the pattern of looking times exhibited across our three experiments, trading off the influences of type numerosity and proximity, modulated by occlusion duration, just as infants do (Fig. 3). Note that because infants' looking times are typically inversely related to expectations, we compare looking times to $1 - P(\text{outcome})$ (*26*). Evaluated quantitatively, the modeled outcome probabilities explain 88% of the variance in infants' mean looking times across the 12 experimental conditions ($r = 0.94$, $df = 10$, $P < 0.0001$). By comparison, each of the three stimulus factors that we manipulated explains significantly less variance across these 12 conditions: occlusion duration, 1%; type numerosity, 12%; and proximity, 47%. Even their best linear combination explains only 61% of variance, with the added cost of two ad hoc free parameters.

In contrast to this analysis, infants—or, indeed, adults (*22*–*24*)—are unlikely to consider more than a small sample of possible trajectories. Accordingly, we have also analyzed the model under severe resource bounds, by using just one or two trajectories sampled from the Bayesian posterior to form expectations. Averaged over simulated participants and trials, this bounded model makes inferences almost identical to the Bayesian ideal (figs. S5 and S6) [$r(10) = 0.92$, $P < 0.05$; $r(10) = 0.93$, $P < 0.05$]. Thus even with very limited processing capacity, infants could make appropriate probabilistic predictions in our task.

Modeling infants' probabilistic and physical intuitions. If infants' expectations in our experiments truly reflect the origins of a broad "common sense" physical reasoning capacity and if this capacity is captured by our Bayesian model, then the same model should be able to account for expectations about a wider range of developmental situations.

Recent studies have suggested that infants and young children understand simple random processes. Observing the random drawing of some balls from a box containing differently colored balls, infants expect colors in the sample to be representative of proportions in the larger population, and vice versa (*18*). Probabilistic expectations may also be induced by the structure of environmental constraints, not only the distribution of object properties. For instance, when 3- and 5-year-olds (*17*) and 12-month-olds see a single ball bouncing within a bounded box containing three exits on one side and one on the opposite side, they anticipate that the ball will exit from the three-exit side; however, if the three-exit side is obstructed, such anticipation is absent. Our model explains all these results with no further assumptions (fig. S2 and Fig. 4). Spatiotemporal continuity as captured by the Brownian motion

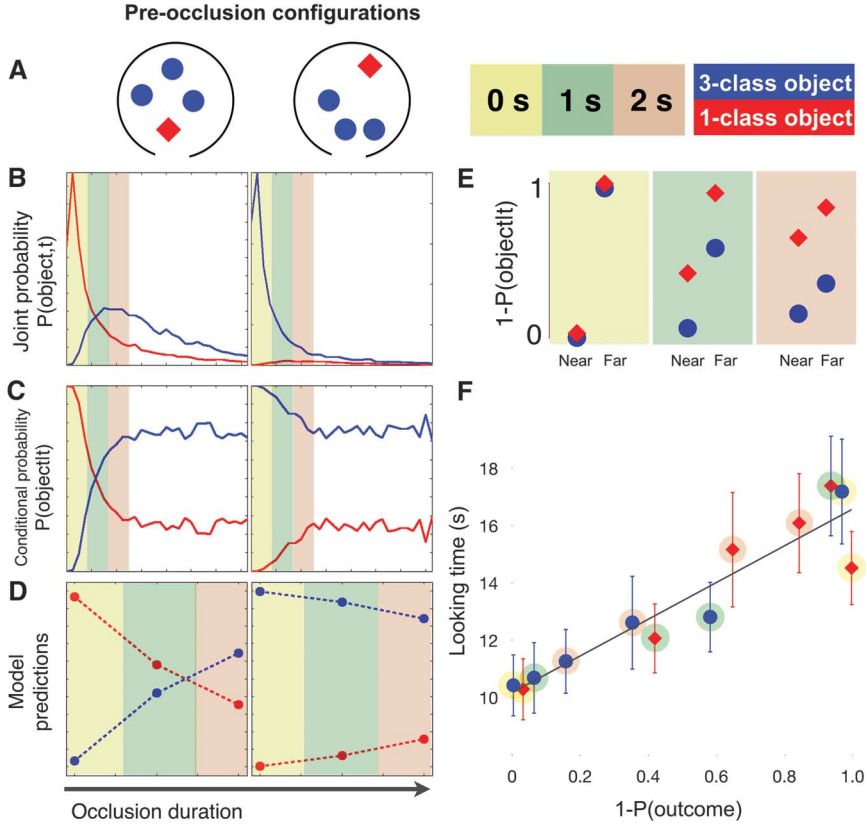

Fig. 3. The ideal Bayesian observer model. Starting with an unambiguous parse of the world into the two types of objects and their preocclusion positions (**A**), the model predicts the probability for each object type to be the first to exit as a function of occlusion duration and preocclusion distance from the exit. (**B**) The joint probability that a particular type of object exits at a particular point in time can be computed from a large number of Monte Carlo samples for each of the two starting scenarios. (**C**) Given the observation that an object first emerges at a particular time, we compute the conditional probability that it is of one type or another. (**D**) The predictions for our experiment consider only three points from the continuous distributions over time, corresponding to short (0 s; yellow), medium (1 s; green), and long (2 s; red) occlusion delays. (**E**) We combine these conditional probabilities from both starting scenarios to predict the joint effects of distance, object type numerosity, and occlusion duration on infants' expectations about which object type will emerge first, as found in experiments 1 to 3 (compare with looking-time data shown in Fig. 2, B to D). (**F**) Correlation between the model predictions (x axis) and infant looking times (y axis, s with SEM) in our three experiments. Each data point corresponds to one experimental condition.

prior drives the basic expectations about randomness, whereas the solidity constraint on Brownian motion incorporates the physical restrictions on possible or likely outcomes for each display.

Under the same physical principles, our model also explains classic findings on how young infants use visual motion to parse the world into a determinate number of objects. Infants' expectations were not originally viewed as rational probabilistic inferences nor analyzed quantitatively, but our model shows how they can be understood in these terms. In one well-known class of ambiguous displays (*27*), a foreground object occludes what could be two disconnected shorter objects or a single longer object with two parts extending above and below the occluder (Fig. 5A). When the display is static, infants show no preference for the one-object or two-object interpretation, but when the two parts move synchronously behind the occluder, infants expect they form a single object and are surprised if shown that they are two separate objects (Fig. 5B). Our model predicts this result by virtue of its stochastic prior on object motion and a natural version of Occam's razor that results from Bayesian inference under such a prior. It is certainly possible for the two parts to move synchronously left and right if they are two independent objects, but it is a coincidence: just one of many possible ways that two objects moving independently and randomly could move and thus relatively unlikely. However, synchronous motion must always occur if the two parts are two sides of a single rigid object, and thus a one-object interpretation receives much higher posterior probability for a Bayesian observer (Fig. 5C). When the objects are stationary, in contrast, there is essentially no evidence either way, and the observer is indifferent.

In another class of ambiguous displays, an object emerges from alternate sides of a single large occluding screen or a split screen with a visible gap in the middle (*28*) (Fig. 5D). Only one object is ever visible at a time, but the motion could be produced by either a single object traveling behind the occluder(s) or else two objects successively emerging from opposite sides. Infants are surprised to see this scene with the visible gap if they have previously seen only a single object placed behind the screen (*28*) (Fig. 5, D and E) but not if they have previously seen two objects. Our ideal observer forms the same expectations: Two objects can easily produce this motion without appearing in the visible gap, but a single object can do so only if it takes a physical jump across the gap in a single time step, which is possible but highly unlikely under the Brownian motion prior (Fig. 5F). Moreover, both infants and our model make the inverse inference: Seeing an object emerge from both sides of the split screen without appearing in the visible gap, they expect there to be two objects behind the screen rather than one (*29*, *30*) (fig. S4). Lastly, both infants and our model can use the spatiotemporal relations between the speed of an object, the size of the occluder, and the duration of the delay between an object's disappearance behind an occluder and reappearance on the other side to infer the likely existence of one or two objects (*31*) (fig. S3).

Across all the studies described above, our model is able to capture the main ordinal trends in how infants' looking times vary by condition, but it does not provide the stronger quantitative fits that we found for our experiments (Fig. 3F). Differences in the model's subjective probabilities are often too extreme relative to the observed differences in infants' looking times (e.g., Figs. 4, E and F, and 5, E and F). There are several possible reasons for this, which suggest ways that future modeling and experimental studies of infant reasoning could be improved. Previous experimental work adopted a variety of designs intended only to uncover qualitative effects of binary stimulus manipulations on looking times; typical studies report data from few conditions, often using qualitatively different test events across experiments or conditions. In contrast, our experiments parametrically varied multiple dynamical aspects of scenes while keeping test events fixed, allowing for a more sensitive test of model predictions. More quantitative predictions for the classic phenomena described above could be tested with novel parametric designs such as those used in our experiments.

There are also several ways that our modeling approach can be improved and refined. Assuming a linear relationship between outcome probabilities and looking times is too simple, and future work should explore more complex, nonlinear dependencies such as log-likelihoods or information-theoretic measures of surprise (*32*). The rich literature on infants' object perception suggests a need for more sophisticated ideal-observer models, with a more detailed specification of how infants represent the physical properties of objects (*33*, *34*). Lastly, an ideal-observer model, even with resource and processing constraints, provides only a coarse approximation to the psychological mechanisms of infant cognition. A more fine-grained processing model might make stronger quantitative predictions for a broader range of experimental designs. Still, it is intriguing that, with only minimal assumptions about infants' computational resources and their knowledge of object motion, we can explain some of the most basic, early developing abilities to parse the world into a discrete set of objects as rational probabilistic inferences.

Conclusion. Preverbal infants' ability to reason about complex unseen events is surprisingly sophisticated: 12-month-olds can represent the crucial spatial, temporal, and logical aspects of dynamic scenes with multiple objects in motion and integrate these cues with optimal context-sensitive weights to form rational expectations consistent with a Bayesian observer model. Although classic work in judgment and decision-making has suggested that people often fail to follow Bayesian principles in deliberate, explicit reasoning, Bayesian models have recently provided compelling accounts of more intuitive, implicit inference and prediction abilities in adults and older children (*35*, *36*). The present studies carry this approach further back to the roots of cognition by demonstrating a systematic relation between infants' looking times and rational probabilistic expectations in a complex task.

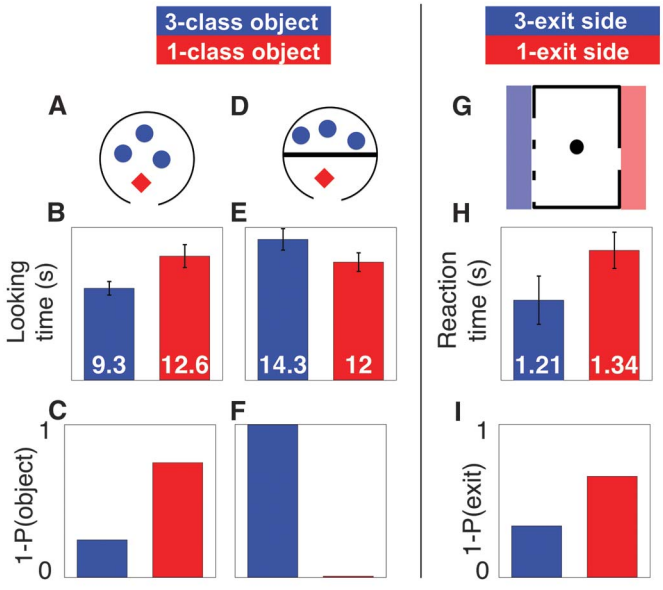

Fig. 4. Model predictions for infants' expectations about random events. (**A**) Schematic representation of experiments from (*17*). Infants saw scenes similar to those of the current experiments, with long preexit occlusions (2 s). (**B**) Infants' mean looking times were longer when an object of the less-numerous type exited (means in s, with SEM). (**C**) The model's predictions for the relative probabilities of which object type is more likely to exit. (**D**) When a barrier separated the objects of the more numerous kind from the exit, (**E**) infants looked longer when one of these objects exited, indicating that they took the physical constraints of the scene into account. (**F**) The solidity constraint of our model yields matching predictions: The common objects are unlikely to "jump" over the barrier and thus unlikely to exit. In another paradigm (**G**), older children see a ball bouncing inside a box with three exits on one side and one exit on the opposite side. After the display is occluded, the ball exits the box. (**H**) Children are slower to react when the ball emerges from the one-exit side. (**I**) The model's constrained Brownian motion predicts that the ball is more likely to exit from the three-exit side.

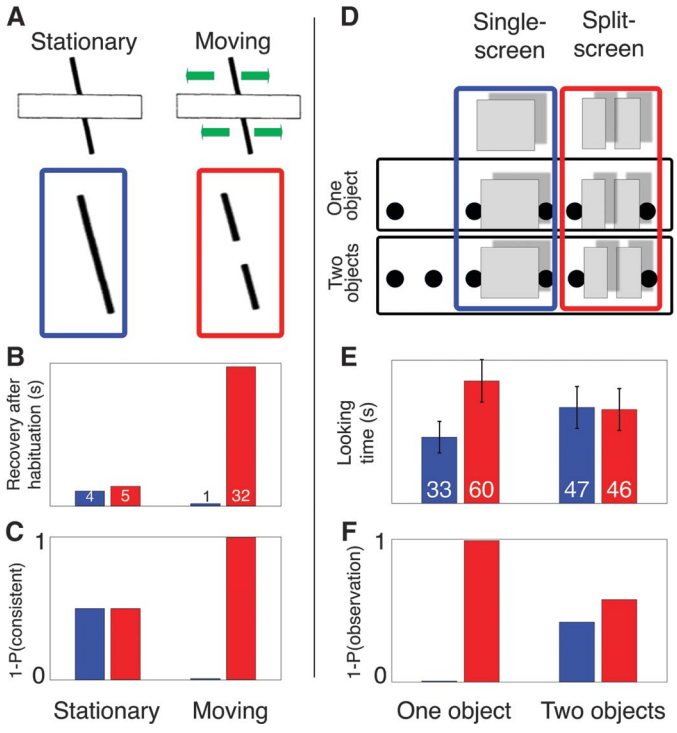

Fig. 5. Model predictions for object cognition in infants. (**A**) Infants as young as 3 months were habituated to two bars behind an occluder that either remained stationary or moved synchronously (*27*). (**B**) After the occluder was removed, infants recovered more quickly from habituation (s) when they saw two independent bars than when they saw a conjoined bar, but only when the bars moved synchronously during habituation (right), not when they were stationary (left). (**C**) The model considers two possible world parses (two independent objects or one conjoined one), but synchronous motion is much less likely for two independent objects. In the stationary condition, two- and one-object parses are equally likely, but in the motion condition the single-object parse becomes much more likely. (**D**) The 2.5-month-old infants were habituated to either one object or two objects, which were then occluded behind one large or two small screens (*28*). Infants saw an object emerge from the left side of the screen and then an object emerge from the right side. (**E**) Infants looked longer when an object emerged from both sides in the two-screen, one-object event, but not in the other events (means in s, with SEM). (**F**) Given an initial unambiguous parse of the display into objects and the one- or two-screen layout, the model samples possible trajectories in which an object emerges on the left followed by the right side of the display without emerging elsewhere. When one object and two screens are present, it is very unlikely for an object to emerge from the right side without being seen in the middle; when two objects are present, or if one large screen is present, this observation is much more likely.

It is unclear how exactly the workings of our model correspond to the mechanisms of infant cognition, but the strong model fits suggest at least a qualitative similarity between the two. We suggest that the commonality lies in the ability to generate physically plausible candidates for future world states, consistent with the observed present. More work is needed to discover the precise form of the representations infants use to effectively construct and weight these hypotheses.

How do these sophisticated inferential abilities arise in development? We have emphasized their one-shot nature: Just as with adults' expectations in Fig. 1, infants' sensitivity to graded outcome probabilities in our displays varies systematically and rationally with the numerosities of different object types, their spatial configuration, and occlusion duration but does not depend on seeing these displays many times as needed for traditional statistical learning. However, the statistics of an infant's experience could still play a role in how this capacity is constructed. Pure reasoning requires the ability to represent the space of possible future events (*37*), as well as some abstract knowledge of how physical objects move, and, although the relevant physical knowledge could be innate (*12*), it could also be acquired through a structured statistical learning approach (*38*) from patterns of object movement (*39*).

More broadly, our work opens the possibility that a cognitive architecture based on probabilistic generative models, complemented by abstract knowledge representations, can account for early common-sense reasoning beyond the limited physical domain we explored. Equipped with richer abstract knowledge, this approach can explain a wide range of common-sense predictions as the result of pure reasoning, such as the ability to make rational inferences about other agents on the basis of core psychological principles (*15*, *40*, *41*) or the ability to reason about more challenging physical situations (as in the displays of Fig. 1) on the basis of more sophisticated physical principles. It thus offers a way to explain how developing humans may come to make progressively richer inferences about their increasingly complex world.

References and Notes

1. J. R. Saffran, E. L. Newport, R. N. Aslin, *J. Mem. Lang.* **35**, 606 (1996).
2. M. Peña, L. L. Bonatti, M. Nespor, J. Mehler, *Science* **298**, 604 (2002).
3. J. Fiser, R. N. Aslin, *J. Exp. Psychol. Learn. Mem. Cogn.* **28**, 458 (2002).
4. S. C. Creel, E. L. Newport, R. N. Aslin, *J. Exp. Psychol. Learn. Mem. Cogn.* **30**, 1119 (2004).
5. D. Kersten, P. Mamassian, A. Yuille, *Annu. Rev. Psychol.* **55**, 271 (2004).
6. L. Cosmides, J. Tooby, *Cognition* **58**, 1 (1996).
7. G. Gigerenzer, U. Hoffrage, *Psychol. Rev.* **102**, 684 (1995).
8. M. D. Hauser, E. L. Newport, R. N. Aslin, *Cognition* **78**, B53 (2001).
9. J. M. Toro, J. B. Trobalón, *Percept. Psychophys.* **67**, 867 (2005).
10. V. Girotto, M. Gonzalez, in *Norms in Human Development*, L. Smith, J. J. Vonèche, Eds. (Cambridge Univ. Press, Cambridge, 2006), pp. 220–236.
11. R. Baillargeon, E. S. Spelke, S. Wasserman, *Cognition* **20**, 191 (1985).
12. E. S. Spelke, K. Breinlinger, J. Macomber, K. Jacobson, *Psychol. Rev.* **99**, 605 (1992).
13. K. Wynn, *Nature* **358**, 749 (1992).
14. A. L. Woodward, *Cognition* **69**, 1 (1998).
15. K. H. Onishi, R. Baillargeon, *Science* **308**, 255 (2005).
16. A. M. Kovács, E. Téglás, A. D. Endress, *Science* **330**, 1830 (2010).
17. E. Téglás, V. Girotto, M. Gonzalez, L. L. Bonatti, *Proc. Natl. Acad. Sci. U.S.A.* **104**, 19156 (2007).
18. F. Xu, V. Garcia, *Proc. Natl. Acad. Sci. U.S.A.* **105**, 5012 (2008).
19. Materials and methods are available as supporting material on *Science* Online.
20. S. P. Johnson *et al.*, *Child Dev.* **74**, 94 (2003).
21. S. Russell, P. Norvig, *Artificial Intelligence: A Modern Approach* (Prentice Hall, Englewood Cliffs, NJ, ed. 3, 2009).
22. S. D. Brown, M. Steyvers, *Cognit. Psychol.* **58**, 49 (2009).
23. E. Vul, M. Frank, G. Alvarez, J. Tenenbaum, in *23rd Annual Conference on Neural Information Processing Systems 2009*, Y. Bengio, D. Schuurmans, J. Lafferty, C. K. I. Williams, A. Culotta, Eds. (Advances in Neural Information Processing Systems 22, Curran, Red Hook, NY, 2009), p. 1955.
24. R. Levy, F. Reali, T. L. Griffiths, in *22nd Annual Conference on Neural Information Processing Systems 2008*, D. Koller, D. Schuurmans, Y. Bengio, L. Bottou, Eds. (Advances in Neural Information Processing Systems 21, Curran, Red Hook, NY, 2008), p. 937.
25. P. N. Johnson-Laird, P. Legrenzi, V. Girotto, M. S. Legrenzi, J.-P. Caverni, *Psychol. Rev.* **106**, 62 (1999).
26. Assuming that relative differences in looking times reflect the relative strengths of infants' expectations given the initial conditions, we normalize these outcome probabilities to sum to 1 over the set of test outcomes that infants saw. Although an information theoretic (logarithmic) measure of surprise may be more general, in this case, where looking times to only one of two alternatives are compared, $1 - P$ is a natural metric to evaluate the relative expectations of these alternatives.
27. P. J. Kellman, E. S. Spelke, *Cognit. Psychol.* **15**, 483 (1983).
28. A. Aguiar, R. Baillargeon, *Cognit. Psychol.* **39**, 116 (1999).
29. F. Xu, S. Carey, *Cognit. Psychol.* **30**, 111 (1996).
30. E. S. Spelke, R. Kestenbaum, *Psychol. Fr.* **31**, 67 (1986).
31. T. Wilcox, A. Schweinle, *Infant Behav. Dev.* **26**, 253 (2003).
32. T. M. Cover, J. A. Thomas, *Elements of Information Theory* (Wiley-Interscience, Hoboken, NJ, ed. 2, 2006), pp. xxiii, 748.
33. C. Kemp, A. Jern, F. Xu, in *23rd Annual Conference on Neural Information Processing Systems 2009*, Y. Bengio, D. Schuurmans, J. Lafferty, C. K. I. Williams, A. Culotta, Eds. (Advances in Neural Information Processing Systems 22, Curran, Red Hook, NY, 2009), p. 925.
34. R. Baillargeon, J. Li, W. Ng, S. Yuan, in *Learning and the Infant Mind*, A. Woodward, A. Needham, Eds. (Oxford Univ. Press, Oxford, 2009), pp. 66–116.
35. T. L. Griffiths, J. B. Tenenbaum, *Psychol. Sci.* **17**, 767 (2006).
36. J. B. Tenenbaum, T. L. Griffiths, C. Kemp, *Trends Cogn. Sci.* **10**, 309 (2006).
37. J. A. Fodor, *The Language of Thought* (Crowell, New York, 1975).

38. J. B. Tenenbaum, C. Kemp, T. L. Griffiths, N. D. Goodman, *Science* **331**, 1279 (2011).
39. P. Sinha, B. Balas, Y. Ostrovsky, J. Wulff, in *Object Categorization: Computer and Human Vision Perspectives*, S. J. Dickinson, A. Leonardis, B. Schiele, M. J. Tarr, Eds. (Cambridge Univ. Press, Cambridge, 2009), pp. 301–323.
40. G. Gergely, G. Csibra, *Trends Cogn. Sci.* **7**, 287 (2003).
41. C. L. Baker, R. Saxe, J. B. Tenenbaum, *Cognition* **113**, 329 (2009).

Acknowledgments: The research was supported by grants Friuli-Venezia-Giulia "PsyScope XL," Ministerio de Ciencia E Innovación PSI2009-08232PSIC, the James S. McDonnell Foundation Causal Learning Research Collaborative grant, Office of Naval Research grants N00014-09-0124 and N00014-07-1-0937, Army Research Office MURI W911NF-08-1-0242, the Swiss and Global-Fondazione Ca' Foscari, and Marie Curie 035975 Disorders and Coherence of the Embodied Self. E.T. and L.L.B. designed the experiments and analyzed the data. E.T. ran the experiments. J.B.T. and E.V. conceived the model and the simulations. E.T., E.V., J.B.T., and L.L.B. wrote the paper. All authors discussed the research and revised the text and the analyses. We thank D. Amati, L. Filippin, F. Gandolfo, N. Goodman, A. Isaja, and N. Sebastian for support and suggestions. J. Mehler and the Language, Cognition, and Development Laboratory in Trieste, Italy made the experimental work possible. We are deeply grateful to them.

Supporting Online Material
www.sciencemag.org/cgi/content/full/332/6033/1054/DC1
Materials and Methods
Figs. S1 to S8
Movies S1 to S5

12 August 2010; accepted 21 April 2011
10.1126/science.1196404

Experimental Repetitive Quantum Error Correction

Philipp Schindler,[1] Julio T. Barreiro,[1] Thomas Monz,[1] Volckmar Nebendahl,[2] Daniel Nigg,[1] Michael Chwalla,[1,3] Markus Hennrich,[1]* Rainer Blatt[1,3]

The computational potential of a quantum processor can only be unleashed if errors during a quantum computation can be controlled and corrected for. Quantum error correction works if imperfections of quantum gate operations and measurements are below a certain threshold and corrections can be applied repeatedly. We implement multiple quantum error correction cycles for phase-flip errors on qubits encoded with trapped ions. Errors are corrected by a quantum-feedback algorithm using high-fidelity gate operations and a reset technique for the auxiliary qubits. Up to three consecutive correction cycles are realized, and the behavior of the algorithm for different noise environments is analyzed.

Information in a quantum computer is extremely vulnerable to noise induced by the environment and thus needs to be protected with quantum error correction (QEC) techniques. Pioneering theoretical work in this field has shown that all errors can be corrected for if imperfections of the quantum operations and measurements are below a certain (error) threshold and the correction can be applied repeatedly (*1*–*3*). Such error thresholds depend on details of the physical system, and quantifying them requires a careful analysis of the system-specific errors, the en- and decoding procedures, and their respective implementation (*4*). It is currently accepted that gate error probabilities ranging from 10^{-4} to 10^{-5} are tolerable (*5*), which seem to be in reach with technical improvements in conjunction with dynamical control techniques (*6*). In addition, fault-tolerant operation requires highly efficient, repeatable algorithms to minimize the computational overhead. So far, all experimental implementations (*7*–*12*) are limited to a single correction cycle, where the only experimental implementation in a scalable system (*10*) relies on projective measurements and classical feedback. Because high-fidelity measurements take time and potentially disturb the qubit system, it can be advantageous to use a measurement-free QEC algorithm based on implicit quantum feedback (*4*, *7*). Also, in contrast to previous expectations (*13*), these measurement-free protocols lead to error thresholds comparable to those of their measurement-based counterparts (*14*).

We demonstrate repeated QEC with a system of trapped $^{40}Ca^{+}$ ions as qubits, and multiple repetitions of the algorithm are enabled by a toolbox consisting of high-fidelity quantum operations (*15*, *16*), an optimized pulse sequence (*17*), and a qubit-reset technique that has a negligible effect on the system of qubits. The performance of the implementation is assessed with quantum process tomography in the presence of phase-flip errors, and its behavior is analyzed for different environments that show correlated and uncorrelated phase noise. Our approach is based on the three-qubit repetition code capable of detecting and correcting phase-flip errors on a single qubit (*1*, *4*). This algorithm protects against phase noise, which is the dominant error source in our ion-trap quantum computer, causing gate errors as well as decoherence.

As indicated in Fig. 1A, each QEC cycle consists of (i) encoding the system qubit $\{|0\rangle, |1\rangle\}$ and two auxiliary qubits (ancillas) into an entangled state, (ii) error incidence, (iii) detecting and correcting the error, and (iv) resetting the ancillas. Initially, the qubit to be protected is in the state $|\Psi\rangle = \alpha|+\rangle + \beta|-\rangle$, where $|\pm\rangle = 1/\sqrt{2}\,(|0\rangle \pm |1\rangle)$, and the two ancilla qubits are both prepared in the state $|1\rangle$. In the encoding stage, they are mapped into the entangled state $\alpha|+++\rangle + \beta|---\rangle$. Next, a single-qubit phase-flip error may change $|\pm\rangle$ to $|\mp\rangle$. In the decoding and correction stage, the error is identified by a simple majority vote, and the system qubit is corrected accordingly. It should be noted that this protocol maps the information in and out of the protected state between QEC cycles. Each cycle is concluded by resetting the ancilla qubits while preserving the information on the system qubit.

The textbook implementation of a single cycle of this QEC procedure would consist of a circuit using four controlled-NOT (CNOT) and one controlled controlled-NOT (Toffoli) gate operations (*4*) (Fig. 1B). Although the process fidelities of available CNOT (92%) (*18*) and Toffoli (80%) (*19*) implementations could possibly be improved, it seems more promising to pursue an approach based on global Mølmer-Sørensen entangling gate operations (fidelity of 99%) (*15*, *20*). These operations provide a universal set of gates in combination with individually addressed Stark-shift gates and collective single-qubit rotations (*17*, *21*). Moreover, the optimization procedure of (*17*) allows us to rigorously simplify the pulse sequence for a complete algorithm based on this set of gates. Two additional refinements lead to the algorithm used for the optimization (Fig. 1B). First, the space of optimized solutions is increased by adding an arbitrary unitary operation, U, acting only on the ancillas before resetting them. Second, the encoding stage can be simplified by adding an operation, D, and its inverse, D^{-1}, that commutes with any phase error. As a result, the encoding stage consists of a single entangling operation, and the decoding stage can be implemented with a total of eight pulses with only three entangling operations (Fig. 1C). Formally, this encoding implements a stabilizer code with the generators $G = \{\sigma_y^{(1)}\sigma_z^{(2)}\sigma_y^{(3)}, \sigma_y^{(1)}\sigma_y^{(2)}\sigma_z^{(3)}\}$, which are tensor products of the Pauli operators $\sigma_{x,y,z}^{(i)}$ acting on qubit i (*4*).

The QEC protocol is realized in an experimental system consisting of a string of three $^{40}Ca^{+}$ ions confined in a macroscopic linear Paul trap. Each

[1]Institut für Experimentalphysik, Universität Innsbruck, Technikerstraße 25, A-6020 Innsbruck, Austria. [2]Institut für Theoretische Physik, Universität Innsbruck, Technikerstraße 25, A-6020 Innsbruck, Austria. [3]Institut für Quantenoptik und Quanteninformation, Österreichische Akademie der Wissenschaften, Otto-Hittmair-Platz 1, A-6020 Innsbruck, Austria.

*To whom correspondence should be addressed. E-mail: markus.hennrich@uibk.ac.at

ion represents a qubit in the $|1\rangle = 4S_{1/2}(m_J = -1/2)$ and $|0\rangle = 3D_{5/2}(m_J = -1/2)$ states. The state of the qubits is then manipulated by a series of laser pulses resonant with the qubit transition. Our universal set of gates consists of (i) collective local operations, $X(\Theta) = \exp(-iS_x\Theta/2)$ and $Y(\Theta) = \exp(-iS_y\Theta/2)$; (ii) single-qubit operations, $Z_k(\Theta) = \exp[-i\sigma_z^{(k)}\Theta/2]$; and (iii) collective entangling Mølmer-Sørensen (*15*, *16*, *20*) operations, $Y^2(\Theta) = \exp(-iS_y^2\Theta/4)$, with $S_{x,y} = \sum_{k=1}^{3}\sigma_{x,y}^{(k)}$. The collective operations are realized with a wide beam exciting all ions simultaneously, and the single-qubit operations are performed with a tightly focused beam affecting only individual ions. An experimental cycle consists of cooling the ion string to the motional ground state, applying the manipulating laser pulses, and measuring the population of the qubit states. This procedure is repeated up to 1000 times to obtain the final quantum state of the qubits.

An important tool, critical to the repeated application of the QEC protocol, is the proper reset of the ancilla qubits, which is carried out with the optical-pumping technique (Fig. 1D). For the reset procedure, the population of the ancilla qubits in state $|0\rangle$ is first transferred into the state $|S'\rangle = 4S_{1/2}(m_J = +1/2)$ by using the addressed beam. This population in $|S'\rangle$ is then excited to the $4P_{1/2}(m_J = -1/2)$ level by a circularly polarized laser beam at a wavelength of 397 nm. Lastly, the population from the $4P_{1/2}$ level spontaneously decays to the $4S_{1/2}$ level (population loss into $3D_{3/2}$ level is avoided by a repump laser resonant with the $3D_{3/2} - 4P_{1/2}$ transition). The electronic state of the system qubit is not affected by the wide pumping laser because it couples only to the ancillas' population in $|S'\rangle$. The effect on the motional state of the ion string was calculated with a multilevel numerical simulation from which we estimate a heating rate of 0.015 phonons per reset step for our experimental parameters. Because the protocol uses only entangling operations of the Mølmer-Sørensen type, which are insensitive to the ion motion in first order, the reset has a negligible effect on the QEC protocol.

The operational quality of the QEC protocol can be assessed by exposing it to correctable errors, that is, single-qubit phase-flip errors. Ideally, the encoded qubit experiences an identity operation. Experimentally, the implemented process is characterized with quantum process tomography (*22*, *23*), which yields a process matrix χ. The performance of the implementation is given by the overlap of the identity process, χ_{id}, with the implemented process, also known as the process fidelity, $F_{proc} = \mathrm{Tr}(\chi \cdot \chi_{id})$. The achieved process fidelities for up to three repetitions (without inducing any errors), F_{none}, are shown in Table 1. The process fidelity, however, does not distinguish between constant operational errors (that could be undone in principle) and decoherence (irreversible processes). A measure that is only sensitive to errors resulting from decoherence is the optimized process fidelity, F_{opt}, as displayed in Table 1. It is defined as the maximum fidelity that could be obtained if an additional fixed single-qubit rotation was perfectly implemented on the output state (*24*).

The error-correcting capability of the implementation is assessed by applying in each cycle either no-error or a single-qubit phase flip $Z_i(\pi)$ on ion i (1 being the system ion and 2 and 3 being the first and second ancillas, respectively) followed by a process tomography for all combinations. Because these single-qubit errors are corrected by the algorithm, the ideal process is again the identity process. The mean process matrix, $\overline{\chi}$, is then reconstructed from the data obtained by averaging over all measured expectation values, as shown for zero to three correction cycles in Fig. 2. The results shown in Table 1 demonstrate that the optimized process fidelities with single-qubit errors, F_{sopt}, and without an induced error, F_{opt}, are the same for one, two, and three correction cycles. From this data, we infer that the QEC protocol corrects single-qubit errors perfectly within our statistical uncertainty. The infidelities of the implementation are mainly caused by imperfections in the entangling gates as discussed in (*24*).

In addition to characterizing the implemented process in the presence of correctable errors, we investigate the algorithm's behavior in a dephasing environment, where also uncorrectable errors occur. For single qubits, a dephasing process can be described by a phase-flip probability p, which reduces the off-diagonal elements of the density matrix by a factor $1 - 2p$ (for complete dephasing $p = 0.5$). In a system of multiple qubits, the probability of simultaneous n-qubit phase flips, which cannot be corrected by the three-qubit QEC protocol, depends on the correlations between the qubits (*24*). We analyze the behavior of the QEC

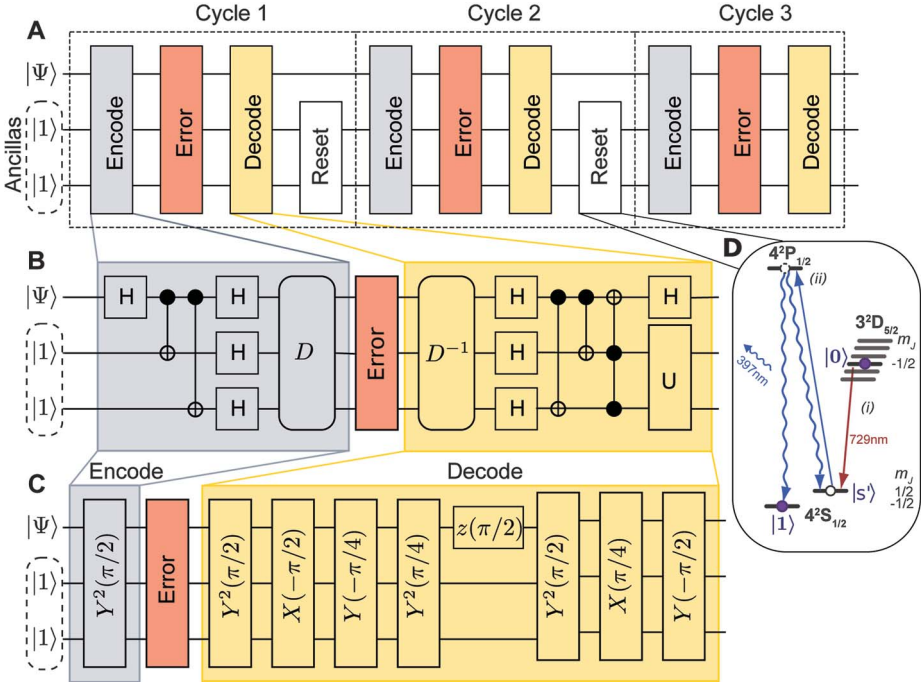

Fig. 1. (**A**) Schematic view of three subsequent error-correction cycles. (**B**) Quantum circuit for the implemented phase-flip error-correction code. The operations labeled *H* are Hadamard gates. (**C**) Optimized pulse sequence implementing a single error-correction cycle. (**D**) Schematic of the reset procedure. The computational qubit is marked by filled dots. The reset procedure consists of (i) shelving the population from $|0\rangle$ to $|s'\rangle = 4S_{1/2}(m_J = +1/2)$ and (ii) optical pumping to $|1\rangle$ (straight blue arrow).

Table 1. Process fidelity for a single uncorrected qubit as well as for one, two, and three error-correction cycles. F_{none} is the process fidelity without inducing any errors. F_{single} is obtained by averaging over all single-qubit errors. F_{opt} and F_{sopt} are the respective process fidelities where constant operations are neglected. The statistical errors are derived from propagated statistics in the measured expectation values where the numbers in parentheses indicate one standard deviation. Dash entries indicate not applicable.

Number of QEC cycles	No error F_{none}	Optimized no error F_{opt}	Single-qubit errors F_{single}	Optimized single-qubit errors F_{sopt}
0	97(2)	97(2)	–	–
1	87.5(2)	90.1(2)	89.1(2)	90.1(2)
2	77.7(4)	79.8(4)	76.3(2)	80.1(2)
3	68.3(5)	72.9(5)	68.3(3)	70.2(3)

algorithm in the presence of the two most prominent noise types, namely uncorrelated and correlated phase noise, where the qubits are affected by independent or one and the same noise source, respectively. In our system, the inherent phase noise is correlated because it originates predominantly from fluctuations in the magnetic field strength and the laser frequency, which are both equal on all qubits (*16*). A controlled amount of this noise can be simply applied by inserting a waiting time between the encoding and the decoding stage. The second noise type, uncorrelated phase noise, can be engineered by performing a weak qubit projection (*4*), which is realized by a short laser pulse on the detection transition once the qubit is encoded (*24*). We characterized the phase noise by Ramsey-type experiments (*24*), which translate phase flips into bit flips. The presence of the respective noise type can then be verified by the probability of simultaneous *n*-qubit bit flips (Fig. 3A).

For both uncorrelated and correlated phase noise, our error correction algorithm performs as depicted in Fig. 3B. Because uncorrectable two- and three-qubit phase flips occur more frequently in the presence of correlated noise (Fig. 3A), the QEC implementation yields lower fidelities. It should be noted though, that correlated phase noise can be completely eliminated by encoding the qubits in decoherence-free subspaces (DFS) (*9*, *25*, *26*) at the expense of a further increased complexity. For uncorrelated phase noise, no (DFS) exist, and therefore only quantum error correction can protect the qubit. In our implementation, a protected qubit shows less noise than an unencoded qubit for an error probability p larger than 0.15 (Fig. 3B). In the investigation with uncorrelated noise, the weak projection collapses each qubit with a small probability into the computational basis. Our data thus indicate that the algorithm can recover the quantum information from this single-qubit state collapse.

Our results demonstrate an implementation of a repeatable error correction algorithm in a system of three trapped-ion qubits. The use of global-entangling and local-qubit operations in an optimized pulse sequence allows for very short and efficient QEC cycles. For uncorrelated errors, a (single-cycle) corrected qubit performs better than an uncorrected qubit for a range of error probabilities. The algorithm can be extended to a five-qubit implementation, where the qubit stays protected during error correction (*17*). Although technically challenging, such an implementation in conjunction with DFS encoding appears as a viable route toward quantum error correction for trapped ions.

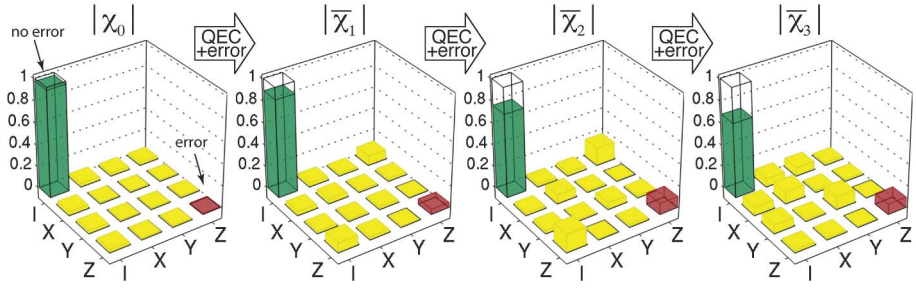

Fig. 2. Mean single-qubit process matrices $\overline{\chi}_n$ (absolute value) for n QEC cycles with single-qubit errors. Transparent bars show the identity process matrix, and the red bar denotes a phase-flip error. These process matrices were reconstructed from a data set averaged over all possible single-qubit errors.

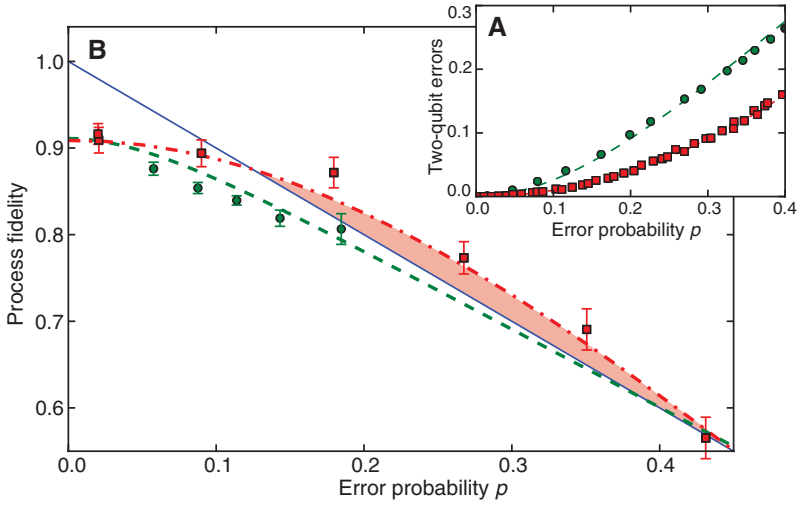

Fig. 3. (**A**) Probability of simultaneous two-qubit phase flips as a function of the single-qubit phase flip probabilities for uncorrelated (square) and correlated (circle) noise measured by a Ramsey-type experiment. (**B**) Process fidelity of the QEC algorithm in the presence of correlated (circle) and uncorrelated (square) phase noise as a function of the single-qubit phase flip probability. The theory is shown for an unencoded qubit (solid line), a corrected qubit in presence of correlated (dashed line), and uncorrelated noise (dash-dot line). Error bars indicate one standard deviation derived from propagated statistics in the measured expectation values.

References and Notes

1. A. R. Calderbank, P. W. Shor, *Phys. Rev. A* **54**, 1098 (1996).
2. A. Steane, *Proc. R. Soc. London Ser. A* **452**, 2551 (1996).
3. J. Preskill, *Proc. R. Soc. London Ser. A* **454**, 385 (1998).
4. M. A. Nielsen, I. L. Chuang, *Quantum Computation and Quantum Information* (Cambridge Univ. Press, Cambridge, 2000).
5. P. Aliferis, A. W. Cross, *Phys. Rev. Lett.* **98**, 220502 (2007).
6. K. Khodjasteh, D. A. Lidar, L. Viola, *Phys. Rev. Lett.* **104**, 090501 (2010).
7. D. G. Cory *et al.*, *Phys. Rev. Lett.* **81**, 2152 (1998).
8. E. Knill, R. Laflamme, R. Martinez, C. Negrevergne, *Phys. Rev. Lett.* **86**, 5811 (2001).
9. N. Boulant, L. Viola, E. M. Fortunato, D. G. Cory, *Phys. Rev. Lett.* **94**, 130501 (2005).
10. J. Chiaverini *et al.*, *Nature* **432**, 602 (2004).
11. T. Aoki *et al.*, *Nat. Phys.* **5**, 541 (2009).
12. T. B. Pittman, B. C. Jacobs, J. D. Franson, *Phys. Rev. A* **71**, 052332 (2005).
13. D. P. DiVincenzo, P. Aliferis, *Phys. Rev. Lett.* **98**, 020501 (2007).
14. G. A. Paz-Silva, G. K. Brennen, J. Twamley, *Phys. Rev. Lett.* **105**, 100501 (2010).
15. J. Benhelm, G. Kirchmair, C. F. Roos, R. Blatt, *Nat. Phys.* **4**, 463 (2008).
16. T. Monz *et al.*, *Phys. Rev. Lett.* **106**, 130506 (2011).
17. V. Nebendahl, H. Häffner, C. F. Roos, *Phys. Rev. A* **79**, 012312 (2009).
18. M. Riebe *et al.*, *Phys. Rev. Lett.* **97**, 220407 (2006).
19. T. Monz *et al.*, *Phys. Rev. Lett.* **102**, 040501 (2009).
20. A. Sørensen, K. Mølmer, *Phys. Rev. Lett.* **82**, 1971 (1999).
21. F. Schmidt-Kaler *et al.*, *Europhys. Lett.* **65**, 587 (2004).
22. I. L. Chuang, M. A. Nielsen, *J. Mod. Opt.* **44**, 2455 (1997).
23. M. Riebe *et al.*, *N. J. Phys.* **9**, 211 (2007).
24. Materials and methods are available as supporting material on *Science* Online.
25. P. Zanardi, M. Rasetti, *Phys. Rev. Lett.* **79**, 3306 (1997).
26. D. A. Lidar, I. L. Chuang, K. B. Whaley, *Phys. Rev. Lett.* **81**, 2594 (1998).

Acknowledgments: We thank C. F. Roos for helpful discussions and R. Gerritsma, G. Paz-Silva, G. Brennen, and J. Twamley for carefully reading the manuscript. We gratefully acknowledge support by the Austrian Science Fund (FWF), by the European Commission [Scalable Quantum Computing with Light and Atoms (SCALA) and Atomic Quantum Technologies (AQUTE) projects], by the Institut für Quanteninformation GmbH, and by the European Research Council. This material is based on work supported in part by the Intelligence Advanced Research Projects Activity. J.T.B. acknowledges support by a Marie Curie International Incoming Fellowship within the 7th European Community Framework Programme.

Supporting Online Material

www.sciencemag.org/cgi/content/full/332/6033/1059/DC1
Materials and Methods
Figs. S1 to S4
References

25 January 2011; accepted 23 March 2011
10.1126/science.1203329

Realizing All-Spin–Based Logic Operations Atom by Atom

Alexander Ako Khajetoorians, Jens Wiebe,* Bruno Chilian, Roland Wiesendanger

An ultimate goal of spintronic research is the realization of concepts for atomic-scale all-spin–based devices. We combined bottom-up atomic fabrication with spin-resolved scanning tunneling microscopy to construct and read out atomic-scale model systems performing logic operations. Our concept uses substrate-mediated indirect exchange coupling to achieve logical interconnection between individual atomic spins. Combined with spin frustration, this concept enables various logical operations between inputs, such as NOT and OR.

In conventional silicon-based information technology, bits of information are represented by charge stored in capacitors and processed by transistor-based switches. The looming fundamental scaling limits of this technology toward nanometer-sized devices (*1*) has led to an exploration of a variety of alternative computation schemes ranging from molecular quantum dot cellular automata (*2*, *3*) and molecular cascades (*4*), to spin capacitors (*5*), magnetic quantum dot cellular automata (*6*), magnetic domain wall devices (*7*–*9*), and eventually strategies for quantum computation (*10*, *11*). In the pursuit of highly energy-efficient and high-speed devices that are compatible with nonvolatile storage technology, spintronic concepts offer much promise (*12*). Such concepts harness the spin degree of freedom of nuclei, electrons, atoms, molecules, or magnetic films rather than the charge of electrons to store and process information. Although many of the proposed devices require spin to charge conversion in order to operate (*5*), it is desirable to have an all-spin–based concept that does not involve any flow of charge. The realization of corresponding model systems with dimensions on the atomic scale is so far lacking.

The tip of a scanning tunneling microscope (STM) has emerged as the tool that can be used to fabricate atomic-scale structures in a bottom-up fashion (*13*–*15*). Moreover, two complementary STM-based methods, spin-polarized scanning tunneling spectroscopy (SP-STS) (*16*) and inelastic STS (*17*), have become the analogs of magnetometry and spin resonance pushed to the single-atom limit. SP-STS has demonstrated the possibility of using the distance-dependent Ruderman-Kittel-Kasuya-Yosida (RKKY) coupling mediated by conduction electrons in metallic substrates to tailor the sign and strength of the magnetic coupling between atomic spins (*18*) as well as with patches of ferromagnetic islands (*16*).

We applied these techniques to realize a model system for logical operations that uses atomic spins of adatoms adsorbed on a nonmagnetic metallic surface and their mutual RKKY interaction in order to transmit and process information (Fig. 1). The atoms have two different states, **0** or **1**, depending on the orientation of their magnetization (down or up, respectively). They are constructed to form antiferromagnetically RKKY-coupled chains ("spin leads") that transmit the information of the state of small ferromagnetic islands ("input islands") to the gate region. The gate region, which comprises two "end atoms" from each spin lead and an "output atom," forms the core where the logic operation is performed. The states of the inputs and the resultant state of the output atom are read out by a scannable magnetic nano-electrode—the magnetic tip of a STM—in a tunneling magnetoresistance device geometry (*16*). Although the STM is used to construct and characterize the device, the tunneling current is not essential for performing the given logic operation. The states of the inputs can be switched independently by external magnetic field pulses $\vec{B}_{pulse}$. Based on an all-spin concept, this model device is principally nonvolatile and functions without the flow of electrons, promising an inherently large energy efficiency.

Triangular cobalt islands grown on the atomically clean (111) surface of a copper single crystal have a remnant mono-domain magnetization oriented perpendicular to the surface ("out-of plane") and serve as nonvolatile input bits (*19*, *20*). For atomic spins, we chose Fe atoms adsorbed at low temperature onto the same surface (fig. S1) (*19*). As a result of a strong magnetic anisotropy energy of ≈1 meV (*21*) and a negligible thermal energy of $k_BT = 25$ μeV (where k_B is the Boltzmann constant) determined by the measurement temperature (T = 0.3 K) (*22*), each atomic spin is constricted to the two states oriented maximally out-of-plane. Isolated Fe atoms are therefore flipping randomly between these two states. However, if an Fe atom sits close to a Co island or another stabilized atom, the distance-dependent oscillatory RKKY interaction stabilizes its spin into one of these two states. This RKKY interaction is on the order of 0.1 meV, and its distance dependence was determined as described in (*16*, *18*) for pairs of Fe atoms and Fe atoms close to Co islands (*19*). As the first step, the atomic spin of the first atom in a spin lead has to be magnetically coupled to the input island by means of the RKKY interaction, which was achieved by using the magnetic tip (*19*) of the STM to move the atom (*13*, *23*) toward the input island to an adequate coupling distance. Figure 2A shows magnetic imaging of several Fe atoms positioned in the vicinity of an input island (α) recorded with a chromium-coated (*19*) STM tip that is sensitive to the out-of-plane component of the magnetization of both the islands and the atoms (yellow or blue indicates the magnetic state **1** or **0**, parallel or antiparallel to the tip magnetization $\vec{M}$, respectively). The first atom was positioned at the

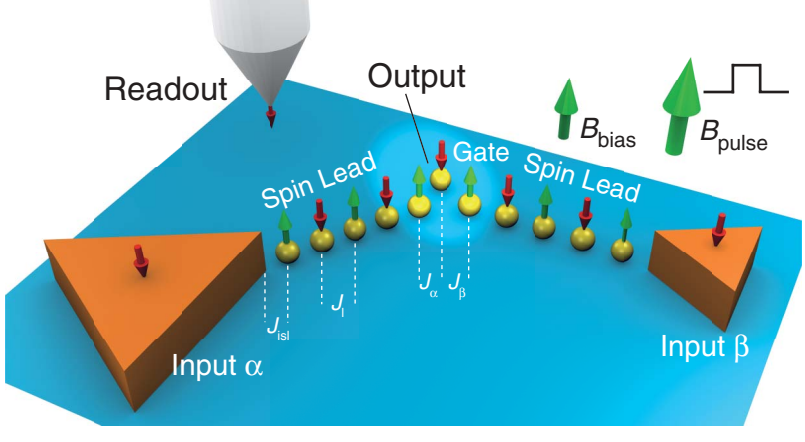

Fig. 1. Device concept for an atomic-spin–based logic gate. Two chains ("spin leads"), which are antiferromagnetically coupled magnetic atoms (yellow spheres) on a nonmagnetic metallic substrate with interatomic couplings J_l, are exchange-coupled by J_{isl} to two "input islands" (α, β) of different size, consisting of patches of ferromagnetic layers. The "end atom" of each spin lead and the final "output atom" form a magnetically frustrated triplet with an antiferromagnetic coupling of $J_\alpha = J_\beta$ which constitutes the logic gate. The spin lead parity (even/odd number of atoms) and the constant biasing field $\vec{B}_{bias}$ determine the logical operation of the gate, and the field pulse $\vec{B}_{pulse}$ is used to switch the inputs. The magnetic tip of a STM is used to construct and characterize the device.

Institute of Applied Physics, Hamburg University, Jungiusstrasse 11, D-20355 Hamburg, Germany.

*To whom correspondence should be addressed. E-mail: jwiebe@physnet.uni-hamburg.de

top corner of the island at a distance where the coupling is antiferromagnetic with an exchange energy of $|J_{isl}| \approx 0.3 - 0.35$ meV. This coupling varies slightly depending on the exact distance to the input island and on the local geometry of the island corner [supporting online material (SOM) text and fig. S2]. Thus, while the input island is in state **1** the atom is in state **0**. In the next step, the spin lead is built atom-by-atom by subsequently adding Fe atoms with an interatomic distance d = 0.923 nm, where the interatomic exchange coupling is antiferromagnetic ($|J_{isl}| \approx 0.1$ meV) (Fig. 2, A to E) for spin leads with lengths of up to six atoms. The read-out signal from the end atom in each spin lead (Fig. 2F) shows that the output is digital and affirms or negates the state of the input for spin leads with an even or odd number of atoms, respectively; thus, odd-number spin leads transmit the inverted input, performing a NOT function.

The next step is to select a second input island (β) in proximity to the first and transmit its state to a position close to the end atom of the first lead by constructing a second spin lead. Both constructed spin leads are illustrated in Fig. 3A, one with six atoms and the other with four atoms, each coupled to the corner of a separate input. The inputs have been chosen to have drastically different sizes and consequently different coercivities $B^{\alpha}_{coe} \approx 1.75$ T and $B^{\beta}_{coe} \approx 0.4$ T, so that their state can be switched independently by using magnetic field pulses $\vec{B}_{pulse}$ of different strength and polarity. Figure 3B shows the device after the application of $B_{pulse} \approx -0.4$ T, which switches input β from state **1** to **0** while input α stays in state **0**. Upon reversal of the input, each atom in the six-atom spin lead reverses its state, and the end atom again affirms the state of the input. There is no obvious change to the opposite lying spin lead coupled to the other input, indicating minimal cross talk between the spin leads.

The last step necessary to construct a logical gate by using our proposed concept is to place an output atom at an appropriate distance between the end atoms of both spin leads, that is, construct the gate region. The interplay between the exchange couplings J_α and J_β of the output atom and J_l of both spin leads (Fig. 1) is pivotal in determining whether the device works as a logical gate. Given that the exchange interaction between each spin lead and its island J_{isl} dominates, and that the mutual interaction between the end atoms in both leads is smaller than J_1, which is a prerequisite for device functionality, there are three principal cases to consider: (i) the "extended chain" case, where $J_l \geq J_\alpha > J_\beta$ or $J_\alpha > J_l > J_\beta$; (ii) the "cross-talk" case, where $J_\alpha \geq J_\beta \geq J_l$; and (iii) the "frustration" case, where $J_l > J_\alpha = J_\beta$. For case (i), the output is only sensitive to the state of one input, and thus the device works as an affirmation or negation of its corresponding input, similar to the demonstration in Fig. 2. For case (ii), the two spin leads cannot be regarded as independent and influence each other. In order to realize basic logical functions, this is undesirable because each end atom of each spin lead should solely reflect its corresponding input. Only the frustration case (iii) offers a viable and flexible solution in the following way: If the two end atoms of each spin lead are in the same state, the output atom will negate that state. If the two end atoms are in opposite states, the output atom is magnetically frustrated, yielding a degeneracy because it wants to align antiparallel to both end atoms. This frustration can easily be broken by applying a biasing magnetic field $\vec{B}_{bias}$, which is weak enough not to change either of the spin lead states or modify the input state but strong enough for the frustrated output to energetically favor one state.

The realization of such a gate using two odd length spin leads is illustrated in Fig. 4, A to D. The interatomic spacing of both spin leads is d = 0.923 nm, resulting in antiferromagnetic coupling $|J_l| \approx 0.1$ meV, and the gate is an equilateral triplet with an interatomic distance of d = 1.35 nm, resulting in antiferromagnetic coupling $|J_\alpha| = |J_\beta| \approx 0.025$ meV. The two inputs are switched independently from Fig. 4A to Fig. 4D by applying $\vec{B}_{pulse}$ of appropriate strength and direction. Each spin lead adjusts to its corresponding input independently of the other input state. The output is in the **0** (**1**) state when both inputs are in the **0** (**1**) state corresponding to the negation of the input by the end atoms of the odd spin leads. If the inputs are in different states, the output aligns parallel to B_{bias} = +50 mT (state **1**), and the device thus works as an OR gate (see truth values below Fig. 4, A to D).

The major loop magnetization curves (*18*, *21*) of both input islands (α, β) as well as of the output atom are shown in Fig. 4, E and F. Clearly, input α has a much larger coercive field ($B^{\alpha}_{coe} \approx 1.75$ T) than that of input β ($B^{\beta}_{coe} \approx 0.4$ T), which allows for a large range of magnetic field pulses ($0.4\ T \leq |B_{pulse}| \leq 1.75\ T$) that can switch the inputs independently. During the initial downward sweep (blue markers), both inputs and the output are in state **1** until the field overcomes the exchange interaction between the output atom and the two end atoms at $B_{crit} = -m \times |J_\alpha + J_\beta| \approx -3.5\mu_B \times 0.05$ meV = –0.25 T (*18*) [where m is the magnetic moment of the Fe atom (*21*)], where the output is forced into state **0**. In the upwards sweep (red markers), the output does not revert back to state **1** until the field once again overcomes $B_{crit} \approx +0.25$ T. Thus, during this major loop the inputs are only inverted

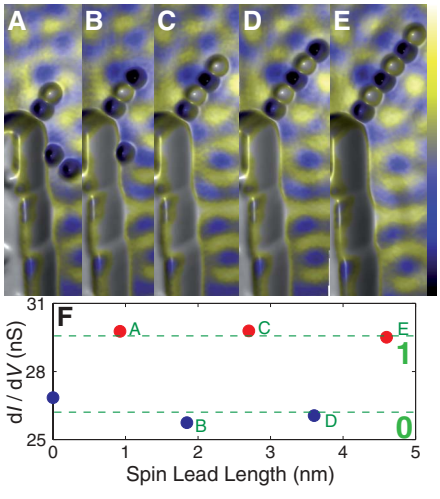

Fig. 2. Construction and read-out of a spin lead. (**A** to **E**) Top view three-dimensional (3D) topographs colored with simultaneously measured spin-resolved d*I*/d*V* map of spin leads of different lengths [two (A) to six (E) atoms] constructed from antiferromagnetically coupled Fe atoms with interatomic distance d = 0.923 nm on Cu(111). The first atom in the spin lead is magnetically stabilized by the corner of a triangular Co input island (bottom left). The color on top of each atom or island reflects its magnetization state (**0**, blue; **1**, yellow; color bar ranges from 26.5 to 30.4 nS). (**F**) d*I*/d*V* signal averaged on the end atom of each lead in (A) to (E) as a function of spin lead length illustrating the digital output of the end atom. B_{bias} = +200 mT; V_{sample} = −10 mV; I_t = 600 pA; V_{mod} = 5 mV [root mean square (rms)].

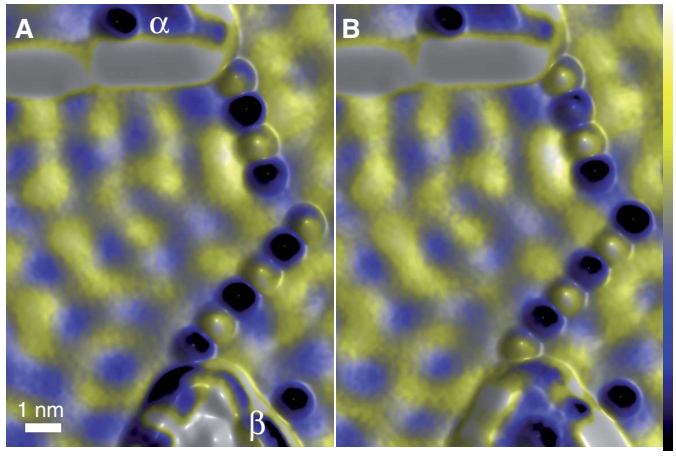

Fig. 3. (**A** to **B**) Switching of a spin lead. Each of the two antiferromagnetic spin leads (d = 0.923 nm) is magnetically coupled to the corner of one of the two Co input islands having different sizes (α, β). By applying $|B_{pulse}| \approx 0.4$ T, the magnetization of the smaller input island (β) is reversed from (A) **1** to (B) **0**. The six-atom spin lead accordingly transmits the information to its end atom, whereas the four-atom spin lead coupled to the input island α remains unaffected. B_{bias} = +200 mT; V_{sample} = −10 mV; I_t = 600 pA; V_{mod} = 5 mV (rms); color bar ranges from 24 to 29 nS.

relative to each other at a field above $|B_{crit}|$, and consequently the frustrated situation in which the output is aligned with $\vec{B}_{bias}$ does not occur. As shown by magnetization curves of the other atoms in the two spin leads (SOM text and fig. S2), the detailed couplings within each spin lead are more complex because of a residual exchange interaction of atoms within each spin lead with the corresponding input island and because of residual cross talk between the leads. Therefore, the magnetic signal strength of each atom in the lead and of the output atom is different. However, we can conclude that as long as $0 < B_{bias} < B_{crit}$ the device works as an OR gate.

Our proposed scheme is quite flexible. In the above example of the OR gate, the orientation of $\vec{B}_{bias}$ and $\vec{M}_{tip}$ was chosen to be parallel. The logical function is changed if this relative orientation is reversed. The logical function can be changed as well by using different combinations of even- and odd-length spin leads. All possible combinations and the resulting logical functions are summarized in Table 1.

There are several open issues to be solved before these realized model systems can be scaled to a larger logic device architecture. In order to drive additional gates, it remains to be demonstrated how to realize an output spin lead and a fan-out by coupling two spin leads to the end atom of an output spin lead. This might be challenging because the magnetic stability of the spin leads will decrease as a function of their length, which would increase the error rate of the end atoms. However, the distance dependence of the RKKY interaction inherently offers flexibility, giving this concept extensive versatility. Although rather weak antiferromagnetic couplings were used for the realized model gate, combinations of antiferromagnetic and stronger ferromagnetic couplings can be achieved by a proper tuning of the interatomic distances in order to stabilize the spin leads. For example, by linking the Fe atoms with Cu adatoms the interaction strength can be increased by an order of magnitude (*24*). For the logical operations presented here, we made use of quasiclassical magnetic moments pointing either up or down. Implementation of quantum mechanical spins with more than two states (*25*) may present an intriguing extension of our demonstrated concept by providing a larger number of states for each atom and could potentially lead to the realization of model systems for quantum information processing.

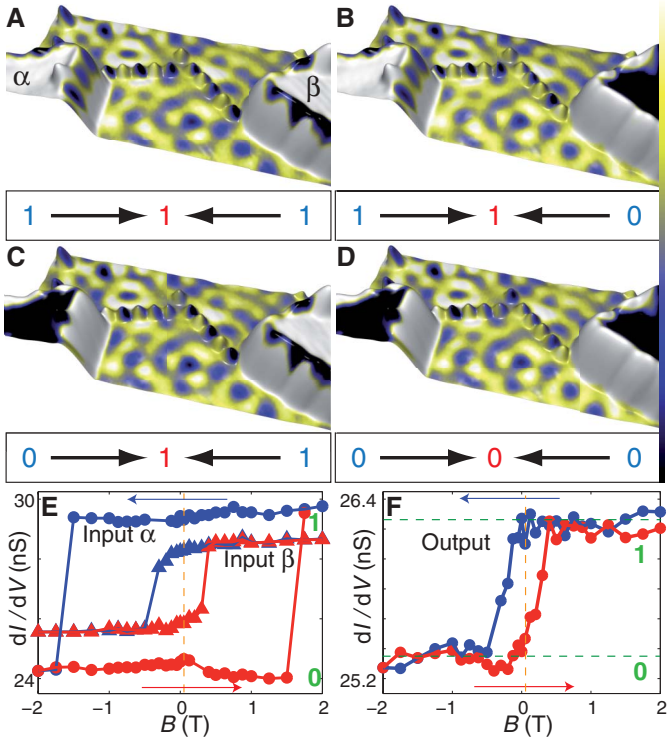

Fig. 4. OR gate. (**A** to **D**) Side view 3D topographs colored with simultaneously measured spin-resolved d*I*/d*V* map of the device for all four possible input permutations (color bar ranges from 24.7 to 26.9 nS). The spin leads have an interatomic distance of $d = 0.923$ nm, and the antiferromagnetic gate triplet is equilateral with $d = 1.35$ nm. By applying out-of-plane magnetic field pulses of different strength and direction [(A) → (B): $B_{pulse} = -0.39$ T, (B) → (C): $B_{pulse} = -2$ T, +0.75 T, (C)→(D): $B_{pulse} = -0.385$ T], each input (α, β) can be controllably switched, and the two spin leads transmit the information to their end atoms. The output atom in the gate triplet reflects the logical operation of the inputs (in the truth table, states of the inputs are labeled blue and of the output red). The biasing field B_{bias} = +50 mT favors the **1** state of the output atom. (**E** and **F**) Major loop magnetization curves of (E) input α (dots), input β (triangles), and (F) output atom of the OR gate (blue symbols indicate downward sweep and red symbols indicate upward sweep). The saturation magnetization values in the two states are labeled **0** and **1** and marked with dashed horizontal lines in (F). The dashed vertical line corresponds to B_{bias}. $V_{sample} = -10$ mV; $I_t = 600$ pA; $V_{mod} = 5$ mV (rms).

Table 1. Possible logical expectations as a function of the relative orientation of biasing field on magnetization, and of the parity of each spin lead.

	α, β odd	α, β even	α even, β odd	α odd, β even
$\vec{B}_{bias} \uparrow\uparrow \vec{M}_{tip}$	OR	NAND	α → β	α ← β
$\vec{B}_{bias} \uparrow\downarrow \vec{M}_{tip}$	AND	NOR	α ↚ β	α ↛ β

References and Notes

1. D. Hisamoto *et al.*, *IEEE Trans. Electron. Dev.* **47**, 2320 (2000).
2. C. S. Lent, P. D. Tougaw, *Proc. IEEE* **85**, 541 (1997).
3. I. Amlani I *et al.*, *Science* **284**, 289 (1999).
4. A. J. Heinrich, C. P. Lutz, J. A. Gupta, D. M. Eigler, *Science* **298**, 1381 (2002).
5. B. Behin-Aein, D. Datta, S. Salahuddin, S. Datta, *Nat. Nano.* **5**, 266 (2010).
6. A. Imre *et al.*, *Science* **311**, 205 (2006).
7. D. A. Allwood *et al.*, *Science* **309**, 1688 (2005).
8. P. Xu *et al.*, *Nat. Nano.* **3**, 97 (2008).
9. S. S. P. Parkin, M. Hayashi, L. Thomas, *Science* **320**, 190 (2008).
10. D. Loss, D. P. DiVincenzo, *Phys. Rev. A* **57**, 120 (1998).
11. P. Neumann *et al.*, *Nat. Phys.* **6**, 249 (2010).
12. S. A. Wolf *et al.*, *Science* **294**, 1488 (2001).
13. D. M. Eigler, E. K. Schweizer, *Nature* **344**, 524 (1990).
14. F. J. Ruess *et al.*, *Small* **3**, 563 (2007).
15. C. R. Moon, L. S. Mattos, B. K. Foster, G. Zeltzer, H. C. Manoharan, *Nat. Nano.* **4**, 167 (2009).
16. F. Meier, L. Zhou, J. Wiebe, R. Wiesendanger, *Science* **320**, 82 (2008).
17. A. J. Heinrich, J. A. Gupta, C. P. Lutz, D. M. Eigler, *Science* **306**, 466 (2004).
18. L. Zhou *et al.*, *Nat. Phys.* **6**, 187 (2010).
19. Materials and methods are available as supporting material on *Science* Online.
20. O. Pietzsch, A. Kubetzka, M. Bode, R. Wiesendanger, *Phys. Rev. Lett.* **92**, 057202 (2004).
21. A. A. Khajetoorians *et al.*, *Phys. Rev. Lett.* **106**, 037205 (2011).
22. J. Wiebe *et al.*, *Rev. Sci. Instrum.* **75**, 4871 (2004).
23. M. F. Crommie, C. P. Lutz, D. M. Eigler, *Science* **262**, 218 (1993).
24. O. O. Brovko, P. A. Ignatiev, V. S. Stepanyuk, P. Bruno, *Phys. Rev. Lett.* **101**, 036809 (2008).
25. C. F. Hirjibehedin, C. P. Lutz, A. J. Heinrich, *Science* **312**, 1021 (2006).

Acknowledgments: Financial support from the European Research Council Advanced Grant "FURORE" by the Deutsche Forschungsgemeinschaft via the SFB668, the Graduiertenkolleg 1286 "Functional Metal-Semiconductor Hybrid Systems," as well as from the Cluster of Excellence "Nanospintronics" funded by the Forschungs- und Wissenschaftsstiftung Hamburg is gratefully acknowledged. The authors thank S. Lounis, M. Potthoff, and R. Wieser for extensive discussions.

Supporting Online Material

www.sciencemag.org/cgi/content/full/science.1201725/DC1
Materials and Methods
SOM Text
Figs. S1 and S2
References

12 December 2010; accepted 6 April 2011
Published online 5 May 2011;
10.1126/science.1201725

Electrically Induced Ferromagnetism at Room Temperature in Cobalt-Doped Titanium Dioxide

Y. Yamada,[1]* K. Ueno,[2,3]* T. Fukumura,[3,4]† H. T. Yuan,[5,6] H. Shimotani,[5,6] Y. Iwasa,[5,6] L. Gu,[2] S. Tsukimoto,[2] Y. Ikuhara,[2,7,8] M. Kawasaki[1,2,5,6]

The electric field effect in ferromagnetic semiconductors enables switching of the magnetization, which is a key technology for spintronic applications. We demonstrated electric field–induced ferromagnetism at room temperature in a magnetic oxide semiconductor, $(Ti,Co)O_2$, by means of electric double-layer gating with high-density electron accumulation (>10^{14} per square centimeter). By applying a gate voltage of a few volts, a low-carrier paramagnetic state was transformed into a high-carrier ferromagnetic state, thereby revealing the considerable role of electron carriers in high-temperature ferromagnetism and demonstrating a route to room-temperature semiconductor spintronics.

Magnetization of ferromagnetic materials is a fundamental quantity in various spintronic devices, such as magnetic random access memories. Magnetization control by electrical means is one of the central issues in semiconductor spintronics and will contribute to lower energy consumption of those devices (*1*, *2*). Ferromagnetic semiconductors possess both spin and charge degrees of freedom as a result of the carrier-mediated exchange interaction (*3*). Therefore, field-effect transistors made of ferromagnetic semiconductors are one of the most promising routes to realizing electrical control of magnetism, which in turn will lead to magnetization switching (*4*). In contrast, electric field control of ferromagnetic metals is limited to varying the magnetic anisotropy, which leads to magnetization rotation (*5*, *6*). The most well-studied ferromagnetic semiconductor, (Ga,Mn)As, has a Curie temperature (T_C) of 190 K (*7*), thus hindering the possibility of electrical control of ferromagnetism at room temperature.

The strong demand for higher-T_C ferromagnetic semiconductors led to the theoretical prediction of higher T_C in wide-gap magnetic semiconductors such as oxides (*8*). Subsequently, a combinatorial approach revealed that a magnetic oxide semiconductor, $(Ti,Co)O_2$, is ferromagnetic with $T_C > 400$ K (*9*). This compound exhibits the ferromagnetic magneto-optical effect and anomalous Hall effect at room temperature (*10*–*12*), thus satisfying important prerequisites to be classified as a ferromagnetic semiconductor (*3*). Electric field control of ferromagnetism should be possible at room temperature if ferromagnetism originates from a carrier-mediated mechanism.

The electric field effect has been used for transforming various electronic and magnetic phases in a wide range of materials (*4*, *13*). Usually, the accumulation of sufficiently high charge density (>10^{14} cm^{-2}) to induce an exotic phase has been difficult because of dielectric breakdown of the gate insulator. Electric double layer transistors (EDLTs) have been developed as a powerful device structure allowing an extremely high electric field effect. EDLTs use a liquid electrolyte instead of a conventional solid gate insulator. Self-organized ions under an applied gate voltage form a nanometer-thick electric double layer to induce an image charge sheet on the channel surface, yielding a very high electric field on the order of 10 MV cm^{-1}.

Epitaxial films of anatase, $Ti_{0.90}Co_{0.10}O_2$ (001), were grown on $LaAlO_3$ (100) substrates by a pulsed laser deposition method (*14*). Bright-field scanning transmission electron microscopy (STEM) imaging and the corresponding energy-dispersive x-ray spectroscopy mapping for each constituent element (Fig. 1, A and B) reveal that Co atoms were distributed homogeneously inside the thin-film region without any segregation at the surface or interface, which is consistent with x-ray diffraction and atomic force microscopy analyses (*14*). In the atomically resolved high-angle annular dark-field STEM (HAADF-STEM) images (Fig. 1, D and E, for the regions indicated in Fig. 1C), the intensity of the atomic column is approximately proportional to the square of the atomic number (*15*). As shown in Fig. 1D, Ti atoms in the anatase TiO_2 buffer layer (upper part) were coherently grown on the $LaAlO_3$ substrate (bottom part), where bright and dark spots correspond to atomic columns of La and Al atoms, respectively. The anatase structure was coherently retained in the $Ti_{0.90}Co_{0.10}O_2$ film (Fig. 1E): The uniform contrast of Ti and Co atoms represents the homogeneous distribution of Co atoms substituting for Ti sites.

Figure 1F schematically shows the structure of an EDLT: A drop of electrolyte contacts the Hall bar channel and the Pt planar gate electrode (an optical microscope image is shown in fig. S1). We used two kinds of electrolyte (*14*). By applying a positive gate voltage, the cations and anions move to the channel and the gate electrode, respectively, and then an electric double layer is formed over the channel surface to accumulate electron carriers in the channel, leading to the emergence of ferromagnetism (Fig. 1G).

To probe the carrier accumulation and its ferromagnetic response, we carried out Hall effect measurements. The Hall resistivity (ρ_H) of $(Ti,Co)O_2$ can be expressed by the sum of the ordinary and anomalous Hall terms, $\rho_H = R_0H + R_S\mu_0M$, where R_0 and R_S are the ordinary and anomalous Hall coefficients, respectively; H is the magnetic field; μ_0 is the vacuum permeability and M is the magnetization (*16*). Accordingly; the anomalous Hall term can be an electrical probe of M and is useful particularly for thin films because of its small magnetization signal. The electron density n is inversely proportional to R_0, $n = (eR_0)^{-1}$, where e is the bare electron charge; the mobility μ can also be evaluated by measuring the resistivity (ρ_{xx}) according to the relation $\mu = R_0/\rho_{xx}$.

The blue curve in Fig. 1H is a transfer curve measured at 320 K for an EDLT with a 33-nm-thick $Ti_{0.90}Co_{0.10}O_2$ channel. The sheet conductance G_{xx} was enhanced above a gate voltage V_G of 3 V, indicating an electron channel field-effect transistor operation. The red circles in Fig. 1, H to J, respectively show G_{xx}, the sheet electron density (n_{2D}), and μ at 300 K measured during the temperature variation experiments (see Fig. 2A). The value of n_{2D} increased from 4.0×10^{13} cm^{-2} at $V_G = 0$ to 2.7×10^{14} cm^{-2} at $V_G = 3.8$ V, whereas μ remained almost constant. The maximum of the accumulated sheet electron density was as high as that observed in an EDLT using the same ionic liquid for gating (*17*). The value of G_{xx} at $V_G = 0$ was reproduced after repeated V_G scans. Hence, the enhancement in G_{xx} was caused by the electrostatic charge accumulation. Note that the extremely high chemical stability of $(Ti,Co)O_2$ prevented the films from undergoing electrochemical reactions during the repeated electric field effect measurements (*18*).

Figure 2A shows the temperature dependence of ρ_{xx} measured during cooling at various values of V_G. The charge accumulation transformed the channel from an insulative state to a metallic one. Shown in Fig. 2, B to D, are the values of conductivity (σ_{xx}), μ, and

[1]Institute for Materials Research, Tohoku University, Sendai 980-8577, Japan. [2]WPI-AIM Research, Tohoku University, Sendai 980-8577, Japan. [3]PRESTO, Japan Science and Technology Agency, Kawaguchi 332-0012, Japan. [4]Department of Chemistry, University of Tokyo, Tokyo 113-0033, Japan. [5]Quantum-Phase Electronics Center and Department of Applied Physics, University of Tokyo, Tokyo 113-8656, Japan. [6]CREST, Japan Science and Technology Agency, Tokyo 102-0075, Japan. [7]Institute of Engineering Innovation, University of Tokyo, Tokyo 113-8656, Japan. [8]Nanostructures Research Laboratory, Japan Fine Ceramics Center, Nagoya 456-8587, Japan.

*These authors contributed equally to this work.
†To whom correspondence should be addressed. E-mail: fukumura@chem.s.u-tokyo.ac.jp

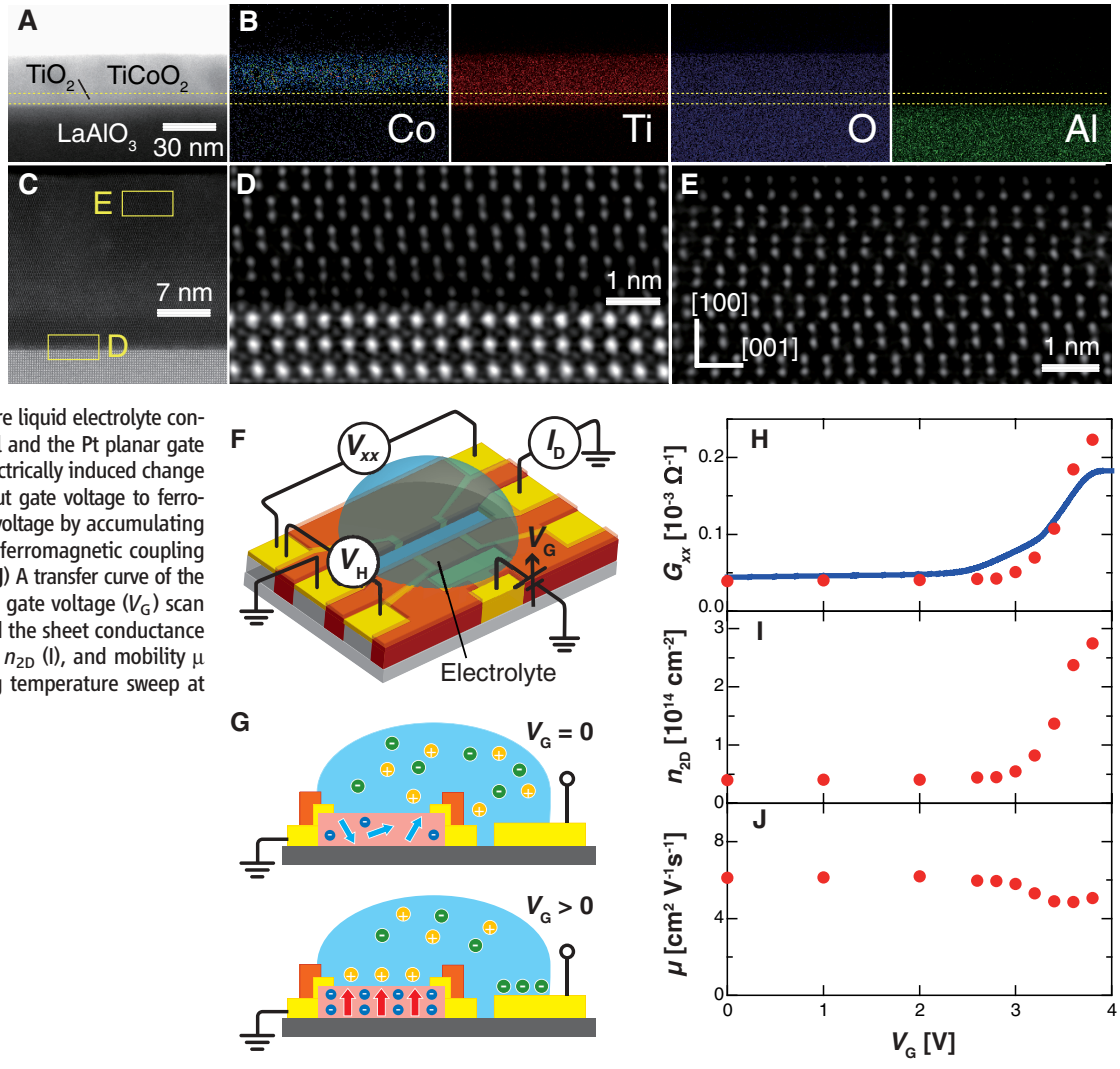

Fig. 1. (**A**) A bright-field STEM image of a $Ti_{0.90}Co_{0.10}O_2$ (001) / TiO_2 (001) / $LaAlO_3$ (100) substrate. (**B**) The corresponding energy-dispersive x-ray spectroscopy mappings for Co, Ti, O, and Al. (**C**) Cross section showing location of images in (D) and (E). (**D** and **E**) Atomically resolved high-resolution HAADF-STEM images at the TiO_2 / $LaAlO_3$ interface (D) and within the $Ti_{0.90}Co_{0.10}O_2$ film (E). (**F**) A schematic of an electric double layer transistor (EDLT), where liquid electrolyte contacts the $Ti_{0.90}Co_{0.10}O_2$ channel and the Pt planar gate electrode. (**G**) Illustration of electrically induced change from paramagnetic state without gate voltage to ferromagnetic state with finite gate voltage by accumulating electron carriers that mediate ferromagnetic coupling between localized spins. (**H** to **J**) A transfer curve of the EDLT at 320 K measured with a gate voltage (V_G) scan rate of 1 mV/s (blue curve) and the sheet conductance G_{xx} (H), sheet electron density n_{2D} (I), and mobility μ (J) at 300 K measured during temperature sweep at each V_G (red circles).

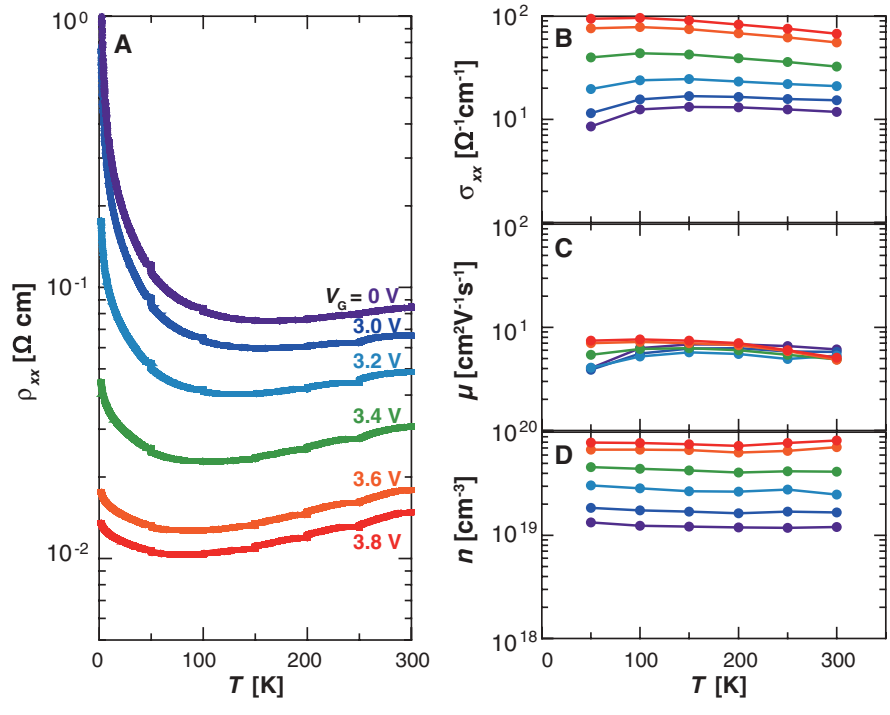

Fig. 2. (**A**) Temperature dependence of resistivity ρ_{xx} in $Ti_{0.90}Co_{0.10}O_2$ channel measured while cooling from 320 K with application of each gate voltage V_G. From 300 to 50 K in decrements of 50 K, the temperature was kept constant while the magnetic field was swept between +0.5 T and −0.5 T for the Hall effect measurements. (**B** to **D**) Temperature dependences of conductivity σ_{xx} (B), mobility μ (C), and electron density n (D) at each V_G; colors correspond to those in (A).

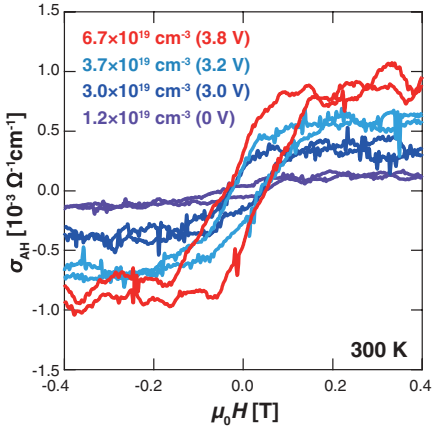

Fig. 3. Magnetic field ($\mu_0 H$, where μ_0 is the vacuum permeability) dependence of the anomalous Hall conductivity σ_{AH} at 300 K, measured at different gate voltages V_G. The values of electron density n at each V_G obtained from the ordinary Hall effect are shown in parentheses. The upper and lower curves for each color correspond to the anomalous Hall conductivity with decreasing and increasing magnetic field, respectively.

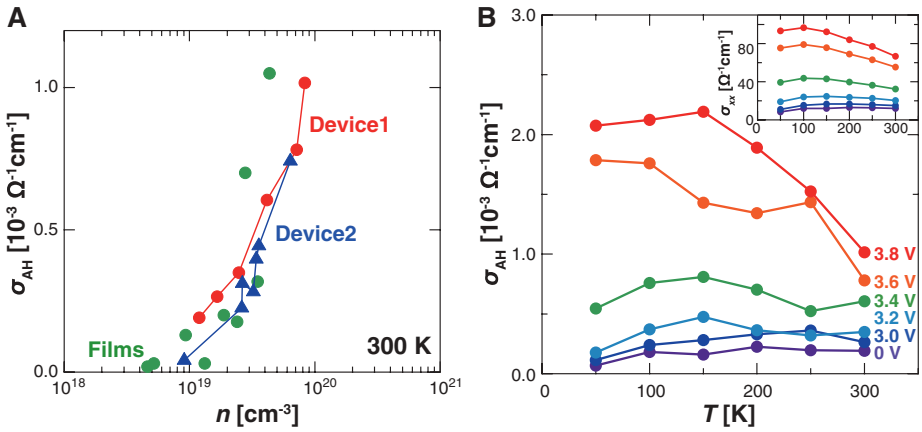

Fig. 4. (**A**) Relationship between anomalous Hall conductivity σ_{AH} and electron density n at 300 K. Red circles and blue triangles denote the data for two different EDLTs (devices 1 and 2, respectively). The applied gate voltage V_G was 0 to 3.8 V for device 1 and 0 to 3.75 V for device 2. Green circles denote the data from nine $Ti_{0.90}Co_{0.10}O_{2-\delta}$ samples, in which the electron density was varied by tuning the concentration of the oxygen vacancy δ. (**B**) Temperature dependence of the anomalous Hall conductivity for each gate voltage V_G. The inset shows temperature dependence of the longitudinal conductivity σ_{xx}, converted from Fig. 2B.

the volume electron density (n) evaluated from the ordinary part of the Hall resistance at each temperature, where n was obtained from n_{2D} divided by the film thickness, assuming a uniform distribution of electron density along the depth, for the sake of comparison with chemically doped samples. The increase in σ_{xx} was dominated by the increase in n.

Such a high-density accumulation of charge carriers had a striking effect on the magnetism at room temperature. Figure 3 shows the magnetic field dependence of anomalous Hall conductivity (σ_{AH}) at each V_G (*19*). At $V_G = 0$, σ_{AH} was almost negligible, indicating that the $Ti_{0.90}Co_{0.10}O_2$ channel was in a paramagnetic state. With increasing V_G, σ_{AH} was enhanced to show the clear emergence of hysteresis, indicating the electric field–induced ferromagnetic state.

The relationship between σ_{AH} and n at 300 K is summarized in Fig. 4A for the two different EDLTs (devices 1 and 2), superposed with the data from nine samples of chemically doped $Ti_{0.90}Co_{0.10}O_{2-\delta}$, in which the oxygen vacancy δ was varied as the electron donor. At $V_G = 0$ V, σ_{AH} was negligible in both devices. By accumulating n greater than $\sim 1 \times 10^{19}$ cm^{-3}, σ_{AH} was steeply increased by the emergence of the ferromagnetic state. These EDLT data showed good agreement with those of the chemically doped samples, plausibly ruling out extrinsic sources such as magnetic nanoparticles as a cause of the increased σ_{AH}, because the electric field changes only the amount of n. The temperature dependence of σ_{AH} at each V_G is shown in Fig. 4B. The amplitude of σ_{AH} was enhanced above V_G of 3.4 V at all temperatures. The inset in Fig. 4B shows the temperature dependence of σ_{xx}. Note that σ_{AH} and σ_{xx} show quite similar temperature dependence, indicating that the electrical conduction induced the ferromagnetic coupling.

The electrically induced ferromagnetism supports the idea that the ferromagnetism originates from a carrier-mediated mechanism (*20*) rather than a non–carrier-mediated one (*21*). The enhanced T_C with a positive V_G is consistent with the polarity of electron carriers, which are expected to mediate the exchange coupling, in contrast with hole carriers in (Ga,Mn)As (*22*). T_C inferred from Fig. 4B might not be a monotonically increasing function of the carrier density, in contrast to the carrier-mediated mechanism seen with (Ga,Mn)As. Thus, a more systematic study of T_C will be needed, with the change of V_G polarity and the temperature dependences, to elucidate the details of the carrier-mediated mechanism.

Our results show that ferromagnetism can be induced in low-carrier paramagnetic $Ti_{0.90}Co_{0.10}O_2$ with a huge amount of electron charge accumulation by using an EDLT geometry. This method offers promise for future semiconductor spintronics operating at room temperature, such as a gate-tunable magnetization inversion (*23*) and the gate-tunable magneto-optical effect (*10*). Such gate-tunable ferromagnetism will also contribute to manipulation of magnetic bits with lower dissipation than that achieved in ferromagnetic metal memories.

References and Notes

1. S. A. Wolf *et al.*, *Science* **294**, 1488 (2001).
2. I. Žutić, J. Fabian, S. Das Sarma, *Rev. Mod. Phys.* **76**, 323 (2004).
3. A. H. MacDonald, P. Schiffer, N. Samarth, *Nat. Mater.* **4**, 195 (2005).
4. H. Ohno *et al.*, *Nature* **408**, 944 (2000).
5. M. Weisheit *et al.*, *Science* **315**, 349 (2007).
6. T. Maruyama *et al.*, *Nat. Nanotechnol.* **4**, 158 (2009).
7. T. Dietl, *Nat. Mater.* **9**, 965 (2010).
8. T. Dietl, H. Ohno, F. Matsukura, J. Cibert, D. Ferrand, *Science* **287**, 1019 (2000).
9. Y. Matsumoto *et al.*, *Science* **291**, 854 (2001).
10. T. Fukumura *et al.*, *Jpn. J. Appl. Phys.* **42**, L105 (2003).
11. H. Toyosaki *et al.*, *Nature Mater.* **3**, 221 (2004).
12. K. Ueno, T. Fukumura, H. Toyosaki, M. Nakano, M. Kawasaki, *Appl. Phys. Lett.* **90**, 072103 (2007).
13. C. H. Ahn, J.-M. Triscone, J. Mannhart, *Nature* **424**, 1015 (2003).
14. See supporting material on *Science* Online.
15. S. J. Pennycook, L. A. Boatner, *Nature* **336**, 565 (1988).
16. C. L. Chien, C. R. Westgate, Eds., *The Hall Effect and Its Applications* (Plenum, New York, 1980).
17. J. T. Ye *et al.*, *Nat. Mater.* **9**, 125 (2010).
18. K. Ueno, H. Shimotani, Y. Iwasa, M. Kawasaki, *Appl. Phys. Lett.* **96**, 252107 (2010).
19. σ_{AH} is a suitable measure for an index of induced ferromagnetism. See supporting material on *Science* Online.
20. M. J. Calderón, S. Das Sarma, *Ann. Phys.* **322**, 2618 (2007) and references therein.
21. K. A. Griffin, A. B. Pakhomov, C. M. Wang, S. M. Heald, K. M. Krishnan, *Phys. Rev. Lett.* **94**, 157204 (2005).
22. M. Endo *et al.*, *Appl. Phys. Lett.* **96**, 022515 (2010).
23. D. Chiba, M. Yamanouchi, F. Matsukura, H. Ohno, *Science* **301**, 943 (2003).

Acknowledgments: Supported by Ministry of Education, Culture, Sports, Science and Technology of Japan KAKENHI grant 21019004 and by Funding Program for Next Generation World-Leading Researchers grant GR029.

Supporting Online Material

www.sciencemag.org/cgi/content/full/332/6033/1065/DC1
Materials and Methods
Figs. S1 to S3
Table S1
References (*24*–*27*)

23 December 2010; accepted 4 April 2011
10.1126/science.1202152

Seismic Imaging of Transition Zone Discontinuities Suggests Hot Mantle West of Hawaii

Q. Cao,[1]* R. D. van der Hilst,[1]* M. V. de Hoop,[2] S.-H. Shim[1]

The Hawaiian hotspot is often attributed to hot material rising from depth in the mantle, but efforts to detect a thermal plume seismically have been inconclusive. To investigate pertinent thermal anomalies, we imaged with inverse scattering of *SS* waves the depths to seismic discontinuities below the Central Pacific, which we explain with olivine and garnet transitions in a pyrolitic mantle. The presence of an 800- to 2000-kilometer-wide thermal anomaly (ΔT_{max} ~300 to 400 kelvin) deep in the transition zone west of Hawaii suggests that hot material does not rise from the lower mantle through a narrow vertical plume but accumulates near the base of the transition zone before being entrained in flow toward Hawaii and, perhaps, other islands. This implies that geochemical trends in Hawaiian lavas cannot constrain lower mantle domains directly.

An open question in studies of Earth's deep interior concerns mantle plumes, and as the archetype for plume-related hotspot activity, Hawaii has long been central to the debate. The canonical view of a narrow thermal plume rising from the lower mantle below the moving Pacific plate (*1*–*5*) has been used in studies of Hawaiian lavas (*6*, *7*), plume-plate interaction (*8*), and effects of convective mantle wind on plume morphology and seamount chain development (*9*, *10*). The deep-plume paradigm has been questioned, however, and alternative explanations include upwelling from a thermal boundary near the base of the transition zone (*11*) and shallow-mantle processes (*12*). Tomographic evidence for the existence, location, and depth of origin of the purported plume is still ambiguous (*13*–*17*) (SOM text 1).

Temperature anomalies associated with a deep plume influence the depth to (pressure-induced) mineral phase boundaries, which can be determined from reflections or conversions of seismic waves (*18*). Important imaging targets are the olivine-wadsleyite and post-spinel transitions in $(Mg,Fe)_2SiO_4$ near, respectively, 410- and 660-km depth (*19*). Because of their opposite Clapeyron slopes, high temperatures would deepen the former and elevate the latter (SOM text 2). Receiver functions (*P*-to-*S* conversions) reveal a thin transition zone southwest of Hawaii (*20*–*22*) and beneath the Hawaii chain (*23*). This suggests high temperatures, but the lateral extent of the anomalies is not constrained because of the small footprint of seismograph networks on and near the islands.

Transition zone discontinuities can be mapped beyond the reach of receiver functions with underside reflections—S^dS, with d reflector depth—which arrive as precursors to surface-reflected *SS* waves at sensors far from the study region (Fig. 1). Conventional methods enhance the weak signals by stacking specular (mirror-like) *SS* reflections across large (10° to 20° wide) geographical bins (*24*–*28*). This averaging yields low spatial resolution, however, and has not yet yielded robust *410* and *660* images beneath Hawaii (SOM text 1). Here we use three-dimensional (3D) inverse scattering of the *SS* wavefield, with a method (adapted from hydrocarbon exploration) known as a generalized Radon transform (GRT) (*29*) (SOM text 3). This also exploits data redundancy, but instead of stacking stationary phases over spatial bins, it integrates signal associated with waves scattered from single image points. The feasibility of GRT imaging with *SS* precursors was first demonstrated for an oceanic region far away from known thermal down- and upwellings (*30*).

We image the transition zone beneath and around Hawaii with ~170,000 broadband (20 to 50 s) records of the *SS* wavefield, from ~4800 earthquakes (magnitude $m_b > 5.2$; focal depth < 75 km) recorded at one or more of a total of ~2250 seismographic stations around the Pacific (Fig. 1, SOM text 3.1). Data coverage is adequate in most of the study region but degrades toward the southwest (SOM fig. S6, C and F). The GRT produces 1D profiles of elasticity contrasts between 250- and 950-km depth at a 0.5° by 0.5° latitude-longitude grid (SOM text 3.2 and 3.3). These images, which are corrected for 3D mantle heterogeneity (using different tomographic models) and for regional variations in *SS* reflection point depth, constrain interfaces at a radial resolution comparable to that of receiver functions. The closely spaced reflectivity profiles show depth variations (topography) of the *410* and *660* and elucidate structure at other depths that could otherwise be dismissed as noise. We used bootstrap analysis to gain insight into the robustness of the images (SOM text 3.5).

Cross sections through the 3D image volume—for example, across Hawaii (Fig. 2)—reveal multiple scatter horizons. In addition to reflectors near 410-km depth and between 650- and 700-km depth, scattering occurs near depths of 350, 500 to 550, and 800 to 900 km. Most are continuous and have substantial topography, but some appear intermittent or split. We focus here on the traditional boundaries of the transition zone. In Fig. 2B we track the *410* and *660* in cross-

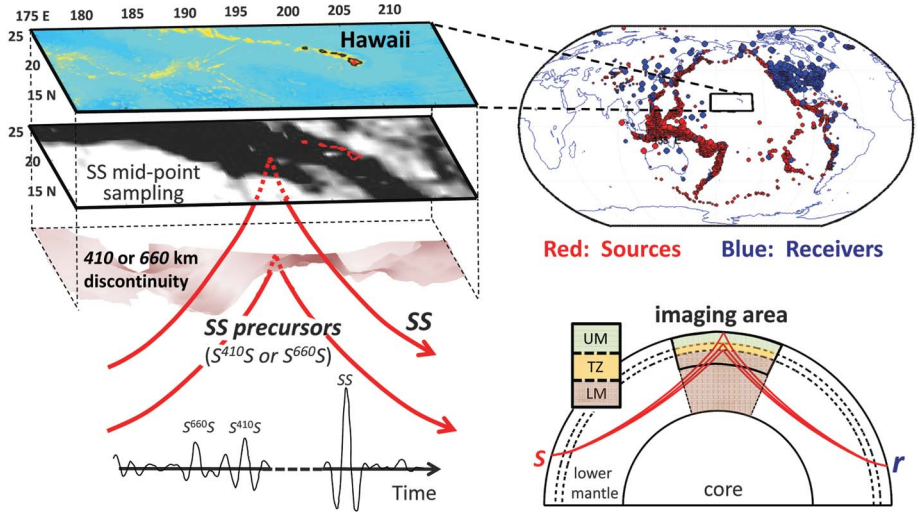

Fig. 1. Left: (Top) Map of study region (175° to 214°E; 12° to 26°N; Mercator projection, perspective view); (middle) geographical distribution of ~170,000 surface mid-points of *SS* waves (the darker the shading, the denser the coverage (SOM text 3.2); (bottom) path geometry of underside reflections at the surface (*SS*) and an upper-mantle discontinuity ($S^{410}S$ or $S^{660}S$); precursor stack showing signal associated with $S^{660}S$, $S^{410}S$, and *SS* waves [after (*27*)]. **Right:** (Top) Geographical distribution of ~4800 sources (red symbols) and ~2250 receivers (blue) from which data are used, and which produces the data coverage shown on the left; (bottom) schematic view of ray geometry of *SS*, $S^{410}S$, and $S^{660}S$ sampling the upper-mantle transition zone below the imaging area (UM, upper mantle; TZ, transition zone; LM, lower mantle).

[1]Department of Earth, Atmospheric, and Planetary Sciences, Massachusetts Institute of Technology, Cambridge, MA 02139, USA. [2]Center for Computational and Applied Mathematics, Purdue University, West-Lafayette, IN 47907, USA.

*To whom correspondence should be addressed. E-mail: qinc@mit.edu (Q.C.), hilst@mit.edu (R.V.D.H.)

section, and depth picks for all grid points yield maps of discontinuity depth (Fig. 3, A and B), transition zone thickness (Fig. 3C), and depth correlation (Fig. 3D).

The depth to *410* varies (on a lateral scale of 500 to 750 km) between 395 and 430 km, and that to *660* varies (more smoothly) between 640 and 705 km. Below and east of Hawaii (region I), the *660* is slightly shallower than the global average (~650 km). Between Hawaii and 165°W (region II) the *660* is more anomalous (~640 km), which confirms results from *P-S* conversions (*20*–*23*) but extends the anomaly further west than first thought. Between 167° and 179°W (region III), the *410* reaches 430 km and the *660* appears anomalously deep (~700 km). West of 180° the interfaces are near global average depths (*29*). The regional average depths of *410* and *660* are 413 km and 665 km, respectively, with the latter biased by large values in region III. The transition zone is thin beneath and northwest of Hawaii and thick in region III (Fig. 3C). The correlation between *410* and *660* is negative in regions I and II and positive in region III (Fig. 3D).

Two types of artifact can influence image quality and accuracy. First, interface depths will be biased if volumetric wave speeds differ from the values that we use for travel-time calculations (SOM text 3.4). This effect is too small to explain the large depth variations across regions II and III, but some trade-off is likely. Spatially coherent depth variations of 10 km or larger are considered meaningful (*30*), but for a conservative interpretation the estimates of interface depths are considered upper bounds. Second, sparse sampling (for instance, west of Hawaii) can degrade noise reduction and spatial resolution. Visual inspection shows that image gathers (SOM text 3.3) are reliable throughout most of the study region, and bootstrapping suggests that the first-order observations in regions I, II, and III are robust at 95% (2σ) confidence level (SOM text 3.5). Parts of the deep structures west of Hawaii are, however, at the edge of what is resolved with currently available data.

Even with these uncertainties, the first-order observations suggest that Hawaii is located above the eastern margin of a large-scale topographic feature comprising an anomalously deep *410* and *660* and a thick transition zone (region III), surrounded by a shallow *660* and a thinner transition zone (regions I, II). This unexpected structural complexity suggests large variations in temperature (and, perhaps, composition) near the upper-lower mantle boundary beneath Hawaii and its environs. To estimate in situ mantle temperatures near the top (ΔT_{410}) and bottom (ΔT_{660}) of the transition zone, we use pressure-temperature dependencies (that is, Clapeyron slopes Γ) of olivine and garnet transitions in a mantle of pyrolitic bulk composition (SOM text 2). Nonpyrolitic compositions are not needed to explain the first-order observations discussed here.

We first interpret the observations in terms of transitions in $(Mg,Fe)_2SiO_4$ olivine: i.e., olivine-wadsleyite [~410 km, $\Gamma_{410} \approx 2.5$ MPa/K (*31*)], wadlseyite-ringwoodite [~520 km, $\Gamma_{520} > 0$ (*32*)], and ringwoodite-perovskite+ferropericlase (post-spinel) [~660 km, $\Gamma_{p\text{-}sp} \approx -2.7$ MPa/K (*33*)]. Temperature maps obtained with these slopes (SOM text 4) reveal a weak perturbation ($\Delta T_{410} \approx \Delta T_{660} \approx 150$ K) below and east of Hawaii (region I) but larger anomalies further west. Interpreting the shallow *660* in region II as updoming of the post-spinel boundary yields $\Delta T_{660} \approx 300$ K, in accord with previous estimates (*20*, *21*), whereas the small ΔT_{410} suggests that the broad anomaly is confined to the base of the transition zone. The 3D structure is complicated, however, and further north a deep *410* and shallow *660* suggest high temperatures in the upper mantle beneath the Hawaii chain (*23*).

The deep *660* (region III) is enigmatic. For $\Gamma_{p\text{-}sp}$ as above, a change in post-spinel depth from 640 to 700 km would imply a temperature difference of ~850 K. Such a large gradient is unrealistic far away from plate margins. The *660* depth could be overestimated if wave speeds above (below) *660* are lower (higher) than the tomographically inferred values used for 3D mantle corrections. Some trade-off is likely, but explaining all signal in this way requires implausible seismic and (probably) thermal anomalies (SOM text 3.4). For realistic values of $\Gamma_{p\text{-}sp}$, ΔT_{660}, and upper mantle velocities, the post-spinel transition does not seem a plausible explanation of the interface near 700-km depth.

Large *410* and *520* depths suggest elevated transition zone temperatures in region III. Multi-anvil experiments have shown (*34*–*36*) that at high temperatures, different phase relations and Al partitioning increase the (seismic) impedance contrast at post-garnet transitions. Such experiments are challenging, however, and important aspects of the phase relations, such as the magnitude of the positive Clapeyron slope ($\Gamma_{p\text{-}gt}$) and the effects of composition on the location and seismic detectability of the post-garnet transition (relative to post-spinel), are still uncertain (SOM text 2). The possibility that the post-garnet transition occurs deeper in hot (and, perhaps, Al_2O_3 rich) mantle than does post-spinel in normal mantle has been invoked to explain geographically isolated findings of a deep *660* (*24*, *27*), and our images may depict a lateral change from post-spinel (in region II) to post-garnet (in III). Given the possible trade-offs and uncertainties in Clapeyron slope and Al_2O_3 content (in pyrolite), estimating ΔT_{660} at the post-garnet transition is fraught with uncertainty, but $\Gamma_{p\text{-}gt} = 3.0$ MPa/K (*37*) would yield an upper bound of 450 K (with a lower bound set by the temperature at the post-spinel transition in region II).

The inference that the mantle near 660-km depth is hot west of Hawaii, over a region that is at least 800 km wide (if restricted to region II) but

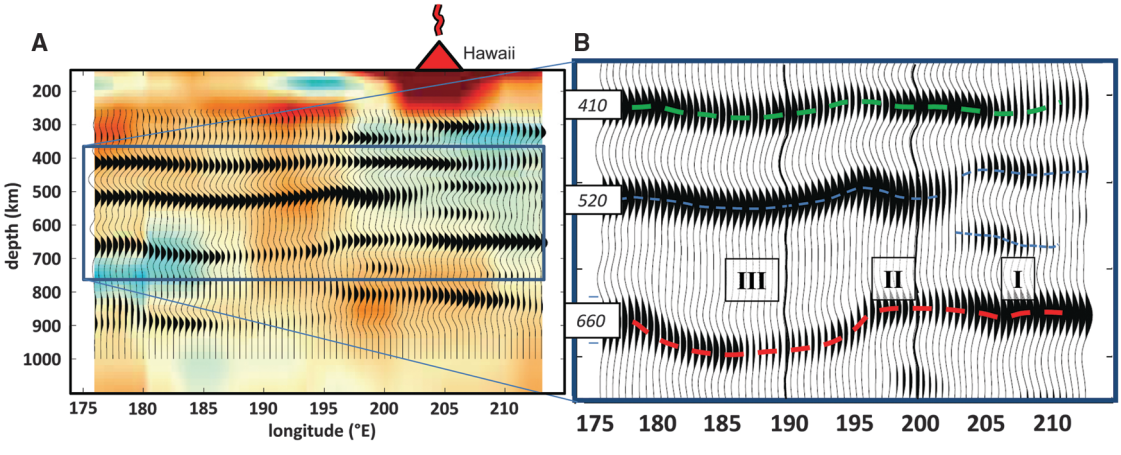

Fig. 2. Seismic section (E-W) across Hawaii (see Fig. 3 for section location). (**A**) Seismic image superimposed on tomographically inferred wave-speed variations (*13*). (**B**) Enlargement of image between 370- and 760-km depth, with interpretation of *410* (dashed green line), *520* (blue), and *660* (red) discontinuities. The depth profiles are corrected for 3D mantle heterogeneity (from tomography) and for the depth to the ocean floor where *SS* reflections occur. Inverse scattering does not assume contiguous reflectors (SOM text 3.2), but alignment suggests lateral continuity. Interfaces appear as a pulse with sidelobes, the width of which depends on frequency of the data and the angle at which image points are sampled (*30*). Horizontal resolution (which depends on illumination) is estimated to be on the order of a few hundred kilometers in the center of the study region (degrading to ~500 km toward the southwest owing to reduced sampling). I, II, and III mark regions discussed in the main text. The image gathers at 190°E and 200°E (highlighted in section on the right) are discussed in SOM text 3.3 and fig. S7).

possibly as broad as 2000 km (if it includes region III), suggests that hot material accumulates and spreads near the top of the lower mantle and that hotspot volcanism may be fueled by secondary upwellings (*5*, *38*) (SOM text 5) from the base of the transition zone (Fig. 4). This is not consistent with tomographic views of a lower mantle plume southeast of Hawaii (*16*, *17*), but currently available travel-time data may not be able to resolve between a continuous plume-like structure and separate anomalies at different depths in the mantle (SOM text 1).

Discontinuity topography reflects local conditions and cannot, by itself, constrain the origin, longevity, and depth extent of the thermal anomaly. However, the temperature contrast and the sustained flux required to feed volcanism at the surface (if, indeed, they are related) indicate that it is not an isolated, ephemeral structure but that it is rejuvenated from below—for instance, by a thermal plume or a larger-scale (thermochemical) mantle dome (*5*). If there is a connection, the transient nature of instabilities rising from the transition zone can help explain irregularities in the evolution (age progression) of the Hawaii-Emperor seamount chain (*10*). Furthermore, the lateral changes of dominant phase transition systems may influence mass exchange between upper and lower mantle. Depending on the combined effects of the width of the post-garnet transition, the density

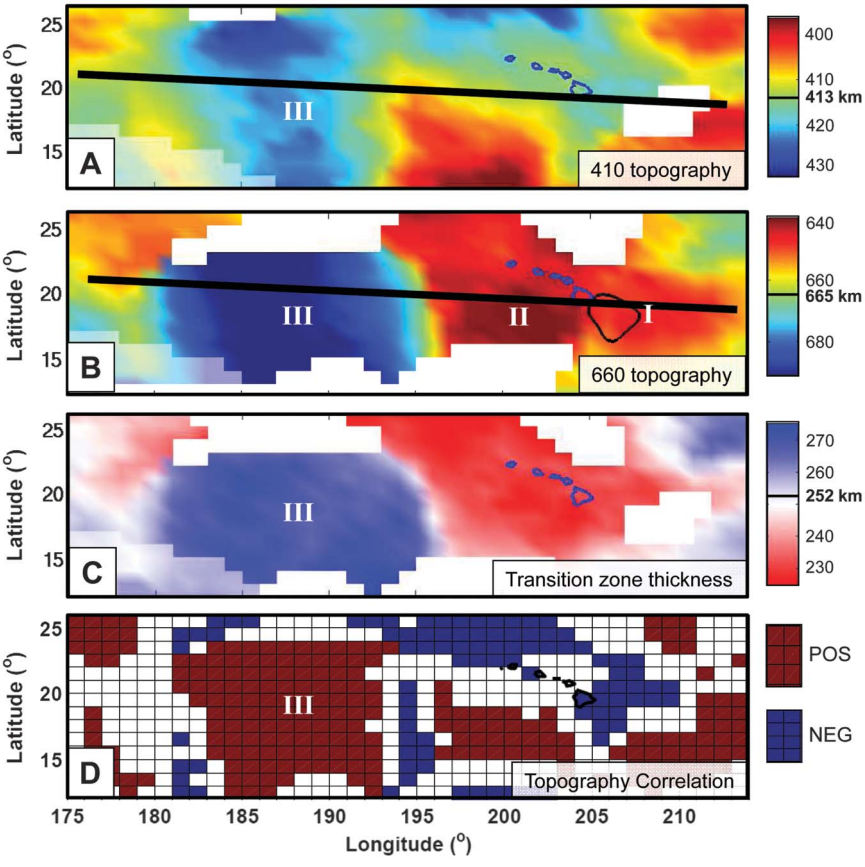

Fig. 3. Discontinuity depths, transition zone thickness, and depth correlations in the study region. (**A**) Topographic map of *410* (regional average 413 km) and (**B**) *660* (regional average 665 km). Thick black solid line depicts location of E-W cross section in Fig. 2, and thin black line in (B) indicates the location (at 700-km depth) of the mantle plume identified in (*16*); see also fig. S2B. I, II, and III mark the regions discussed in the main text. (**C**) The difference between *410* and *660* depths suggests that a relatively thin transition zone (passing through Hawaii) surrounds a thick transition (between 180° and 195°E, Region III). (**D**) Correlation between *410* and *660* depth variations (in regions where *410* and *660* topography exceeds 2.5 and 5 km, respectively). Interface depths are (weakly) negatively correlated beneath Hawaii, but conspicuous positive correlation appears in region III. In (A) to (C), regions where the *410* or *660* could not be identified unambiguously are left blank, and light shading indicates areas of relatively poor data coverage.

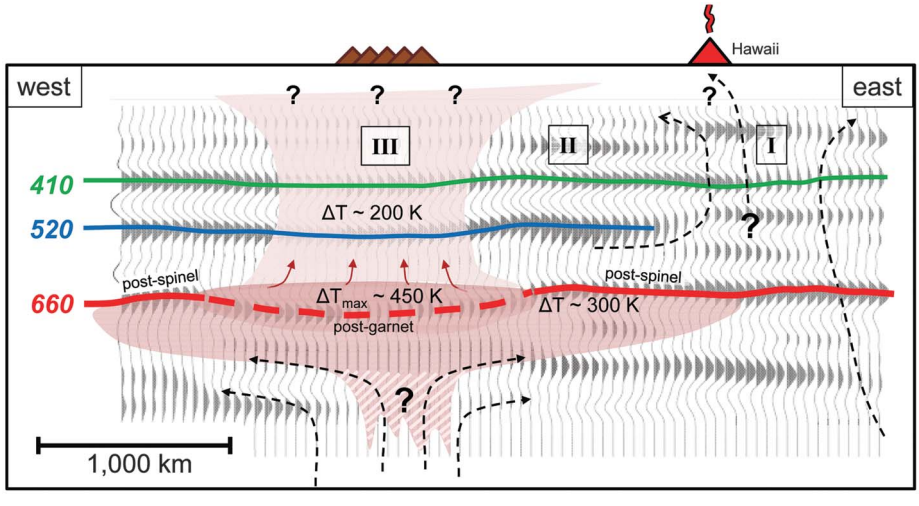

Fig. 4. Cartoon of broad anomaly near base of the transition zone west of Hawaii, superimposed on a scattering image (Fig. 2). Green, blue, and red lines depict interfaces near depths of 410, 520, and 660 km. The deep *410* and *520* west of Hawaii suggest higher-than-average temperatures ($\Delta T_{410} \approx 200$ K) in the upper mantle and transition zone, but with current data coverage we cannot distinguish between a large single anomaly and multiple smaller ones. Updoming of the *660* beneath region II is consistent with elevation of post-spinel transition in hot mantle regions (with $\Delta T_{660} \approx 300$ K), whereas deepening to ~700 km beneath III (red dashed line) may indicate change of dominant transition system to garnet (with $\Delta T_{660,\ max} \approx 450$ K). The positive Clapeyron slope of the latter may aid flux of lower mantle material into the transition zone (thin red arrows). Pathways of flow from the deep anomaly to Earth's surface are not resolved by the data used, but Hawaii volcanism may result from upwellings from the (edge of the) broad anomaly (for instance, just east of Hawaii, region I, Fig. 3).

contrasts at each of the high-temperature transitions (i.e., spinel ↔ garnet+magnesiowüstite ↔ perovskite+magnesiowüstite), the value of $\Gamma_{p\text{-}gt}$, and composition, post-garnet transitions may facilitate the formation of secondary upwellings and thus contribute to the elevated upper-mantle temperatures in region III, a positive geoid anomaly, and, perhaps, the richness of bathymetric features away from seamount chains. Finally, any temporary ponding of lower-mantle flow at *660* suggests that pipe flow or zonation of mantle plumes (*7*, *39*–*41*) must be shallow-mantle phenomena, and that isotope signatures of surface lavas cannot be used to map geochemical domains in the lower mantle.

References and Notes

1. J. T. Wilson, *Can. J. Phys.* **42**, 893 (1963).
2. W. J. Morgan, *Nature* **230**, 42 (1971).
3. G. F. Davies, *J. Geophys. Res.* **93**, 10467 (1988).
4. N. H. Sleep, *J. Geophys. Res.* **95**, 6715 (1990).
5. V. Courtillot, A. Davaille, J. Besse, J. Stock, *Earth Planet. Sci. Lett.* **205**, 295 (2003).
6. S. R. Hart, E. H. Hauri, L. A. Oschmann, J. A. Whitehead, *Science* **256**, 517 (1992).
7. D. Hanano, D. Weis, J. S. Scoates, S. Aciego, D. J. DePaolo, *Geochem. Geophys. Geosyst.* **11**, Q01004 (2010).
8. N. M. Ribe, U. R. Christensen, *Earth Planet. Sci. Lett.* **171**, 517 (1999).
9. B. Steinberger, R. J. O'Connell, *Geophys. J. Int.* **132**, 412 (1998).
10. J. Tarduno, H.-P. Bunge, N. Sleep, U. Hansen, *Science* **324**, 50 (2009).
11. C. J. Allègre, *Philos. Trans. R. Soc. Lond. A* **360**, 2411 (2002).
12. D. L. Anderson, *Geophys. Res. Lett.* **27**, 3623 (2000).
13. S. P. Grand, *Philos. Trans. R. Soc. Lond. A* **360**, 2475 (2002).
14. C. Li, R. D. van der Hilst, E. R. Engdahl, S. Burdick, *Geochem. Geophys. Geosyst.* **9**, Q05018 (2008).
15. R. Montelli *et al.*, *Science* **303**, 338 (2004).
16. C. J. Wolfe *et al.*, *Science* **326**, 1388 (2009).
17. C. J. Wolfe *et al.*, *Earth Planet. Sci. Lett.* **303**, 267 (2011).
18. G. Helffrich, *Rev. Geophys.* **38**, 141 (2000).
19. T. Katsura, E. Ito, *J. Geophys. Res.* **94**, 15663 (1989).
20. X. Li *et al.*, *Nature* **405**, 938 (2000).
21. J. A. Collins, F. L. Vernon, J. A. Orcutt, R. A. Stephen, *Geophys. Res. Lett.* **29**, 1522 (2002).
22. I. Wölbern *et al.*, *Geophys. J. Int.* **166**, 767 (2006).
23. Y. Shen, C. J. Wolfe, S. C. Solomon, *Earth Planet. Sci. Lett.* **214**, 143 (2003).
24. A. Deuss, S. A. T. Redfern, K. Chambers, J. H. Woodhouse, *Science* **311**, 198 (2006).
25. J. Lawrence, P. M. Shearer, *Geophys. J. Int.* **174**, 143 (2008).
26. A. Deuss, *Surv. Geophys.* **30**, 301 (2009).
27. C. Houser, Q. Williams, *Earth Planet. Sci. Lett.* **296**, 255 (2010).
28. N. Schmerr, E. Garnero, A. McNamara, *Earth Planet. Sci. Lett.* **294**, 143 (2010).
29. Materials and Methods are available on *Science* Online.
30. Q. Cao, P. Wang, R. D. van der Hilst, M. V. de Hoop, S.-H. Shim, *Phys. Earth Planet. Inter.* **180**, 80 (2010).
31. H. Morishima *et al.*, *Science* **265**, 1202 (1994).
32. The Clapeyron slope of the wadsleyite to ringwoodite transition is positive (*42*) but not well constrained experimentally.
33. T. Irifune *et al.*, *Science* **279**, 1698 (1998).
34. D. J. Weidner, Y. Wang, *J. Geophys. Res.* **103**, (B4), 7431 (1998).
35. K. Hirose, *J. Geophys. Res.* **107**, (B4), 2078 (2002).
36. N. Nishiyama, T. Yagi, *J. Geophys. Res.* **108**, 2255 (2003).
37. M. Akaogi, E. Ito, *Phys. Earth Planet. Inter.* **114**, 129 (1999).
38. L. Cserepes, D. A. Yuen, *Earth Planet. Sci. Lett.* **183**, 61 (2000).
39. D. J. DePaolo, E. M. Stolper, *J. Geophys. Res.* **101**, (B5), 11643 (1996).
40. J. Blichert-Toft, F. Albarède, *Earth Planet. Sci. Lett.* **282**, 190 (2009).
41. C. G. Farnetani, A. W. Hofmann, *Earth Planet. Sci. Lett.* **282**, 314 (2009).
42. A. Suzuki *et al.*, *Geophys. Res. Lett.* **27**, 803 (2000).

Acknowledgments: This research was supported by the CSEDI (Collaborative Studies of Earth's Deep Interior, grant EAR-0757871) and CMG (Collaborative Mathematical Geosciences, grant DMS-0724778) programs of the U.S. National Science Foundation and a Shell research fellowship awarded to Q.C. The seismic waveforms used here were all retrieved from the Data Management Center of IRIS (Incorporated Research Institutions for Seismology).

Supporting Online Material

www.sciencemag.org/cgi/content/full/332/6033/1068/DC1
Materials and Methods
SOM Text
Figs. S1 to S11
References (*43*, *44*)

11 January 2011; accepted 21 April 2011
10.1126/science.1202731

Computational Design of Virus-Like Protein Assemblies on Carbon Nanotube Surfaces

Gevorg Grigoryan,[1]* Yong Ho Kim,[2]* Rudresh Acharya,[1] Kevin Axelrod,[3] Rishabh M. Jain,[3] Lauren Willis,[3] Marija Drndic,[3] James M. Kikkawa,[3] William F. DeGrado[1,2]†

There is a general need for the engineering of protein-like molecules that organize into geometrically specific superstructures on molecular surfaces, directing further functionalization to create richly textured, multilayered assemblies. Here we describe a computational approach whereby the surface properties and symmetry of a targeted surface define the sequence and superstructure of surface-organizing peptides. Computational design proceeds in a series of steps that encode both surface recognition and favorable intersubunit packing interactions. This procedure is exemplified in the design of peptides that assemble into a tubular structure surrounding single-walled carbon nanotubes (SWNTs). The geometrically defined, virus-like coating created by these peptides converts the smooth surfaces of SWNTs into highly textured assemblies with long-scale order, capable of directing the assembly of gold nanoparticles into helical arrays along the SWNT axis.

De novo protein design has historically been used to test the principles governing protein folding and assembly (*1*–*3*). These principles have also been extended to the design of structures capable of binding metal ions (*4*, *5*), peptides (*6*–*8*), DNA (*9*, *10*), inorganic materials (*11*), and proteins that catalyze reactions similar to those found in nature (*12*–*15*). However, protein design might have greater impact when applied to the engineering of controllable, structurally defined molecular assemblies (*16*). A solution to this problem would enable the manipulation and organization of objects on the molecular and atomic levels, a major challenge of modern nanoscience.

We describe a general approach for designing molecules that assemble along geometrically specific surfaces into a predefined superstructure. Earlier studies focused on amphiphilic peptides that encourage binding and assembly at soft interfaces (*17*–*19*), but without explicit consideration of interpeptide packing geometry that defines the nano- to macrostructure of the overall complex. A good design strategy for encoding a specific mode of assembly is to engineer a protein structural unit that presents functional groups compatible with the targeted surface and associates into a periodic superstructure with a geometric repeat matching that of the targeted substrate (Fig. 1A). However, an infinite continuum of such symmetry-matching arrangements can be generated out of common protein structural units. Thus, the most challenging aspect of designing such a surface-organizing assembly is the identification of a reasonable superstructure geometry, a problem we address in this study. Here, we apply our approach to design peptides that wrap single-walled carbon nanotubes (SWNTs) in a structurally specific manner, creating a richly textured molecular surface. Previously studied biomolecules that interact with SWNTs include single-stranded DNA molecules (*20*, *21*), nanotube-binding peptides selected by phage-display (*22*), and synthetic peptides with chemical features that favor SWNT binding (*23*, *24*). Beyond interacting with and solubilizing SWNTs, a unique and relatively unexplored potential offered by biomolecules is the ability to program structurally specific modes of surface assembly, enabling

[1]Department of Biochemistry and Biophysics, University of Pennsylvania, Philadelphia, PA 19104, USA. [2]Department of Chemistry, University of Pennsylvania, Philadelphia, PA 19104, USA. [3]Department of Physics and Astronomy, University of Pennsylvania, Philadelphia, PA 19104, USA.

*These authors contributed equally to this work.
†To whom correspondence should be addressed. E-mail: wdegrado@mail.med.upenn.edu

nucleation of further superstructure, functionalization, and manipulation (*25*).

Our design process consists of three selection rules, which successively restrict the space of possible peptide-surface assemblies and ultimately dictate peptide sequence (Fig. 1). Selection rule one identifies groups compatible with the target surface, as well as a protein structural unit capable of displaying such groups in a productive manner (Fig. 1B). Selection rule two defines the intersubunit packing of these units on the target surface. Symmetry operations are used to create an elementary unit cell, which is then replicated to match the geometric repeat of the surface (Fig. 1C). A continuum of assemblies remains possible at this point, each creating new protein-protein interfaces, within the unit cell and between neighboring unit cells. The key insight is provided by selection rule three, which ensures that these interfaces are designable—that is, they can be accommodated in a stable and specific manner (Fig. 1D). Designable protein structural motifs occur frequently in nature, such that a structural database search can be used to assess the feasibility of specific intersubunit packing in addition to revealing sequence features that encode it (*26*). In summary, the three selection rules define the intrinsic recognition motif, and its packing into a higher-order assembly in accord with the long-range order of the underlying surface.

These selection rules emerged from our efforts to engineer peptides targeting common species of SWNTs. In picking a functional group for contacting the SWNT (selection rule one), we avoided strong hydrophobic recognition motifs employed in earlier studies (*23*), instead relying on weaker protein-SWNT interactions to encourage the cooperative formation of the intended higher-order assembly (Fig. 1A). We therefore chose the C_α methylene of Gly or the C_β methyl of Ala, presented in a repeating manner on an α helix as the elementary structural unit.

Selection rule two stipulates that the arrangement of protein structural units should match the symmetry of the underlying surface. The cylindrical shape of a SWNT suggested an assembly with rotational or rotational-screw symmetry, so we considered α-helical coiled coils forming a supercoil along the SWNT axis (Fig. 1E). Common SWNTs have relatively hydrophobic surfaces and radii in the range of ~3.75 to 4.1 Å [for the (5,6), (5,7), and (3,8) chiralities]. This, together with the choice of a small side chain for surface recognition, defined the radius of the coiled coil to be ~9 Å, restricting the stoichiometry of the bundle to between five and seven units (*26*). We chose an antiparallel hexamer over a parallel α-helical bundle to exploit the additional degree of freedom (axial shift) available to antiparallel interfaces (*26*). Although SWNTs are relatively smooth, their electronic surface is not entirely homogeneous, and we considered that it may be advantageous in design to match the pitch angle of the helices formed by overlapping benzenoid rings down SWNT surfaces (Fig. 1E) (*27*).

Although the first two selection rules identified a specific topology, a large number of possible bundles with reasonable interfaces could be generated based on the four remaining parameters: (i) the inter-helical separation, (ii) starting helical phase, (iii) superhelical pitch, and (iv) helical axial shift. Allowing 50 discrete values for each parameter within geometrically feasible ranges results in 6,250,000 possible design templates. We had previously found that no more than 1 in 100 α-helical coiled coils constructed using geometrically feasible parameter values are, in fact, designable with natural amino acids (*26*). Therefore, in selection rule three, we searched for assembly parameters that optimized the designability of the modeled interfaces, leading to a single most designable template for each targeted SWNT.

To assess designability, we used a rapid distance-matrix–based method for searching tertiary motifs in the Protein Data Bank (PDB) that are geometrically similar to the query interface (Fig. 2A). The number of matches within a given cutoff of the query interface amounts to a metric of its designability, and sequences of the matches help

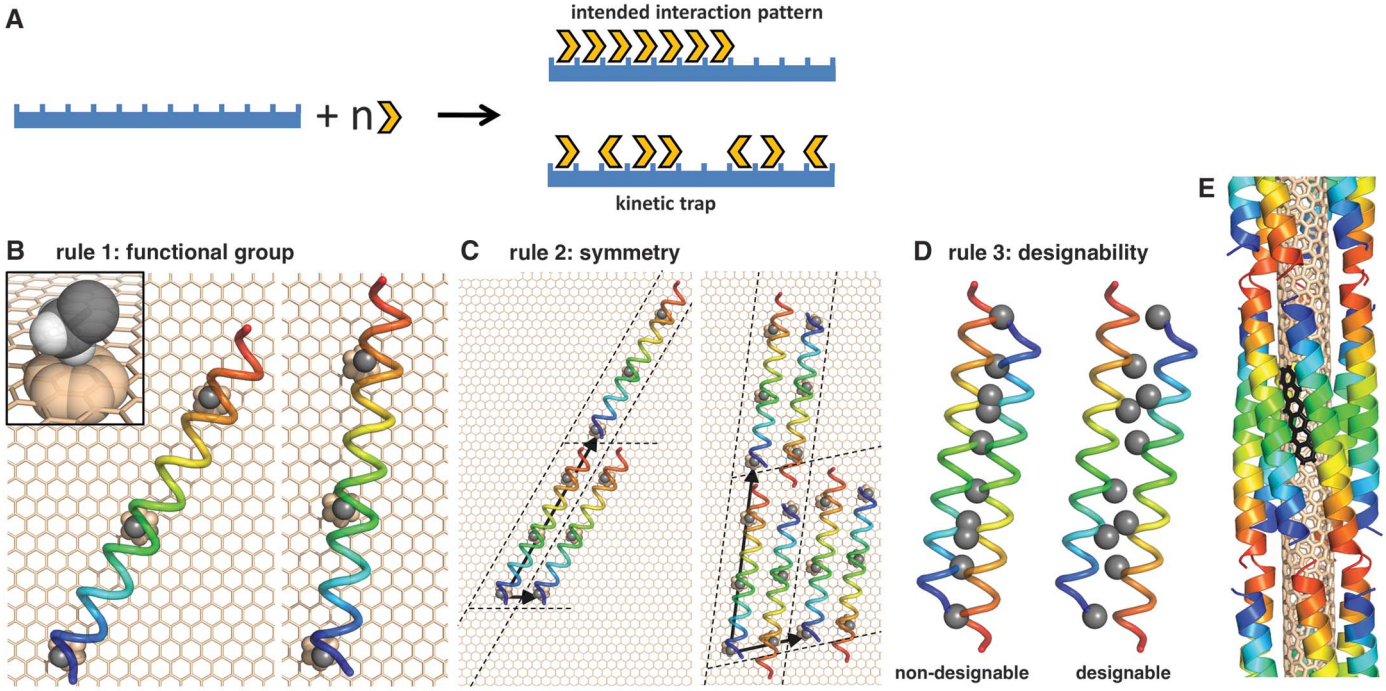

Fig. 1. (**A**) Simplified diagram of the surface assembly process (*34*). The design goal is to achieve ordered arrays of peptide subunits on the target surface (global order; top outcome in the figure) and to avoid kinetic traps of surface binding (local order; bottom outcome), which can be caused by overly strong interactions between individual subunits and the surface. (**B** to **D**) The general design framework is illustrated on the example of decorating a graphene sheet. (B) Selection rule one: C_β methyl group of Ala and the α helix are picked as the surface-contacting functional group and structural unit, respectively. (C) Selection rule two: Two possible unit cells, a single helix and an antiparallel dimer, are shown along with the corresponding Bravais-lattice vectors defining unit-cell images. (D) Assemblies containing undesignable interfaces are discarded in selection rule three (differences in designability are usually much more subtle than illustrated here for clarity). (**E**) Optimal template geometry designed to target the (3,8) SWNT surface (the array of adjacent benzenoid rings in black illustrates the helical pattern of the SWNT).

define features encoding intersubunit packing. Because this information is gathered from a wide range of structural contexts, sequences of the matches should be highly divergent at all positions except those that are particularly critical to the stability and structural specificity of the motif. The conserved positions are held constant in design, whereas the variable positions provide handles for encoding additional features, such as interaction with SWNTs; modulation of solubility, stability, and specificity; or recruitment of additional functionality.

The selection rules were implemented into an automated procedure and applied to the design of assemblies on the surfaces of SWNTs (3,8), (5,7), and (5,6), matching both size and pitch angle to each SWNT [corresponding pitch angles were –14.7°, –5.5°, and –3°, respectively (*27*)]. An antiparallel hexamer has two geometrically distinct helix-helix interfaces (Fig. 2A, inset). The designability of these interfaces in the optimal template was starkly different among the three pitch angles (Fig. 2, A and B). For example, the optimal –14.7° template identified 119 and 89 natural motifs that were within 0.6 Å C_α root mean square deviation (RMSD) of the two helix-helix interfaces making up this assembly. The corresponding values for the best –5.5° structure were 4 and 7, and none were found within this cutoff for the –3° structure. Thus, the –14.7° template would be considered a much more designable target using common, genetically encoded amino acids.

Profiles of residue propensities in aligned sequences (Fig. 2C) show that optimal designability is reached when the two unique interfaces of the hexamer are quite different: One should be a "tight" Ala coil-like interface, whereas the other should resemble an antiparallel Leu zipper-like motif. Note that this information is obtained automatically, without resorting to extensive side-chain repacking calculations on candidate backbone structures.

Having chosen the –14.7° structure as the target, we followed two paths to complete the design process. In the first, a sequence was computationally optimized to adopt this hexameric antiparallel bundle around the (3,8) SWNT, constraining the strongly conserved positions from propensity profiles (positions "d" and "e"; Fig. 2C). Standard computational design techniques were applied to select the remaining variable positions [section 1.2 in the supporting online material (*27*)] producing two sequences, HexCoil-Gly and HexCoil-Ala (Fig. 3A), differing only in the identity of the SWNT-contacting position (Gly or Ala, respectively).

In a second approach, we sought a preassembled scaffold from within the PDB that would be geometrically compatible with wrapping a SWNT and amenable to further design. Our designability analysis revealed a bundle remarkably similar to our –14.7° template (0.9 Å C_α RMSD over 156 residues) in the inner ring of helices of a domain-swapped helical protein (called DSD; PDB code 1G6U) (Fig. 3E and figs. S4 and S5) (*28*). Additionally, the strong sequence features discovered for the (3,8)-optimal template (Fig. 2C) were also present in DSD. Therefore, the central pore-lining Glu and Lys residues of DSD were converted to Gly or Ala to accommodate a SWNT, resulting in peptides designated DSD-Gly and DSD-Ala.

The hierarchic principles of our design approach suggest that a large portion of the driving force for assembly should originate from modestly

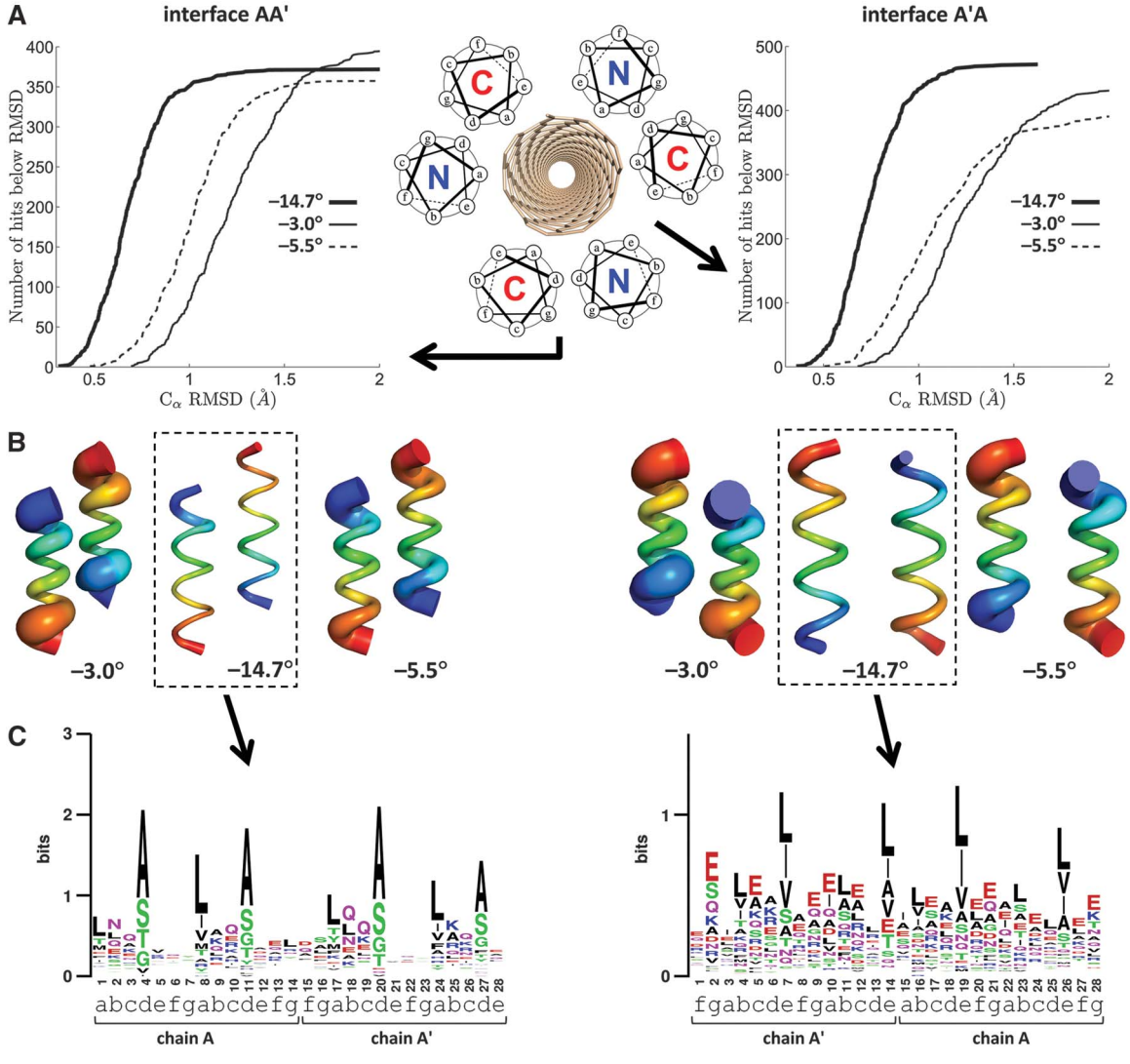

Fig. 2. Designability analysis in selection rule three. The two unique interfaces of an antiparallel homohexamer are designated here as AA′ and A′A and illustrated in the left and right columns, respectively. (**A**) Number of matches as a function of the C_α RMSD cutoff. (**B**) Structural variation in the top 100 best matches. Tube thickness is equal to the mean square deviation of the corresponding atom within the ensemble of top 100 matches. The blue-to-red coloring indicates the N-to-C terminal direction. (**C**) Sequence logo diagrams for the two interfaces of the (3,8)-targeted template derived from unique matches with C_α RMSD below 0.5 and 0.6 Å for AA′ and A′A, respectively (*35*). Heptad assignments, in the context of the full hexamer, are indicated for each sequence position.

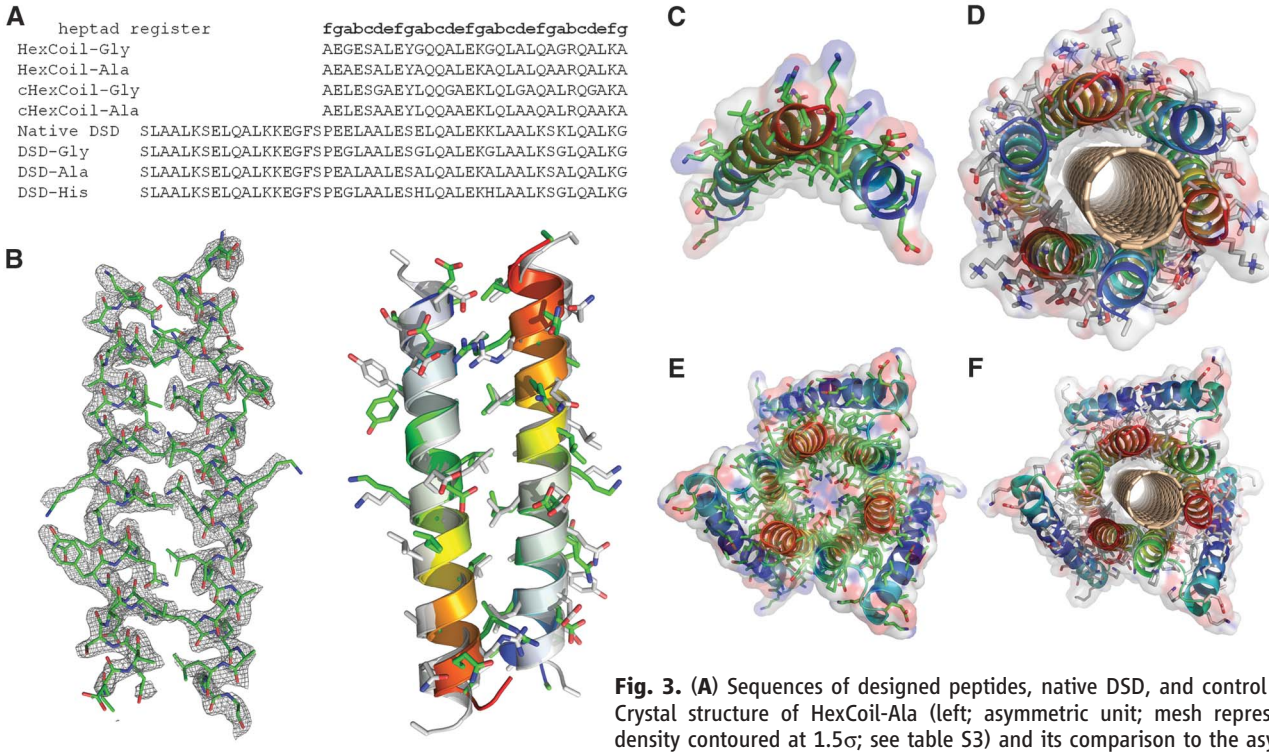

Fig. 3. (**A**) Sequences of designed peptides, native DSD, and control peptides. (**B**) Crystal structure of HexCoil-Ala (left; asymmetric unit; mesh represents electron density contoured at 1.5σ; see table S3) and its comparison to the asymmetric unit of the designed oligomer (right; gray structures correspond to the design). (**C**) The Ala-rich surface of the asymmetric unit of the HexCoil-Ala crystal structure is well poised to interact with a SWNT. (**D**) Model structure of HexCoil-Gly with a (3,8) SWNT. Blue-to-red coloring indicates the N-to-C terminal direction. (**E**) Crystal structure of native DSD. (**F**) Model of DSD-Ala with a (3,8) SWNT. Van der Waals surfaces are shown semitransparently in (C) to (F).

favorable helix-helix interactions, which should stabilize the basic antiparallel dimeric unit, even in the absence of SWNTs. Without the underlying solid substrate, the hexameric bundle structure might not be the most stable one formed, but we expected to see assembly into related bundles in which the dimeric interface was preserved. Indeed, sedimentation equilibrium analytical ultracentrifugation showed DSD-Gly and DSD-Ala to exist in a dimer-hexamer equilibrium between 10 and 100 μM peptide concentration (fig. S7). HexCoil-Ala associated into tetramers (fig. S8), whose structure was solved using diffraction data extending to 2.44 Å resolution by x-ray crystallography (Fig. 3, B and C; PDB accession code 3S0R). The asymmetric unit consists of an antiparallel dimer, whose structure is within 1.2 Å of the designed model (calculated over the backbone of 20 central residues per monomer). The designed Ala-rich face is well-situated to interact with the surface of the SWNT (Fig. 3C). Finally, far ultraviolet circular dichroism spectroscopy of these peptides confirmed their helical content in solution and when bound to SWNT (fig. S9). HexCoil-Gly, which contains multiple helix-destabilizing Gly residues, assembled only in the presence of SWNTs (fig. S9), showing surface-induced folding similar to previously designed surface-binding peptides (*29*, *30*).

The peptides formed water-soluble assemblies of SWNTs, producing aqueous suspensions that were stable for months. Two-dimensional photoluminescence (2D-PL) spectra were used to identify individual SWNT chiralities through their characteristic resonances (*31*) and to rule out aggregation of SWNTs, which induces energy transfer between different species (*32*). Designed peptides produce SWNT suspensions with 2D-PL peaks corresponding to (5,6), (5,7), and (3,8) chiralities (Fig. 4, A to C). The de novo designed peptides HexCoil-Ala and HexCoil-Gly sequester significantly more SWNTs into solution, compared with DSD variants (Fig. 4B). Interestingly, though the (3,8) species is a minor product in the mixture of SWNTs used in our experiments, HexCoil-Ala and HexCoil-Gly show a dominant peak corresponding to this chirality (Fig. 4, B and C). This is of particular importance given that the target substrate for these designs was indeed the (3,8)-species SWNT.

A number of control peptides were prepared to evaluate the structural mode of SWNT/peptide assembly. To probe the role of the small Ala and Gly residues contacting the SWNT, native DSD and an analog of DSD-Gly with two of its Gly residues changed to His were studied. Furthermore, to test the role of helix-helix packing in HexCoil-Gly and HexCoil-Ala, the apolar residues at the "d" and "e" positions that pack at the two distinct helix-packing interfaces and the SWNT-contacting "a" position were interchanged (fig. S12). The resulting peptides, cHexCoil-Gly and cHexCoil-Ala (Fig. 3A), have identical amino acid compositions, hydrophobicity, and helical faces, and nearly identical hydrophobic moments (a measure of amphiphilicity) as their parents, but differ in their abilities to engage in the detailed packing interactions intended to stabilize surface assemblies. These negative control peptides (native DSD, DSD-His, cHexCoil-Gly, or cHexCoil-Ala) were very inefficient at solubilizing SWNTs (Fig. 4A and fig. S12), verifying the intended mode of SWNT contact and suggesting that the success of our designs rests on the ability to form favorable intersubunit interactions and a higher-order assembly.

Once SWNTs are wrapped by peptides in a structurally determined way, their solvent-exposed surfaces can be further elaborated to direct the assembly, or even the synthesis, of a third biological or nonbiological layer. To illustrate this, we used the peptide/SWNT assembly to direct nucleation and assembly of gold nanoclusters in a geometrically defined manner. The DSD-Gly peptide appeared advantageous for these studies, as its peripheral helices packing against the central hexameric ring allow for the construction of independent outward-facing binding sites along a larger-radius superhelix, facilitating microscopic imaging. A single Cys was introduced near the N terminus of DSD-Gly, such that pairs of symmetry-related helices created convergent gold-binding sites (Fig. 4G and fig. S11). Addition of Au(III) under reducing conditions led to the appearance of 2- to 4-nm gold clusters visible by transmission electron microscopy (TEM) (Fig. 4 and fig. S3). Consistent with the design model, the pattern of spots is linear and systematically in-phase, and the observed interparticle spacing of 47 Å is

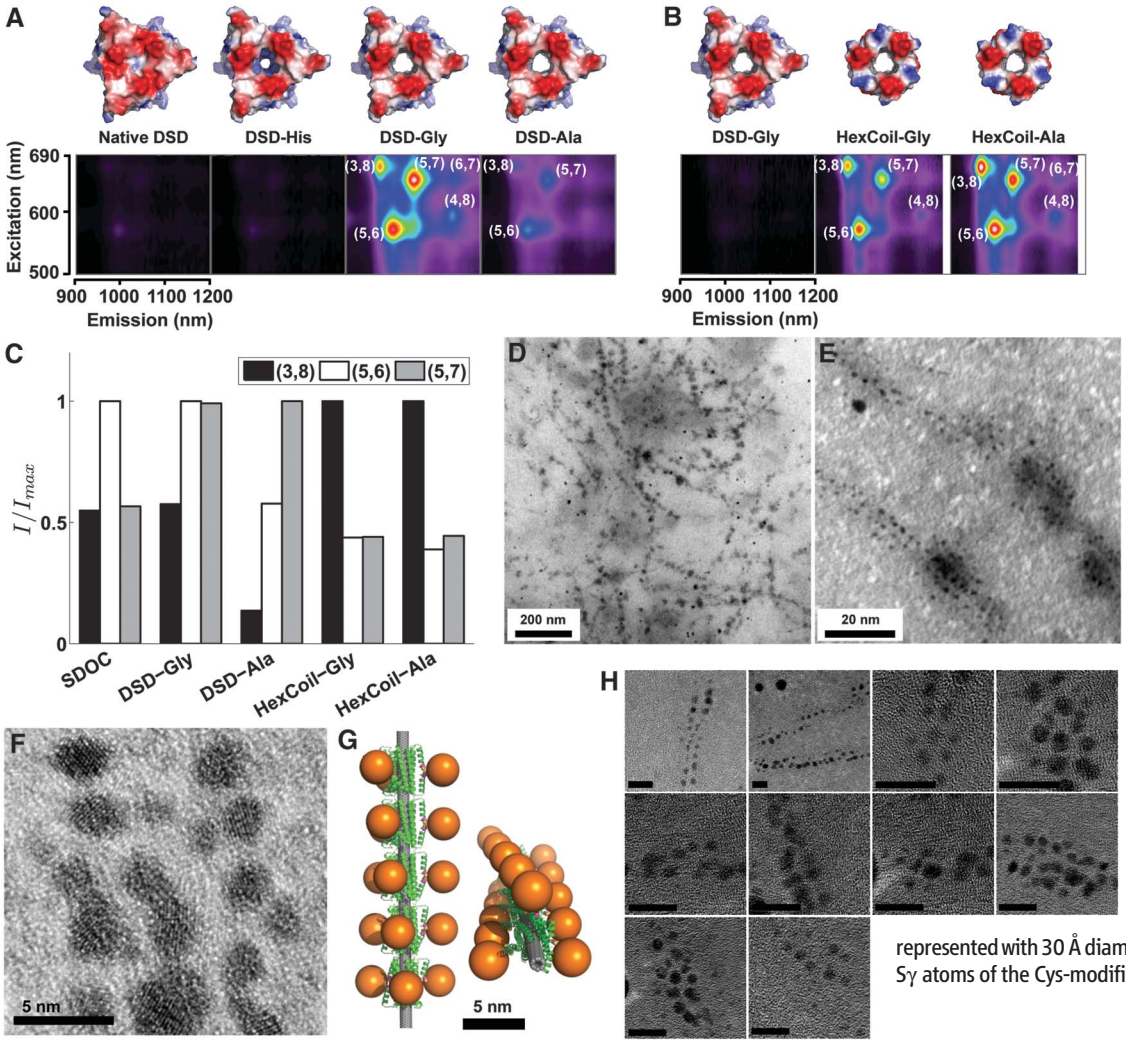

Fig. 4. 2D-PL and TEM analysis of SWNT/peptide complexes. (**A** and **B**) 2D-PL spectra of SWNT suspensions produced by (A) DSD-based peptides and (B) de novo designed peptides (pseudocolor scale is internally consistent within each section). (**C**) Fitting photoluminescence maps to a sum of 2D Lorentzians provides the total intensity weight contribution of each SWNT species, *I*. Shown are relative contributions of the three most contributing SWNT types in suspensions produced by four peptides and, for reference, the common surfactant sodium deoxy cholate (SDOC) (spectrum in fig. S14). In each case, weights are normalized to the most contributing species. (**D** to **F** and **H**) TEM images of gold nanoparticles grown on Cys-modified DSD-Gly hexamers wrapped around individual SWNTs. Panel (E) is a higher magnification version of (D), and panel (F) contains a high-resolution TEM image. Scale bars are 10 nm in (H). (**G**) Computational model of the complex. Gold particles are represented with 30 Å diameter spheres attached to the Cys Sγ atoms of the Cys-modified DSD-Gly.

in very good agreement with the model's prediction of 52 Å (figs. S1 to S3) (*27*).

The selection rules described here provide an objective reproducible method for designing surface-binding peptides. Their aim is to assure that all effects are favorable for the formation of the intended assembly. Optimal interaction geometry between protein units, physicochemical compatibility between the surface and the protein, and matching between the geometry of the assembly and the symmetry of the substrate are all encoded at the same time in a "minimally frustrated" design. In applying this strategy to SWNT surfaces, we expected that the dominant surface features would be the radius and the water-repellant nature; thus, the driving force for assembly would originate primarily from matching the size and hydrophobicity of the SWNT, as well as intersubunit packing. Indeed, this strategy worked. The intended SWNTs were bound, thereby converting the very short-scale periodicity of a SWNT surface to long-scale periodicity of a SWNT/protein assembly, as illustrated by using the complex to further direct the nucleation of an additional layer of gold nanoclusters.

SWNTs present a challenging case for organizing structurally specific assemblies because of their relatively featureless surfaces. Other molecular surfaces, such as ionic structures or boron nitride nanotubes (*33*), are likely to have much higher heterogeneity in presented atomic groups, leading to better potential for anisotropy with respect to surface interactions. In such cases, we would expect that the orientation of the coating assembly relative to the crystal lattice would be a very important discriminator and director of order. It is encouraging that even with the rather simple and smooth surfaces of SWNTs, we have already achieved a substantial level of success. The DSD versus HexCoil series of peptides illustrate different endpoints of the design process. Whereas the DSD scaffold was serendipitously discovered to approximately match the assembly geometry optimized via our approach, HexCoil-Ala and HexCoil-Gly were designed de novo to bind the (3,8) SWNT. Thus, it is encouraging that the latter peptides are more efficient and considerably more selective agents for solubilizing the desired target, showing a strong preference for solubilizing this tube type despite it being a minor component in a mixture of SWNTs. It is possible that the interfaces in the HexCoil peptides, which are unencumbered by the presence of a more involved tertiary packing, are sufficiently preorganized to allow selective binding, but not so rigid as to require a perfect fit for selective recognition to take place.

In summary, biological systems specialize in assembly, and hybrid nano-bio structures provide a powerful way to direct the assembly and tune the properties of nanomaterials. Computational protein design provides the means to do so in a highly directed and functionally relevant manner.

References and Notes

1. M. H. Cordes, A. R. Davidson, R. T. Sauer, *Curr. Opin. Struct. Biol.* **6**, 3 (1996).
2. B. I. Dahiyat, S. L. Mayo, *Science* **278**, 82 (1997).
3. B. Kuhlman *et al.*, *Science* **302**, 1364 (2003).
4. D. Ghosh, V. L. Pecoraro, *Curr. Opin. Chem. Biol.* **9**, 97 (2005).
5. J. R. Calhoun *et al.*, *Biopolymers* **80**, 264 (2005).
6. G. Ghirlanda, J. D. Lear, A. Lombardi, W. F. DeGrado, *J. Mol. Biol.* **281**, 379 (1998).
7. J. Reina *et al.*, *Nat. Struct. Biol.* **9**, 621 (2002).
8. G. Grigoryan, A. W. Reinke, A. E. Keating, *Nature* **458**, 859 (2009).
9. J. Ashworth *et al.*, *Nature* **441**, 656 (2006).

10. J. S. Kim, C. O. Pabo, *Proc. Natl. Acad. Sci. U.S.A.* **95**, 2812 (1998).
11. D. L. Masica, S. B. Schrier, E. A. Specht, J. J. Gray, *J. Am. Chem. Soc.* **132**, 12252 (2010).
12. D. Röthlisberger *et al.*, *Nature* **453**, 190 (2008).
13. L. Jiang *et al.*, *Science* **319**, 1387 (2008).
14. D. Häring, M. D. Distefano, *Bioconjug. Chem.* **12**, 385 (2001).
15. J. Kaplan, W. F. DeGrado, *Proc. Natl. Acad. Sci. U.S.A.* **101**, 11566 (2004).
16. R. Fairman, K. S. Akerfeldt, *Curr. Opin. Struct. Biol.* **15**, 453 (2005).
17. W. F. DeGrado, J. D. Lear, *J. Am. Chem. Soc.* **107**, 7684 (1985).
18. S. Segman, M. R. Lee, V. Vaiser, S. H. Gellman, H. Rapaport, *Angew. Chem. Int. Ed. Engl.* **49**, 716 (2010).
19. H. Rapaport, *Supramol. Chem.* **18**, 445 (2006).
20. M. Zheng *et al.*, *Science* **302**, 1545 (2003).
21. X. Tu, S. Manohar, A. Jagota, M. Zheng, *Nature* **460**, 250 (2009).
22. S. Wang *et al.*, *Nat. Mater.* **2**, 196 (2003).
23. G. R. Dieckmann *et al.*, *J. Am. Chem. Soc.* **125**, 1770 (2003).
24. A. Ortiz-Acevedo *et al.*, *J. Am. Chem. Soc.* **127**, 9512 (2005).
25. E. Katz, I. Willner, *ChemPhysChem* **5**, 1084 (2004).
26. G. Grigoryan, W. F. DeGrado, *J. Mol. Biol.* **405**, 1079 (2011).
27. Materials and methods are available as supporting material on *Science* Online.
28. G. Ghirlanda, J. D. Lear, N. L. Ogihara, D. Eisenberg, W. F. DeGrado, *J. Mol. Biol.* **319**, 243 (2002).
29. L. A. Capriotti, T. P. Beebe Jr., J. P. Schneider, *J. Am. Chem. Soc.* **129**, 5281 (2007).
30. P. Nygren, M. Lundqvist, K. Broo, B. H. Jonsson, *Nano Lett.* **8**, 1844 (2008).
31. M. J. O'Connell *et al.*, *Science* **297**, 593 (2002).
32. O. N. Torrens, D. E. Milkie, M. Zheng, J. M. Kikkawa, *Nano Lett.* **6**, 2864 (2006).
33. D. Golberg, Y. Bando, C. C. Tang, C. Y. Zhi, *Adv. Mater. (Deerfield Beach Fla.)* **19**, 2413 (2007).
34. A. K. Chakraborty, A. J. Golumbfskie, *Annu. Rev. Phys. Chem.* **52**, 537 (2001).
35. G. E. Crooks, G. Hon, J. M. Chandonia, S. E. Brenner, *Genome Res.* **14**, 1188 (2004).

Acknowledgments: This work was supported by the NSF Materials Research Science and Engineering Center DMR05-20020 grant (to J.M.K., M.D., and W.F.D.), NIH grant no. GM54616 (to W.F.D.), a NSF National Science and Engineering Center grant no. DMR-0425780 (to W.F.D. and M.D.), NSF grant no. DMR-0907226 (to J.M.K.), and NIH grant no. 5F32GM084631-02 (to G.G.). K.A. acknowledges support from the Roy and Diana Vagelos Program in the Molecular Life Sciences, and L.W. acknowledges funding from the NSF–Integrative Graduate Education and Research Traineeship program (grant DGE-0221664). We would like to thank K. A. McAllister for training Y.H.K. in peptide synthesis, and A. E. Keating for comments on the manuscript.

Supporting Online Material
www.sciencemag.org/cgi/content/full/332/6033/1071/DC1
Materials and Methods
Figs. S1 to S15
Tables S1 to S3
References (*26*, *36*–*61*)

8 October 2010; accepted 13 April 2011
10.1126/science.1198841

Impact of Antarctic Circumpolar Current Development on Late Paleogene Ocean Structure

Miriam E. Katz,[1]* Benjamin S. Cramer,[2] J. R. Toggweiler,[3] Gar Esmay,[4] Chengjie Liu,[5] Kenneth G. Miller,[4] Yair Rosenthal,[4,6] Bridget S. Wade,[7] James D. Wright[4]

Global cooling and the development of continental-scale Antarctic glaciation occurred in the late middle Eocene to early Oligocene (~38 to 28 million years ago), accompanied by deep-ocean reorganization attributed to gradual Antarctic Circumpolar Current (ACC) development. Our benthic foraminiferal stable isotope comparisons show that a large $\delta^{13}C$ offset developed between mid-depth (~600 meters) and deep (>1000 meters) western North Atlantic waters in the early Oligocene, indicating the development of intermediate-depth $\delta^{13}C$ and O_2 minima closely linked in the modern ocean to northward incursion of Antarctic Intermediate Water. At the same time, the ocean's coldest waters became restricted to south of the ACC, probably forming a bottom-ocean layer, as in the modern ocean. We show that the modern four-layer ocean structure (surface, intermediate, deep, and bottom waters) developed during the early Oligocene as a consequence of the ACC.

The Antarctic Circumpolar Current (ACC) is a dominant feature of present-day ocean circulation and climate, influencing the strength of meridional overturning circulation, transition depth from surface to deep ocean, gas-exchange rate between atmosphere and deep ocean, and global surface heat distribution (*1*–*4*). Wind-driven ACC upwelling is the major mode of water transport from the ocean interior to the surface, setting the density structure for the ocean interior from the Southern Ocean to high northern latitudes (*5*). The ACC also stabilizes asymmetrical meridional overturning circulation, with more-dense southern-sourced water constrained to bottom depths below the ACC (>2500 m) and overlain by northern-sourced deep waters (Fig. 1).

The ACC "engine" began to develop in the middle Eocene with shallow flow through the Drake Passage between Antarctica and South America (*6*, *7*), followed by rapid deepening of the Tasman gateway between Antarctica and Australia from the late Eocene to early Oligocene (*8*, *9*) and more-gradual deepening of the Drake Passage through the remainder of the Oligocene (*7*) (Fig. 1). It has been proposed that the modern characteristics of the ACC and its effects on deepwater circulation did not develop until the late Oligocene (*9*–*12*). However, a persistent difference in Southern Ocean benthic foraminiferal $\delta^{18}O$ values relative to those of the Pacific and North Atlantic that developed by the early Oligocene did not require a deep ACC; shallow-depth ACC circulation is sufficient for thermal isolation of the high-latitude Southern Ocean from warm surface subtropical gyres (*1*–*4*, *13*), with the potential to affect deepwater source regions. Changes in benthic and planktonic microfossil communities (*14*, *15*), North Atlantic and Pacific drift accumulation (*16*, *17*), and erosional hiatuses in the deep ocean (*18*) support the idea that gradual deep ocean changes occurred through the middle Eocene to late Oligocene.

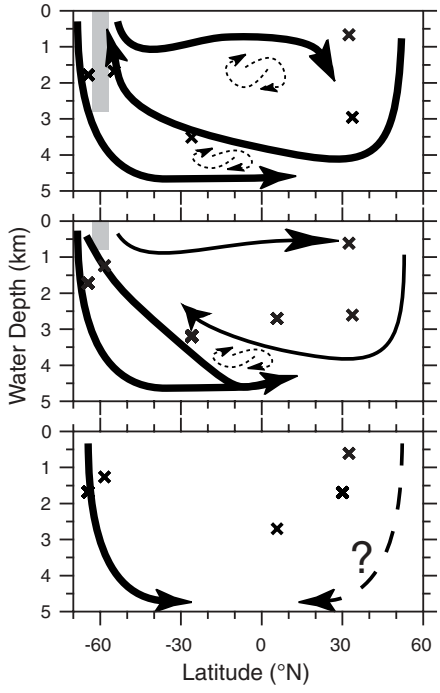

Fig. 1. Effect of progressive ACC deepening on water masses. X's indicate the paleodepths of isotopic records used to reconstruct Eocene-Oligocene water masses in this study. (**Bottom**) No ACC, analogous to pre–mid-Eocene; SCW dominates the deep ocean. (**Middle**) A multilayer ocean begins to develop with a shallow ACC, analogous to the early Oligocene. (**Top**) Multilayer modern ocean with deep ACC, analogous to the late Oligocene to the present.

[1]Department of Earth and Environmental Sciences, Rensselaer Polytechnic Institute, Troy, NY 12180, USA. [2]Theiss Research, Eugene, OR, USA. [3]Geophysical Fluid Dynamics Lab/National Oceanic and Atmospheric Administration, Princeton, NJ, USA. [4]Department of Earth and Planetary Sciences, Rutgers University, Piscataway, NJ 08854, USA. [5]ExxonMobil Exploration, Post Office Box 4778, Houston, TX 77210-4778, USA. [6]Institute of Marine and Coastal Sciences, Rutgers University, New Brunswick, NJ 08901, USA. [7]School of Earth and Environment, University of Leeds, Leeds LS2 9JT, UK.

*To whom correspondence and requests for materials should be addressed. E-mail: katzm@rpi.edu

Although Oligocene isotopic patterns and interbasinal gradients are well documented for deepwater locations (*13*), little is known about intermediate-water evolution during this time of large-scale circulation changes. Intermediate-water circulation today is a consequence of the ACC, which blocks warm surface waters entrained in subtropical gyres from reaching Antarctica; this thermally isolates the continent and the surrounding ocean, allowing large-scale ice sheets to persist. At the boundary between the eastward-flowing ACC and westward-flowing Antarctic Coastal Current, Ekman divergence leads to substantial upwelling of deep water, which is then replaced by the formation of Antarctic Bottom Water (AABW) and North Atlantic Deep Water (NADW). The AABW circulation cell is closed by AABW mixing into NADW and locally recirculated water that upwells at the ACC. The NADW circulation cell is closed by the northward flow of nutrient-rich Antarctic Intermediate Water (AAIW) that feeds the downwelling in the North Atlantic. In the warmer Oligocene ocean, North Pacific deepwater formation should have been at least as strong as in the North Atlantic (*19*) and may have mixed similarly with southern-sourced waters. NADW and AAIW strength and the NADW-AABW boundary are therefore strongly affected by the strength and depth of the ACC.

We provide direct evidence to constrain intermediate-water development associated with the evolution of the ACC in the late Eocene to early Miocene. We present benthic foraminiferal isotopes with Mg/Ca data from two North American Atlantic continental slope locations (Fig. 2) with well-preserved foraminifera and excellent age control (figs. S1 and S2 and tables S1 to S3), providing a continuous record from the late middle Eocene to early Miocene: (i) Ocean Drilling Program (ODP) Site 1053 (Blake Nose, 1629 m present depth, ~1500 to 1750 m paleodepth); and (ii) Atlantic Slope Project corehole 5 (ASP-5; 250 m present depth, 600 m paleodepth, North Carolina slope) (table S4).

Global oxygen isotope events recorded at ASP-5 (such as Oi-1, Oi-2, Oi-2a, Oi-2b, and Mi-1) and the Mg/Ca-inferred cooling associated with Oi-1 (Fig. 2) support the validity of our age model. Our Site 1053 data fill the late Eocene hiatus at ASP-5, providing context for the inter- and intrabasinal $\delta^{13}C$ changes observed in the Oligocene (Fig. 2). There is no clear distinction among $\delta^{13}C$ values at ASP-5, Site 1053, and the deep North Atlantic during the Eocene. ASP-5 $\delta^{18}O$ values are lower than those in the deeper North Atlantic, including Site 1053, reflecting warmer temperatures at shallower paleodepths.

The abrupt growth of continent-scale Antarctic ice sheets in the earliest Oligocene is reflected in the global >1 per mil (‰) increase in benthic foraminiferal $\delta^{18}O$ (called Oi-1) (*20*, *21*). At ASP-5, a 1.1‰ increase culminates in Oi-1, whereas Mg/Ca indicates a ~2.5°C cooling, suggesting that about half of the $\delta^{18}O$ increase was due to ice-sheet growth (Fig. 2). This is consistent with records from two shallow-water locations (*22*, *23*) free of carbonate saturation issues that may bias deepwater Mg/Ca temperature estimates. The ASP-5 ~2.5°C cooling is the first from a mid-depth location; it is generally assumed that the deep-ocean $\delta^{18}O$ increase also partly reflects a cooling, but the large change in deep-ocean carbonate saturation has prevented a direct estimate of the magnitude (*24*).

Coincident with Oi-1, a >0.5‰ difference developed between benthic foraminiferal $\delta^{18}O$ values from the Southern Ocean and South Atlantic relative to values from the North Atlantic and Pacific (Fig. 3), in contrast to the lack of statistically significant interbasinal offsets throughout the Paleocene to middle Eocene (*13*). This early Oligocene isotopic differentiation indicates a temperature difference similar to the ~2°C difference between modern northern- and southern-sourced deep water; therefore, analogous to modern ocean structure, early Oligocene isotopic differentiation reflects proto-ACC intensification through the Drake Passage (*13*) (Fig. 1).

Unlike the significant $\delta^{18}O$ offsets, deepwater interbasinal $\delta^{13}C$ gradients remained low in the Oligocene, consistent with Eocene gradients (*13*, *25*, *26*) (Fig. 3). In contrast, a ~1.2‰ $\delta^{13}C$ offset developed between ASP-5 and deepwater sites in all basins by ~30 to 31 million years ago (Ma) and persisted across Mi-1 into the early Miocene (Fig. 3). This $\delta^{13}C$ offset indicates greater oxidation of organic matter at ASP-5, at a time when a stable Gulf Stream (*27*) was unlikely to account for the $\delta^{13}C$ decrease at ASP-5. In the modern North Atlantic, the vertical $\delta^{13}C$ gradient between deep and intermediate waters is <0.5‰. In contrast, the larger Oligocene vertical $\delta^{13}C$ gradient is analogous to the modern Pacific gradient (fig. S3).

In the modern ocean, AAIW that forms along the northern edge of the ACC (Fig. 1) keeps the thermocline ventilated to ~700 to 1000 m in the Atlantic and Pacific and sets the depth of the low-O_2 layer (relative to surrounding waters), although this depth can vary along the continental slope (*28*) (fig. S3). This low-O_2 layer typically lies just below the salinity minimum, which itself marks the limit of AAIW ventilation (*28*). The oxidation of organic matter in the surface ocean and low ventilation rates in the deep ocean lead to a rapid reduction in oxygenation with depth through the upper few hundred meters of the water column. The depth of the modern low-O_2 layer is set primarily by a decrease in ventilation at the lower boundary of AAIW. Therefore, ventilation by AAIW leads to a relatively deep low-O_2 and low-$\delta^{13}C$ layer (~700 to 1000 m).

In the absence of a mode water similar to modern AAIW, high O_2 consumption rates near the surface would result in a much shallower low-O_2 and low-$\delta^{13}C$ layer. This appears to have been the case during the Eocene, when $\delta^{13}C$ values at 600 m (ASP-5) were similar to those in the deep ocean as a result of rapid oxidation of organic matter shallower than ASP-5. With expansion to northern mid-latitudes (ASP-5),

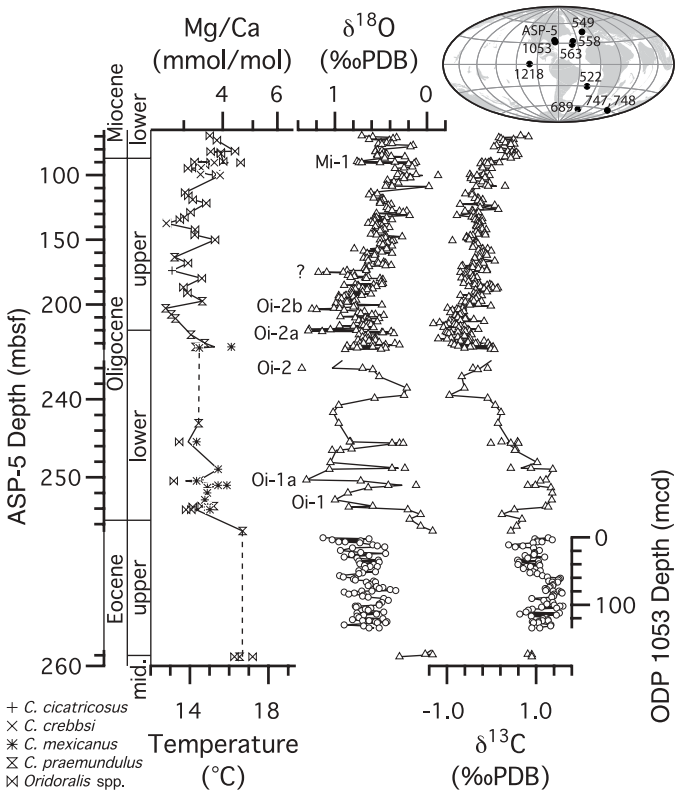

Fig. 2. Location map inset into analyses of benthic foraminiferal (*Cibicidoides* spp.) $\delta^{18}O$ and $\delta^{13}C$ values from ASP-5 (triangles) and Site 1053 (circles) and Mg/Ca values from ASP-5 (*Cibicidoides* and *Oridorsalis* species, symbol key provided). The traces pass through the mean value for samples with multiple analyses. The ASP-5 depth axis is split according to age model so that the equivalent age scale is approximately linear; the Site 1053 record is inserted within an ASP-5 hiatus. The temperature (T) axis is calculated using Mg/Ca = 1.528 exp(0.09 T) (*36*) and is scaled to match the range of the $\delta^{18}O$ axis, using $T = 16.1 - 4.64(\delta^{18}O_{bf} - \delta^{18}O_{sw}) + 0.09(\delta^{18}O_{bf} - \delta^{18}O_{sw})^2$ [quadratic approximation by (*37*) to relationship found by (*38*)] (bf, benthic foraminifera; sw, seawater). No correction was applied for genus/species offsets in the Mg/Ca record. PDB, Pee Dee belemnite values.

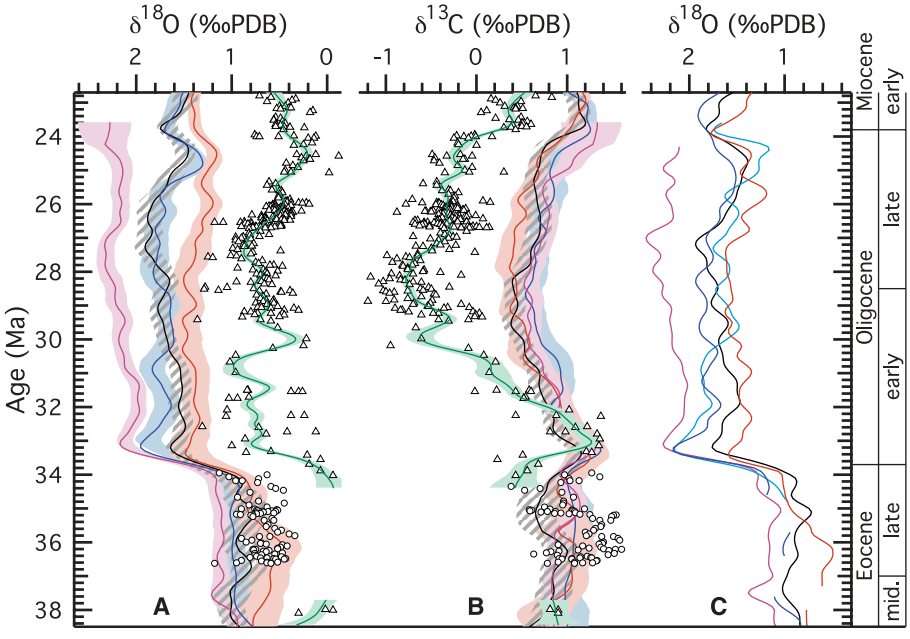

Fig. 3. Comparison of stable isotopic data with trend lines from ASP-5 and ODP Site 1053 (green) with deep-ocean stable isotope trends from (*13*) (A, $\delta^{18}O$; B, $\delta^{13}C$). Locations are indicated as follows: Pacific (gray slashes), North/Equatorial Atlantic (red), South Atlantic/sub-Antarctic (blue), and high-latitude Southern (purple). Data trends were calculated using a LOESS smoothing with 0.8-million-year window. A color band indicates the 95% confidence level for trend estimates. The $\delta^{13}C$ offset between ASP-5 and the deep basins between Oi-1 and the hiatus (~33.5 to 34 Ma) indicates that using $\delta^{13}C$ stratigraphy in this short interval would improve our age model. We do not do this because the $\delta^{13}C$ records are the main focus of our paper and therefore cannot be used in the age model. C: Sub-Antarctic $\delta^{18}O$ values shift away from Southern Ocean values toward North Atlantic values beginning ~31 to 30 Ma. Locations are indicated as follows: Southern Ocean Site 689 (purple); sub-Antarctic Site 748 (>~25 Ma) and Site 747 (<~25 Ma) (dark blue); South Atlantic Site 522 (light blue); Pacific Site 1218 (black); and North Atlantic Site 549 (>~25 Ma), Site 558 (<~34 Ma), and Site 563 (<~33 Ma) (red). Data are compiled in (*13*). See Fig. 2 for locations.

better-oxygenated intermediate waters oxidized more organic matter, released ^{12}C, and drove benthic foraminiferal $\delta^{13}C$ to lower values, similar to modern AAIW ventilation of the Pacific. However, the $\delta^{13}C$ offset between ASP-5 and the deep North Atlantic was larger in the Oligocene than in the modern Pacific, and therefore the offset may reflect higher $\delta^{13}C$ in the Oligocene deep ocean relative to intermediate waters. This difference may be attributed to deep Atlantic waters that were younger in the Oligocene than deep Pacific waters are today.

Strengthening and deepening of the ACC in the early Oligocene would have enhanced the formation of southern-sourced intermediate water (via downwelling at the northern edge of the ACC); this is recorded in the decreasing $\delta^{13}C$ values at ASP-5 at ~31 to 30 Ma. In addition, changes in the ACC would have restricted the coldest water to below the ACC and allowed the incursion of northern-component water (NCW, analogous to NADW) progressively farther south in the Atlantic (Fig. 1), resulting in the shift of $\delta^{18}O$ values at South Atlantic Site 522 away from colder Southern Ocean values and toward the warmer North Atlantic values (Fig. 3). The gradual confinement of southern-component water (SCW) by the ACC occurred over several million years; $\delta^{18}O$ values at sub-Antarctic Sites 747 and 748 remained closer to those in the high-latitude Southern Ocean than in the Pacific for ~3 million years after the $\delta^{18}O$ decrease at lower-latitude Site 522 and $\delta^{13}C$ decrease at ASP-5 (Fig. 3). Together, these early isotopic changes indicate that the modern four-layer ocean structure (surface, intermediate, deep, and bottom waters) first developed during the early Oligocene (Figs. 1 and 3).

At the same time, early Oligocene subsidence of the Greenland-Scotland Ridge (GSR) facilitated NCW production in the Norwegian-Greenland Sea (*29*, *30*). GSR subsidence continued to its greatest depth (240 to 320 m) at ~31 Ma (*29*). Decreasing εNd values support increased NCW flow at this time (*31*–*33*). ASP-5 isotope records indicate an early Oligocene transition in the mid-depth western North Atlantic, before a fully opened Drake Passage and deep ACC, which is consistent with models that predict that a shallow-depth ACC would affect thermocline waters throughout the Atlantic (*2*). This predates initial uplift of the Isthmus of Panama by at least 15 million years (*34*, *35*), precluding any impact on changing intermediate waters in the Oligocene North Atlantic. We speculate that southern-sourced intermediate water, enhanced by the developing ACC, facilitated NCW production as the GSR subsided and the Drake Passage and Tasman Rise continued to open (Figs. 1 and 3).

The evolution of deep and intermediate water circulation and the ACC beginning in the latter part of the Eocene corresponds to the "doubthouse climate" interval: the transition from early Paleogene greenhouse climates to the icehouse climates that have dominated the rest of the Cenozoic. Our Atlantic slope data and inter- and intrabasinal isotopic comparisons indicate that ocean thermal structure and circulation were affected at an early stage of opening of the Drake Passage. Our results indicate that changes in tectonic gateways affected late middle Eocene to early Miocene ocean circulation, which in turn affected global climate.

References and Notes

1. M. D. Cox, *J. Phys. Oceanogr.* **19**, 1730 (1989).
2. J. R. Toggweiler, H. Bjornsson, *J. Quat. Sci.* **15**, 319 (2000).
3. W. P. Sijp, M. H. England, *J. Clim.* **18**, 1957 (2005).
4. W. P. Sijp, M. H. England, *J. Phys. Oceanogr.* **34**, 1254 (2004).
5. J. R. Toggweiler, B. Samuels, *J. Phys. Oceanogr.* **28**, 1832 (1998).
6. H. D. Scher, E. E. Martin, *Science* **312**, 428 (2006).
7. R. Livermore, C.-D. Hillenbrand, M. Meredith, G. Eagles, *Geochem. Geophys. Geosyst.* **8**, Q01005 (2007).
8. N. Exon, J. Kennett, M. Malone, in *Proceedings of the Ocean Drilling Program, Scientific Results*, N. Exon, J. Kennett, M. Malone, Eds. (ODP, College Station TX, 2004), vol. 189, pp. 1–37.
9. C. E. Stickley *et al.*, *Paleoceanography* **19**, PA4027 (2004).
10. P. F. Barker, E. Thomas, *Earth Sci. Rev.* **66**, 143 (2004).
11. H. A. Pfuhl, I. N. McCave, *Earth Planet. Sci. Lett.* **235**, 715 (2005).
12. M. Lyle, S. Gibbs, T. C. Moore, D. K. Rea, *Geology* **35**, 691 (2007).
13. B. S. Cramer, J. R. Toggweiler, J. D. Wright, M. E. Katz, K. G. Miller, *Paleoceanography* **24**, PA4216 (2009).
14. M. E. Katz, R. C. Tjalsma, K. G. Miller, *Micropaleontology* **49** (suppl. 2), 1 (2003).
15. M.-P. Aubry, D. Bord, in *The Late Eocene Earth—Hothouse, Icehouse, and Impacts*, C. Koeberl, A. Montanari, Eds. (Geological Society of America, Denver, CO, 2009), Geological Society of America Special Paper 452, pp. 279–301.
16. C. N. Wold, *Paleoceanography* **9**, 917 (1994).
17. D. K. Rea, I. A. Basov, L. A. Krissek, L. S. Party, in *Proceedings of the Ocean Drilling Program, Scientific Results*, D. Rea, L. Basov, D. Scholl, J. Allan, Eds. (ODP, College Station, TX, 1995), vol. 145, pp. 577–596.
18. J. D. Wright, K. G. Miller, in *The Antarctic Paleoenvironment: A Perspective on Global Change*, J. P. Kennett, D. A. Warnke, Eds. (American Geophysical Union, Washington, DC, 1993), vol. 56, pp. 1–25.
19. A. M. de Boer, J. R. Toggweiler, D. M. Sigman, *J. Phys. Oceanogr.* **38**, 435 (2008).
20. K. G. Miller *et al.*, *Science* **310**, 1293 (2005).
21. K. G. Miller, J. D. Wright, R. G. Fairbanks, *J. Geophys. Res.* **96**, 6829 (1991).
22. M. E. Katz *et al.*, *Nat. Geosci.* **1**, 329 (2008).
23. C. H. Lear, T. R. Bailey, P. N. Pearson, H. K. Coxall, Y. Rosenthal, *Geology* **36**, 251 (2008).
24. C. Lear, R. Rosenthal, *Geology* **34**, 985 (2006).
25. K. G. Miller, R. G. Fairbanks, in *The Carbon Cycle and Atmospheric CO_2: Natural Variations Archean to Present*, E. T. Sundquist, W. S. Broecker, Eds. (American Geophysical Union, Washington DC, 1985), pp. 469–486.
26. L. Diester-Haass, J. Zachos, in *From Greenhouse to Icehouse; the Marine Eocene-Oligocene Transition*, D. R. Prothero, L. C. Ivany, E. A. Nesbitt, Eds. (Columbia Univ. Press, New York, 2003), pp. 397–416.
27. P. R. Pinet, P. Popenoe, *Geol. Soc. Am. Bull.* **96**, 618 (1985).
28. L. D. Talley, in *The South Atlantic: Present and Past Circulation*, G. Wefer, W. H. Berger, G. Siedler, D. J. Webb, Eds. (Springer-Verlag, Berlin, 1996), pp. 219–238.
29. M. Abelson, A. Agnon, A. Almogi-Labin, *Earth Planet. Sci. Lett.* **265**, 33 (2008).

30. J. D. Wright, K. G. Miller, *Paleoceanography* **11**, 157 (1996).
31. H. D. Scher, E. E. Martin, *Paleoceanography* **23**, PA1205 (2008).
32. H. D. Scher, E. E. Martin, *Earth Planet. Sci. Lett.* **228**, 391 (2004).
33. R. K. Via, D. J. Thomas, *Geology* **34**, 441 (2006).
34. G. H. Haug, R. Tiedemann, *Nature* **393**, 673 (1998).
35. E. E. Martin, B. A. Haley, *Geochim. Cosmochim. Acta* **64**, 835 (2000).
36. M. Raitzsch, H. Kuhnert, J. Groeneveld, T. Bickert, *Geochem. Geophys. Geosyst.* **9**, Q05010 (2008).
37. B. E. Bemis, H. J. Spero, J. Bijma, D. W. Lea, *Paleoceanography* **13**, 150 (1998).
38. S.-T. Kim, J. R. O'Neil, *Geochim. Cosmochim. Acta* **61**, 3461 (1997).

Acknowledgments: This research was supported by NSF grants OCE 06-23256 (M.E.K., K.G.M., B.S.W., and J.D.W.), OCE 09-28607 (B.S.C. and M.E.K.), EAR03-07112 (K.G.M.), and EAR05-06720 (K.G.M.). This research used samples provided by the ODP, which is sponsored by NSF and participating countries under management of the Joint Oceanographic Institutions, Inc. The authors declare that they have no competing financial interests.

Supporting Online Material

www.sciencemag.org/cgi/content/full/332/6033/1076/DC1
Methods
SOM Text
Figs. S1 to S3
Tables S1 to S4
References

23 December 2010; accepted 13 April 2011
10.1126/science.1202122

Early Warnings of Regime Shifts: A Whole-Ecosystem Experiment

S. R. Carpenter,[1]* J. J. Cole,[2] M. L. Pace,[3] R. Batt,[1] W. A. Brock,[4] T. Cline,[1] J. Coloso,[3] J. R. Hodgson,[5] J. F. Kitchell,[1] D. A. Seekell,[3] L. Smith,[1] B. Weidel[1]

Catastrophic ecological regime shifts may be announced in advance by statistical early warning signals such as slowing return rates from perturbation and rising variance. The theoretical background for these indicators is rich, but real-world tests are rare, especially for whole ecosystems. We tested the hypothesis that these statistics would be early warning signals for an experimentally induced regime shift in an aquatic food web. We gradually added top predators to a lake over 3 years to destabilize its food web. An adjacent lake was monitored simultaneously as a reference ecosystem. Warning signals of a regime shift were evident in the manipulated lake during reorganization of the food web more than a year before the food web transition was complete, corroborating theory for leading indicators of ecological regime shifts.

Massive ecosystem changes affect water supplies, fisheries, productivity of rangelands and forests, and other ecosystem services (*1*, *2*). Nonlinear regime shifts often come as surprises. However, recent research has revealed statistical signals that precede some nonlinear transitions, such as rising autocorrelation, steep increases in variance, and extreme changes in skewness and shift in variance spectra toward low frequencies (*3*–*7*). If the transition is approached slowly and the right variables are sampled frequently, warnings may be evident well before the regime shift is complete. Empirical evidence for early warnings of environmental regime shifts comes from a time series of major changes in paleoclimate (*8*), spatial pattern of dryland vegetation during desertification (*9*), variability of exploited fisheries (*10*, *11*), and laboratory studies (*12*). Here, we present a test of early warning indicators from a large-scale multiyear field experiment using a manipulated and a reference ecosystem.

Gradual addition or removal of top predators destabilizes food webs, and extreme manipulations of predators cause trophic cascades, a type of regime shift that alters food web structure and ecosystem processes such as primary production, ecosystem respiration, and nutrient cycling (*13*, *14*). Predator-driven transitions in lakes involve nonlinear dynamics of fish, zooplankton, and phytoplankton populations (*15*). Over 3 years, we gradually added a top predator, largemouth bass (*Micropterus salmoides*), to a lake dominated by planktivorous fishes to destabilize the food web and induce a trophic cascade leading to dominance of the food web by piscivores (*16*). A nearby lake, dominated by adult largemouth bass, was not manipulated and served as a reference ecosystem. The reference ecosystem allows us to evaluate the possibility that responses were caused by external drivers rather than the manipulation (*15*). Planktivorous fishes, zooplankton, and phytoplankton were monitored daily in both lakes for 3 years of summer stratification (2008 to 2010) (*16*).

Predicted responses of the food web follow from previous experiments in these lakes (*15*) and an ecosystem model calibrated for the manipulated lake (*17*). Before manipulation, the manipulated ecosystem was dominated by a variety of small fishes [hereafter planktivores (*16*)], and largemouth bass were few. We expected that the addition of largemouth bass would trigger recruitment of juvenile bass that were planktivorous initially but became omnivorous, adding benthos and fish to their diets, as they grew. Piscivory by largemouth bass would cause planktivorous fishes to seek refuge from predation by occupying littoral refugia and shoaling (aggregating). Eventually piscivory would drive planktivorous fishes to low densities. As planktivory declined in the open water, larger-bodied zooplankton (including migratory *Daphnia pulex*) would increase in relative abundance. Increased grazing would lead to cyclic oscillations of zooplankton and phytoplankton biomass. Thus, the food web transition would exhibit a sequence of nonlinear changes resulting from shoaling and diel movements of consumers, species replacement, and predator-prey cycles as the manipulated ecosystem became more similar to the reference ecosystem. We hypothesized that dynamics during this transitional period would generate early warning signals of a regime shift toward a piscivore-dominated food web.

Transitional dynamics of the food web were consistent with our expectations (Fig. 1). In the manipulated lake, 39 adult largemouth bass were present at the beginning of the experiment. We added 12 largemouth bass on day 193 of 2008, and 15 largemouth bass on each of days 169 and 203 of 2009. Enhancement of adult largemouth bass triggered a recruitment event in 2009, leading to 1281 young-of-year largemouth bass (95% confidence interval of 1088 to 1560) by day 240 of 2009. Numbers of this cohort (1+ in Fig. 1C) declined through 2010, whereas surviving individuals grew in body mass and became piscivorous. Planktivore numbers in the manipulated lake declined through the study as piscivory increased and were similar to those of the reference lake by about day 230 of 2010 (Fig. 1F).

The spatial pattern of planktivores was occasionally patchy in 2008 and 2009, indicated by high values in the discrete Fourier transform (DFT) of spatial data (*16*, *18*) (Fig. 2). Patchy distributions were more frequent and of longer duration in 2010. Patchy distributions indicate shoaling behavior, a likely response to predation risk.

Zooplankton biomass of the manipulated lake declined during the summers of 2008 and 2009 and became strongly oscillatory in 2010 (Fig. 1). Through 2009 and 2010, dominance of the zooplankton shifted toward larger-bodied cladocerans, including *D. pulex*, in the manipulated lake (fig. S1), consistent with previous whole-lake experiments in which body size but not biomass of zooplankton responded to fish manipulations (*15*, *19*). Phytoplankton biomass as measured by chlorophyll a of the manipulated lake displayed strong oscillations in 2009 and the first half of 2010. By day 230 of 2010, manipulated and reference lakes were similar in planktivore numbers, zooplankton biomass, and chlorophyll.

Modeling predicts that early warning indicators would appear after the largemouth bass addition in 2008 and continue until stabilization of a new food web dominated by largemouth bass

[1]Center for Limnology, University of Wisconsin, Madison, WI 53706, USA. [2]Cary Institute of Ecosystem Studies, Millbrook, NY 12545, USA. [3]Department of Environmental Sciences, University of Virginia, Charlottesville, VA 22904, USA. [4]Department of Economics, University of Wisconsin, Madison, WI 53706, USA. [5]Department of Biology, St. Norbert College, De Pere, WI 54115, USA.

*To whom correspondence should be addressed. E-mail: srcarpen@wisc.edu

(*17*). It is not necessary to observe complete convergence of the food webs, because in order to be useful the early warnings must be seen before the food webs converge. Specifically, after 2008 we expected periods of increased variability, return rates near zero, lag-1 autocorrelations near one, skewness far from zero, and shifts in variance spectra toward low frequencies if the theory of early warning indicators was supported. We focused on chlorophyll, which responds strongly to food web fluctuations and can be measured at high frequency and precision (*20*, *21*). Chlorophyll variability was somewhat lower in the manipulated lake than in the reference lake during the 3 years before manipulation (table S2).

High-frequency measurements of chlorophyll (every 5 min) had similar spectra in both lakes in 2008 (Fig. 3). In 2009 and 2010, however, spectral power shifted to low frequencies in the manipulated lake relative to the reference lake (yellow and tan colors in graphs for 2009 and 2010, Fig. 3). This shift toward lower-frequency variance is characteristic of regime shifts (*3*), including dynamics of chlorophyll in model simulations of trophic cascades in this manipulated lake (*17*). Early warning indicators calculated for daily chlorophyll concentrations were consistent with theoretical expectations (Fig. 4). In 2009 and 2010, there are times when the variance was much higher in the manipulated lake than in the reference lake, and the return time in the manipulated lake was close to zero. Variance was high in the manipulated lake for most of 2009 and early 2010. The coefficient of variation (standard deviation/mean) was also elevated in the manipulated lake through 2009 and early 2010 (fig. S2). The return rate was close to zero in 2009 (days 185 to 210) and 2010 (until day 206) (Fig. 4). Autocorrelations near one, which are also associated with near-zero return rates, occurred in the manipulated lake from about days 180 to 215 of 2009 and from about days 160 to 210 of 2010 (fig. S2). Skewness, an indicator of asymmetry associated with alternate states (*6*), reached high values in 2009 and cycled from low to high values in 2010 (Fig. 4). These changes in skewness are consistent with shifts between alternate states (*6*). The spectral ratio (*16*), a measure of the strength of the shift in variance from high to low frequencies (*22*), was elevated in the manipulated lake in late 2008, much of 2009, and the first half of 2010.

Regime shifts are characterized by nonlinear dynamics. A conservative test for nonlinearity [bootstrap Brock-Dechert-Scheinkman test on generalized autoregressive conditional heteroskedasticity residuals for daily chlorophyll data (*16*)] rejects the hypothesis of linearity for the manipulated lake and does not reject the hypothesis of linearity for the reference lake (*23*). This result is consistent with nonlinear dynamics because of a regime shift in the manipulated lake but not the reference lake. Diverse nonlinear models have been proposed for dynamics of plankton (*24*–*28*). The precise mechanism of the nonlinear transitions is not known for our experiment; it could be one of the processes proposed in the literature or something else. These early warning signals are expected to occur for a wide class of nonlinear transitions (*7*). Even though the mechanism is not known, manipulation of an apex predator triggered a nonlinear food web transition that was signaled by early warning indicators more than a year before the food web transition was complete. Thus, the early warning indicators appear to be useful even in cases where the form of the potential regime shift is not known.

This experiment created ideal conditions for detection of early warning indicators under field conditions in a whole ecosystem. The regime shift was driven at a slow rate compared with the frequency of sampling and the response rate of the plankton. A reference system was used to assess the indicators in an unmanipulated system subject to the same weather and watershed influences. Both the manipulated and reference ecosystems were sampled at high frequency by using identical methods, leading to relatively large data sets for evaluation of the indicators. In other situations, it may be difficult to identify meaningful changes in the indicators. Modeling studies have pointed out a number of limitations of these early warning indicators (*7*, *18*, *22*, *29*, *30*). False early warnings can be generated by aggregation of linear processes or by exogenous shocks. Errors of this kind are not likely in our experiment because the regime shift was induced experimentally, multiple indicators are consistent in the manipulated lake, the reference lake shows no indications of exogenous shocks (e.g., regional weather events), and a conservative statistical test is consistent with nonlinear dynamics in the manipulated but not the reference lake. Early warnings, however, may fail in cases where

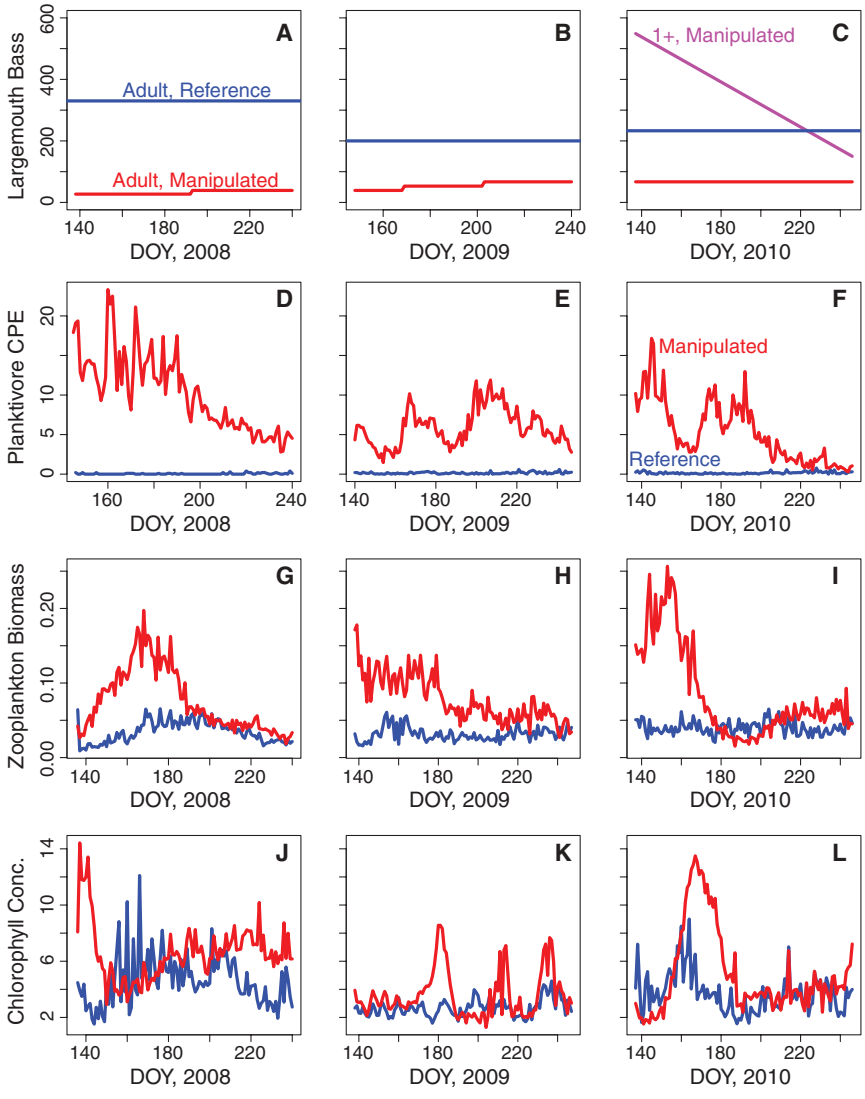

Fig. 1. Time series of the food webs in manipulated (red) and reference (blue) lakes in 2008 to 2010. DOY indicates day of the year. (**A** to **C**) Largemouth bass adult population in each lake. For the manipulated lake in 2010, numbers of year 1+ bass (recruited in 2009) are shown in magenta. (**D** to **F**) Planktivorous fish density (animals caught per trap per hour) estimated as catch per effort (CPE) in minnow traps deployed in the littoral zone. (**G** to **I**) Zooplankton biomass (g m^{-2}). (**J** to **L**) Chlorophyll concentration (mg m^{-3}) in the mixed layer.

the system is forced too fast across a critical threshold, where observation errors are large, or where signals are dampened by interactions among multiple nonlinear processes. Our experiment was designed to minimize these limitations and thereby maximize the possibility of detecting early warnings.

Theory indicates that early warning signals should be discernible before regime shifts in aquatic or terrestrial ecosystems as well as other

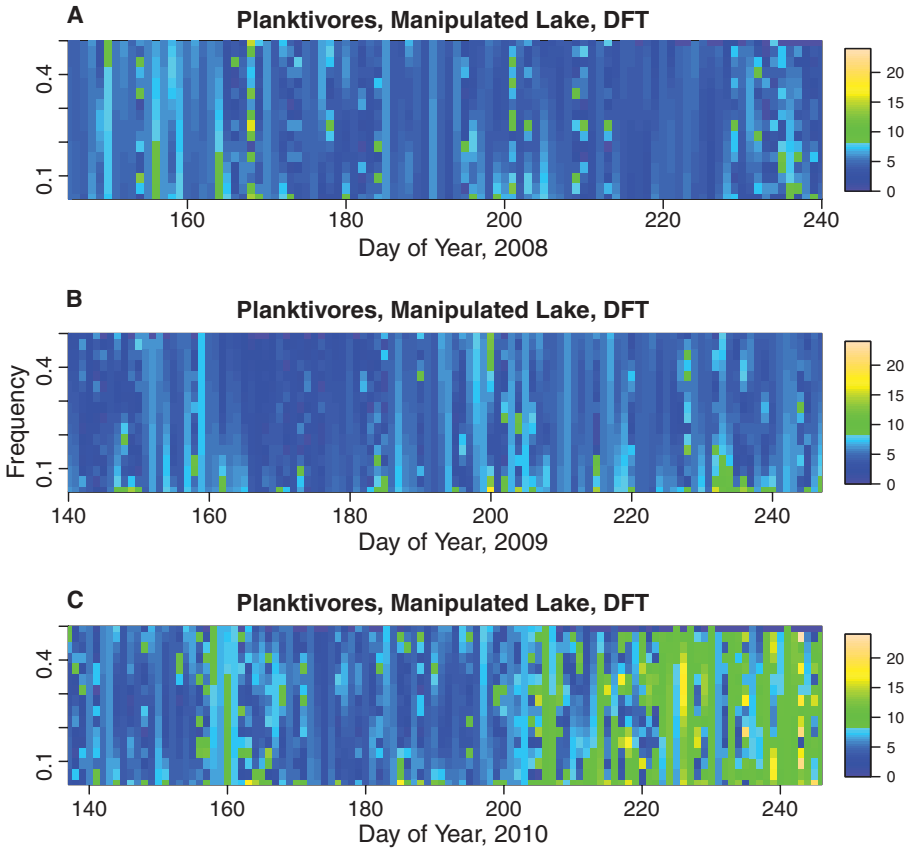

Fig. 2. DFT of the spatial sequence of minnow (planktivorous fish) trap catches around the perimeter of the manipulated lake on each day of sampling in 2008 (**A**), 2009 (**B**), and 2010 (**C**). Spatial frequency (per trap) is plotted versus day of the year, with DFT ordinate [a measure of variance (*16*)] shown by colors (see legend). High ordinates indicate clustering of planktivores at a particular spatial frequency (*18*). Spatial frequency is inversely related to spatial extent; for example, a frequency of 0.1 corresponds to 1 in 10 traps or a total of 3 traps in our array of 30 traps. In the reference lake, catch numbers were too small to estimate the DFT.

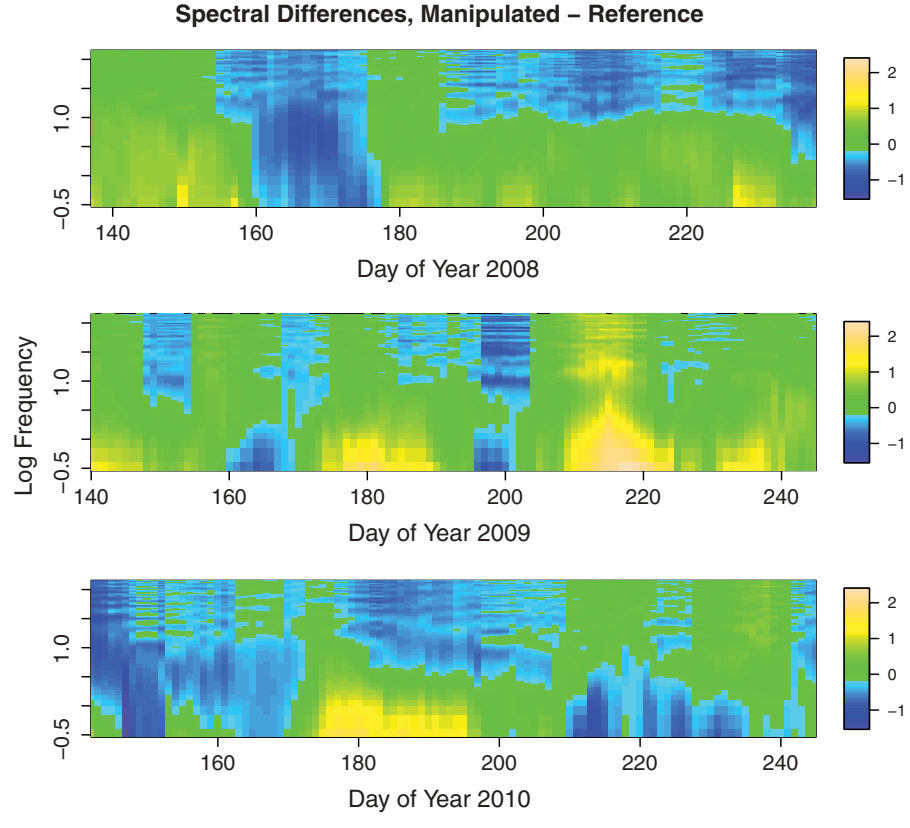

Fig. 3. Difference between manipulated and reference lakes in spectra for high-frequency chlorophyll observations in 2008 (**top**), 2009 (**middle**), and 2010 (**bottom**). On each date in each lake, spectra were computed for the preceding 7 days by using observations recorded every 5 min by floating sensors (*16*). Frequency (per day, $\log_{10}$ transformed) is plotted versus day of the year, with differences in spectra ($\log_{10}$ transformed) indicated by colors (see legend). Green colors indicate little difference in spectral power between lakes, blue colors indicate that spectral power of the manipulated lake was lower than that of the reference lake, and yellow or tan colors indicate that the spectral power of the manipulated lake was greater than that of the reference lake. High spectral power at low frequencies is associated with nonlinear transitions (*3*, *17*, *22*).

types of nonlinear systems, even in cases where the driver is not known (*7*). Spatial statistics may prove especially useful for terrestrial or benthic habitats (*7*, *9*, *17*). Expanding availability of automated sensors and remote sensing increases opportunities for measuring early warning signals. Comparison with a reference ecosystem was important for discerning changes in our experiment. Networks for long-term ecological observation, such as the U.S. Long-Term Ecological Research network (www.lternet.edu), increase the possibility of detecting early warnings through comparisons across sites and among regions.

Early warning signals are potentially useful for managing ecosystem services that are subject to catastrophic change, such as unwanted shifts in freshwater quality or production of fisheries and rangelands. In our experiment, early warnings were discernible while a transition was underway, but the experiment was not designed to assess whether a regime shift could be reversed by intervention after detection. Modeling suggests that some but not all regime shifts can be reversed by prompt intervention after early warnings are detected (*22*, *31*). Reversibility through detection of signals and subsequent intervention is a key question for future field experiments.

Ecosystems are subject to increasing human pressures that can lead to drastic changes, including shifts to unwanted states (*2*). In this whole-lake field experiment, early warnings were detected in a food web undergoing a regime shift. Statistical indicators related to variability, autocorrelation, and recovery time provide new tools for empirical studies of nonlinear dynamics in field studies of ecosystems or other complex systems. Thus, our findings should prompt further field experiments to evaluate early warnings for massive change in ecosystems and other complex systems. This research could reveal new indicators of vulnerability to large environmental changes and thereby improve ecosystem management in a rapidly changing and interconnected world.

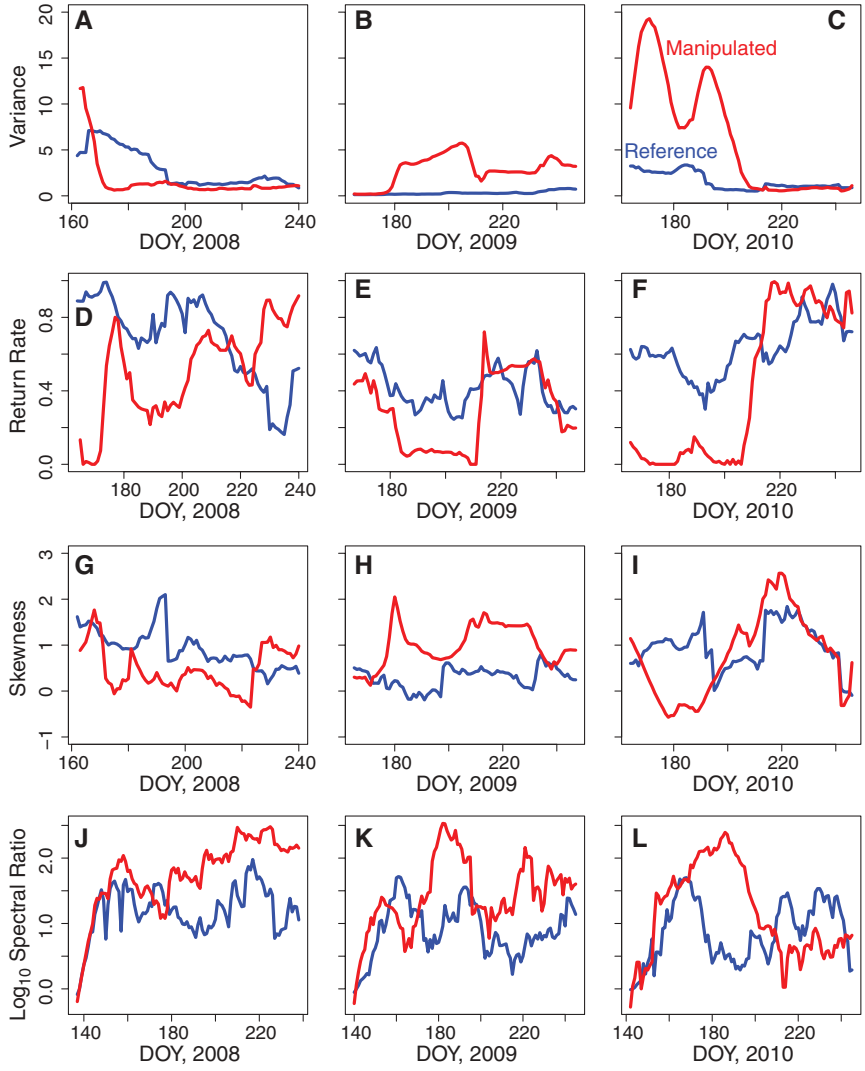

Fig. 4. Potential early warning indicators computed from daily chlorophyll time series in the mixed layer in the manipulated (red) and reference (blue) lakes in 2008, 2009, and 2010. On each date in each lake, statistics were computed for the preceding 28 days by using daily observations (*16*). (**A** to **C**) Variance; high values are associated with nonlinear transitions. (**D** to **F**) Return rate from small perturbations computed by autoregressive modeling (*16*). Values near zero are associated with nonlinear transitions. (**G** to **I**) Coefficient of skewness. Values far from zero (the value for a normal distribution) are associated with nonlinear transitions. (**J** to **L**) Spectral ratio ($\log_{10}$ transformed) of power at low frequencies (less than once per day) to power at high frequencies (from once per 3 hours to once per 15 min) computed from chlorophyll measurements made every 5 min. High spectral ratios are associated with nonlinear transitions (*22*).

References and Notes

1. M. Scheffer, S. Carpenter, J. A. Foley, C. Folke, B. Walker, *Nature* **413**, 591 (2001).
2. Millennium Ecosystem Assessment, *Ecosystems and Human Well-Being: Our Human Planet: Summary for Decision Makers* (Island, Washington, DC, 2005).
3. T. Kleinen, H. Held, G. Petschel-Held, *Ocean Dyn.* **53**, 53 (2003).
4. S. R. Carpenter, W. A. Brock, *Ecol. Lett.* **9**, 311 (2006).
5. E. H. van Nes, M. Scheffer, *Am. Nat.* **169**, 738 (2007).
6. V. Guttal, C. Jayaprakash, *Ecol. Lett.* **11**, 450 (2008).
7. M. Scheffer *et al.*, *Nature* **461**, 53 (2009).
8. V. Dakos *et al.*, *Proc. Natl. Acad. Sci. U.S.A.* **105**, 14308 (2008).
9. S. Kéfi *et al.*, *Nature* **449**, 213 (2007).
10. C. H. Hsieh *et al.*, *Nature* **443**, 859 (2006).
11. M. A. Litzow, J. D. Urban, B. J. Laurel, *Ecol. Appl.* **18**, 1331 (2008).
12. J. M. Drake, B. D. Griffen, *Nature* **467**, 456 (2010).
13. M. L. Pace, J. J. Cole, S. R. Carpenter, J. F. Kitchell, *Trends Ecol. Evol.* **14**, 483 (1999).
14. J. Terborgh, J. Estes, Eds., *Trophic Cascades* (Island, Washington, DC, 2010).
15. S. R. Carpenter, J. F. Kitchell, Eds., *Trophic Cascades in Lakes* (Cambridge Univ. Press, Cambridge, 1993).
16. Materials and methods are available as supporting material on *Science* Online.
17. S. R. Carpenter, W. A. Brock, J. J. Cole, J. F. Kitchell, M. L. Pace, *Ecol. Lett.* **11**, 128 (2008).
18. S. R. Carpenter, W. A. Brock, *Ecosphere* **1**, art10 (2010).
19. S. R. Carpenter *et al.*, *Ecol. Monogr.* **71**, 163 (2001).
20. V. S. Kuwahara, G. Chang, X. Zheng, T. D. Dickey, S. Jiang, *J. Oceanogr.* **64**, 691 (2008).
21. K. Weston, N. Greenwood, L. Fernand, D. J. Pearce, D. B. Sivyer, *J. Sea Res.* **60**, 262 (2008).
22. R. Biggs, S. R. Carpenter, W. A. Brock, *Proc. Natl. Acad. Sci. U.S.A.* **106**, 826 (2009).
23. W. A. Brock, J. A. Scheinkman, W. D. Dechert, B. LeBaron, *Econom. Rev.* **15**, 197 (1996).
24. F. Doveri, M. Scheffer, S. Rinaldi, S. Muratori, Y. Kuznetsov, *Theor. Popul. Biol.* **43**, 159 (1993).
25. J. Huisman, F. J. Weissing, *Nature* **402**, 407 (1999).
26. M. Scheffer, S. Rinaldi, Y. Kuznetsov, *Can. J. Fish. Aquat. Sci.* **57**, 1208 (2000).
27. M. Scheffer, S. Rinaldi, J. Huisman, F. J. Weissing, *Hydrobiologia* **491**, 9 (2003).
28. A. D. Barton, S. Dutkiewicz, G. Flierl, J. Bragg, M. J. Follows, *Science* **327**, 1509 (2010); 10.1126/science.1184961.
29. W. A. Brock, S. R. Carpenter, *Ecol. Monogr.* **80**, 353 (2010).
30. A. Hastings, D. B. Wysham, *Ecol. Lett.* **13**, 464 (2010).
31. R. Contamin, A. M. Ellison, *Ecol. Appl.* **19**, 799 (2009).

Acknowledgments: This research was supported by the NSF. C. Brousseau, M. Dougherty, A. Farrell, R. Johnson, S. Klobucar, J. Kurtzweil, K. Lee, T. Matthys, K. McDonnell, H. Pack, T. Walsworth, and L. Zinn provided technical help. We thank the staff of the University of Notre Dame Environmental Research Center for assistance.

Supporting Online Material

www.sciencemag.org/cgi/content/full/science.1203672/DC1
Materials and Methods
Figs. S1 to S4
Tables S1 and S2

1 February 2011; accepted 8 April 2011
Published online 28 April 2011;
10.1126/science.1203672

Initiation of Proximal-Distal Patterning in the Vertebrate Limb by Signals and Growth

Kimberly L. Cooper,[1]* Jimmy Kuang-Hsien Hu,[1]* Derk ten Berge,[2] Marian Fernandez-Teran,[3] Maria A. Ros,[3] Clifford J. Tabin[1]†

Two broad classes of models have been proposed to explain the patterning of the proximal-distal axis of the vertebrate limb (from the shoulder to the digit tips). Differentiating between them, we demonstrate that early limb mesenchyme in the chick is initially maintained in a state capable of generating all limb segments through exposure to a combination of proximal and distal signals. As the limb bud grows, the proximal limb is established through continued exposure to flank-derived signal(s), whereas the developmental program determining the medial and distal segments is initiated in domains that grow beyond proximal influence. In addition, the system we have developed, combining in vitro and in vivo culture, opens the door to a new level of analysis of patterning mechanisms in the limb.

The mechanisms that pattern the vertebrate limb mesenchyme so that the correct size, shape, and number of elements condense at precise locations have been argued in the literature for decades. Broadly, models of proximal-distal (PD) patterning can be divided into two general classes. One, exemplified by the progress zone model (*1*), posits that progressive distalization of limb pattern is based on an autonomous clocklike mechanism inherent to the undifferentiated mesenchymal cells. The second postulates that instructive cues from surrounding tissues are responsible for specifying the PD segments (*2*, *3*). It has proven surprisingly difficult to differentiate between the autonomous and nonautonomous models experimentally. Here we try to address this issue by focusing on the establishment of the most proximal segment, the stylopod, as distinct from the more distal limb.

In the early vertebrate limb bud, mesenchymal cells encounter members of the fibroblast growth factor (FGF) family produced by the distal ectoderm and retinoic acid (RA) produced in the flank (*2*, *4*). To clarify the roles these signals play in PD patterning, we have taken advantage of recently described conditions that allow limb bud cells to be maintained and manipulated in an undifferentiated state in vitro. When primary limb bud cells from Hamburger and Hamilton (*5*) stage 18 (HH18) chick embryos are cultured at high density, they quickly differentiate into chondrocytes (*6*). However, in the presence of Wnt3a and FGF8 proteins, both of which are normally secreted from the ectoderm, the cells remain proliferative and undifferentiated (*7*). As these cells are cultured, they continue to express markers, such as *Axin2*, *Dusp6*, and *Msx1*, which are characteristic of undifferentiated limb mesenchyme (*7*). The expression of PD markers in these cultured cells has not been examined. Whereas none of the known segmental markers are themselves required for PD specification [see discussion in Tabin and Wolpert (*3*)], at later stages during development in vivo, *Meis1*, *Hoxa11*, and *Hoxa13* domains are congruent with the eventual stylopod, zeugopod, and autopod limb segments, respectively. We used quantitative reverse transcription polymerase chain reaction (RT-PCR) to detect these segmentally expressed limb markers in cells cultured in vitro (*8*). It has been proposed that cells falling out of range of distal signals in the limb bud become fixed in their PD pattern as they begin to differentiate—the so-called "differentiation front" (*3*). Consistent with this, dissociated primary distal HH18 mesenchymal cells expressing *Meis1*, but not *Hoxa11* or *Hoxa13*, when first placed in culture with serum alone, maintained this profile at the onset of differentiation as *Sox9* was up-regulated, before the formation of cartilage nodules. In contrast, we found that over time cells cultured with Wnt3a and FGF8 lost expression of the proximal marker, *Meis1*, and up-regulated expression of *Hoxa11*, a marker of the middle limb segment, followed by a distal marker, *Hoxa13*, an expression profile similar to distal cells of an intact limb bud (Fig. 1).

In vivo, early limb bud cells are also exposed to RA from the flank in addition to FGF and Wnt activity. RA was previously shown to induce *Meis1* expression, and it has been proposed to act as a proximal patterning signal (*2*, *3*). Although this endogenous role of RA has recently been challenged, at least in the developing mouse limb bud (*9*, *10*), the chick results indicate that RA, at minimum, may mimic or share redundancy with additional factor(s). As such, exogenous RA may act as a proxy for endogenous factors with analogous proximalizing activity (*2*, *11*). Therefore, we next added all-*trans* RA at physiological concentrations (*12*) to the cultures with Wnt3a and FGF8. When primary limb cells were cultured with all three factors and, hence, exposed to a

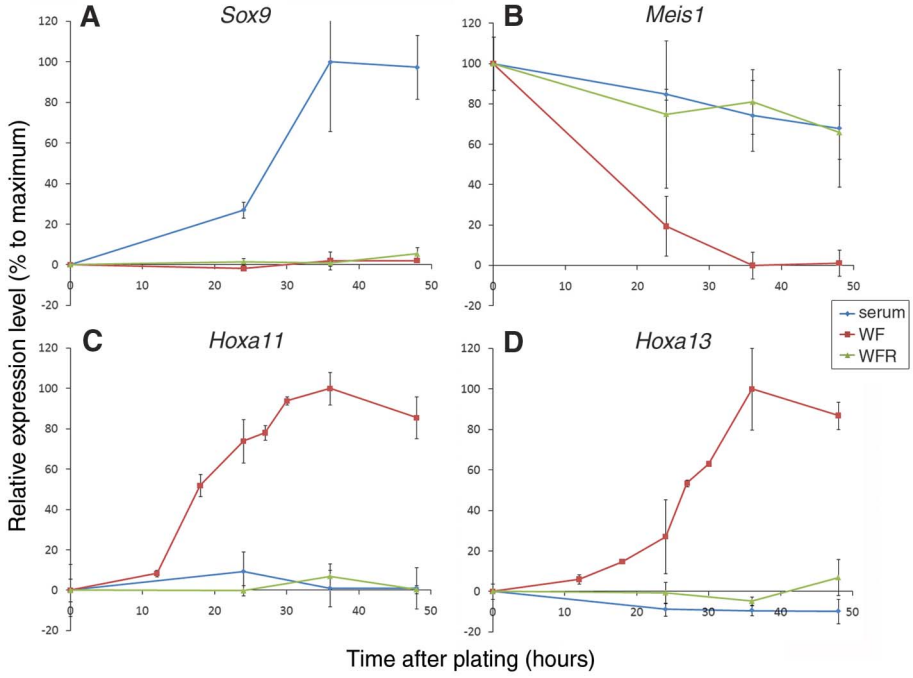

Fig. 1. Wnt3a, FGF8, and RA act together to maintain markers of early limb mesenchyme in culture. Dissociated fresh HH18 distal limb bud cells were cultured with serum only (serum), serum + Wnt3a and FGF8 (WF), or serum + Wnt3a, FGF8, and RA (WFR) for increasing amounts of time. (**A**) *Sox9*, (**B**) *Meis1*, (**C**) *Hoxa11*, and (**D**) *Hoxa13* expression levels were measured by quantitative PCR and normalized to β-*actin* expression.

[1]Harvard Medical School, Department of Genetics, 77 Avenue Louis Pasteur, Boston, MA 02115, USA. [2]Erasmus Medical Center, Erasmus MC Stem Cell Institute, Department of Cell Biology, Post Office Box 2040, 3000 CA Rotterdam, Netherlands. [3]Universidad de Cantabria Instituto de Biomedicina y Biotecnologia (CSIC-UC-IDICAN), C/ Herrera Oria s/n, E-39011 Santander, Spain.

*These authors contributed equally to this work.
†To whom correspondence and requests for materials should be addressed. E-mail: tabin@genetics.med.harvard.edu

signaling milieu comparable to what is seen by the early limb bud mesenchyme, *Meis1* expression was maintained, and *Hoxa11* and *Hoxa13* were not up-regulated (Fig. 1). Although this expression profile is similar to that of primary mesenchymal cells cultured in serum alone, the latter rapidly differentiate. In contrast, cells cultured with Wnt3a, FGF8, and RA remain undifferentiated while the expression of genes characteristic of the early limb mesenchyme is maintained. At higher doses, FGF8 appears to overcome the effect of RA to a limited extent, which results in a partial decrease in *Meis1* expression and a concomitant increase in *Hoxa11* expression (fig. S1).

To directly assess the developmental potential of cultured primary cells after exposure to various combinations of signals, we made use of a classic technique referred to as constructing a "recombinant limb." Dissociated mesenchymal cells are reaggregated, placed within a jacket of limb bud ectoderm, and grafted onto a host embryo (*13*). After several days of development in the host egg, recombinant limbs are patterned by endogenous signals and form recognizable skeletal structures (*14*, *15*).

Recombinant limbs, made from limb mesenchyme cultured under various conditions, were first assessed 3 days after grafting to determine how expression of the segmental markers resolved in this in vivo setting. As in normal limb development, these markers are expressed in a segment-specific manner in recombinants generated from freshly dissociated HH18 limb mesenchyme (Fig. 2, A to C). In contrast, recombinants made from mesenchymal cells cultured for 36 hours in Wnt3a and FGF8 lacked proximal *Meis1* expression but did express *Hoxa11* in a middle domain and *Hoxa13* distally (Fig. 2, D to F). Thus, limb mesenchyme cultured without RA shuts off *Meis1* expression in vitro and does not reactivate its expression when reexposed to flank signals in vivo. However, recombinants made from cells exposed to Wnt3a, FGF8, and RA in culture continued to express *Meis1* proximally, *Hoxa11* centrally, and *Hoxa13* distally (Fig. 2, G to I), comparable to fresh recombinants and normal limb buds.

Similar to previous studies, recombinant limbs made from fresh HH18 leg bud mesenchyme that were allowed to develop for 14 days after grafting formed segmented skeletons approximating the PD organization of normal limbs including apparent femur, fused tibia and fibula, and digits (Fig. 3A) When made from cells cultured for as little as 12 hours in medium with serum alone, which (as noted above) rapidly initiate chondrogenic differentiation in vitro, they lost the ability to form more than a small cartilaginous nodule in ovo (fig. S2A). When similar recombinants were made from limb mesenchyme that was cultured with Wnt3a and FGF8 for 18, 24, or 36 hours, there was a progressive loss of proximal structures (Figs. 4, D and F, and 3C, respectively; fig. S2; and table S1), such that those cultured for 36 hours were reduced to a cartilage nodule embedded in the flank and a single digit. This loss of ability of cells cultured in Wnt3a and FGF8 to form proximal skeletal elements was not due to detectable decrease in proliferation, increase in apoptosis, or inhibition of chondrogenesis within the recombinants (fig. S3). In contrast, primary limb cells cultured for 36 hours with Wnt3a, FGF8, and RA and then assayed in recombinant limbs gave rise to multiple well-formed segments, similar to those produced in recombinants made with fresh HH18 mesenchyme, although typically smaller in size and often exhibiting a bend or break at the thinnest point in the middle of the second skeletal segment (Fig. 3B, and table S1). Our best interpretation of these skeletons is one of three segments—stylopod, zeugopod, and autopod, which is also consistent with the three distinct domains of segmental gene expression at earlier stages, discussed above.

This interpretation critically depends on our ability to correctly identify the skeletal structures resulting from recombinant limbs. Most problematic is the identification as a digit of the small rod-like ossified element that forms in recombinants made from mesenchyme cultured for 36 hours with Wnt3a and FGF8, but in the absence of RA (Fig. 3C). We therefore used a second criterion for establishing the identity of these structures using cultured leg bud mesenchyme repackaged in wing bud ectoderm. The identity of ectodermal appendages, feathers and scales, is induced by the underlying mesenchyme late in embryonic development (*16*). The proximal part of the chick leg is covered with feathers, whereas scales cover the feet (including metatarsals and digits). Similarly, recombinant limbs generated from freshly dissociated HH18 leg mesenchyme formed feather-covered proximal elements and scale-covered feet with claws, another digit-specific structure. The elements we identified as digits in the recombinants made after culture with Wnt3a and FGF8 were invariably covered by scales and ended in claws (Fig. 3D). Similarly, the multisegmented recombinants produced by cells cultured in Wnt3a, FGF8, and RA displayed scales only over the distal elements we identified as digits, also terminating in claws (Fig. 3, E to H). Although this approach identifies the distal-most element as digit, both of the proximal segments of recombinants made with cells grown in all three factors are exclusively covered in feathers. Section in situ detection of *Meis1* surrounding the proximal-most cartilage of recombinants harvested after 4 days in ovo clearly delineates this element as stylopod (fig. S4).

Thus, mesenchymal cells cultured in the combination of all three signaling molecules to which early limb cells are normally exposed maintain the capacity to form both proximal and distal structures despite the passage of time and con-

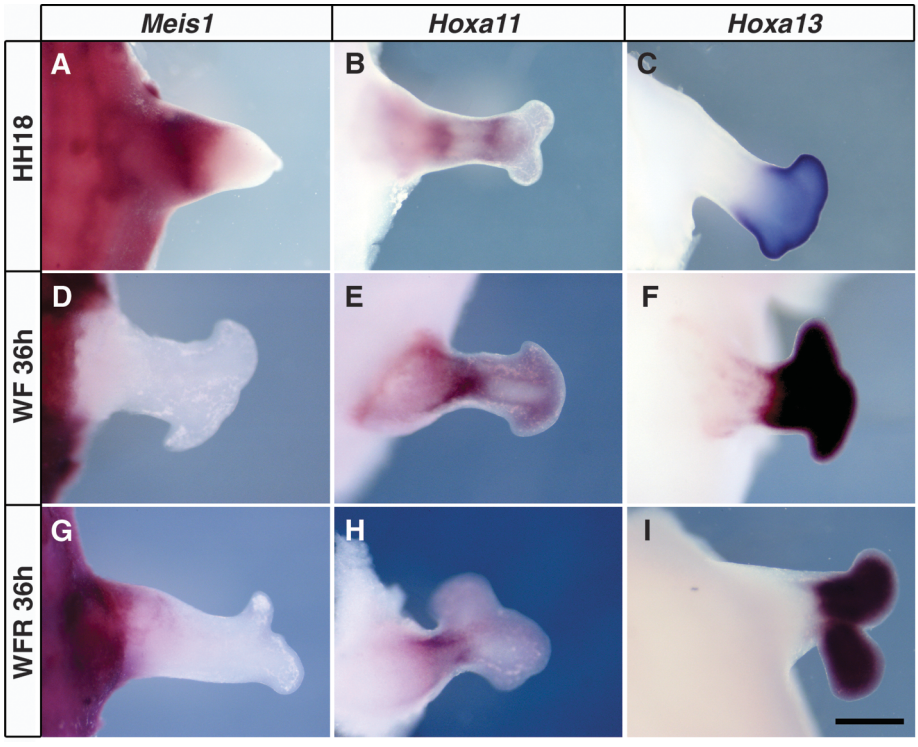

Fig. 2. Expression of *Meis1*, *Hoxa11*, and *Hoxa13* delineate segmental domains in recombinant limbs. Whole-mount in situ hybridization with *Meis1*, *Hoxa11*, and *Hoxa13* probes 72 hours after grafting. (**A** to **C**) Recombinants using freshly dissociated HH18 hindlimb cells. (**D** to **F**) Recombinants using HH18 hindlimb cells cultured for 36 hours in Wnt3a and FGF8. (**G** to **I**) Recombinants using HH18 hindlimb cells cultured for 36 hours in the presence of Wnt3a, FGF8, and RA. Scale bars: 500 μm in (A) to (C) and 800 μm in (D) to (I).

tinued proliferation. Indeed cells cultured in either Wnt3a and FGF8 or Wnt3a, FGF8, and RA divide with a cell cycle time of ~11 hours (11.43 ± 1.4 hours and 10.82 ± 1.25 hours, respectively) (movie S1), comparable to what has been reported for early limb mesenchyme in vivo (*17*, *18*). This strongly argues against a mechanism linking PD specification to a cell cycle–based internal clock (*1*, *19*, *20*).

Freshly harvested HH18 limb bud cells give rise to multiple segments of the PD axis in a recombinant limb. Previous studies using a different experimental approach have also indicated plasticity of proximal HH20 limb bud cells in response to their environment (*21*). However, undifferentiated cells from the distal HH24 limb bud are committed to forming only autopod structures [Fig. 4A and Dudley *et al*. (*22*)], in spite of exposure to endogenous proximal signals after grafting to a host embryo. To determine whether this fate restriction is irreversible under culture conditions that maintain the ability of HH18 limb cells to form all three segments, we cultured dissociated distal HH24 limb mesenchyme in the presence of Wnt3a, FGF8, and RA for 36 hours. We found that when placed in a recombinant limb, these cells were at most capable of forming a single digit with terminal claw (Fig. 4B and table S1).

Although the combination of Wnt3a, FGF8, and RA cannot reverse digit specification once it starts, our data indicate that these factors are sufficient to maintain early limb mesenchyme in a state capable of giving rise to the full PD pattern. We propose that the trigger for initiating the process of specification of the zeugopod and autopod is the cessation (due to displacement) of RA exposure. If this model is correct, then cells initially cultured with Wnt3a, FGF8, and RA, and hence held in an early limb mesenchyme-like state, should start to lose the ability to form proximal structures in vitro as soon as RA is removed from the media. Indeed, we found that primary HH18 leg bud mesenchyme cultured for 18 hours in all three factors and then for 18 hours in only Wnt3a and FGF8 developed two segments, comparable to primary cells assayed immediately after culture for 18 hours in Wnt3a and FGF8 (Fig. 4, C and D; fig. S2B; and table S1). Similarly, HH18 limb cells cultured for 12 hours in all three factors followed by 24 hours in Wnt3a and FGF8 alone formed a digit with a shorter proximal element similar to those assayed after culture in Wnt3a and FGF8 for 24 hours (Fig. 4, E and F; fig. S2C; and table S1).

These data strongly suggest that exposure to the combined activities of Wnt3a, FGF8, and RA in the early limb bud or in culture maintains the

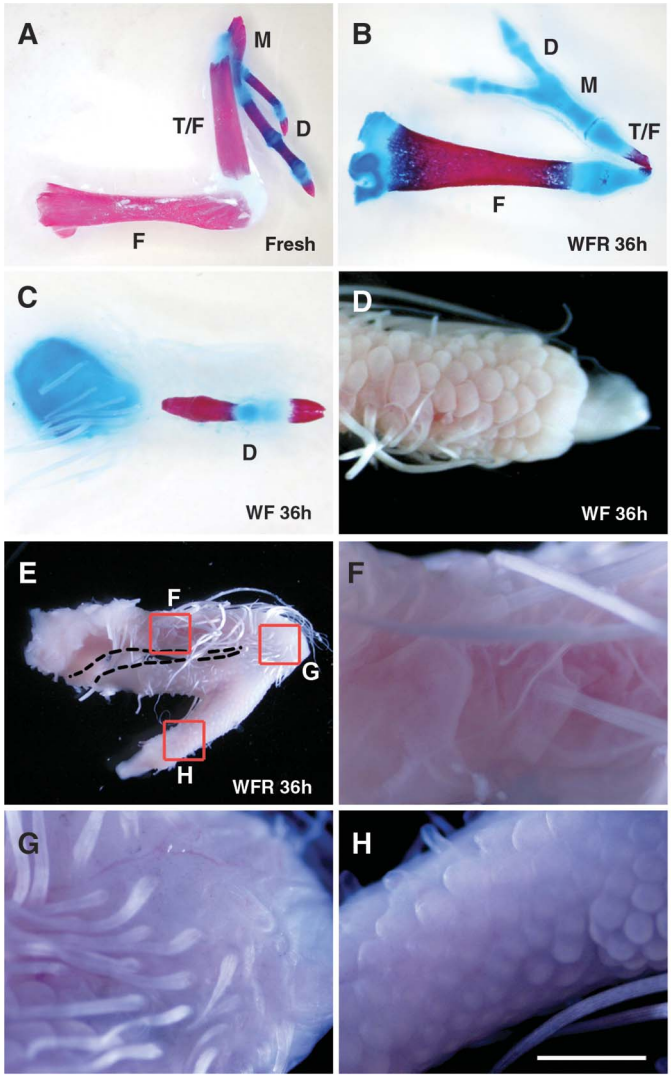

Fig. 3. Wnt3a, FGF8, and RA together maintain the potential of cells to form the complete PD axis. (**A**) Freshly dissociated HH18 hindlimb cells formed three distinct limb segments 14 days after grafting. Although not shown, proximal and middle segments were covered with feathers, and digits with terminal claws were covered by scales. (**C** and **D**) Cells cultured for 36 hours in the presence of Wnt3a and FGF8 (WF) lost the ability to form all but a single scale-covered digit extending from a cartilage nodule embedded in the flank (n = 25 out of 28 with one segment). (**B** and **E** to **H**) Cells cultured for 36 hours in Wnt3a, FGF8, and RA (WFR) formed an elongated feather-covered proximal segment, a short feather-covered middle segment, and a scale-covered digit with a terminal claw (n = 13 out of 24 with three segments). F, femur; T/F, tibia and fibula; M, metatarsal; D, digits. Scale bars: 5 mm in (A) and (E), 2.5 mm in (B) and (C), 1.6 mm in (D), and 1 mm in (F) to (H).

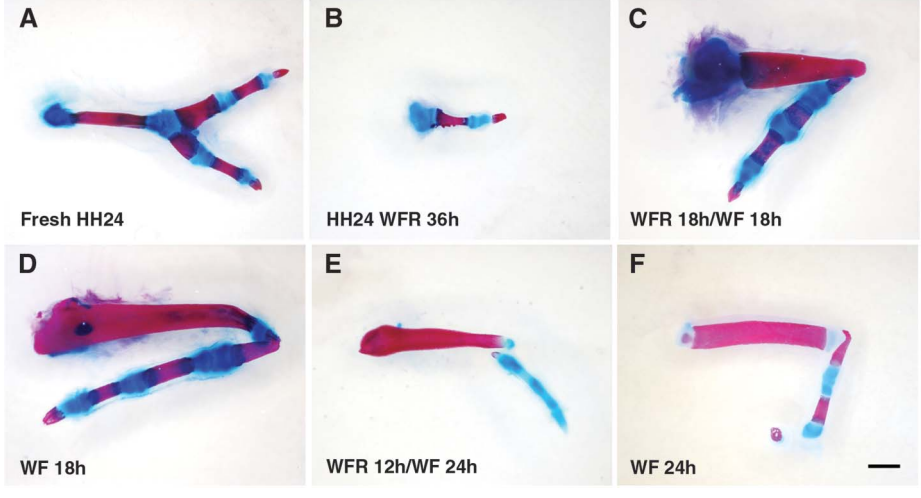

Fig. 4. PD potential is restricted by time spent out of the influence of RA. (**A**) Recombinants made from freshly dissociated distal HH24 hindlimb cells. (**B**) Recombinants of distal HH24 cells cultured for 36 hours in Wnt3a, FGF8, and RA (WFR) (n = 8). (**C** and **D**) Recombinants of HH18 cells cultured for 18 hours in the presence of all three factors followed by 18 hours with Wnt3a and FGF8 (WF) resembled recombinants grafted immediately after culture in Wnt3a and FGF8 for 18 hours (C) n = 28; (D) n = 12. (**E** and **F**) HH18 cells cultured for 12 hours in all three factors followed by 24 hours in Wnt3a and FGF8 formed recombinants that resembled those cultured for 24 hours in the two factors alone (E) n = 12; (F) n = 9. Scale bars: 1.5 mm in (A) and (B) and 1 mm in (C) to (F).

potential to form both proximal and distal structures. As the limb bud grows, the proximal cells fall out of range of distal signals that act, in part, to keep the cells undifferentiated (*7*). Cells closer to the flank therefore differentiate and form proximal structures under the influence of proximal signals. Meanwhile, the potential of distal mesenchymal cells becomes restricted over time to zeugopod and autopod fates by virtue of their growing beyond the range of proximally produced RA. Similar conclusions were reached independently by Roselló-Díez *et al.* (*11*), as discussed in the accompanying paper.

References and Notes

1. D. Summerbell, J. H. Lewis, L. Wolpert, *Nature* **244**, 492 (1973).
2. N. Mercader *et al.*, *Development* **127**, 3961 (2000).
3. C. Tabin, L. Wolpert, *Genes Dev.* **21**, 1433 (2007).
4. F. V. Mariani, C. P. Ahn, G. R. Martin, *Nature* **453**, 401 (2008).
5. H. Hamburger, V. Hamilton, *J. Morphol.* **88**, 49 (1951).
6. P. B. Ahrens, M. Solursh, R. S. Reiter, *Dev. Biol.* **60**, 69 (1977).
7. D. ten Berge, S. A. Brugmann, J. A. Helms, R. Nusse, *Development* **135**, 3247 (2008).
8. Materials and methods are available as supporting material on *Science* Online.
9. X. Zhao *et al.*, *Curr. Biol.* **19**, 1050 (2009).
10. T. J. Cunningham, C. Chatzi, L. L. Sandell, P. A. Trainor, G. Duester, *Dev. Dyn.* **240**, 1142 (2011).
11. A. Roselló-Díez, M. Ros, M. Torres, *Science* **332**, 1086 (2011).
12. F. A. Mic, A. Molotkov, D. M. Benbrook, G. Duester, *Proc. Natl. Acad. Sci. U.S.A.* **100**, 7135 (2003).
13. E. Zwilling, *Dev. Biol.* **9**, 20 (1964).
14. M. Fernandez-Teran, M. E. Piedra, M. A. Ros, J. F. Fallon, *Cell Tissue Res.* **296**, 121 (1999).
15. M. A. Ros, B. K. Simandl, A. W. Clark, J. F. Fallon, *Methods Mol. Biol.* **137**, 245 (2000).
16. M. E. Rawles, *J. Embryol. Exp. Morphol.* **11**, 765 (1963).
17. H. Herrmann, A. C. Marchok, E. F. Baril, *Natl. Cancer Inst. Monogr.* **26**, 303 (1967).
18. R. L. Searls, M. Y. Janners, *Dev. Biol.* **24**, 198 (1971).
19. J. H. Lewis, *J. Embryol. Exp. Morphol.* **33**, 419 (1975).
20. S. Pascoal *et al.*, *J. Mol. Biol.* **368**, 303 (2007).
21. K. M. Krabbenhoft, J. F. Fallon, *Dev. Biol.* **131**, 373 (1989).
22. A. T. Dudley, M. A. Ros, C. J. Tabin, *Nature* **418**, 539 (2002).
23. K. Willert *et al.*, *Nature* **423**, 448 (2003).
24. K. Sato, Y. Koizumi, M. Takahashi, A. Kuroiwa, K. Tamura, *Development* **134**, 1397 (2007).
25. J. L. Galloway, I. Delgado, M. A. Ros, C. J. Tabin, *Nature* **460**, 400 (2009).
26. C. E. Nelson *et al.*, *Development* **122**, 1449 (1996).

Acknowledgments: We thank R. Nusse for generously providing Wnt3a protein, G. Martin for helpful discussions, M. Torres for sharing data before publication, and J. Gros for assistance with confocal live imaging. This work was supported by an NIH grant, R37HD032443, to C.T. and by BFU2008-00397, from the Spanish Ministry of Science and Innovation to M.R.

Supporting Online Material

www.sciencemag.org/cgi/content/full/332/6033/1083/DC1
Materials and Methods
Figs. S1 to S4
Table S1
References
Movie S1

25 October 2010; accepted 29 March 2011
10.1126/science.1199499

Diffusible Signals, Not Autonomous Mechanisms, Determine the Main Proximodistal Limb Subdivision

Alberto Roselló-Díez,[1] María A. Ros,[2] Miguel Torres[1]*

Vertebrate limbs develop three main proximodistal (PD) segments (upper arm, forearm, and hand) in a proximal-to-distal sequence. Despite extensive research into limb development, whether PD specification occurs through nonautonomous or autonomous mechanisms is not resolved. Heterotopic transplantation of intact and recombinant chicken limb buds identifies signals in the embryo trunk that proximalize distal limb cells to generate a complete PD axis. In these transplants, retinoic acid induces proximalization, which is counteracted by fibroblast growth factors from the distal limb bud; these related actions suggest that the first limb-bud PD regionalization results from the balance between proximal and distal signals. The plasticity of limb progenitor cell identity in response to diffusible signals provides a unifying view of PD patterning during vertebrate limb development and regeneration.

The vertebrate limb bud arises from the lateral plate as a bulge of mesenchymal cells encased within an ectodermal hull. Late limb buds of all tetrapods contain three proximodistal (PD) segments, each expressing specific homeobox genes. The stylopod (upper limb) expresses *Meis1/2*, the zeugopod (lower limb) expresses *Hoxa11*, and the autopod (hand/foot) *Hoxa13* (*1*, *2*), although none of these markers is sufficient to specify limb-segment identity. The transition between stylopod (proximal) and nonstylopod (distal) structures represents the main PD subdivision of tetrapod limbs (*3*, *4*). In the distal limb bud, the pool of undifferentiated cells responsible for limb generation is maintained by fibroblast growth factor (FGF) and Wnt signals produced by a distal epithelial structure called the apical ectodermal ridge (AER) (*5*). However, the importance of these and other signals in PD patterning remains controversial. Whereas the progress zone model proposes autonomous progressive distalization of undifferentiated cells under permissive AER influence (*6*, *7*), classical transplantation experiments provide evidence for nonautonomous signals (*8*, *9*). More recently, a two-signal model was proposed, with retinoic acid (RA) as proximalizer and FGFs as distalizers (*10*–*13*); however, endogenous proximal signals have not been identified, and the role of endogenous RA has been questioned by genetic analyses in the mouse (*14*).

To investigate limb-proximalizing signals in the chicken embryo, we transplanted distal leg tips [200 μm thick, Hamilton-Hamburger (*15*) stage 19 to 20 (HH19-20)] to two potentially proximalizing regions: the somites and proximal wing bud of HH20 embryos (*16*) (fig. S1, A and B). These transplants were compared with transplants to tissues not expected to contain limb-proximalizing signals: HH24 distal wing bud (prospective zeugopod) and anterior HH20 hindbrain (fig. S1, A and B).

Graft development in these experiments was not influenced by the grafting site (Fig. 1, A and B and fig. S1D). These results thus support previous reports indicating autonomy of distal limb grafts (*6*, *7*, *17*). An alternative explanation, however, is that proximalizing signals were suppressed by distalizing FGFs from the graft's AER (*10*). We tested this by treating the grafts with the FGFR1 inhibitor SU5402. Whereas untreated grafts transplanted to the somites did not express the proximal marker *Meis1* and maintained *Hoxa11* 22 hours post grafting (hpg) (Fig. 1, C and D), SU5402-treated grafts expressed *Meis1* along the entire PD axis and lost *Hoxa11* expression (Fig. 1, E and F). Presumably, SU5402 action is enhanced by its effect on AER degeneration, which further diminishes FGF signaling. Notably, neither control nor SU5402-treated grafts to prospective HH24 zeugopod or anterior HH20 hindbrain activated *Meis1* or down-regulated *Hoxa11* expression 22 hpg (Fig. 1, I and J, and fig. S2, B to I), which indicated that the changes observed require a specific signal from the somites and not just release from FGF signaling. The somite region thus specifically contains signals that proximalize the limb bud expression profile, but these signals are counteracted by strong FGF activity from the AER.

The somite region expresses the RA-synthesizing enzyme RALDH2 and the RA target *RARβ* (*18*) and contains biologically active RA levels (*13*), whereas anterior hindbrain and distal limb bud do not (fig. S1, A and B). To test whether endogenous RA was required for the proximalizing activity of the somites, we treated grafts with beads soaked in SU5402 plus RA antagonist (RAA). In this case, *Meis1* expression was not

[1]Departamento de Desarrollo y Reparación Cardiovascular, Centro Nacional de Investigaciones Cardiovasculares, Instituto de Salud Carlos III, c/ Melchor Fernández Almagro, 3, E-28029 Madrid, Spain. [2]Instituto de Biomedicina y Biotecnología de Cantabria (CSIC-UC-SODERCAN) and University of Cantabria, c/ Herrera Oria s/n, E-39011 Santander, Spain.

*To whom correspondence should be addressed. E-mail: mtorres@cnic.es

up-regulated, and *Hoxa11* expression was maintained (Fig. 1, G and H), which indicated that specifically blocking RA signaling disrupts the somite region's proximalizing activity. Changes in skeletal patterning after these treatments could not be determined, because AER inhibition in SU5402-treated grafts disrupted further limb bud growth. We thus looked for an alternative approach.

Recombinant limbs (RLs) are made by dissociating limb mesenchymal cells and then reaggregating and packing them into an ectodermal hull, producing a ~500-μm-long structure (*19*). RLs can be made exclusively from undifferentiated distal HH19-20 cells (*17*). In the resulting RL, most of the originally distal cells are located beyond the range of high FGF signaling from the AER, which allows investigation of the response of distal cells to proximal signals without the influence of distal signals. We grafted RLs made from the distal 100-μm region of HH19-20 limb buds to the somites of HH20 hosts (sRLs) or to the prospective zeugopod of HH24 hosts (zRLs).

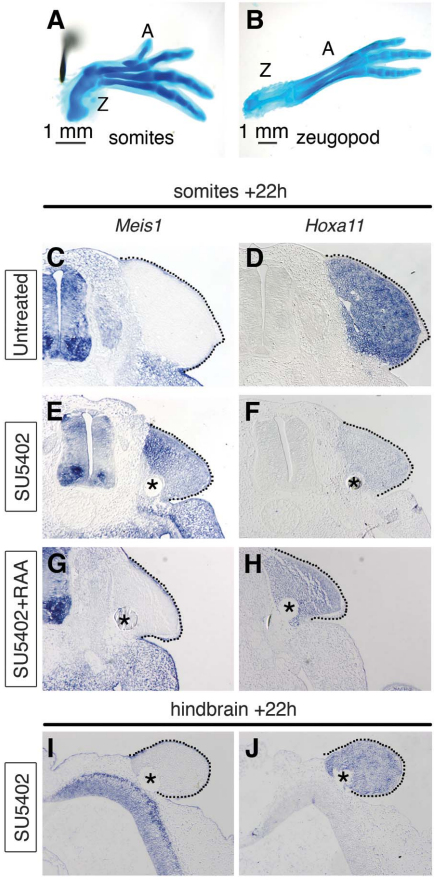

Fig. 1. Endogenous RA reprograms distal limb bud cells when FGF signaling is diminished. (**A** and **B**) Skeletal preparations from HH19-20 200-μm leg grafts, 6 days after implantation at the somites [(A), n = 19] and prospective zeugopod [(B), n = 19]. Z, zeugopod; A, autopod. (**C** to **J**) HH19-20 200-μm limb grafts were treated and transplanted as indicated. *Meis1* and *Hoxa11* expression is shown on adjacent sections 22 hpg [(C and D), n = 6; (E and F), n = 6; (G and H), n = 7; (I and J), n = 5]. Asterisks, beads.

As previously described (*17*), sRLs formed the three main limb segments (Fig. 2Ab); in contrast, zRLs formed only the two distal segments (Fig. 2Aa). Because the skeletal elements formed from RLs are often dysmorphic, we established a new approach to determine their PD identity. We found that the perichondrial-periosteal area of skeletal elements in late differentiating limbs retains segment-specific *Meis1* and *Hox* expression, which allows molecular identification of skeletal elements' PD identity (fig. S3A). This approach confirmed that the three segments formed by sRLs correspond to the normal PD sequence of limb segments (fig. S3B). Moreover, the proximal-most element formed in sRLs invariably expressed *Meis1* but not *Hoxa11* (Fig. 2, Bb and Cb), whereas the proximal-most element in zRLs expressed *Hoxa11* but not *Meis1* (Fig. 2, Ba and Ca). These results demonstrate that formation of a complete PD axis depends on signals from the graft environment.

We next explored the mechanism that allows production of a complete axis from sRLs but not zRLs. We first confirmed that alterations in cell death, proliferation, or sorting patterns of RL cells do not contribute to the differences observed (figs. S4 and S5). We then determined that, in undisturbed limb buds, the fate of the cells used to make RLs is zeugopod and autopod (fig. S6), consistent with published fate maps (*20*). Thus, sRLs form a stylopod through the proximalization of distal limb bud cells, whereas, in zRLs, cells maintain their original potential.

Although the RA targets *Meis1* and *RARβ* (*10*, *18*) are not expressed in the cells used to make RLs (figs. S1 and S6), both were induced in early sRLs, but not in most zRLs (fig. S7). To test whether RA signaling in the somite area could be involved in RL proximalization, sRLs were treated with RAA. Instead of three PD elements, RAA-treated sRLs formed only zeugopod and autopod, as shown by morphology (Fig. 2Ac) and late expression of PD markers (Fig. 2, Bc and Cc). In addition, early RAA-treated sRLs also failed to express *Meis1* and *RARβ* (fig. S7). Consistently, zRLs treated with RA-soaked beads expressed both markers and developed all three PD segments (Fig. 2Ad and fig. S7). These experiments show that RA signaling correlates with *Meis1* expression and stylopod formation in RLs.

The question remains, however, as to why RA cannot induce PD axis duplications during limb development when it does so in distal blastemas during regeneration (*21*–*23*). A possible explanation is that distal limb bud cells proximalized by exposure to RA might merge with the proximal limb bud cells, precluding production of a tandem duplication phenotype (*10*). To test this, we inserted RA beads into HH19-20 distal limb bud tips (200 μm thick) and transplanted them to the anterior hindbrain, far from the developing limb (Fig. 3A). Whereas control

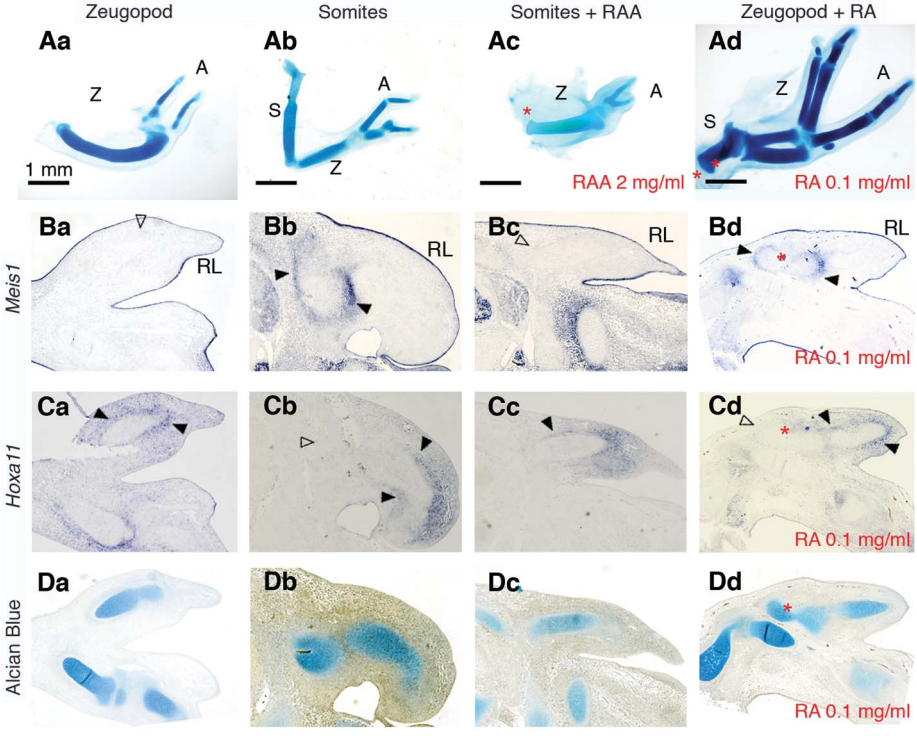

Fig. 2. Distal mesenchymal cells in recombinant limbs alter their PD identity in response to endogenous RA. (**Aa** to **Ad**) Skeletal preparations from RLs 6 days after grafting, obtained as indicated. n = 6, 8, 5, 2, respectively. (**Ba** to **Dd**) *Meis1* and *Hoxa11* mRNA detection and cartilage staining (Alcian blue) on adjacent sections of RLs analyzed 3 days after grafting. Filled and empty arrowheads mark the presence and absence, respectively, of expression surrounding differentiated skeletal elements. n = 4, 3, 4, 2, respectively. Asterisks, beads. S, stylopod; Z, zeugopod; A, autopod.

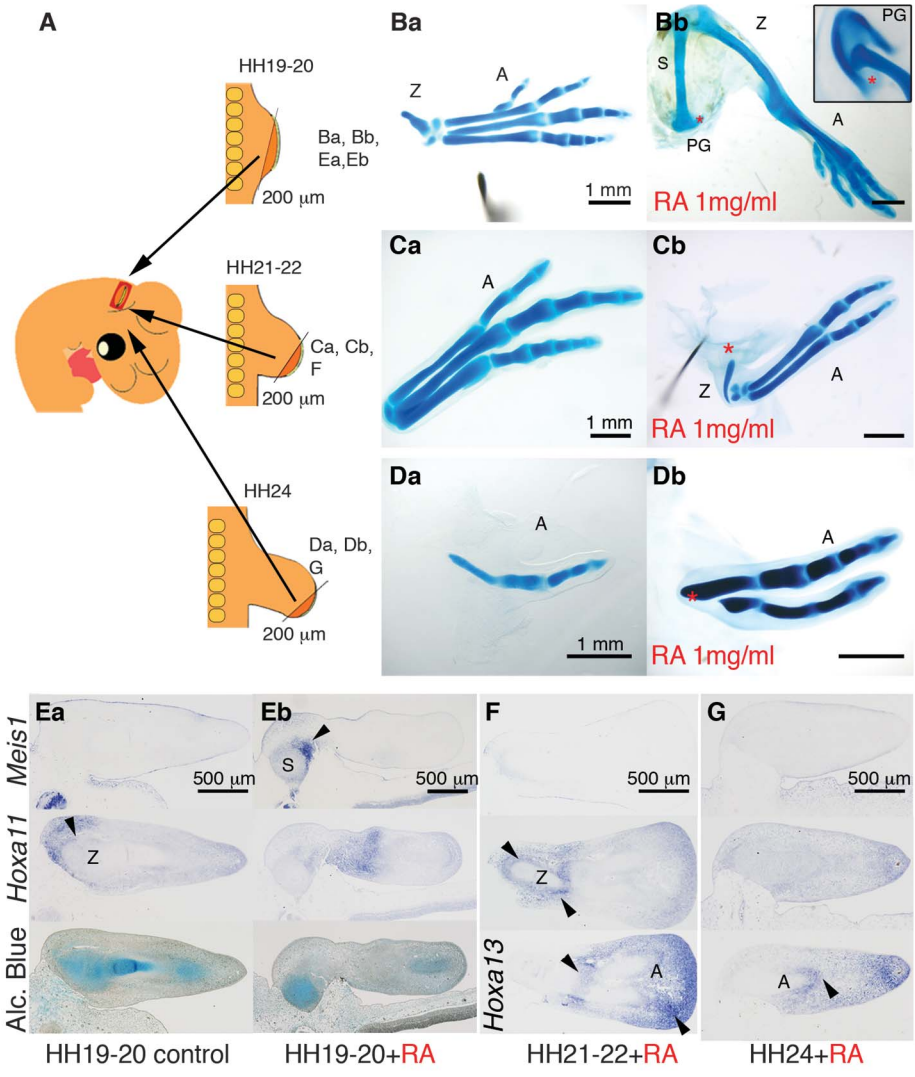

Fig. 3. Exogenous RA overcomes the distalizing effect of FGF signaling and leads to generation of the whole PD axis. (**A**) Grafting procedure. (**Ba** to **Db**) Skeletal preparations from 6 days after grafting transplants. Untreated HH19-20 grafts (Ba) started at various zeugopod levels (n = 10 out of 14) or proximal autopod (n = 4 out of 14), whereas the RA-treated grafts (Bb) started at the pelvic girdle (PG, inset) (n = 4 out of 5) or proximal stylopod (n = 1 out of 5). Whereas control HH21-22 grafts developed autopod [(Ca), n = 7], RA-treated ones formed zeugopod [(Cb), n = 6 out of 7]. HH24 donors developed autopod in both conditions [(Da) and (Db), n = 5 and 6, respectively]. (**Ea** to **G**) Adjacent sections showing gene expression and histological analysis of skeletal elements formed by control HH19-20 grafts (Ea) and RA-treated HH19-20 (Eb), HH22 (F), and HH24 (G) grafts. Asterisks, beads. Arrowheads mark expression surrounding skeletal elements.

transplants developed an incomplete PD axis, usually beginning at the zeugopod level (Fig. 3Ba), RA-treated transplants developed a complete PD axis starting at the pelvic girdle or stylopod (Fig. 3Bb). Expression analysis confirmed that the proximal-most skeletal element of control grafts expressed *Hoxa11* and not *Meis1* (Fig. 3Ea), whereas it expressed *Meis1* and not *Hoxa11* in RA-treated grafts (Fig. 3Eb). Exogenously applied RA thus overcomes AER's FGF distalizing activity in early developing limbs, producing distal-to-proximal transformations similar to those observed in regenerating limb blastemas. In transplants using HH22 donors, controls produced only autopod (Fig. 3Ca), whereas RA promoted zeugopod formation and *Hoxa11*, but not *Meis1*, expression in the proximal-most skeletal element (Fig. 3, Cb and F). Finally, RA had no effect on HH24 grafts, which only formed autopod and expressed *Hoxa13* (Fig. 3, Da, Db, and G). These results indicate that RA can proximalize cells with different PD fates, but limb bud responsiveness to RA is progressively lost.

Our results, together with those in the accompanying study by Cooper *et al.* (*24*), indicate that signals, not autonomous mechanisms, establish the main PD subdivision of vertebrate limbs. We also demonstrate the presence of a proximalizing signal in the embryo trunk and show its ability to induce proximal limb structures in RL transplantation experiments. Our results suggest that RA signaling is the trunk proximalizing signal; however, we cannot exclude that it might be activating or mimicking alternative endogenous signals. Rather than absolute signal levels, our study suggests that the balance between FGF and the candidate proximal signal RA instructs PD identity, a finding with potential relevance to other patterning processes (*25*, *26*). In addition, the PD molecular code found in differentiating skeletal elements will be a very useful tool in patterning and evolutionary studies.

References and Notes

1. C. E. Nelson *et al.*, *Development* **122**, 1449 (1996).
2. N. Mercader *et al.*, *Int. J. Dev. Biol.* **53**, 1483 (2009).
3. N. Mercader *et al.*, *Nature* **402**, 425 (1999).
4. S. González-Crespo *et al.*, *Nature* **394**, 196 (1998).
5. D. ten Berge, S. A. Brugmann, J. A. Helms, R. Nusse, *Development* **135**, 3247 (2008).
6. D. Summerbell, J. H. Lewis, L. Wolpert, *Nature* **244**, 492 (1973).
7. D. Summerbell, J. H. Lewis, *J. Embryol. Exp. Morphol.* **33**, 621 (1975).
8. M. Kieny, M.-P. Pautou, *Rouxs Arch. Dev. Biol.* **183**, 177 (1977).
9. D. Summerbell, *J. Embryol. Exp. Morphol.* **41**, 137 (1977).
10. N. Mercader *et al.*, *Development* **127**, 3961 (2000).
11. F. V. Mariani, C. P. Ahn, G. R. Martin, *Nature* **453**, 401 (2008).
12. C. Tabin, L. Wolpert, *Genes Dev.* **21**, 1433 (2007).
13. K. Yashiro *et al.*, *Dev. Cell* **6**, 411 (2004).
14. X. Zhao *et al.*, *Curr. Biol.* **19**, 1050 (2009).
15. V. Hamburger, H. L. Hamilton, *J. Morphol.* **88**, 49 (1951).
16. Materials and methods are available as supporting material on *Science* Online.
17. A. T. Dudley, M. A. Ros, C. J. Tabin, *Nature* **418**, 539 (2002).
18. T. F. Hayamizu, S. V. Bryant, *Dev. Biol.* **166**, 123 (1994).
19. M. A. Ros, G. E. Lyons, S. Mackem, J. F. Fallon, *Dev. Biol.* **166**, 59 (1994).
20. N. Vargesson *et al.*, *Development* **124**, 1909 (1997).
21. M. Maden, *J. Embryol. Exp. Morphol.* **77**, 273 (1983).
22. M. Maden, *Dev. Biol.* **98**, 409 (1983).
23. S. Saxena, I. A. Niazi, *Indian J. Exp. Biol.* **15**, 435 (1977).
24. K. L. Cooper *et al.*, *Science* **332**, 1083 (2011).
25. R. Diez del Corral *et al.*, *Neuron* **40**, 65 (2003).
26. A. Goldbeter, D. Gonze, O. Pourquié, *Dev. Dyn.* **236**, 1495 (2007).

Acknowledgments: We thank K. Storey and R. Diez del Corral for plasmids and C. Tabin for sharing unpublished results. Supported by grants RD06/0010/0008, BFU2009-08331/BMC (M.T.) and BFU2008-00397 (M.A.R.), from the Spanish Ministry of Science and Innovation (MICINN) and fellowship CPI/0051/2007 (A. R.-D.) from Madrid's Regional Government (CAM). The CNIC is supported by the MICINN and the Pro-CNIC Foundation.

Supporting Online Material

www.sciencemag.org/cgi/content/full/332/6033/1086/DC1
Materials and Methods
Figs. S1 to S7
References

25 October 2010; accepted 30 March 2011
10.1126/science.1199489

Structural Basis for Methyl Transfer by a Radical SAM Enzyme

Amie K. Boal,[1] Tyler L. Grove,[2] Monica I. McLaughlin,[2] Neela H. Yennawar,[3] Squire J. Booker,[2]* Amy C. Rosenzweig[1]*

The radical *S*-adenosyl-L-methionine (SAM) enzymes RlmN and Cfr methylate 23*S* ribosomal RNA, modifying the C2 or C8 position of adenosine 2503. The methyl groups are installed by a two-step sequence involving initial methylation of a conserved Cys residue (RlmN Cys^{355}) by SAM. Methyl transfer to the substrate requires reductive cleavage of a second equivalent of SAM. Crystal structures of RlmN and RlmN with SAM show that a single molecule of SAM coordinates the [4Fe-4S] cluster. Residue Cys^{355} is *S*-methylated and located proximal to the SAM methyl group, suggesting the SAM that is involved in the initial methyl transfer binds at the same site. Thus, RlmN accomplishes its complex reaction with structural economy, harnessing the two most important reactivities of SAM within a single site.

Methyl transfer is essential in the synthesis of cellular metabolites and clinically relevant natural products and in the modification of RNA, DNA, lipids, and proteins. The majority of methyl transfer reactions use *S*-adenosyl-L-methionine (SAM) (*1*) and proceed by S_N2 displacement (*2*, *3*). Until recently, this mechanism was generally accepted as the only means of SAM-dependent methylation (*4*), even for methyl groups transferred to weakly nucleophilic carbon atoms (*5*). The identification and characterization of two ribosomal RNA (rRNA) modification enzymes (RlmN and Cfr) (*6*–*10*) that use SAM to methylate electrophilic rather than nucleophilic carbon centers has changed this view. RlmN and Cfr catalyze methylation of a 23*S* rRNA nucleotide [adenosine 2503 (A2503)] (*6*–*10*) ultimately located within the peptidyltransferase center of the 50*S* subunit of the bacterial ribosome near the entrance to the nascent peptide exit tunnel (*11*). RlmN methylates the C2 position of A2503 (fig. S1), which is a housekeeping modification important in translational fidelity and the nascent peptide response (*9*, *12*, *13*). The related protein Cfr, recently found in a hospital isolate of a methicillin-resistant strain of *Staphylococcus aureus* (*14*, *15*), catalyzes a similar modification at C8 of A2503 (fig. S1) (*6*), which confers resistance to several classes of antibiotics that target the large subunit of the ribosome (*16*–*18*). Inactivation of RlmN in *S. aureus* and loss of C2 modification is also linked to increased linezolid antibiotic resistance (*19*, *20*).

RlmN and Cfr belong to the radical SAM (RS) superfamily of enzymes (*10*), catalysts that use SAM as an oxidant to perform difficult and often complex transformations by radical mechanisms (*21*–*23*). RS superfamily enzymes use a [4Fe–4S] cluster to supply the requisite electron for reductive cleavage of SAM, usually to L-methionine and a 5′-deoxyadenosyl 5′-radical (5′-dA•) (*22*, *24*–*26*). In RlmN and Cfr, SAM is

[1]Departments of Molecular Biosciences and of Chemistry, Northwestern University, Evanston, IL 60208, USA. [2]Departments of Chemistry and of Biochemistry and Molecular Biology, Pennsylvania State University, University Park, PA 16802, USA. [3]Huck Institutes of the Life Sciences, Pennsylvania State University, University Park, PA 16802, USA.

*To whom correspondence should be addressed. E-mail: squire@psu.edu (S.J.B.); amyr@northwestern.edu (A.C.R.)

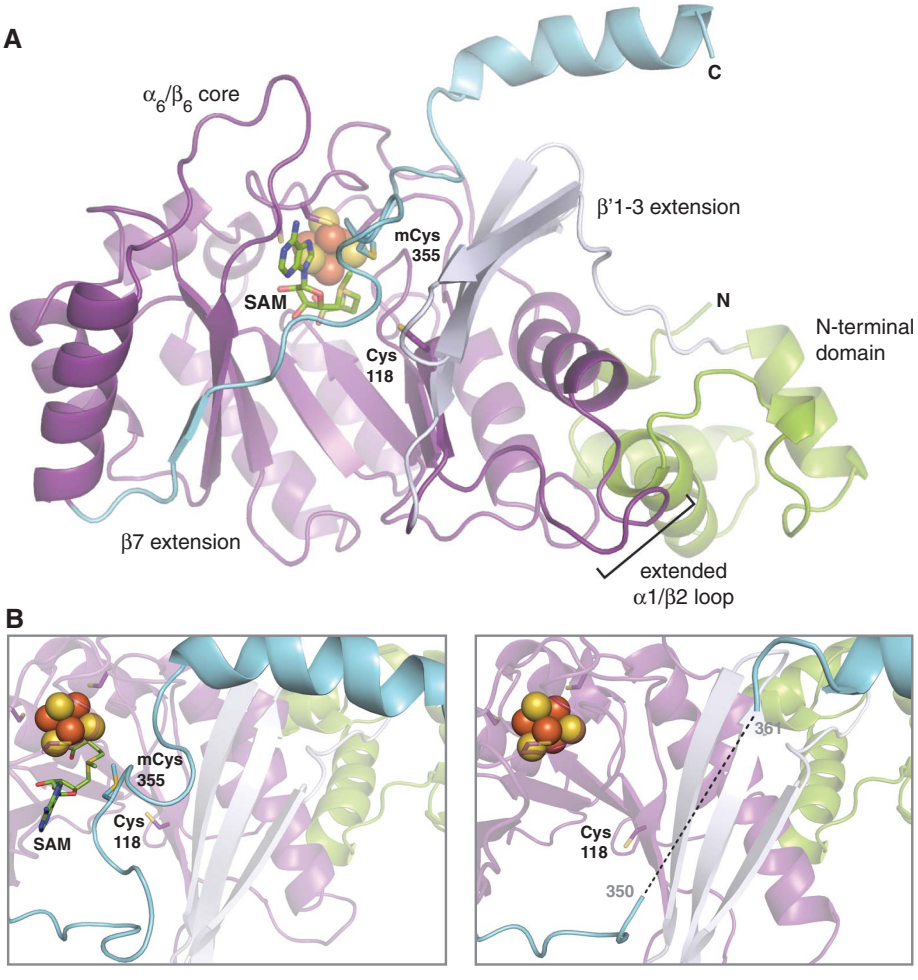

Fig. 1. The structure of *E. coli* RlmN with SAM (**A**). The α_6/β_6 partial barrel core is shown in dark purple, a three-strand β extension to the core (β′1-3 extension) is shown in light purple, an N-terminal helical accessory domain is shown in green, and a C-terminal extension (β7 extension) culminating in an α helix is shown in blue. The [4Fe-4S] cluster cofactor is represented as a space-filling model, and SAM is shown in stick format colored by atom type. Cys ligands to the [4Fe-4S] cluster and mechanistically important residues Cys^{118} and $mCys^{355}$ are shown as purple and blue sticks, respectively, and colored by atom type. (**B**) A top-down view comparing the RlmN active site in the (right) absence and (left) presence of SAM. An unmodeled region (residues 351 to 360) in the RlmN structure obtained without SAM is represented as a dashed line.

the source of both the 5′-dA• and the appended methyl group (*10*). Thus, these enzymes activate SAM for two distinct reactions: reductive cleavage to generate 5′-dA• and methyl transfer. As in all other characterized RS proteins (*22*, *24*–*26*), the expected role of the 5′-dA• would be to abstract a hydrogen atom from the substrate—in this case, the C2 (RlmN) or C8 (Cfr) hydrogen atom from A2503, activating the substrate for subsequent methylation. However, two recent studies suggest that in Cfr and RlmN, 5′-dA• activates the methyl component added to the substrate rather than the substrate itself (*7*, *27*). Yan and Fujimori proposed that 5′-dA• abstracts a hydrogen atom from the methyl substituent of a second simultaneously bound SAM molecule, which then performs a radical addition at C2 of A2503. The resultant adduct is resolved by a hydride shift (*7*, *27*). In contrast, data reported by Grove *et al*. indicate that both the RlmN and Cfr reactions proceed by a ping-pong mechanism (fig. S2) (*7*). The methyl group from one SAM molecule is initially appended to a conserved Cys residue (Cys^{355} in RlmN) in a typical S_N2 displacement (*28*). This SAM-derived one-carbon unit is then attached to the RNA by radical addition initiated by a 5′-dA• formed from a second molecule of SAM. Lastly, this covalent intermediate is resolved by formation of a disulfide bond between the methyl-carrying Cys (mCys) residue and a second conserved Cys residue (Cys^{118} in RlmN).

The crystal structures of *Escherichia coli* RlmN in the absence and presence of SAM (table S1) reveal a monomeric enzyme with two protein molecules in the asymmetric unit. The core of the protein forms an α_6/β_6 partial barrel (Fig. 1A) harboring a [4Fe-4S] cluster coordinated by a canonical CX_3CX_2C motif located at the carboxy edge of the barrel and enclosed by two long loop regions. This overall fold and an open coordination site at the [4Fe-4S] cluster—allowing the enzyme to bind a SAM cosubstrate—are structural hallmarks of the RS superfamily (*29*–*35*). The RlmN core structure is most similar to that of pyruvate formate-lyase activating enzyme (PFL-AE) (2.6 Å rmsd for 220 Cα carbon atoms) (fig. S3), which is noteworthy because PFL-AE also targets a large macromolecule.

Unlike PFL-AE, which represents a minimal architecture among RS enzymes (*30*, *35*), RlmN contains several extensions to the core structure (Fig. 1A). An N-terminal accessory domain is connected to the core via three additional β strands (β′1-3 extension) that extend the barrel laterally. The 60-residue N-terminal domain is composed of four short α helices and differs in structure from accessory domains in other crystallographically characterized RS superfamily members (*29*–*35*). The domain is a variant of the HhH_2 fold (fig. S4), a structure that mediates substrate recognition in proteins that target nucleic acids (*36*, *37*). Although typically involved in DNA interaction, a similar domain is also found in the MraW family of methyltransferases (*37*), enzymes recently demonstrated to methylate rRNA (*38*). In the RlmN core, the loop between α1 and β2 is extended by 10 residues as compared with PFL-AE and adopts different conformations in each molecule in the asymmetric unit (figs. S3 and S5). The β7 strand extends across the open side of the barrel (β7 extension) and interacts with the β′1-3 extension, terminating in a 10-residue region (residues 351 to 360) (Fig. 1B, left), disordered in the absence of SAM and not included in the model in the RlmN structure (Fig. 1B, right). The sequence of this region is strictly conserved among RlmN and Cfr homologs and includes residue Cys^{355}, a key catalytic residue that is methylated in the first step of the proposed mechanism (*7*). Residues 361 to 374 comprise a helix that forms no contacts with the rest of the chain (the nearest neighbor is ~10 Å) in the absence of SAM and interacts instead with a symmetry-related molecule in the crystal lattice (fig. S6).

In the 2.05 Å–resolution structure of RlmN with SAM bound (RlmN+SAM), SAM is coordinated to the [4Fe-4S] cluster, and several structural changes near the enzyme active site are observed. The SAM coordination mode, via its α-amino and α-carboxy moieties (Fig. 2A and fig. S7), is typical of all structurally characterized RS enzymes (*29*–*34*), as is the distance between the SAM sulfonium atom and the unique iron site of the cluster (3.2 Å). This distance is shorter than that to the nearest bridging μ-sulfido ion (3.7 Å), which is consistent with a mechanism for SAM cleavage originally proposed by Frey and coworkers (*39*–*41*). The other interactions between SAM and the surrounding protein include packing of the SAM adenine ring into a hydrophobic cleft and hydrogen bonding interactions, largely to ordered solvent (fig. S8). The sole direct hydrogen bonding interaction involving the adenine ring, between its exocyclic amine and the backbone carbonyl of Asn^{312}, causes a ~2.5 Å shift of the backbone, which moves the Asn side chain over the face of the adenine ring (fig. S9). A hydrogen bonding network involving the SAM adenine Hoogsteen face, ordered solvent, and Asn^{312}

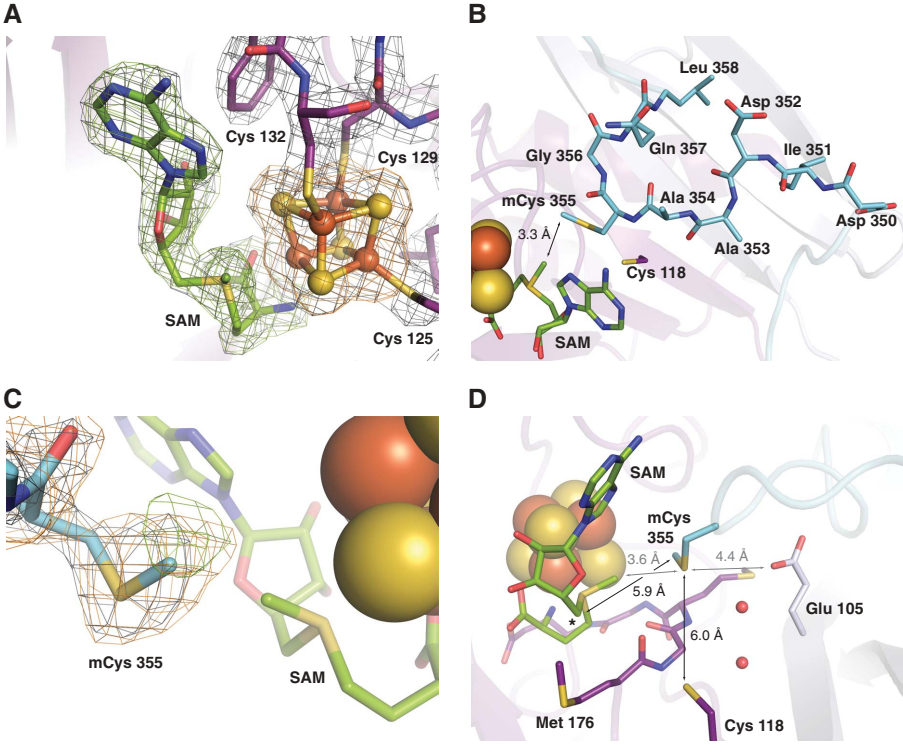

Fig. 2. Selected views of the RlmN active site. (**A**) $2F_o$-F_c electron density map (gray mesh, 1.5σ) for residues 125 to 132 (containing the CX_3CX_2C motif), the [4Fe-4S] cluster, and the SAM cosubstrate in the RlmN+SAM structure. An omit map contoured at 3.0σ for SAM (green mesh) and the [4Fe-4S] cluster (orange mesh) is superimposed. (**B**) A top-down view of the highly conserved 351-to-360 linker region as modeled in the RlmN+SAM structure. The linker is represented in stick format colored by atom type. A loop (residues 310 to 320) located in front of the SAM cofactor is omitted for clarity. (**C**) $2F_o$-F_c electron density map (gray mesh, 1.0σ) for residue 355 in the RlmN+SAM structure. Omit maps for the *S*-methyl group of residue 355 (green mesh, 2.2σ) and the entire residue (orange mesh, 1.9σ) are superimposed. (**D**) A side view of the active site. The conserved MGMGE sequence motif in the α_6/β_6 core is shown in stick format and colored by atom type. Selected conserved residues and ordered water molecules are shown as sticks and spheres, respectively. The 5′ position of the SAM cosubstrate is denoted by an asterisk. Distances relevant to the methyl transfer reaction are drawn as gray lines, and those relevant to $mCys^{355}$ activation and disulfide formation are shown as black lines.

extends to the region encompassing residues 351 to 360 (fig. S8), resulting in observable electron density that could be modeled for one of the two molecules in the asymmetric unit (fig. S10).

Residues 351 to 360 lie across the top of the carboxyl end of the barrel in the RlmN+SAM structure forming a short loop that dips into the active site (Fig. 2B) and contain a conserved motif (IDAACGQL, residues 351 to 358) preceded by an additional conserved glycine (Gly^{348}) and aspartate (Asp^{350}) (*8*). The conserved glycines and alanines may confer conformational variability. The region remains flexible even in the presence of SAM, as evidenced by temperature factors of 40 to 50 $Å^2$ relative to ~20 $Å^2$ for the rest of the model and weak backbone connectivity upon contouring the $2F_o$-F_c map above 1 σ. The side chain of residue 355 is at the tip of the loop and protrudes into the active site in close proximity to the methionine moiety (3.3 Å) (Fig. 2B) of the coordinated SAM molecule. Modeling this residue as a cysteine resulted in positive difference electron density adjacent to the side-chain sulfur atom, eliminated by inclusion of a methyl group appended to the side chain [*S*-methylcysteine (mCys)] (Fig. 2C). The $mCys^{355}$ sulfur atom is located ~6 Å from both the side-chain of Cys^{118} and the 5′ position of the SAM deoxyadenosine group (Fig. 2D and fig. S11). The structure thus represents the binding of the second SAM and strongly supports key downstream steps in the proposed mechanism (*7*).

The active site contains a conserved MGMGE sequence (residues 176 to 180) on the strand adjacent to that containing Cys^{118} (Fig. 2D). This sequence aligns with a GGE motif conserved in RS enzymes and found near the SAM binding pocket (*30*, *35*). The N-terminal methionine, Met^{176}, is contiguous to the SAM cosubstrate. Binding of SAM results in a peptide flip in the backbone carbonyl of Met^{176}, moving it out of a typical β-strand backbone configuration (fig. S12). Consequently, the Met^{176} carbonyl oxygen atom points toward the $mCys^{355}$ side chain and the SAM methyl substituent. Cys^{118} adopts a different rotamer, the adjacent residues shift slightly, and the sulfur atom of Cys^{118} is brought closer to the SAM cofactor and $mCys^{355}$ as compared with its location in the RlmN structure without SAM.

Observation of the $mCys^{355}$ modification in the RlmN+SAM crystal structure (Fig. 2C) supports the proposed ping-pong mechanism (*7*). Furthermore, the structure suggests that SAM-dependent methyl transfer to Cys^{355} could occur from a SAM bound to the [4Fe-4S] cluster. The position of $mCys^{355}$, 3.6 Å from the SAM methyl substituent (Fig. 2D and fig. S13), may permit methyl transfer via S_N2 displacement (*7*). Additional structural aspects that would be favorable for this reaction include positioning of a conserved residue Glu^{105} (~4 Å away) to deprotonate Cys^{355}, which is critical in reaction initiation, and hydrogen bond acceptors Met^{176} backbone carbonyl oxygen (*42*) and [4Fe-4S] μ-sulfido atoms (*43*) within 3.5 Å of the SAM methyl group, which is potentially important in stabilizing the transition state or product methyl configuration (Fig. 2D and fig. S13). The observation that SAM is bound to the [4Fe–4S] cluster similarly to other structurally characterized RS enzymes, the absence of any other clear SAM binding site (structurally or via bioinformatic analysis), and the proximity of Cys^{355} and the activated methyl group of SAM all suggest that RlmN and Cfr, in accordance with the principle of "economy in the evolution of binding sites" (*44*), evolved a single SAM-binding pocket to facilitate two different reactions.

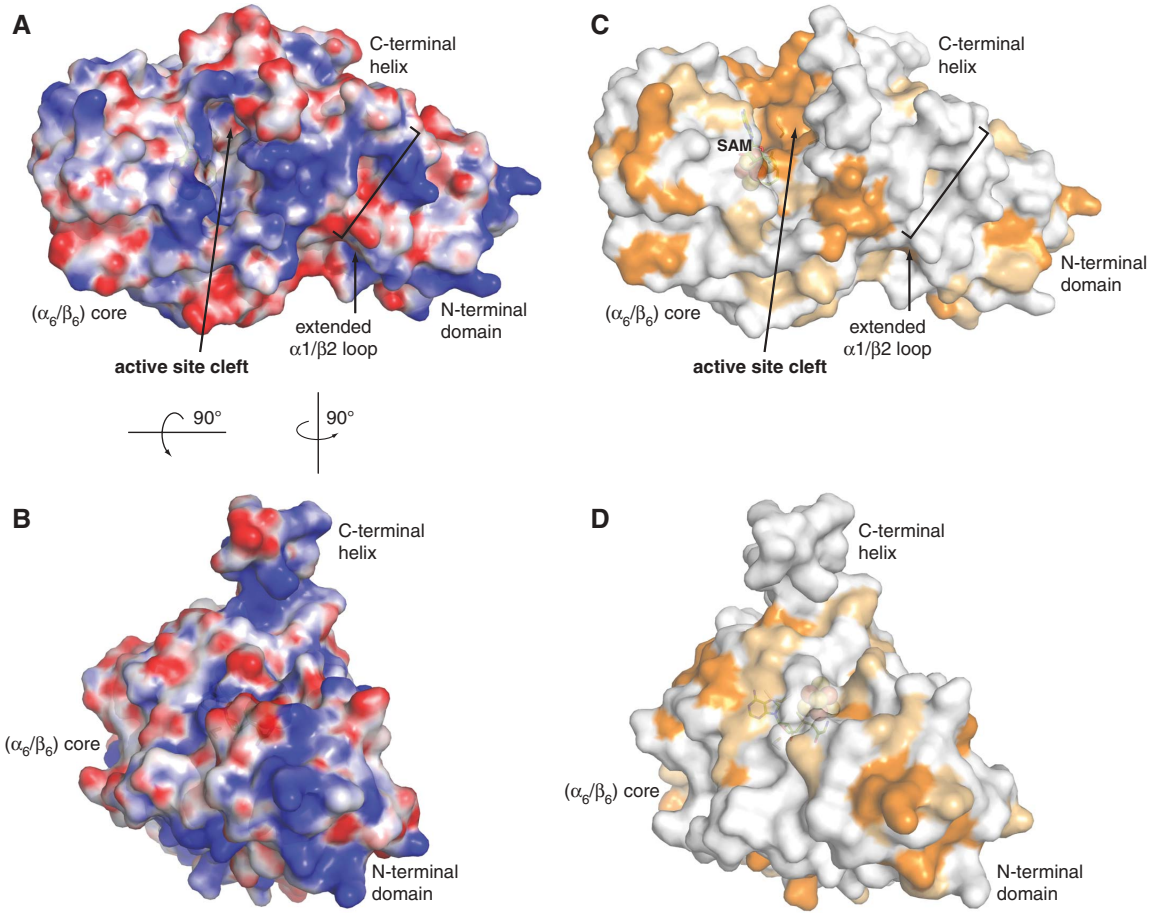

Fig. 3. Electrostatic surface potential (**A** and **B**) and Cfr sequence conservation (**C** and **D**) maps of the RlmN structure. (A) Surface colored by electrostatic potential (*49*). (B) View rotated 90° about the vertical axis and 90° about the horizontal axis from view (A). (C) Map of sequence conservation between *E. coli* RlmN and *S. aureus* Cfr in a pairwise alignment. Strictly conserved residues are shown in orange, neutral substitutions are shown in tan, and variable regions are shown in white. Residues 344 to 350 from the β7 extension (which includes conserved residues Arg^{344}, Gly^{348}, and Asp^{350}) are omitted to afford a better view of the active site cavity. (D) View rotated 90° about the vertical axis and 90° about the horizontal axis from view (C).

In the mechanism proposed by Grove *et al.* (*7*), 5′-dA• abstracts a hydrogen from the methyl group of $mCys^{355}$, and the resulting Cys-appended methyl radical attacks the substrate adenine ring. Methyl transfer to C2 results in a covalent adduct between the substrate and Cys^{355}, resolved by formation of a disulfide bond between Cys^{355} and Cys^{118}. The location of $mCys^{355}$ in the structure, 6 Å equidistant from the 5′ position on the deoxyadenosine moiety of SAM and the side chain of Cys^{118} (Fig. 2D), is consistent with this mechanism. Conserved charged residues, including Glu^{105} and Lys^{94}, and ordered solvent molecules (Fig. 2D), are well positioned to orient the substrate and/or facilitate acid/base chemistry during the reaction (*45*). The location of $mCys^{355}$ in a flexible loop probably confers mobility to facilitate its role in methyl acquisition and substrate addition. The structural homology of this loop to analogous regions in the glycyl radical enzymes pyruvate formate-lyase (fig. S14) (*30*, *46*) and class III ribonucleotide reductase (*47*, *48*) is striking and underscores that these systems perform fundamentally similar transformations: the generation of a carbon-centered radical at a specific site on a protein side chain with a requirement for controlled mobility of the resulting radical within an enzyme/substrate complex.

The RlmN structures also provide insight into the nature and location of the rRNA binding site. The electrostatic surface potential (*49*) for RlmN (Fig. 3, A and B) suggests that the substrate may approach the active site from the bottom of the barrel (Fig. 3A and fig. S15). This surface involves the core barrel, its extensions, and the extra domain, implicating the accessory elements in substrate interaction. The N-terminal domain displays a distinct band of positive charge (Fig. 3B), a feature observed in the specificity domain for rRNA assembly helicase that binds helices 90 to 92 in domain V (*50*), which is a portion of the ribosome necessary for RlmN activity (*10*). A large interaction surface for an rRNA polyanion is consistent with the observation that RlmN most effectively methylates its substrate base in the context of large fragments of 23*S* rRNA (*10*).

The RlmN structures have important implications for the evolution of Cfr, which confers antibiotic resistance by methylating C8 of A2503 (*6*). The two enzymes have similar mechanisms, and RlmN is proposed to be an evolutionary precursor to Cfr (*7*, *8*). To understand how specificity for the C8 position might have evolved in Cfr, residues conserved among both enzymes in a pairwise alignment of *E. coli* RlmN and *S. aureus* Cfr were mapped onto the RlmN structure (Fig. 3, C and D, and fig. S15). The catalytic residues in the active site (*7*) are strictly conserved, as are most of the surrounding residues within the core of the barrel, which supports the proposal that the enzymes use a common mechanism for C-methylation. The high degree of sequence conservation near the active site (figs. S16 and S17) suggests that methylation site specificity during the reaction may be controlled in part by more distant structural elements. In Cfr, two large conformationally flexible regions in the RlmN structure (fig. S18) are absent. These include the extended loop between α1 and β2, located between the active site cavity and N-terminal accessory domain, and the C-terminal helix connected to the mechanistically critical 351 to 360 linker. If loss of these motifs allows Cfr to modify a different site, their distance from the active site is noteworthy and leaves open the possibility that the enzyme/substrate complex uses an extended interaction surface to fine tune control of substrate binding and site selectivity.

References and Notes

1. G. D. Markham, in *Encyclopedia of Life Sciences* (Wiley, New York, 2010).
2. R. W. Woodard, M. D. Tsai, H. G. Floss, P. A. Crooks, J. K. Coward, *J. Biol. Chem.* **255**, 9124 (1980).
3. M. F. Hegazi, R. T. Borchardt, R. L. Schowen, *J. Am. Chem. Soc.* **101**, 4359 (1979).
4. P. A. Frey, A. D. Hegeman, *Enzymatic Reaction Mechanisms* (Oxford Univ. Press, New York, 2007).
5. D. F. Iwig, A. T. Grippe, T. A. McIntyre, S. J. Booker, *Biochemistry* **43**, 13510 (2004).
6. A. M. Giessing *et al.*, *RNA* **15**, 327 (2009).
7. T. L. Grove *et al.*, *Science* **332**, 604 (2011).
8. K. H. Kaminska *et al.*, *Nucleic Acids Res.* **38**, 1652 (2010).
9. S. M. Toh, L. Xiong, T. Bae, A. S. Mankin, *RNA* **14**, 98 (2008).
10. F. Yan *et al.*, *J. Am. Chem. Soc.* **132**, 3953 (2010).
11. N. Ban *et al.*, *Cell* **93**, 1105 (1998).
12. J. A. Kowalak, E. Bruenger, J. A. McCloskey, *J. Biol. Chem.* **270**, 17758 (1995).
13. N. Vázquez-Laslop, H. Ramu, D. Klepacki, K. Kannan, A. S. Mankin, *EMBO J.* **29**, 3108 (2010).
14. S. Schwarz, C. Werckenthin, C. Kehrenberg, *Antimicrob. Agents Chemother.* **44**, 2530 (2000).
15. S. M. Toh *et al.*, *Mol. Microbiol.* **64**, 1506 (2007).
16. C. Kehrenberg, S. Schwarz, L. Jacobsen, L. H. Hansen, B. Vester, *Mol. Microbiol.* **57**, 1064 (2005).
17. K. S. Long, J. Poehlsgaard, C. Kehrenberg, S. Schwarz, B. Vester, *Antimicrob. Agents Chemother.* **50**, 2500 (2006).
18. L. K. Smith, A. S. Mankin, *Antimicrob. Agents Chemother.* **52**, 1703 (2008).
19. J. M. Lamarre, B. P. Howden, A. S. Mankin, *Antimicrob. Agents Chemother.*, published online 28 March 2011 (10.1128/AAC.00183-11).
20. W. Gao *et al.*, *PLoS Pathog.* **6**, e1000944 (2010).
21. S. J. Booker, *Curr. Opin. Chem. Biol.* **13**, 58 (2009).
22. P. A. Frey, A. D. Hegeman, F. J. Ruzicka, *Crit. Rev. Biochem. Mol. Biol.* **43**, 63 (2008).
23. H. J. Sofia, G. Chen, B. G. Hetzler, J. F. Reyes-Spindola, N. E. Miller, *Nucleic Acids Res.* **29**, 1097 (2001).
24. M. Fontecave, E. Mulliez, S. Ollagnier-de-Choudens, *Curr. Opin. Chem. Biol.* **5**, 506 (2001).
25. P. A. Frey, S. J. Booker, *Adv. Protein Chem.* **58**, 1 (2001).
26. J. T. Jarrett, *Curr. Opin. Chem. Biol.* **7**, 174 (2003).
27. F. Yan, D. G. Fujimori, *Proc. Natl. Acad. Sci. U.S.A.* **108**, 3930 (2011).
28. $mCys^{355}$ was discovered upon observation that incubation of RlmN with deuterium-labeled SAM ([*methyl*-$^2H_3$]-SAM) under single-turnover conditions yielded unlabeled C2-methyladenosine (*7*). The Cys^{355} methyl modification was not identified in the study by Yan and Fujimori (*27*), perhaps because of differences in enzyme preparation that result in either a low yield of $mCys^{355}$ or low intrinsic enzyme activity that functionally manifests as multiple turnover conditions in their assay. Yan and Fujimori do report small amounts of unlabeled product that could be attributed to methyl transfer from $mCys^{355}$ present in the as-isolated enzyme.
29. F. Berkovitch, Y. Nicolet, J. T. Wan, J. T. Jarrett, C. L. Drennan, *Science* **303**, 76 (2004).
30. J. L. Vey *et al.*, *Proc. Natl. Acad. Sci. U.S.A.* **105**, 16137 (2008).
31. G. Layer, J. Moser, D. W. Heinz, D. Jahn, W. D. Schubert, *EMBO J.* **22**, 6214 (2003).
32. P. Hänzelmann, H. Schindelin, *Proc. Natl. Acad. Sci. U.S.A.* **101**, 12870 (2004).
33. P. Hänzelmann, H. Schindelin, *Proc. Natl. Acad. Sci. U.S.A.* **103**, 6829 (2006).
34. Y. Nicolet *et al.*, *J. Biol. Chem.* **283**, 18861 (2008).
35. Y. Nicolet, C. L. Drennan, *Nucleic Acids Res.* **32**, 4015 (2004).
36. X. G. Shao, N. V. Grishin, *Nucleic Acids Res.* **28**, 2643 (2000).
37. D. J. Miller *et al.*, *Protein Sci.* **12**, 1432 (2003).
38. S. Kimura, T. Suzuki, *Nucleic Acids Res.* **38**, 1341 (2010).
39. Y. Nicolet, P. Amara, J. M. Mouesca, J. C. Fontecilla-Camps, *Proc. Natl. Acad. Sci. U.S.A.* **106**, 14867 (2009).
40. N. J. Cosper, S. J. Booker, F. Ruzicka, P. A. Frey, R. A. Scott, *Biochemistry* **39**, 15668 (2000).
41. J. A. Kampmeier, *Biochemistry* **49**, 10770 (2010).
42. B. D. Allen, D. J. O'Leary, *J. Am. Chem. Soc.* **125**, 9018 (2003).
43. W. M. Westler, I. J. Lin, A. Perczel, F. Weinhold, J. L. Markley, *J. Am. Chem. Soc.* **133**, 1310 (2011).
44. P. A. Frey, in *The Enzymes: Mechanisms of Catalysis,* D. S. Sigman, P. D. Boyer, Eds. (Academic Press, San Diego, CA, 1992), vol. 20, pp. 142–187.
45. The finding that methylation of C2 of A2503 proceeds without exchange of solvent hydrons into the product suggests that a monoprotic base abstracts the proton at C2 and returns it to the methyl group. The structure is consistent with Glu^{105}, located 4 Å away from $mCys^{355}$, as a candidate for the monoprotic base. Substitution of the corresponding residue in Cfr (Glu^{91}) to alanine abrogates methylation, but causes a stop at A2503 in reverse transcription of the resulting RNA. Elimination of the base that removes the proton at C2 (fig. S2, step 5) might result in a covalent adduct between the protein and the RNA substrate, which could manifest as a stop in reverse transcriptase assays. The proposed role for Glu^{105} as a general base in both methyl transfer to Cys^{355} and to the substrate adenine, in combination with its central location in the active site and potential for multiple hydrogen bonding interactions with the backbone of the 351 to 360 linker (figs. S8 and S13), suggests that this residue may be multifunctional in RlmN-mediated catalysis.
46. A. Becker *et al.*, *Nat. Struct. Biol.* **6**, 969 (1999).
47. D. T. Logan, J. Andersson, B. M. Sjöberg, P. Nordlund, *Science* **283**, 1499 (1999).
48. K. M. Larsson, J. Andersson, B. M. Sjöberg, P. Nordlund, D. T. Logan, *Structure* **9**, 739 (2001).
49. N. A. Baker, D. Sept, S. Joseph, M. J. Holst, J. A. McCammon, *Proc. Natl. Acad. Sci. U.S.A.* **98**, 10037 (2001).
50. J. W. Hardin, Y. X. Hu, D. B. McKay, *J. Mol. Biol.* **402**, 412 (2010).

Acknowledgments: This work has been supported by NIH grants GM58518 (A.C.R.) and GM63847 (S.J.B.) and a National Research Service Award fellowship to A.K.B. Use of the Advanced Photon Source was supported by the U.S. Department of Energy, Office of Science, Office of Basic Energy Sciences, under contract DE-AC02-06CH11357. Use of the LS-CAT Sector 21 was supported by the Michigan Economic Development Corporation and the Michigan Technology Tri-Corridor (grant 085P1000817). GM/CA CAT has been funded in whole or in part with Federal funds from the National Cancer Institute (Y1-CO-1020) and the National Institute of General Medical Science (Y1-GM-1104). Coordinates and structure factors have been deposited in the Protein Data Bank with accession codes 3RF9 (RlmN) and 3RFA (RlmN+SAM).

Supporting Online Material

www.sciencemag.org/cgi/content/full/science.1205358/DC1
Materials and Methods
Figs. S1 to S18
Table S1
References

9 March 2011; accepted 8 April 2011
Published online 28 April 2011;
10.1126/science.1205358

Human Cytomegalovirus Directly Induces the Antiviral Protein Viperin to Enhance Infectivity

Jun-Young Seo, Rakina Yaneva, Ella R. Hinson, Peter Cresswell*

Viperin is an interferon-inducible protein that is directly induced in cells by human cytomegalovirus (HCMV) infection. Why HCMV would induce viperin, which has antiviral activity, is unknown. We show that HCMV-induced viperin disrupts cellular metabolism to enhance the infectious process. Viperin interaction with the viral protein vMIA resulted in viperin relocalization from the endoplasmic reticulum to the mitochondria. There, viperin interacted with the mitochondrial trifunctional protein that mediates β-oxidation of fatty acids to generate adenosine triphosphate (ATP). This interaction with viperin, but not with a mutant lacking the viperin iron-sulfur cluster–binding motif, reduced cellular ATP generation, which resulted in actin cytoskeleton disruption and enhancement of infection. This function of viperin, which was previously attributed to vMIA, suggests that HCMV has coopted viperin to facilitate the infectious process.

The importance of the type 1 interferon (IFN) pathway in directing the antiviral response is well established (*1*, *2*). Although many proteins are induced by IFN stimulation or viral infection (*1*, *2*), the functions of most of them remain unexplored. Moreover, despite the antiviral effects of IFN-inducible proteins, some viruses directly induce them for reasons that are largely not well understood. Viperin is an IFN-inducible iron-sulfur (Fe-S) cluster–binding antiviral protein (*3*–*5*). It is induced in various cell types by both type I and II IFNs, polyinosinic:polycytidylic acid, double-stranded RNA (dsRNA), viral DNA, and lipopolysaccharide and by infection with many viruses, including human cytomegalovirus (HCMV) (*5*–*13*). Although viperin inhibits HCMV infection when preexpressed in cells (*5*), the virus directly induces viperin expression independently of IFN production (*13*). This suggests that viperin induction might be advantageous to the virus.

As an initial approach to the potential mechanism, we investigated the intracellular distribution of viperin during HCMV infection (*14*). We previously showed that viperin is redistributed from the endoplasmic reticulum (ER) through the Golgi to the virus assembly compartment (AC) upon HCMV infection and suggested that this reflected a strategy to evade the antiviral effects of ER-localized viperin (*5*). Consistent with previous studies, IFN-induced viperin localized to the ER (fig. S1A). We were surprised, however, to observe that viperin induced in human foreskin fibroblasts (HFFs) by HCMV infection could be detected in association with mitochondria at 1 day post infection (dpi) (fig. S1B) and at the AC at 3 to 4 dpi (fig. S1C). The viral mitochondrial inhibitor of apoptosis (vMIA) is an HCMV-encoded protein known to traffic to mitochondria (*15*–*18*), which suggested a possible mechanism for mitochondrial targeting of viperin during HCMV infection. We observed that viperin co-localized with vMIA to the mitochondria at 1 dpi (Fig. 1A). At 3 dpi viperin was redistributed to the AC, although vMIA remained associated with the mitochondria (Fig. 1A). Coimmunoprecipitation experiments showed that endogenous viperin and vMIA can interact with each other in virally

Department of Immunobiology, Howard Hughes Medical Institute, Yale University School of Medicine, 300 Cedar Street, New Haven, CT 06520–8011, USA.

*To whom correspondence should be addressed. E-mail: peter.cresswell@yale.edu

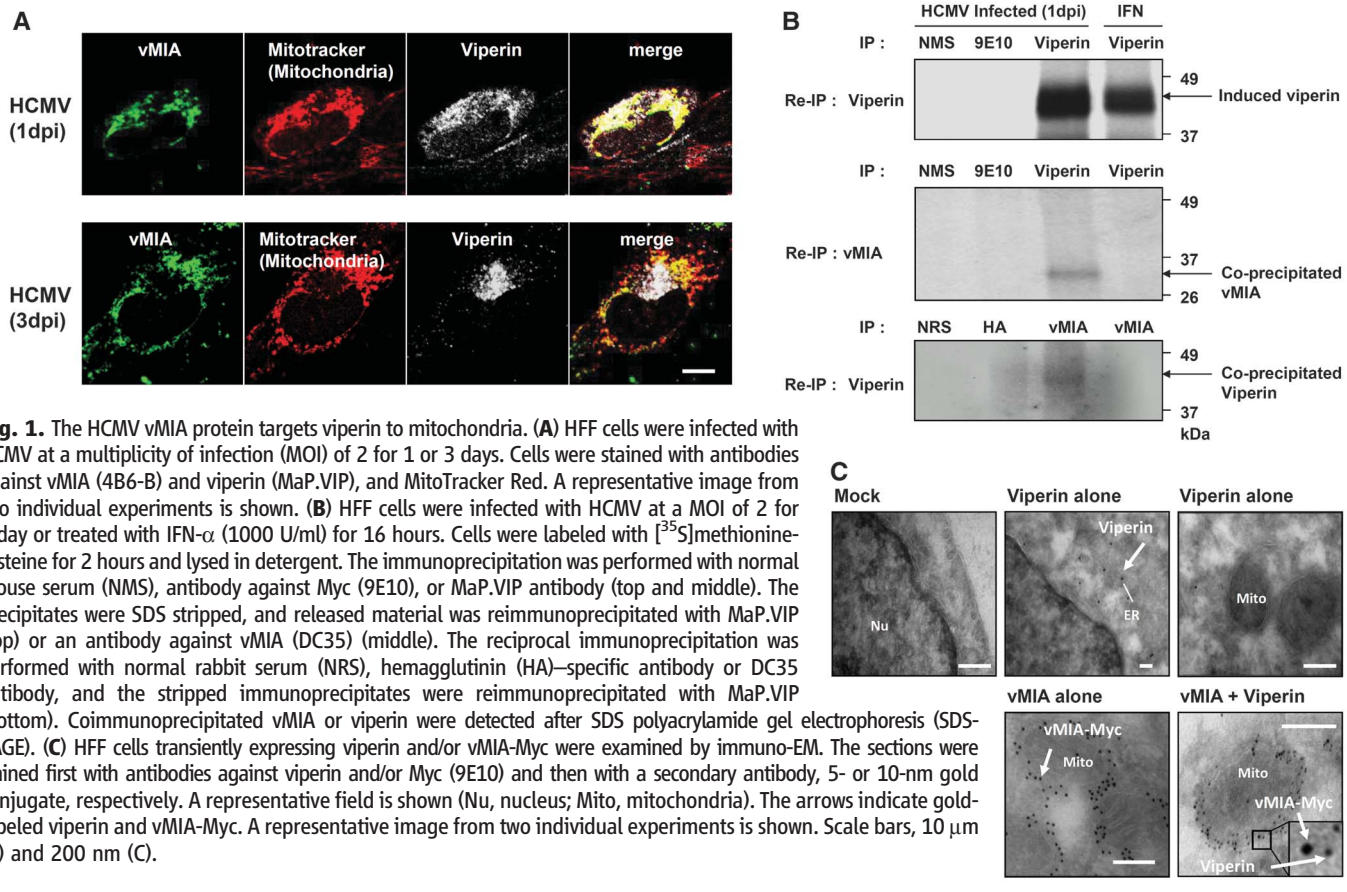

Fig. 1. The HCMV vMIA protein targets viperin to mitochondria. (**A**) HFF cells were infected with HCMV at a multiplicity of infection (MOI) of 2 for 1 or 3 days. Cells were stained with antibodies against vMIA (4B6-B) and viperin (MaP.VIP), and MitoTracker Red. A representative image from two individual experiments is shown. (**B**) HFF cells were infected with HCMV at a MOI of 2 for 1 day or treated with IFN-α (1000 U/ml) for 16 hours. Cells were labeled with [^{35}S]methionine-cysteine for 2 hours and lysed in detergent. The immunoprecipitation was performed with normal mouse serum (NMS), antibody against Myc (9E10), or MaP.VIP antibody (top and middle). The precipitates were SDS stripped, and released material was reimmunoprecipitated with MaP.VIP (top) or an antibody against vMIA (DC35) (middle). The reciprocal immunoprecipitation was performed with normal rabbit serum (NRS), hemagglutinin (HA)–specific antibody or DC35 antibody, and the stripped immunoprecipitates were reimmunoprecipitated with MaP.VIP (bottom). Coimmunoprecipitated vMIA or viperin were detected after SDS polyacrylamide gel electrophoresis (SDS-PAGE). (**C**) HFF cells transiently expressing viperin and/or vMIA-Myc were examined by immuno-EM. The sections were stained first with antibodies against viperin and/or Myc (9E10) and then with a secondary antibody, 5- or 10-nm gold conjugate, respectively. A representative field is shown (Nu, nucleus; Mito, mitochondria). The arrows indicate gold-labeled viperin and vMIA-Myc. A representative image from two individual experiments is shown. Scale bars, 10 μm (A) and 200 nm (C).

infected cells (Fig. 1B). The viperin interaction with vMIA was confirmed in transiently expressing cells by cross-linking followed by solubilization and immunoprecipitation (fig. S2A) and by fluorescent protein-fragment complementation analysis (PCA) (fig. S2, B to E). Analysis by immuno–electron microscopy (immuno-EM) (Fig. 1C) or confocal immunofluorescence microscopy (fig. S2F) also confirmed that the vMIA interaction directly induced viperin targeting to mitochondria.

vMIA has been reported to be responsible for the disruption of the actin cytoskeleton observed after HCMV infection that is believed to facilitate infection (*19*–*23*). The vMIA-induced redistribution of viperin to mitochondria suggested that this effect might be indirect. To examine this question, we used murine embryonic fibroblasts (MEFs) from viperin-depleted (knockout, KO) mice or COS-7 cells, in which endogenous viperin is not induced by double-stranded DNA transfection as it is with HFFs (fig. S3, A and B). The redistribution of viperin by vMIA was also seen in cotransfected MEFs (fig. S3C). We monitored alterations of the actin cytoskeleton in cells transiently expressing vMIA and/or viperin by staining with phalloidin (Fig. 2 and fig. S4). Consistent with previous reports (*19*, *20*), cytoskeletal organization was markedly disrupted, with loss of stress fibers, in wild-type (WT) MEFs expressing vMIA alone, in which endogenous viperin is induced by the transfection protocol (Fig. 2A). However, the actin cytoskeleton was indistinguishable from that of nontransfected cells when vMIA was expressed in viperin KO MEFs, where no endogenous viperin is induced (Fig. 2A). When viperin and vMIA were coexpressed in viperin KO MEFs, the actin cytoskeleton was dramatically disrupted (Fig. 2B). This suggests that viperin is required for the vMIA-induced disruption of the actin cytoskeleton. The actin cytoskeleton was maintained in all cell types expressing viperin alone (fig. S4A). The same patterns of cytoskeletal disruption were also observed in COS-7 cells (fig. S4B). We quantified the actin stress fibers by measuring the phalloidin intensity in three-dimensional images of cells transiently expressing vMIA and/or viperin (fig. S4C). In comparison

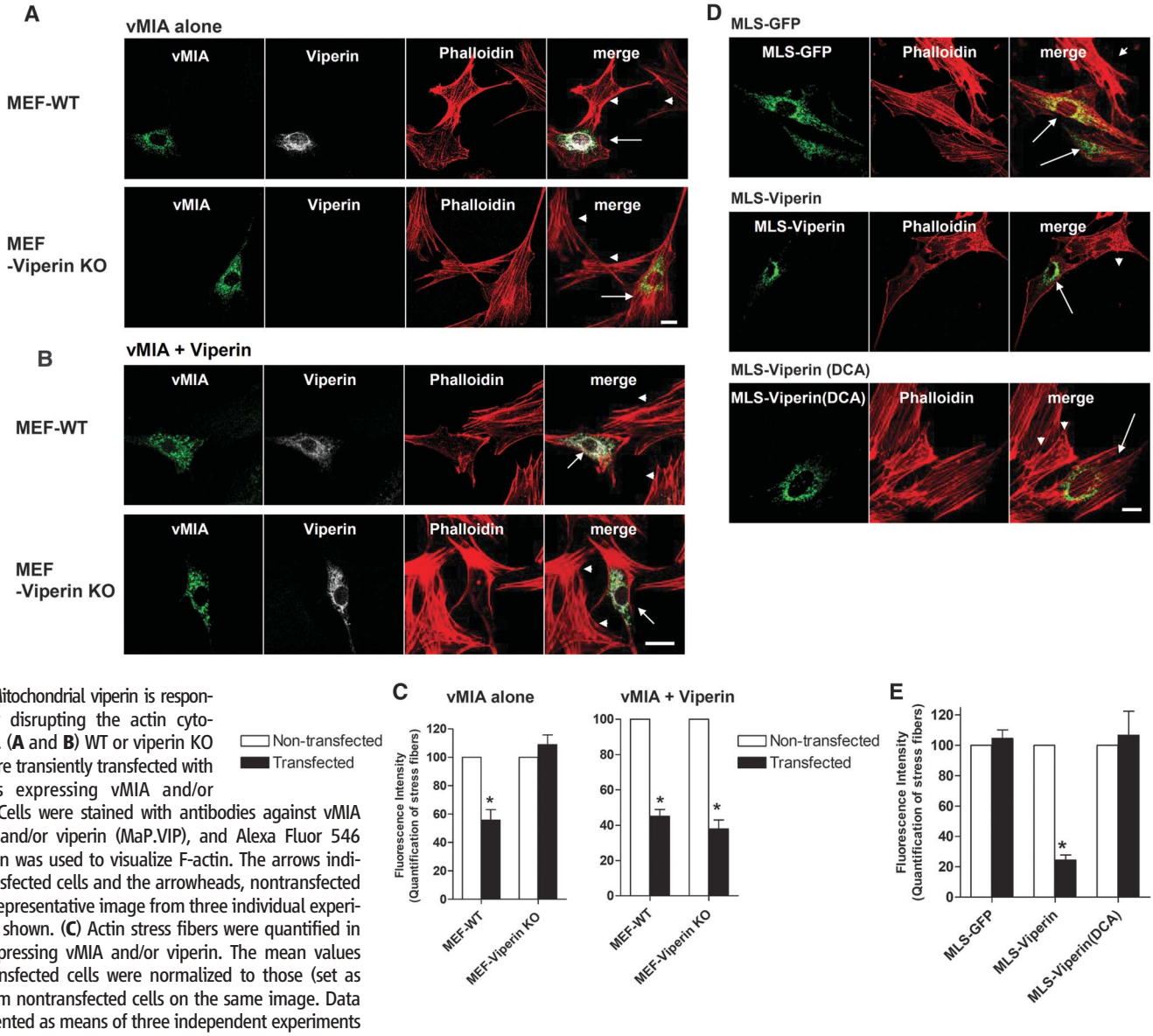

Fig. 2. Mitochondrial viperin is responsible for disrupting the actin cytoskeleton. (**A** and **B**) WT or viperin KO MEFs were transiently transfected with plasmids expressing vMIA and/or viperin. Cells were stained with antibodies against vMIA (4B6-B) and/or viperin (MaP.VIP), and Alexa Fluor 546 phalloidin was used to visualize F-actin. The arrows indicate transfected cells and the arrowheads, nontransfected cells. A representative image from three individual experiments is shown. (**C**) Actin stress fibers were quantified in MEFs expressing vMIA and/or viperin. The mean values from transfected cells were normalized to those (set as 100) from nontransfected cells on the same image. Data are presented as means of three independent experiments (n = 6 to 7) ± SEM. *P < 0.001. (**D**) The N-terminal 42 residue α-helical region of viperin WT or viperin (DCA) was replaced by a mitochondrial localization sequence (MLS, amino acids 2 to 34) of vMIA. The MLS was directly fused to enhanced green fluorescent protein (EGFP) as a negative control. Viperin KO MEFs transiently expressing the indicated chimeric viperin proteins were stained with MaP.VIP antibody and Alexa Fluor 546 phalloidin. The arrows indicate transfected cells and the arrowheads, nontransfected cells. A representative image from three individual experiments is shown. (**E**) Actin stress fibers were quantified as described above. Data are presented as means of three independent experiments (n = 5 to 8) ± SEM. *P < 0.001. Scale bars, 20 μm (A, B, and D).

with nontransfected cells, the phalloidin intensities in WT MEFs expressing vMIA alone, or both WT and viperin KO MEFs coexpressing viperin and vMIA, were reduced by about 50 to 60%, whereas the intensity in viperin KO MEFs expressing vMIA alone was not reduced (Fig. 2C). These results suggest that viperin targeting to mitochondria is required for the disruption of the actin cytoskeleton.

To identify viperin elements involved in the disruption of the actin cytoskeleton, two mutated constructs were used. In the first, residues 1 to 42 were deleted [viperin (ΔN)] to eliminate ER association (*24*), and in the second, two cysteine residues (88 and 91) were mutated to alanine to eliminate Fe-S cluster association [viperin (DCA)]. When viperin (ΔN) and vMIA or viperin (DCA) and vMIA were coexpressed in viperin KO MEFs, viperin (ΔN) was distributed throughout the cytoplasm, whereas viperin (DCA) colocalized with vMIA in mitochondria (fig. S5A). The lack of vMIA interaction with viperin (ΔN) and the interaction of vMIA with viperin (DCA) were confirmed by PCA analysis (fig. S5, B and C). When we examined the cells coexpressing these proteins, however, we observed that the actin cytoskeleton was maintained (fig. S5, D and E). These data indicated a requirement for both mitochondrial localization and Fe-S cluster binding for the viperin-mediated effects.

To determine whether vMIA played any additional role in the process, we generated chimeric WT and Fe-S cluster–binding mutant viperin constructs in which the N-terminal amphipathic α helix, responsible for ER and lipid droplet association (*24*, *25*), was replaced by the mitochondrial localization sequence (MLS) of vMIA (fig. S6, A to C). We also generated a fusion construct with the MLS linked to green fluorescent protein (GFP) directly. We then examined the status of the actin cytoskeleton in viperin KO MEFs or COS-7 cells expressing each chimeric protein (Fig. 2, D and E, and fig. S6D). Although the actin cytoskeleton was maintained in cells expressing MLS-GFP, it was disrupted by 60 to 70% in cells expressing MLS-viperin, which indicated that directly targeted viperin mediates actin cytoskeleton disruption independently of vMIA. Similar results were produced in viperin KO MEFs expressing a chimeric viperin protein in which the N-terminal amphipathic α helix was replaced by the MLS of Tom70, a host cellular mitochondrial protein (fig. S7); this finding excluded the possibility that the MLS from vMIA was responsible for the effect. The actin cytoskeleton was maintained in cells expressing MLS-viperin (DCA), again showing that Fe-S cluster binding is necessary for cytoskeletal disruption (Fig. 2, D and E, and fig. S6D).

Previous studies have shown that the actin cytoskeleton is disrupted by both ATP depletion and ischemia (*26*–*28*) and possibly by vMIA-mediated inhibition of mitochondrial ATP generation (*19*). To determine whether the reduction of ATP generation is mediated by vMIA or by associated viperin, we measured intracellular ATP levels in viperin KO MEFs expressing vMIA-Myc, WT viperin, or viperin mutants (Fig. 3A). ATP levels were reduced only in cells expressing MLS-viperin, by ~50%, which indicates that mitochondrially targeted, Fe-S cluster–binding viperin is responsible for the decrease (Fig. 3A).

A proteomics analysis of viperin-interacting proteins suggested that the ATP reduction induced by targeting viperin to mitochondria could involve a viperin interaction with the β subunit of the mitochondrial trifunctional protein (TFP) (fig. S8A). TFP is a multienzyme complex, composed of four α subunits (HADHA) and four β subunits (HADHB), that catalyzes the last three steps of fatty acid β-oxidation, a major mechanism of cellular ATP production (*29*, *30*). We confirmed the interaction of HADHB with viperin by co-immunoprecipitation and by chemical cross-linking followed by solubilization and immunoprecipitation (Fig. 3B and fig. S8, B and C).

To assess whether the viperin interaction with HADHB affects cellular bioenergetics, we measured fatty acid oxidation levels, ADP/ATP ratios, and the ratios of the reduced form of nicotinamide adenine dinucleotide/nicotinamide adenine dinucleotide ($NADH/NAD^+$) in transfected viperin KO MEFs (fig. S8, D to F). Palmitate oxidation was reduced by 30% (fig. S8D), ADP/ATP ratios increased by 100% (fig. S8E), and $NADH/NAD^+$ ratios reduced by 35% only in cells expressing MLS-viperin (fig. S8F). Thus, mitochondrial localization and Fe-S cluster binding both appear to be essential for metabolic disruption.

To confirm that viperin interaction with HADHB is responsible for the metabolic effects observed, we adopted a genetic approach, measuring cellular ATP levels in patient-derived TFP-deficient human fibroblasts transiently expressing vMIA-Myc, WT viperin, or viperin mutants, with or without GFP tags (Fig. 3, C and D). In WT HFF cells expressing vMIA-Myc (which induces

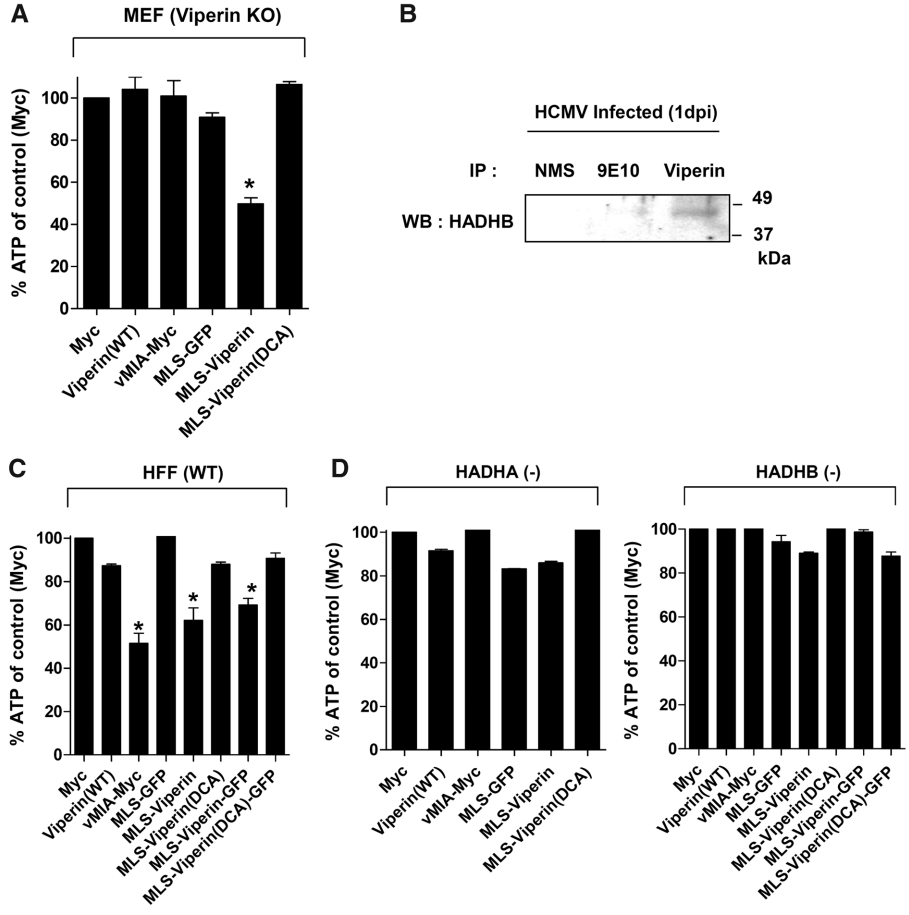

Fig. 3. Viperin interaction with mitochondrial TFP mediates reduction of cellular ATP levels. (**A**) Cellular ATP levels were measured in viperin KO MEFs transiently expressing the indicated proteins. The control value from Myc alone was set as 100%. Data are presented as means of three independent experiments ± SEM. *$P < 0.001$. (**B**) Endogenous viperin interaction with the β subunit (HADHB) of TFP. HFF cells were infected with HCMV at a MOI of 2 for 1 day. Cells were lysed and immunoprecipitated with normal mouse serum (NMS) or antibodies against Myc (9E10) or viperin (MaP.VIP), and Western blots were probed using antibody against HADHB. (**C** and **D**) Cellular ATP levels were measured from WT (C) or TFP-deficient HFF cells [HADHA(–) or HADHB(–)] (D) transiently expressing the indicated proteins. Data are presented as means of at least two independent experiments ± SEM. *$P < 0.001$.

endogenous viperin), MLS-viperin and MLS-viperin-GFP, the ATP levels were reduced to 50 to 70% of control levels (Fig. 3C). In HADHA-deficient or HADHB-deficient fibroblasts, however, ATP levels were unaffected (Fig. 3D), as was the actin cytoskeleton (fig. S8, G and H). Taken together, the data indicate that interaction of the mitochondrially targeted viperin with HADHB reduces TFP activity, which lowers cellular ATP levels and disrupts the actin cytoskeleton.

Finally, to assess whether viperin induced by HCMV infection also mediates actin cytoskeleton disruption, induction in HFFs [HFtelo cells expressing telomerase (*31*)] was suppressed by stably expressing two different short hairpin RNAs (shRNAs) (Fig. 4A). We then examined the actin cytoskeleton in viperin knockdown (KD) HFtelo cells after infection (Fig. 4A). In contrast to cells expressing no shRNA or control luciferase shRNA, in viperin KD cells the pattern of actin stress fibers was indistinguishable from that in non-infected cells (Fig. 4A), as were the ATP levels (Fig. 4B). We then asked if, as expected (*21*, *22*), eliminating stress fiber disruption affected HCMV replication. We determined the kinetics of replication for viruses recovered from viperin KD cells by single-step growth assays. Although HCMV production was unaffected at 3 days post infection, after 6 days it was reduced by more than 10-fold in the viperin KD cells compared with control shRNA-expressing cells (Fig. 4C). To exclude the possibility that viperin shRNA expression induced IFN- or dsRNA-dependent expression of other IFN-stimulated genes (ISGs) that might inhibit HCMV replication, we examined the expression of a variety of ISGs and found no induction (fig. S9, A and B). As a control for the specificity of the shRNA effects, we generated a recombinant HCMV (HCMV.mVIP) in which the loci US7-US16, nonessential for in vitro replication, were replaced by mouse viperin-GFP under an inducible promoter such that expression could be enhanced by the addition of doxycycline (fig. S9C). Expression of mouse viperin-GFP, not susceptible to the effects of the human-specific shRNAs, by HCMV.mVIP rescued the WT HCMV phenotype in viperin shRNA-expressing cells, both in terms of viral replication (Fig. 4D) and actin stress-fiber disruption (fig. S9D).

HCMV specifically targets viperin to mitochondria and uses its ability to inhibit TFP-mediated ATP generation to disrupt the actin cytoskeleton, which facilitates viral replication. These effects, previously attributed to vMIA, result from the ability of vMIA to recruit induced endogenous viperin to mitochondria. Although mitochondrial viperin reduced ATP levels, it did not induce apoptosis in transiently transfected cells when we used terminal deoxynucleotidyl transferase–mediated deoxyuridine triphosphate nick end labeling (TUNEL) assays (fig. S10), which suggested that HCMV uses viperin to reduce ATP levels sufficiently to induce actin cytoskeleton disruption but not apoptosis. Although the precise mechanism by which viperin exerts its effect on TFP function remains unclear, immuno-EM showed that viperin and TFP are both detectable at the outer and inner mitochondrial membranes (fig. S11). Viperin interaction with TFP on the outer membrane may inhibit internalization and maturation of TFP, or viperin association with TFP on the inner membrane could directly inhibit its enzymatic activity.

We have observed a shift to glycolysis, which reduces the pH of the culture medium (fig. S12), when viperin is overexpressed in cells; this finding implies that TFP inhibition can occur with WT viperin. Presumably, this effect is exacerbated when viperin is driven to mitochondria by vMIA interaction or by providing it with an MLS. Cells may normally regulate a viperin mitochondrial function that is exploited by HCMV to inhibit

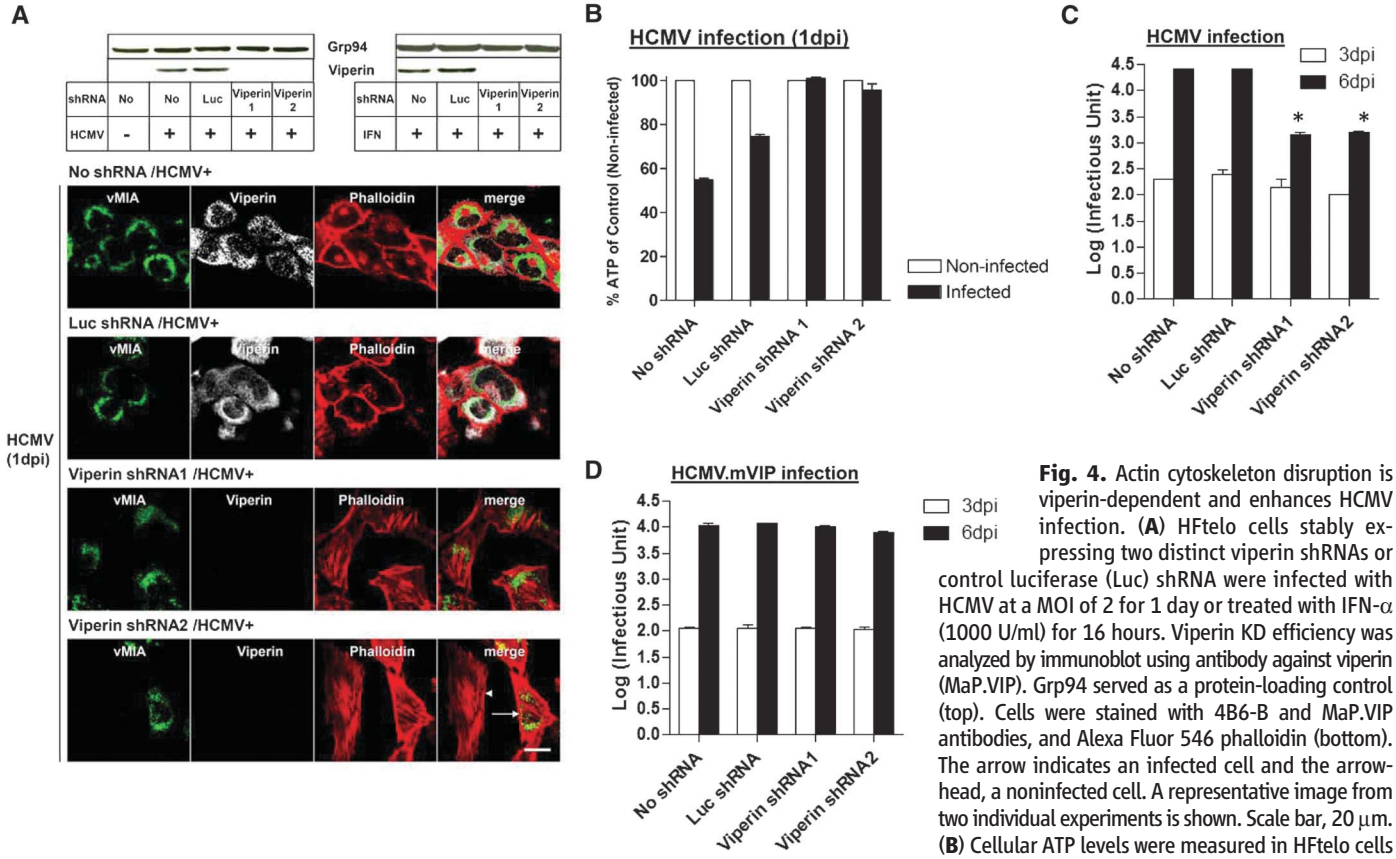

Fig. 4. Actin cytoskeleton disruption is viperin-dependent and enhances HCMV infection. (**A**) HFtelo cells stably expressing two distinct viperin shRNAs or control luciferase (Luc) shRNA were infected with HCMV at a MOI of 2 for 1 day or treated with IFN-α (1000 U/ml) for 16 hours. Viperin KD efficiency was analyzed by immunoblot using antibody against viperin (MaP.VIP). Grp94 served as a protein-loading control (top). Cells were stained with 4B6-B and MaP.VIP antibodies, and Alexa Fluor 546 phalloidin (bottom). The arrow indicates an infected cell and the arrowhead, a noninfected cell. A representative image from two individual experiments is shown. Scale bar, 20 μm. (**B**) Cellular ATP levels were measured in HFtelo cells stably expressing the indicated shRNAs after infection with HCMV at a MOI of 2 for 1 day. The control (uninfected) was set as 100%. Data are presented as means ± SEM of duplicate samples and are representative of two individual experiments. (**C** and **D**) HFtelo cells stably expressing the indicated shRNAs were infected with HCMV (C) or recombinant HCMV.mVIP, in which the loci US7 to US16 were replaced by doxycycline (Dox)–inducible mouse viperin-GFP (D), at an MOI of 0.2, and supernatants were harvested 3 or 6 dpi. Dox (2 μg/ml) was added on day 0 and 3 (D). Virus yield was quantified by a fluorescence-based virus infectivity assay. Data are presented as means ± SEM of duplicate samples and are representative of two individual experiments. *$P < 0.001$.

TFP-mediated ATP generation and to facilitate viral replication.

References and Notes

1. A. G. Bowie, L. Unterholzner, *Nat. Rev. Immunol.* **8**, 911 (2008).
2. A. J. Sadler, B. R. Williams, *Nat. Rev. Immunol.* **8**, 559 (2008).
3. K. S. Duschene, J. B. Broderick, *FEBS Lett.* **584**, 1263 (2010).
4. G. Shaveta, J. Shi, V. T. Chow, J. Song, *Biochem. Biophys. Res. Commun.* **391**, 1390 (2010).
5. K. C. Chin, P. Cresswell, *Proc. Natl. Acad. Sci. U.S.A.* **98**, 15125 (2001).
6. M. A. Rivieccio *et al.*, *J. Immunol.* **177**, 4735 (2006).
7. K. J. Ishii *et al.*, *Nat. Immunol.* **7**, 40 (2006).
8. M. Severa, E. M. Coccia, K. A. Fitzgerald, *J. Biol. Chem.* **281**, 26188 (2006).
9. H. S. Suh *et al.*, *J. Virol.* **81**, 9838 (2007).
10. P. Boudinot *et al.*, *J. Gen. Virol.* **81**, 2675 (2000).
11. J. Fink *et al.*, *PLoS Negl. Trop. Dis.* **1**, e86 (2007).
12. D. Jiang *et al.*, *J. Virol.* **82**, 1665 (2008).
13. H. Zhu, J. P. Cong, T. Shenk, *Proc. Natl. Acad. Sci. U.S.A.* **94**, 13985 (1997).
14. Materials and methods are available as supporting material on *Science* Online.
15. V. S. Goldmacher *et al.*, *Proc. Natl. Acad. Sci. U.S.A.* **96**, 12536 (1999).
16. V. S. Goldmacher, *Biochimie* **84**, 177 (2002).
17. H. O. Al-Barazi, A. M. Colberg-Poley, *J. Virol.* **70**, 7198 (1996).
18. A. M. Colberg-Poley, M. B. Patel, D. P. Erezo, J. E. Slater, *J. Gen. Virol.* **81**, 1779 (2000).
19. D. Poncet *et al.*, *J. Cell Biol.* **174**, 985 (2006).
20. R. Sharon-Friling, J. Goodhouse, A. M. Colberg-Poley, T. Shenk, *Proc. Natl. Acad. Sci. U.S.A.* **103**, 19117 (2006).
21. N. L. Jones, J. C. Lewis, B. A. Kilpatrick, *Eur. J. Cell Biol.* **41**, 304 (1986).
22. S. Cudmore, I. Reckmann, M. Way, *Trends Microbiol.* **5**, 142 (1997).
23. X. Wang, D. Y. Huang, S. M. Huong, E. S. Huang, *Nat. Med.* **11**, 515 (2005).
24. E. R. Hinson, P. Cresswell, *J. Biol. Chem.* **284**, 4705 (2009).
25. E. R. Hinson, P. Cresswell, *Proc. Natl. Acad. Sci. U.S.A.* **106**, 20452 (2009).
26. E. A. Shelden, J. M. Weinberg, D. R. Sorenson, C. A. Edwards, F. M. Pollock, *J. Am. Soc. Nephrol.* **13**, 2667 (2002).
27. R. Bacallao, A. Garfinkel, S. Monke, G. Zampighi, L. J. Mandel, *J. Cell Sci.* **107**, 3301 (1994).
28. N. Golenhofen, R. B. Doctor, R. Bacallao, L. J. Mandel, *Kidney Int.* **48**, 1837 (1995).
29. K. Bartlett, S. Eaton, *Eur. J. Biochem.* **271**, 462 (2004).
30. S. Eaton *et al.*, *Biochem. Soc. Trans.* **28**, 177 (2000).
31. W. A. Bresnahan, G. E. Hultman, T. Shenk, *J. Virol.* **74**, 10816 (2000).

Acknowledgments: We thank C. Rahner in the Yale Center for Cell and Molecular Imaging for EM and the Keck Biotechnology Resource Laboratory for protein identification. The work was supported by the Howard Hughes Medical Institute. J.-Y.S. and P.C. conceived the study and designed experiments. J.-Y.S. performed experiments. R.Y. and E.R.H. performed assays and produced reagents. J.-Y.S. and P.C. analyzed and interpreted the data, and wrote the manuscript. All authors contributed to the final version of the manuscript.

Supporting Online Material

www.sciencemag.org/cgi/content/full/science.1202007/DC1
Materials and Methods
Figs. S1 to S12
References

21 December 2010; accepted 12 April 2011
Published online 28 April 2011;
10.1126/science.1202007

Deciphering the Rhizosphere Microbiome for Disease-Suppressive Bacteria

Rodrigo Mendes,[1]*† Marco Kruijt,[1]*‡ Irene de Bruijn,[1]§ Ester Dekkers,[1] Menno van der Voort,[1] Johannes H. M. Schneider,[2] Yvette M. Piceno,[3] Todd Z. DeSantis,[3,4] Gary L. Andersen,[3] Peter A. H. M. Bakker,[5] Jos M. Raaijmakers[1]¶

Disease-suppressive soils are exceptional ecosystems in which crop plants suffer less from specific soil-borne pathogens than expected owing to the activities of other soil microorganisms. For most disease-suppressive soils, the microbes and mechanisms involved in pathogen control are unknown. By coupling PhyloChip-based metagenomics of the rhizosphere microbiome with culture-dependent functional analyses, we identified key bacterial taxa and genes involved in suppression of a fungal root pathogen. More than 33,000 bacterial and archaeal species were detected, with Proteobacteria, Firmicutes, and Actinobacteria consistently associated with disease suppression. Members of the γ-Proteobacteria were shown to have disease-suppressive activity governed by nonribosomal peptide synthetases. Our data indicate that upon attack by a fungal root pathogen, plants can exploit microbial consortia from soil for protection against infections.

Similar to other eukaryotes, plants and their microbiomes can be viewed as "superorganisms" in which the plant relies, in part, on the soil microbiota for specific functions and traits. In return, plants exude up to 21% of their photosynthetically fixed carbon in the root-soil interface (*1*), i.e., the rhizosphere, thereby feeding the microbial communities and influencing their activity and diversity. For decades, studies about the interplay between plants and rhizosphere microorganisms have focused on pathogens, symbiotic rhizobia, and mycorrhizal fungi, yet there is evidence that other groups of soil microorganisms can affect plant growth and health (*2*). It even has been postulated that plants actively recruit beneficial soil microorganisms in their rhizospheres to counteract pathogen assault (*3*). One well-known phenomenon is the occurrence of disease-suppressive soils, a property conferred by the resident microbiota via as yet unknown mechanisms (*4*, *5*). Hence, the aim of this study is to decipher the rhizosphere microbiome to identify such disease-suppressive microbes and to unravel the mechanisms by which they protect plants against root diseases.

We used a high-density 16*S* ribosomal DNA (rDNA) oligonucleotide microarray, referred to as the PhyloChip (*6*, *7*), to identify key bacterial and archaeal community members in the rhizosphere of plants grown in a disease-suppressive soil. We subsequently targeted and isolated specific bacterial taxa to elucidate the biosynthetic genes and pathways underlying pathogen control.

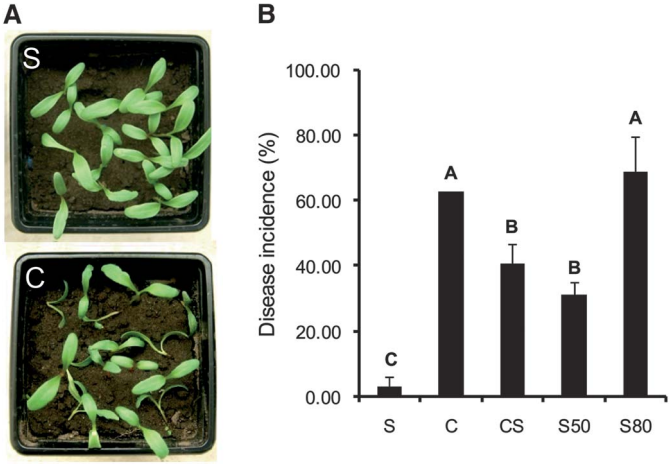

Fig. 1. (**A**) Effect of *R. solani* infection on growth of sugar beet seedlings in disease-suppressive (S) and disease-conducive (C) soils. (**B**) Percentage (mean ± SEM, $N = 4$) of seedlings with damping-off symptoms in suppressive soil (S), conducive soil (C), conducive soil amended with 10% (w/w) of suppressive soil (CS), or suppressive soil heat-treated at 50°C (S50) or 80°C (S80). Different letters above the bars indicate statistically significant differences ($P < 0.05$, Student-Newman-Keuls).

[1]Laboratory of Phytopathology, Wageningen University, Droevendaalsesteeg 1, Wageningen 6700 EE, Netherlands. [2]Institute of Sugar Beet Research, Van Konijnenburgweg 24, Bergen op Zoom 4611 HL, Netherlands. [3]Ecology Department, Lawrence Berkeley National Lab, Cyclotron Road 1, Berkeley, CA 94720, USA. [4]Second Genome, Inc., Owens Street 1700, San Francisco, CA 94158, USA. [5]Plant-Microbe Interactions, Department of Biology, Utrecht University, Padualaan 8, Utrecht 3584 CH, Netherlands.

*These authors contributed equally to this work.
†Present address: Brazilian Agricultural Research Corporation, Embrapa Environment, Jaguariuna, Brazil.
‡Present address: Monsanto Holland, Bergschenhoek, Netherlands.
§Present address: Institute of Medical Sciences, Aberdeen, Scotland, UK.
¶To whom correspondence should be addressed. E-mail: jos.raaijmakers@wur.nl

The soil we investigated is suppressive to *Rhizoctonia solani*, an economically important fungal pathogen of many crops including sugar beet, potato, and rice. This soil was identified in field surveys in the Netherlands conducted by the Institute of Sugar Beet Research in 2004. In the years before its discovery, sugar beet plants grown in this field were severely affected by *R. solani*, suggesting that, similar to other suppressive soils, a disease outbreak is required for the onset of suppressiveness (*4*, *5*). When tested under greenhouse conditions with sugar beet as the host plant, this soil maintained its exceptional disease-suppressive activity toward *R. solani*, whereas a soil with similar physical-chemical properties (table S1), obtained from the margin of the same field, showed a high disease incidence (disease-conducive) (Fig. 1). In the absence of the fungal pathogen, no significant differences in plant growth and health were observed between the suppressive and conducive soils (table S2).

Most suppressive soils lose their disease-suppressive activity when pasteurized (*4*, *5*). When the *Rhizoctonia*-suppressive soil was heat treated at 50°C, disease suppressiveness was partially lost; treatment at 80°C resulted in a complete loss of suppressiveness, i.e., disease incidence increased to a level similar to that of the disease-conducive soil (Fig. 1B and fig. S1). Gamma irradiation too resulted in loss of suppressiveness (fig. S2). Soil-transfer experiments, in which small amounts (1 to 10% w/w) of suppressive soil were mixed with conducive soil before plant cultivation, showed that in a 1:9 (w/w) ratio of the *Rhizoctonia*-suppressive soil to the conducive soil, disease suppressiveness was partially transferred (Fig. 1 and fig. S1). Collectively, these results indicated that disease suppressiveness toward *R. solani* was microbiological in nature.

Metagenomic DNA was isolated from the rhizosphere microbiota of sugar beet plants grown in soils that exhibited different levels of disease suppressiveness: (i) suppressive soil; (ii) conducive soil; (iii) conducive soil amended with 10% (w/w) suppressive soil; (iv) suppressive soil heat-treated at 50°C; (v) suppressive soil heat-treated at 80°C; and (vi) suppressive soil inoculated with *R. solani* to identify any bacterial and archaeal taxa that responded to the presence of the fungal pathogen (fig. S3).

A total of 33,346 bacterial and archaeal operational taxonomic units (OTUs) were detected in the rhizosphere microbiome (Fig. 2A), a richness that surpasses that described in other studies (*7*, *8*). The overall distribution of the predominant bacterial phyla ranged from 1% for the Chloroflexi and Cyanobacteria to 20% and 39% for the Firmicutes and Proteobacteria, respectively; unclassified bacterial phyla represented a relatively large group (16%) (fig. S4).

When comparing the six soil treatments with different levels of disease suppressiveness, no significant differences were found in the number of detected bacterial taxa (Fig. 2A). However, when the abundance of the detected taxa was taken into account, we found six clusters of samples that corresponded to the six soil treatments (Fig. 2B and fig. S5). These results suggest that the relative abundance of several bacterial taxa is a more important indicator of disease suppression than the exclusive presence of specific bacterial taxa.

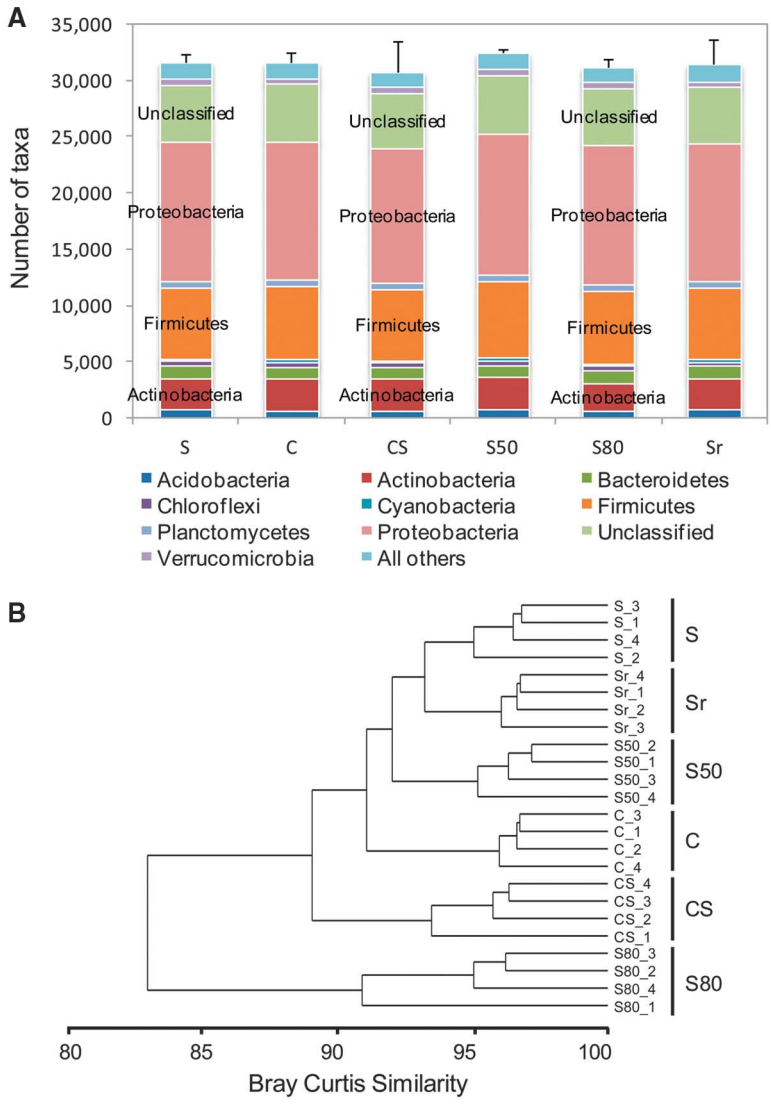

Fig. 2. (**A**) Number of OTUs passing stage 1 PhyCA (mean ± SEM, $N = 4$). (**B**) Cluster analysis (Bray-Curtis) of the rhizosphere microbiomes of sugar beet seedlings grown in soils with different levels of disease suppressiveness. Sr, suppressive soil amended with *R. solani*; other abbreviations as in Fig. 1. In (B), numbers 1 to 4 refer to the replicates of each treatment.

The γ- and β-Proteobacteria (Pseudomonadaceae, Burkholderiaceae, Xanthomonadales) and the Firmicutes (Lactobacillaceae) were identified as the most dynamic taxa associated with disease suppression: These were all more abundant in suppressive soil than in conducive soil; more abundant in the transplantation soil (conducive soil + 10% suppressive soil) than in the conducive soil; and more abundant in the suppressive soil when *R. solani* was present (Fig. 3 and table S3). Separate clustering analyses confirmed their association with disease suppressiveness (fig. S6). The Actinobacteria too were more abundant in suppressive than in conducive soil and were the most dynamic taxa in the suppressive soil amended with the fungal pathogen (Fig. 3).

Culture-based approaches for identifying functional groups involved in disease suppressiveness of soils have focused on bacterial taxa that are easy to grow and amenable to genetic and genomic analyses (*4*). For example, Pseudomonadaceae have been found to contribute to the natural suppressiveness of soils against the fungal pathogens *Fusarium oxysporum* and *Gaeumannomyces graminis* (*4*, *5*). Notably, the culture-independent PhyloChip analysis we conducted also pointed to a prominent role for γ-Proteobacteria, especially Pseudomonadaceae, in soil suppressiveness against *R. solani*. Hence, we focused subsequent studies on this group of bacteria.

Cultures of rhizosphere suspensions of sugar beet plants grown in disease-suppressive or

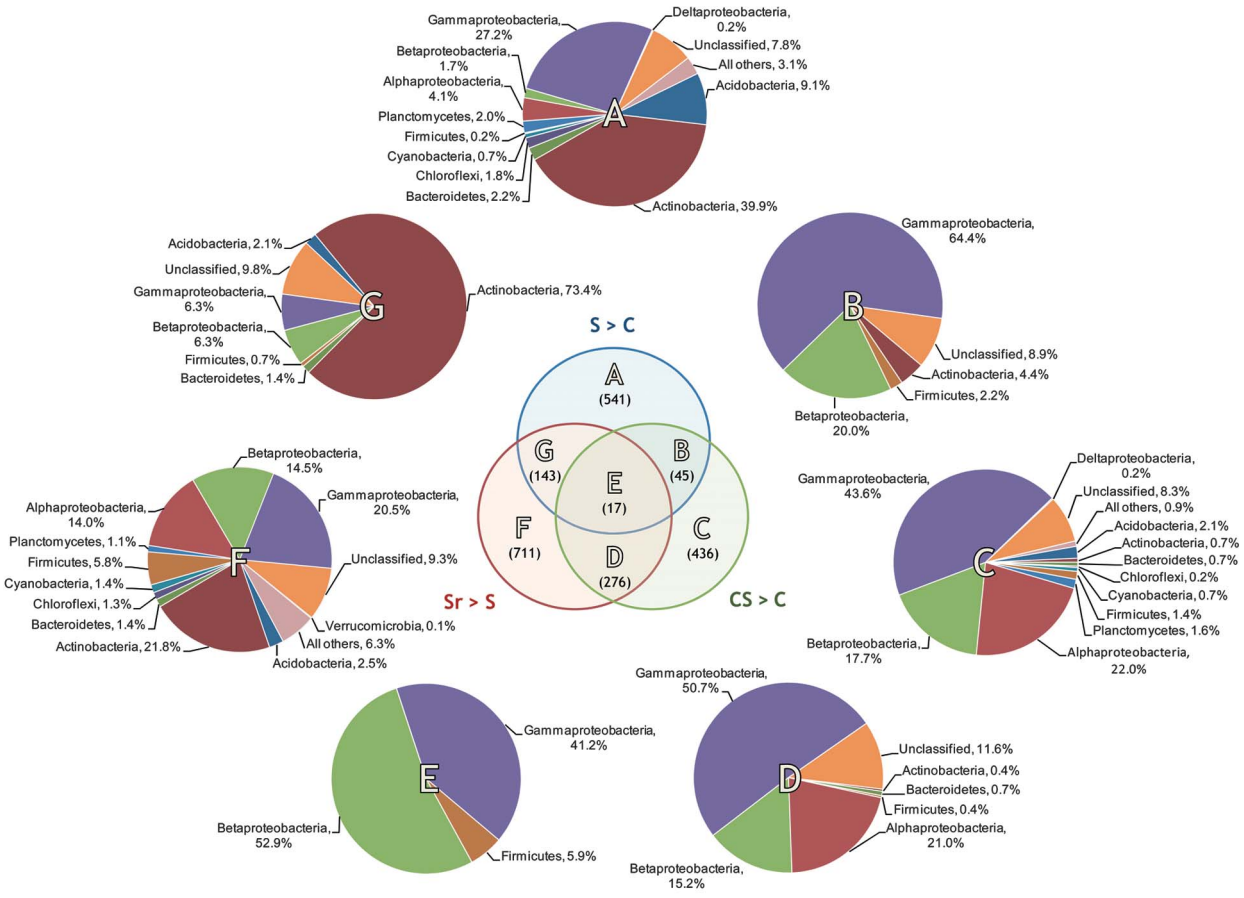

Fig. 3. Bacterial and archaeal taxa associated with disease suppressiveness. Shown are taxa that are more abundant in (i) suppressive (S) than in conducive soil (C) (pie A), (ii) "transplantation soil" (C+10%S) than in C (pie C), and (iii) S amended with *R. solani* (Sr) than in S (pie F). Pairwise comparisons (N = 4) depict the compositions of the top 10% of most dynamic taxa. Numbers of taxa in each subset are in parentheses. In pie charts A to G, names of taxonomic groups are followed by their frequency. The top 10% of most dynamic taxa that meet all three criteria are shown in pie E and in table S3.

disease-conducive soils were randomly selected, purified, and tested for activity against *R. solani* (table S4). Most of the antagonistic bacterial isolates from the suppressive soil (i.e., 104 out of 111) were obtained from the growth medium that is semiselective for the Pseudomonadaceae. DNA fingerprinting by BOX–polymerase chain reaction (PCR) grouped the antagonistic isolates from the suppressive soil into 10 haplotypes (SH-A to SH-J). 16*S* rDNA sequencing confirmed that these isolates belonged to the Pseudomonadaceae (Fig. 4A). Alignments and BLAST searches in the PhyloChip database, using the 16*S* rDNA sequences, verified that these haplotypes were closely related (94 to 98% identity) to the five most dynamic Pseudomonadaceae (table S3) and were more abundant in suppressive than in conducive soil (Fig. 4B).

Haplotypes SH-A (38 isolates), SH-B (21 isolates), and SH-C (37 isolates) constituted 90% of the antagonistic bacterial isolates from the disease-suppressive soil and were selected for further functional analyses. Plant bioassays with representative isolates of each of these three haplotypes showed that only strain SH-C52

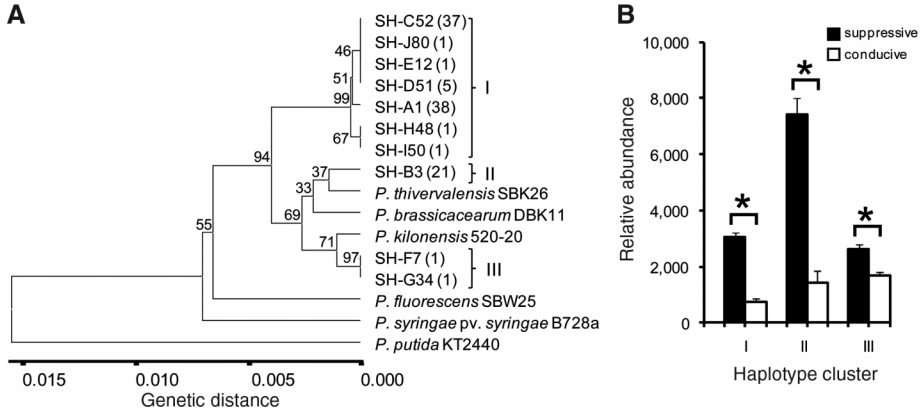

Fig. 4. (**A**) Hierarchical clustering of 16*S* rDNA genes of bacterial strains isolated from the rhizosphere of sugar beet seedlings grown in disease-suppressive soil. Different *Pseudomonas* species and type strains were used as references. Among the isolates that inhibit growth of *R. solani*, 10 haplotypes (SH-A to SH-J) were identified by BOX-PCR. Numbers of isolates of each haplotype are indicated in parentheses, and three haplotype clusters (I to III) were designated. (**B**) Relative abundance of haplotype clusters I to III in suppressive and conducive soils on the basis of PhyloChip analysis. 16*S* rDNA sequences of haplotypes SH-A to SH-J were used in BLAST searches in the PhyloChip database, and the best hits (table S5) were used to calculate the relative abundance of haplotype clusters I to III (mean ± SEM, N = 4). An asterisk indicates a statistically significant difference (P < 0.01, Student's t test) between suppressive and conducive soils.

protected sugar beet seedlings from infection by *R. solani* (fig. S7). Random transposon mutagenesis generated two mutants of strain SH-C52 with no in vitro activity against *R. solani*. The single transposon insertions were mapped to a nonribosomal peptide synthetase (NRPS) gene with 69% sequence identity to *syrE*, the gene of the syringomycin-syringopeptin (*syr-syp*) biosynthetic pathway in *Pseudomonas syringae* pv. *syringae* (*9*). NRPS-mutant O33 colonized the rhizosphere to the same extent as its parental strain SH-C52, but did not protect sugar beet seedlings from fungal infection (fig. S7). Subsequent genetic analyses revealed that the putative biosynthetic pathway consisted of two gene clusters, designated *thaAB* and *thaC1C2D*, which were predicted to encode a nine–amino acid chlorinated lipopeptide (fig. S8).

The multifaceted approach adopted in this study, linking culture-independent and culture-dependent analyses, shows that plants, like mammals and insects (*10*–*12*), can rely on specific constituents of the microbial community for protection against pathogen infections. We showed that the γ-Proteobacteria, and specifically members of the Pseudomonadaceae, protect plants from fungal infection through the production of a putative chlorinated lipopeptide encoded by NRPS genes. Functional analysis further revealed a significant difference in plant disease suppression between haplotypes SH-A and SH-C (fig. S7), suggesting that in situ antifungal activity is governed by individual members of this bacterial taxon. Next to the Pseudomonadaceae, several other bacterial taxa were found in this study to be associated with disease suppressiveness (Fig. 3). Some of these taxa, including the Burkholderiaceae, Xanthomonadales, and Actinobacteria, harbor genera and species with activity against plant pathogenic fungi, including *R. solani* (*13*). These findings suggest that the complex phenomenon of disease suppressiveness of soils cannot simply be ascribed to a single bacterial taxon or group, but is most likely governed by microbial consortia. The observation that bacterial strains, which lack activity against pathogens when tested alone, can act synergistically when part of microbial consortia (*14*) further exemplifies the complexity of adopting Koch's postulates for identification of microorganisms involved in disease suppressiveness of soils. The bacteria and biosynthetic pathway identified here provide a set of microbial and genetic markers to elucidate whether and how plants recruit beneficial soil microorganisms for protection against infections.

References and Notes

1. H. Marschner, *Mineral Nutrition of Higher Plants* (Academic Press, London, ed. 2, 1995).
2. T. Bisseling, J. L. Dangl, P. Schulze-Lefert, *Science* **324**, 691 (2009).
3. R. J. Cook *et al.*, *Proc. Natl. Acad. Sci. U.S.A.* **92**, 4197 (1995).
4. D. Haas, G. Défago, *Nat. Rev. Microbiol.* **3**, 307 (2005).
5. D. M. Weller, J. M. Raaijmakers, B. B. M. Gardener, L. S. Thomashow, *Annu. Rev. Phytopathol.* **40**, 309 (2002).
6. T. C. Hazen *et al.*, *Science* **330**, 204 (2010).
7. K. M. DeAngelis *et al.*, *ISME J.* **3**, 168 (2009).
8. P. D. Schloss, J. Handelsman, *PLOS Comput. Biol.* **2**, e92 (2006).
9. H. Feil *et al.*, *Proc. Natl. Acad. Sci. U.S.A.* **102**, 11064 (2005).
10. R. E. Ley *et al.*, *Science* **320**, 1647 (2008).
11. J. Qin *et al.*, MetaHIT Consortium, *Nature* **464**, 59 (2010).
12. J. J. Scott *et al.*, *Science* **322**, 63 (2008).
13. J. Postma, R. W. A. Scheper, M. T. Schilder, *Soil Biol. Biochem.* **42**, 804 (2010).
14. P. Garbeva, M. W. Silby, J. M. Raaijmakers, S. B. Levy, W. D. Boer, *ISME J.* (2011).

Acknowledgments: We thank T. Bisseling for critical reading and valuable suggestions. We acknowledge assistance by L. Sibbel-Wagemakers, N. Pangesti, M. de Milliano, N. Sharma, R. de Vries, P.M.S. van Oorschot, A. H. L. Schoone, and Y. Bakker. This work was financially supported by grants from Netherlands Science Organisation (NWO)–ERGO (#838.06.101) and Netherlands Genomics Initiative–Ecogenomics, Netherlands. Additional work was performed at Lawrence Berkeley National Laboratory (LBNL) (contract DE-AC02-05CH11231 with the U.S. Department of Energy). The 16*S* rDNA sequences are available on GenBank under accessions HQ848634 to HQ848643, and the *thaABCD* sequences under accession HQ888764. LBNL has a patent on the PhyloChip assay and Second Genome has licensed this assay from LBNL. Although the G3 PhyloChip is under patent (and under exclusive license to Second Genome), the data generated from the use of the chip are not patented or restricted. T.Z.dS. owns stock in Second Genome valued at under $10,000.

Supporting Online Material

www.sciencemag.org/cgi/content/full/science.1203980/DC1
Materials and Methods
Figs. S1 to S8
Tables S1 to S5

8 February 2011; accepted 20 April 2011
Published online 5 May 2011;
10.1126/science.1203980

Differences Between Tight and Loose Cultures: A 33-Nation Study

Michele J. Gelfand,[1]* Jana L. Raver,[2] Lisa Nishii,[3] Lisa M. Leslie,[4] Janetta Lun,[1] Beng Chong Lim,[5] Lili Duan,[6] Assaf Almaliach,[7] Soon Ang,[8] Jakobina Arnadottir,[9] Zeynep Aycan,[10] Klaus Boehnke,[11] Pawel Boski,[12] Rosa Cabecinhas,[13] Darius Chan,[14] Jagdeep Chhokar,[15] Alessia D'Amato,[16] Montse Ferrer,[17] Iris C. Fischlmayr,[18] Ronald Fischer,[19] Marta Fülöp,[20] James Georgas,[21] Emiko S. Kashima,[22] Yoshishima Kashima,[23] Kibum Kim,[24] Alain Lempereur,[25] Patricia Marquez,[26] Rozhan Othman,[27] Bert Overlaet,[28] Penny Panagiotopoulou,[29] Karl Peltzer,[30] Lorena R. Perez-Florizno,[31] Larisa Ponomarenko,[32] Anu Realo,[33] Vidar Schei,[34] Manfred Schmitt,[35] Peter B. Smith,[36] Nazar Soomro,[37] Erna Szabo,[18] Nalinee Taveesin,[38] Midori Toyama,[39] Evert Van de Vliert,[40] Naharika Vohra,[41] Colleen Ward,[42] Susumu Yamaguchi[43]

With data from 33 nations, we illustrate the differences between cultures that are tight (have many strong norms and a low tolerance of deviant behavior) versus loose (have weak social norms and a high tolerance of deviant behavior). Tightness-looseness is part of a complex, loosely integrated multilevel system that comprises distal ecological and historical threats (e.g., high population density, resource scarcity, a history of territorial conflict, and disease and environmental threats), broad versus narrow socialization in societal institutions (e.g., autocracy, media regulations), the strength of everyday recurring situations, and micro-level psychological affordances (e.g., prevention self-guides, high regulatory strength, need for structure). This research advances knowledge that can foster cross-cultural understanding in a world of increasing global interdependence and has implications for modeling cultural change.

How "other" cultures differ from one's own has piqued the curiosity of scholars and laypeople across the centuries. As long ago as 400 B.C.E., Herodotus documented a wide variety of cultural practices that he observed in his travels in *The Histories* (*1*). Only in the past few decades have scientists begun to move beyond descriptive accounts of cultural differences to empirically assess ways in which national cultures vary. We examine a neglected source of cultural variation that is dominating the geo-political landscape and has the potential to be a major source of cultural conflict: the difference between nations that are "tight"—have strong norms and a low tolerance of deviant behavior—and those that are "loose"—have weak norms and a high tolerance of deviant behavior.

Early anthropological research showed the promise of this distinction. In his study of 21 traditional societies, Pelto (*2*) documented wide variation in the expression of and adherence to social norms. The Hutterites, Hanno, and Lubara were among the tightest societies, with very strong norms and severe sanctions for norm violation, whereas the Kung Bushman, Cubeo, and the Skolt Lapps were among the loosest societies, with ambiguous norms and greater permissiveness for norm violation. Pelto speculated that these societies may have different ecologies, with tight societies having a higher population per square mile and a higher dependence on crops as compared to loose societies. Later research indeed showed that agricultural societies (e.g., the Temne of Sierra Leone), which require strong norms to foster the coordination necessary to grow crops for survival, had strict child-rearing practices and children who were high

on conformity. Hunting and fishing societies (e.g., the Inuit) had lenient child-rearing practices and children who were low on conformity (*3*, *4*).

Despite evidence of the importance of this contrast in traditional societies, there exists no insight into how tightness-looseness operates in modern nations. The goal of this research is to fill this void. Drawing on theorizing in cultural psychology (*5*, *6*), we propose that tightness-looseness is part of a complex, loosely integrated system that involves processes across multiple levels of analysis (Fig. 1). We theorize that the strength of social norms and tolerance of deviant behavior—the core distinction between tight and loose cultures—is afforded by numerous distal ecological and human-made societal threats and societal institutions and practices. The strength of social norms and tolerance of deviant behavior is further reflected and promoted in the predominance of strong versus weak situations that are recurrent in everyday local worlds, and is reinforced through psychological processes that are attuned to situational requirements. We provide an empirical test that shows how ecological, historical, and institutional factors, along with everyday situations and psychological processes, together constitute cultural systems.

We predict that tightness-looseness is afforded by a broad array of ecological and human-made societal threats (or lack thereof) that nations have historically encountered (*4*, *7*). Ecological and human-made threats increase the need for strong norms and punishment of deviant behavior in the service of social coordination for survival—whether it is to reduce chaos in nations that have high population density, deal with resource scarcity, coordinate in the face of natural disasters, defend against territorial threats, or contain the spread of disease. Nations facing these particular challenges are predicted to develop strong norms and have low tolerance of deviant behavior to enhance order and social coordination to effectively deal with such threats. Nations with few ecological and human-made threats, by contrast, have a much lower need for order and social coordination, affording weaker social norms and much more latitude (*8*).

The strength of social norms and tolerance of deviant behavior is also afforded by and reflected in prevailing institutions and practices. Institutions in tight nations have narrow socialization that restricts the range of permissible behavior, whereas institutions in loose nations encourage broad socialization that affords a wide range of permissible behavior (*9*). Relative to loose nations, tight nations are more likely to have autocratic governing systems that suppress dissent, to have media institutions (broadcast, paper, Internet) with restricted content and more laws and controls, and to have criminal justice systems with higher monitoring, more severe punishment (e.g., the death penalty), and greater deterrence and control of crime. Tight nations will also be more religious, thereby reinforcing adherence to moral conventions and rules that can facilitate social order and coordination (*10*). Challenges to societal institutions (e.g., demonstrations, boycotts, strikes) will be much less common in tight nations than in loose ones. These institutions and practices simultaneously reflect and support the strength of norms and tolerance of deviance that exists in nations.

Tightness-looseness is manifested not only in distal ecological, historical, and institutional contexts but also in everyday situations in local worlds (e.g., at home, in restaurants, classrooms, public parks, libraries, the workplace) that individuals inhabit (*5*, *6*). We theorize that tightness-looseness is reflected in the predominance of strong versus weak everyday situations (*11*, *12*). Strong situations have a more restricted range of appropriate behavior, have high censuring potential, and leave little room for individual discretion. Weak situations place few external constraints on individuals, afford a wide range of behavioral options, and leave much room for individual discretion. Situational strength has been long discussed among psychologists, sociologists, and anthropologists (*11*–*14*) but has yet to be linked to cultural variation. Tight nations are expected to have a much higher degree of situational constraint which restricts the range of behavior deemed appropriate across everyday situations (e.g., classrooms, libraries, public parks, etc.). By contrast, loose nations are expected to have a much weaker situational structure, affording a much wider range of permissible behavior across everyday situations. The strength (or weakness) of everyday recurring situations within nations simultaneously reflects and supports the degree of order and social coordination in the larger cultural context.

We further theorize that there is a close connection between the strength (versus weakness) of everyday situations and the chronic psychological processes of individuals within nations. In this view, individuals' psychological processes become naturally attuned to, and supportive of, the situational demands in the cultural system (*15*). Individuals who are chronically exposed to stronger (versus weaker) situations in their everyday local worlds have the continued subjective experience that their behavioral options are limited, their actions are subject to evaluation, and there are potential punishments based on these evaluations. Accordingly, individuals in nations with high situational constraint will have self-guides that are more prevention-focused (*16*) and thus will be more cautious (concerned with avoiding mistakes) and dutiful (focused on behaving properly), and will have higher self-regulatory strength (higher impulse control) (*17*), a higher need for structure (*18*), and higher self-monitoring ability (*19*, *20*). Put simply, the higher (or lower) degree of social regulation that exists at the societal level is mirrored in the higher (or lower) amount of self-regulation at the individual level in tight and loose nations, respectively. Such psychological processes simultaneously reflect and support the strength of social norms and tolerance of deviance in the larger cultural context.

To provide a systematic analysis of tightness-looseness in modern societies, we gathered data

[1]Department of Psychology, University of Maryland, College Park, MD 20742, USA. [2]Queen's School of Business, Kingston, Ontario K7L 3N6, Canada. [3]Cornell University Industrial Labor Relations School, Ithaca, NY 14853, USA. [4]Carlson School of Management, University of Minnesota, Minneapolis, MN 55455, USA. [5]Ministry of Defense, Singapore and Nanyang Business School, Defense Technology Towers, 5 Depot Road, #16-01 Tower B, Singapore. [6]McKinsey & Company, Washington, DC 20036, USA. [7]BIP Institute of Psychology Ltd., Vita Towers, 11 Ben-Gurion Street, Bney-Brak 51260, Israel. [8]Nanyang Technological University, Nanyang Avenue 639798, Singapore. [9]Kaplaskjolsvegur 29, IS-107 Reykjavik, Iceland. [10]Department of Psychology, Koc University, Sariyer 34450, Turkey. [11]Bremen International Graduate School of Social Sciences, Jacobs University Bremen, D-28759 Bremen, Germany. [12]Warsaw School of Social Sciences and Humanities, 03-815 Warsaw, Poland. [13]University of Minho, Campus de Gualtar, 4710-057 Braga, Portugal. [14]Department of Psychology, Chinese University of Hong Kong, 3rd Floor, Sino Building, Shatin, N.T., Hong Kong. [15]Indian Institute of Management, Ahmedabad-380015, India. [16]CENTRUM Catolica, Pontificia Universidad Catolica del Peru, Lima 33, Peru. [17]Social Psychology Department, University of Valencia, Avenida Blasco Ibáñez, 21, 46010 Valencia, Spain. [18]Johannes Kepler University, Institute for International Management, Altenbergerstrasse 69, 4040 Linz, Austria. [19]School of Psychology, Centre for Applied Cross-Cultural Psychology, Victoria University of Wellington, PO Box 600, Wellington, New Zealand. [20]Institute for Psychology, Hungarian Academy of Sciences, Victor Hugo Street 18-22, Budapest 1132, Hungary. [21]University of Athens, 11 Herodou Attikou, Athens 106 74, Greece. [22]School of Psychological Science, La Trobe University, Bundoora, Victoria 3086, Australia. [23]Psychological Sciences University of Melbourne, Victoria 3010, Australia. [24]School of Social Sciences, Sungkyunkwan University, Myungryun-dong 3 ga, Jongno-gu, Seoul 110-745, Korea. [25]ESSEC Business School, Av. Bernard Hirsch, B.P. 50105, 95021 Cergy Pontoise Cedex, France. [26]University of San Diego, 235 Olin Hall, 5998 Alcala Park, San Diego, CA 92131, USA. [27]21 Jalan 5C/6, 43650 B B Bangi, Selangor, Malaysia. [28]KU Leuven, Naamsestraat 67, B-3000 Leuven, Belgium. [29]University of Patras, 26500 Rio, Patras, Greece. [30]Human Sciences Research Council, Private Bag X41, Pretoria 0001, South Africa. [31]Investigadora Colegio de la Fontera Norte, Km 18.5 carretera escénica Tijuana - Ensenada, San Antonio del Mar, Tijuana, Baja California C.P. 22560, México. [32]Psychology Department, Odessa National University, Dvorianskaya str. 2, Odessa 67027, Ukraine. [33]Department of Psychology, University of Tartu, Tiigi 78, Tartu 50410, Estonia. [34]Department of Strategy and Management, Norwegian School of Economics and Business Administration, Breiviksveien 40, 5045 Bergen, Norway. [35]Universität Koblenz-Landau, Fortstraße 7, D-76829 Landau, Germany. [36]Department of Psychology, University of Sussex, Falmer, Brighton BN1 9QH, UK. [37]Department of Psychological Testing, Guidance and Research, University of Sindh, Elsa Kazi Campus, Hyderabad 71000, Pakistan. [38]33 Soonvijai 4, Bangkok 10310, Thailand. [39]Department of Psychology Gakushuin University, 1-5-1 Mejiro, Toshima-ku, Tokyo 171-8588, Japan. [40]University of Groningen, Grote Kruisstraat 2/1, 9712 TS Groningen, Netherlands. [41]Indian Institute of Management, Wing 12, IIM Campus, Vastrapur, Ahmedabad, Gujarat 380015, India. [42]School of Psychology, P.O. Box 600, Victoria University of Wellington, Wellington 6140, New Zealand. [43]Department of Social Psychology, Graduate School of Humanities and Sociology, University of Tokyo, Hongo 7-3-1, Bunkyo-ku, Tokyo 113-0033, Japan.

*To whom correspondence should be addressed. E-mail: mgelfand@psyc.umd.edu

from 6823 respondents across 33 nations (*20*). Sample characteristics are shown in Table 1 (*21*). In each nation, we surveyed individuals from a wide range of occupations as well as university students. Data on ecological and historical threats and societal institutions were collected from numerous established databases (*20*). When possible, historical data were included (e.g., population density in 1500, history of conflict 1918–2001, historical prevalence of pathogens).

Tightness-looseness (the overall strength of social norms and tolerance of deviance) was measured on a six-item Likert scale that assessed the degree to which social norms are pervasive, clearly defined, and reliably imposed within nations. Example scale items include "There are many social norms that people are supposed to abide by in this country," "In this country, if someone acts in an inappropriate way, others will strongly disapprove," and "People in this country almost always comply with social norms." The results show strong support for the reliability and validity of the measure (*20*). Ecological factor analyses and Procrustes factor analysis in all 33 nations illustrate that the scale exhibits factor validity and measurement equivalence. Analyses show that the strength of social norms and tolerance of deviance is a shared collective construct: There is high within-nation agreement in each nation [$r_{\text{within-group}}(M)$ = 0.85], high between-nation variability [$F(32, 6{,}774) = 31.23$, $P < 0.0001$; intraclass correlation (ICC)(1) = 0.13], and high reliability of the tightness-looseness scale means [ICC(2) = 0.97]. The scale has high convergent validity with expert ratings, unobtrusive measures, and survey data from representative samples; is able to adequately discriminate between cultural regions; and is distinct from other cultural dimensions (*20*) (tables S1 and S2).

The degree of constraint across a wide range of everyday social situations was measured through adaptations to Price and Bouffard's established measure (*20*). Participants rated the appropriateness of 12 behaviors (i.e., argue, eat, laugh, curse/swear, kiss, cry, sing, talk, flirt, listen to music, read newspaper, bargain) across 15 situations (i.e., bank, doctor's office, job interview, library, funeral, classroom, restaurant, public park, bus, bedroom, city sidewalk, party, elevator, workplace, movies), resulting in a total of 180 behavior-situation ratings (*20*). For a given situation, the mean appropriateness ratings across behaviors indicate the degree of situational constraint: Low values indicate that there are few behaviors considered appropriate in that situation, whereas high values indicate that a wide range of behaviors are considered appropriate in that situation. Country-level scores of situational constraint were derived by averaging scores across situations. Analyses illustrate that the situational constraint measure is a shared collective construct within nations (*20*): There is high within-nation agreement about the level of constraint in everyday situations in each nation [$r_{\text{within-group}}(M) = 0.99$], high between-nation variability in situational constraint [$F(32, 6790) = 92.9$, $P < 0.0001$; ICC(1) = 0.31], and high reliability of the situational constraint means [ICC(2) = 0.99]. There is strong construct validity of the measure (*20*). Respondents in each nation also provided direct ratings regarding whether the 15 situations had clear rules for appropriate behavior, called for certain behaviors and not others, required people to monitor their behavior or "watch what they do," and allowed individuals to choose their behavior (reverse-coded), the average of which is highly correlated with the behavior-situation ratings ($r = 0.74$, $P < 0.001$). The correlation of the current situational constraint data in the United States with those reported by Price and Bouffard is 0.92 ($P < 0.001$) (*20*), which suggests that the degree of constraint across situations is generally stable across time.

Psychological processes (prevention focus, self-regulation strength, need for order, self-monitoring) were assessed with well-validated measures (*20*). Procrustes factor analysis of all of the measures across the 33 nations all evidenced high equivalence and high degrees of cross-national variation (*20*).

To test our predictions, we first examine the relationships between tightness-looseness and ecological and historical institutions. Because many of these variables are associated with national wealth, we controlled for nations' GNP per capita to examine their unique relationships with tightness-looseness. We next illustrate how tightness-looseness is related to the strength of everyday situations and examine the cross-level relationship between the strength of situations and numerous psychological processes with the use of hierarchical linear modeling. We provide a test of the overall model with multilevel structural equation analysis (*20*).

Table S3 illustrates that nations that have encountered ecological and historical threats have much stronger norms and lower tolerance of deviant behavior. Tight nations have higher population density in the year 1500 ($r = 0.77$, $P = 0.01$), in the year 2000 in the nation ($r = 0.31$, $P = 0.10$), and in the year 2000 in rural areas ($r = 0.59$; $P = 0.02$), and also have a higher projected population increase ($r = 0.40$, $P = 0.03$). Tight nations have a dearth of natural resources, including a lower percentage of farmland ($r = -0.37$, $P = 0.05$), higher food deprivation ($r = 0.52$, $P < 0.01$), lower food supply and production ($r = -0.36$, $P = 0.05$, and -0.40, $P = 0.03$, respectively), lower protein and fat supply (rs = -0.41 and -0.46, Ps = 0.03 and 0.01), less access to safe water ($r = -0.50$, $P = 0.01$), and lower air quality ($r = -0.44$, $P = 0.02$), relative to loose nations. Tight nations face more disasters such as floods, tropical cyclones, and droughts ($r = 0.47$, $P = 0.01$) and have had more territorial threats from their neighbors during the period 1918–2001 ($r = 0.41$, $P = 0.04$). Historical prevalence of pathogens was higher in tight

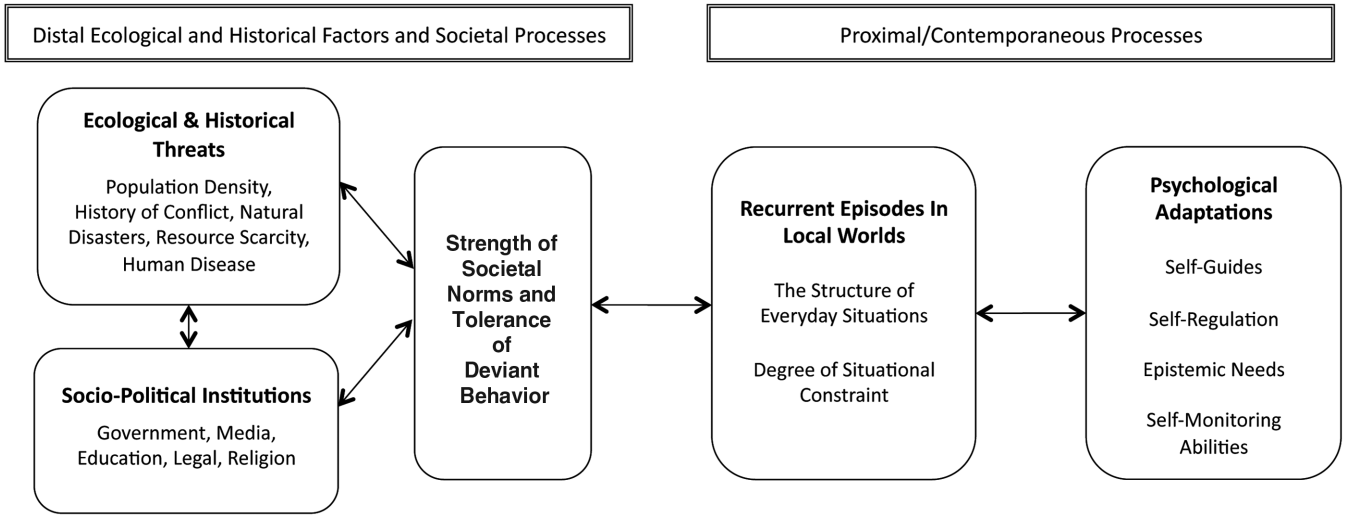

Fig. 1. A systems model of tightness-looseness.

nations ($r = 0.36$, $P = 0.05$), as were the number of years of life lost to communicable diseases ($r = 0.59$, $P < 0.01$), the prevalence of tuberculosis ($r = 0.61$, $P < 0.01$), and infant and child mortality rates (rs = 0.42, $P = 0.02$, and 0.46, $P = 0.01$).

Tightness-looseness is reflected in societal institutions and practices (table S3). Tight nations are more likely to have autocratic rule that suppresses dissent ($r = 0.47$, $P = 0.01$), less open media overall ($r = -0.53$, $P < 0.01$), more laws and regulations and political pressures and controls for media (rs = 0.37 to 0.62, Ps ≤ 0.05), and less access to and use of new communication technologies ($r = -0.38$, $P = 0.04$). Tight nations also have fewer political rights and civil liberties (rs = −0.50 and −0.45, Ps ≤ 0.01). Criminal justice institutions in tight nations are better able to maintain social control: There are more police per capita ($r = 0.31$, $P = 0.12$), stricter punishments (i.e., retention of the death penalty) ($r = 0.60$, $P < 0.01$), and lower murder rates and burglary rates (rs = −0.45 and −0.47, Ps < 0.01) and overall volume of crime ($r = -0.37$, $P = 0.04$). Tight nations are more religious, with more people attending religious services per week ($r = 0.54$, $P < 0.01$) and believing in the importance of god in life ($r = 0.37$, $P < 0.05$) (*20*). The percentage of people participating in collective actions (e.g., signing petitions, attending demonstrations) is much lower in tight nations ($r = -0.40$, $P = 0.03$), and more people report that they would never engage in such actions ($r = 0.36$, $P = 0.05$) in comparison to loose nations.

Tightness-looseness is also related to the strength of everyday recurring situations within nations. As predicted, there is much higher situational constraint in tight versus loose nations ($r = 0.55$, $P < 0.01$) (*22*). In other words, there is much higher constraint across everyday situations—including the bank, public park, library, restaurant, bus, workplace, party, classroom, and the like—in loose nations, and much lower constraint across such everyday situations in tight nations (*20*). Hierarchical linear modeling intercept-as-outcomes models showed that higher levels of situational constraint are significantly related to greater prevention self-guides [higher cautiousness: $\gamma_{01} = 1.48$, $t(31) = 7.54$, $P < 0.01$; higher dutifulness: $\gamma_{01} = 1.11$, $t(31) = 5.05$, $P < 0.01$], greater self-regulation strength [higher impulse control: $\gamma_{01} = 1.18$, $t(31) = 6.60$, $P < 0.01$], higher needs for structure [$\gamma_{01} = 2.67$, $t(31) = 5.76$, $P < 0.01$], and higher self-monitoring [$\gamma_{01} = 0.94$, $t(31) = 3.69$, $P < 0.01$] (*23*). This suggests that societal members' psychological characteristics are attuned to and supportive of the degree of constraint versus latitude in the larger cultural context. Multilevel structural equation analyses that simultaneously tested the proposed relations in Fig. 1 illustrated very good fit to the data (*20*).

In all, the data illustrate that tightness-looseness, a critical aspect of modern societies that has been heretofore unexplored, is a part of a

Table 1. Sample characteristics of the 33 nations.

Nation	Data collection site(s)	Language of survey	Number of participants	Mean age (±SD)	Percentage female	Percentage students	Tightness score
Australia	Melbourne	English	230	25.4 ± 10.0	69.1	63.9	4.4
Austria	Linz	German	194	31.6 ± 11.8	51.5	41.8	6.8
Belgium	Leuven (Flanders region)	Dutch	138	33.3 ± 14.3	73.2	50.7	5.6
Brazil	São Paulo	Portuguese	196	27.5 ± 9.4	72.3	40.3	3.5
Estonia	Tartu	Estonian	188	32.0 ± 16.8	86.6	52.1	2.6
France	Paris, Cergy	English	111	25.2 ± 4.1	37.8	67.6	6.3
Germany (former East)	Chemnitz	German	201	31.6 ± 12.2	66.7	49.3	7.5
Germany (former West)	Rhineland-Palatine/Frankfurt	German	312	32.5 ± 14.5	63.8	51.6	6.5
Greece	Athens	Greek	275	30.9 ± 11.3	56.7	45.1	3.9
Hong Kong	Hong Kong	Chinese	197	27.3 ± 11.7	68.0	53.8	6.3
Hungary	Budapest, Szeged	Hungarian	256	30.8 ± 10.9	42.2	48.0	2.9
Iceland	Reykjavík	Icelandic	144	36.3 ± 13.3	67.4	41.7	6.4
India	Ahmedabad, Bhubneswar, Chandigarh, Coimbatore	Hindi	222	27.8 ± 9.6	54.1	52.3	11.0
Israel	Tel-Aviv, Ramat-Gan, Jerusalem, Petach-Tikva	Hebrew	194	30.2 ± 10.7	60.3	48.5	3.1
Italy	Padova	Italian	217	29.6 ± 10.3	40.1	53.0	6.8
Japan	Tokyo, Osaka	Japanese	246	33.2 ± 14.9	55.7	48.8	8.6
Malaysia	Bandar Baru Bangi	Malay	202	29.5 ± 9.1	49.5	45.0	11.8
Mexico	Mexico City	Spanish	221	27.7 ± 11.6	42.1	40.3	7.2
Netherlands	Groningen	Dutch	207	29.8 ± 11.9	55.6	53.1	3.3
New Zealand	Wellington	English	208	29.9 ± 13.0	64.4	61.1	3.9
Norway	Bergen	Norwegian	252	31.8 ± 11.0	56.7	46.0	9.5
Pakistan	Hyderabad	Urdu	190	30.0 ± 9.8	51.1	52.6	12.3
People's Republic of China	Beijing	Chinese	235	29.4 ± 11.5	45.9	53.2	7.9
Poland	Warsaw	Polish	210	28.5 ± 12.4	65.2	51.9	6.0
Portugal	Braga	Portuguese	207	28.5 ± 11.6	54.6	58.0	7.8
Singapore	Singapore	English	212	26.1 ± 6.7	59.0	49.1	10.4
South Korea	Seoul	Korean	196	26.2 ± 7.5	61.2	73.5	10.0
Spain	Valencia	Spanish	172	30.2 ± 9.6	66.9	40.1	5.4
Turkey	Istanbul	Turkish	195	32.0 ± 14.4	53.3	45.6	9.2
Ukraine	Odessa	Ukrainian	184	30.8 ± 12.7	56.5	44.6	1.6
United Kingdom	Brighton	English	185	29.9 ± 11.5	67.0	51.4	6.9
United States	Washington, DC; Maryland; Virginia	English	199	31.4 ± 13.7	60.3	48.2	5.1
Venezuela	Caracas	Spanish	227	35.8 ± 10.0	60.4	1.3	3.7
Totals/means			**6823**	**30.1 ± 11.3**	**58.6**	**49.2**	**6.5**

system of interrelated distal and proximal factors across multiple levels of analysis. In addition to explicating how tight and loose cultures vary in modern societies, this research has implications for understanding and modeling how tight and loose cultures are maintained and changed. Substantial top-down or bottom-up changes in any of the levels in the model may trigger a rippling effect to other levels, resulting in changes in tight or loose cultures.

As culture is fundamentally a system, causal inferences regarding the direction of the relationships need further examination, particularly given that they are likely reciprocal. Future research should also apply the basic principles of the current work to explore variation in tightness-looseness at other levels of analysis (e.g., regions).

We also note that the samples in this study are not representative of each nation. However, the diverse backgrounds of the participants, high agreement among different subgroups, and correlations with other measures drawn from representative samples lend confidence to the generalizability of the results (*20*).

This research illuminates the multitude of differences that exist across tight and loose cultures. From either system's vantage point, the "other system" could appear to be dysfunctional, unjust, and fundamentally immoral, and such divergent beliefs could become the collective fuel for cultural conflicts. Indeed, as Herodotus (*1*) remarked centuries ago, "if one were to order all mankind to choose the best set of rules in the world, each group would, after due consideration, choose its own customs; each group regards its own as being the best by far" (p. 185). Such beliefs fail to recognize that tight and loose cultures may be, at least in part, functional in their own ecological and historical contexts. Understanding tight and loose cultures is critical for fostering cross-cultural coordination in a world of increasing global interdependence.

References and Notes

1. Herodotus, *The Histories* (Oxford, New York, 1998; R. Waterfield, Transl.).
2. P. J. Pelto, *Trans Action* **5**, 37 (1968).
3. H. Barry III, I. L. Child, M. K. Bacon, *Am. Anthropol.* **62**, 51 (1959).
4. J. W. Berry, *Adv. Exp. Soc. Psychol.* **12**, 177 (1979).
5. S. Kitayama, *Psychol. Bull.* **128**, 89 (2002).
6. A. Fiske, S. Kitayama, H. R. Markus, R. Nisbett, in *The Handbook of Social Psychology*, D. Gilbert, S. T. Fiske, G. Lindzey, Eds. (Oxford, New York, 1998), vol. 2, pp. 915–981.
7. H. C. Triandis, *The Analysis of Subjective Culture* (Wiley, New York, 1972).
8. We acknowledge that these relationships are only probabilistic, as cultures can find equifinal solutions to ecological and historical threats (*24*). Moreover, the degree of tightness-looseness in societies can further reinforce the ecological context (*6*), making these relationships potentially reciprocal.
9. J. J. Arnett, *J. Marriage Fam.* **57**, 617 (1995).
10. A. Norenzayan, A. F. Shariff, *Science* **322**, 58 (2008).
11. W. Mischel, in *Personality at the Crossroads*, E. Magnusson, N. S. Endler, Eds. (Erlbaum, Hillsdale, NJ, 1977).
12. R. H. Price, D. L. Bouffard, *J. Pers. Soc. Psychol.* **30**, 579 (1974).
13. E. D. Boldt, *Can. J. Sociol.* **3**, 349 (1978).
14. E. Goffman, *Behavior in Public Places: Notes on the Social Organization of Gatherings* (Greenwood, Westport, CT, 1963).
15. S. Kitayama, H. R. Markus, H. Matsumoto, V. Norasakkunkit, *J. Pers. Soc. Psychol.* **72**, 1245 (1997).
16. E. T. Higgins, *Psychol. Rev.* **94**, 319 (1987).
17. R. F. Baumeister, T. F. Heatherton, *Psychol. Inq.* **7**, 1 (1996).
18. S. L. Neuberg, J. T. Newsom, *Personal. Processes Indiv. Diff.* **65**, 113 (1993).
19. M. Snyder, *J. Pers. Soc. Psychol.* **30**, 526 (1974).
20. See supporting material on *Science* Online.
21. Most samples corresponded to nations; however, where subnational boundaries could be identified on the basis of historical circumstances, they were treated as separate samples (e.g., East and West Germany; Hong Kong and People's Republic of China).
22. For ease of interpretation, the situational constraint score was reversed such that high values are indicative of higher constraint.
23. We also ran these analyses with a split-sample approach (*25*) to eliminate single-source bias as an alternative explanation for our findings. Within each country we randomly assigned participants to one of two groups: One group provided the situational constraint scores and the other group provided the individual-difference scales. These hierarchical linear modeling results were the same as with the full sample.
24. D. Cohen, *Psychol. Bull.* **127**, 451 (2001).
25. C. Ostroff, A. J. Kinicki, M. A. Clark, *J. Appl. Psychol.* **87**, 355 (2002).

Acknowledgments: Supported by NSF grant 9910760 and U.S. Army Research Lab and Research Office grant W911NF-08-1-0144 (M.J.G.), Turkish Academy of Sciences (Z.A.), Polish Academy of Sciences (P.B.), Australian Research Council (Y.K.), and Estonian Ministry of Science (A.R.). We thank C. B. Bruss and R. Mohr for their help in preparing this manuscript.

Supporting Online Material

www.sciencemag.org/cgi/content/full/332/6033/1100/DC1
Materials and Methods
Tables S1 to S6
References

14 September 2010; accepted 6 April 2011
10.1126/science.1197754

MINIATURIZED CHROMATOGRAPHIC COLUMNS

PreDictor RoboColumn units are miniaturized chromatographic columns prepacked with GE Healthcare BioProcess chromatography media to enable high throughput process development (HTPD). PreDictor RoboColumn units support fully automated chromatographic separation workflows using robotic liquid handling workstations. The prepacked columns are available with a wide range of chromatography resins for ion exchange, affinity, multimodal, and hydrophobic interaction chromatography techniques. PreDictor RoboColumn units are designed for parallel screening of chromatographic conditions. Each row of eight columns is supplied with one chromatography media and individual columns can be easily arranged on a 96-position array plate. The columns are available in 50, 200, and 600 µl volumes and are compatible with solutions commonly used in the purification of biopharmaceuticals.

GE Healthcare

For info: 800-526-3593 | www.gelifesciences.com

CALIBRATION REAGENTS

Four Thermo Scientific Pierce Calibration Solutions are now offered for calibration of Thermo Scientific Mass Spectrometers, including the Thermo Scientific LTQ Orbitrap series and the Thermo Scientific TSQ Vantage series. The Pierce Calibration Solutions are ready-to-use liquid formulations that consist of highly purified ionizable molecules that produce strong peaks. The four reagents include Pierce ESI Negative Ion Calibration Solution, Pierce LTQ ESI Positive Ion Calibration Solution, Pierce LTQ Velos ESI Positive Ion Calibration Solution, and Pierce Triple Quadrupole Calibration Solution. All calibration solutions are manufactured in an ISO 9001 environment with strict specifications in quality-controlled lots and are provided in leak-proof, high-purity PTFE bottles for easy storage.

Thermo Fisher Scientific

For info: 800-874-3723 | www.thermoscientific.com/pierce

LIPID CHARACTERIZATION SOFTWARE

SimLipid analyzes lipid mass spectrometric data for characterizing lipids, greatly advancing lipidome data analysis. SimLipid can annotate mass spectra with identified lipid structures and abbreviations as well. SimLipid profiles lipids by matching the experimental MS spectra with its own comprehensive, robust, and annotated database, consisting of nine lipid classes and 1948 lipid species. It retrieves lipids that correspond with the observed m/z and user specified filter criteria. Alongside the probable lipid structure important information such as the lipid ID, lipid abbreviation, systematic name, lipid category, lipid mass, chemical formula, and other database links is also made available. In addition, users can look up the database using lipid abbreviation, mass, chemical composition, or lipid ID.

Premier Biosoft International

For info: 888-847-7494 | www.premierbiosoft.com

PROTEIN SAMPLE PREPARATION

The Perfinity Workstation is a multicolumn apparatus that automates protein separations and mass spectrometry (MS) sample preparation for more efficient liquid chromatography/mass spectrometry (LC/MS) analysis. The Perfinity Workstation uses Shimadzu hardware components in conjunction with five Perfinity Optimized columns that each perform a step of the MS sample-preparation process—affinity selection, buffer exchange, digestion, desalting, and reverse-phase separation. The automated integration of these steps enables users to start with serum and have peptides ready for LC/MS analysis in 10 minutes. The automated process removes much of the equipment and labor associated with MS analyses of proteins. The Perfinity Workstation combines the selectivity of antibodies with the resolving power of chromatography. Buffer exchange and desalting are performed online. The reduction in sample-processing time enables users to screen a variety of conditions rapidly.

Shimadzu Scientific Instruments

For info: 800-477-1227 | www.ssi.shimadzu.com

BENCHTOP MASS SPECTROMETER

The Waters Xevo G2 Tof (time-of-flight) mass spectrometer with UPLC/MS and QuanTof technology offers the most sensitive, exact mass quantitative and qualitative performance of any benchtop mass spectrometer system for scientists who need to confidently identify and quantify unknown compounds in complex samples. Powered by QuanTof technology, the Xevo G2 Tof brings SYNAPT G2 technology in an accessible, benchtop system for a new level of quantitative and qualitative performance. QuanTof technology combines an innovative high-field pusher and dual-stage reflectron with a novel ion detection system in an optimized time-of-flight geometry. Together these features provide a new dimension of high resolution, exact mass and quantitative performance uniquely available at acquisition rates that are compatible with UPLC separations.

Waters Corporation

For info: 800-252-4752 | www.waters.com

Electronically submit your new product description or product literature information! Go to **www.sciencemag.org/products/newproducts.dtl** for more information.

Newly offered instrumentation, apparatus, and laboratory materials of interest to researchers in all disciplines in academic, industrial, and governmental organizations are featured in this space. Emphasis is given to purpose, chief characteristics, and availability of products and materials. Endorsement by *Science* or AAAS of any products or materials mentioned is not implied. Additional information may be obtained from the manufacturer or supplier.

SHIMADZU

Exceeding Expectations as a Truly Innovative Mass Spectrometry Company

Be sure to discover our newest instruments & platforms:

LCMS-8030 Triple Quadrupole Mass Spectrometer
GCMS-QP2010 Ultra Gas Chromatograph Mass Spectrometer
Perfinity Workstation (Automated Sample Prep for MS)

ASMS

at *Booth #91* and/or *Capitol Ballrooms 5, 6, 7*
at the 59th ASMS Conference June 5-9, 2011

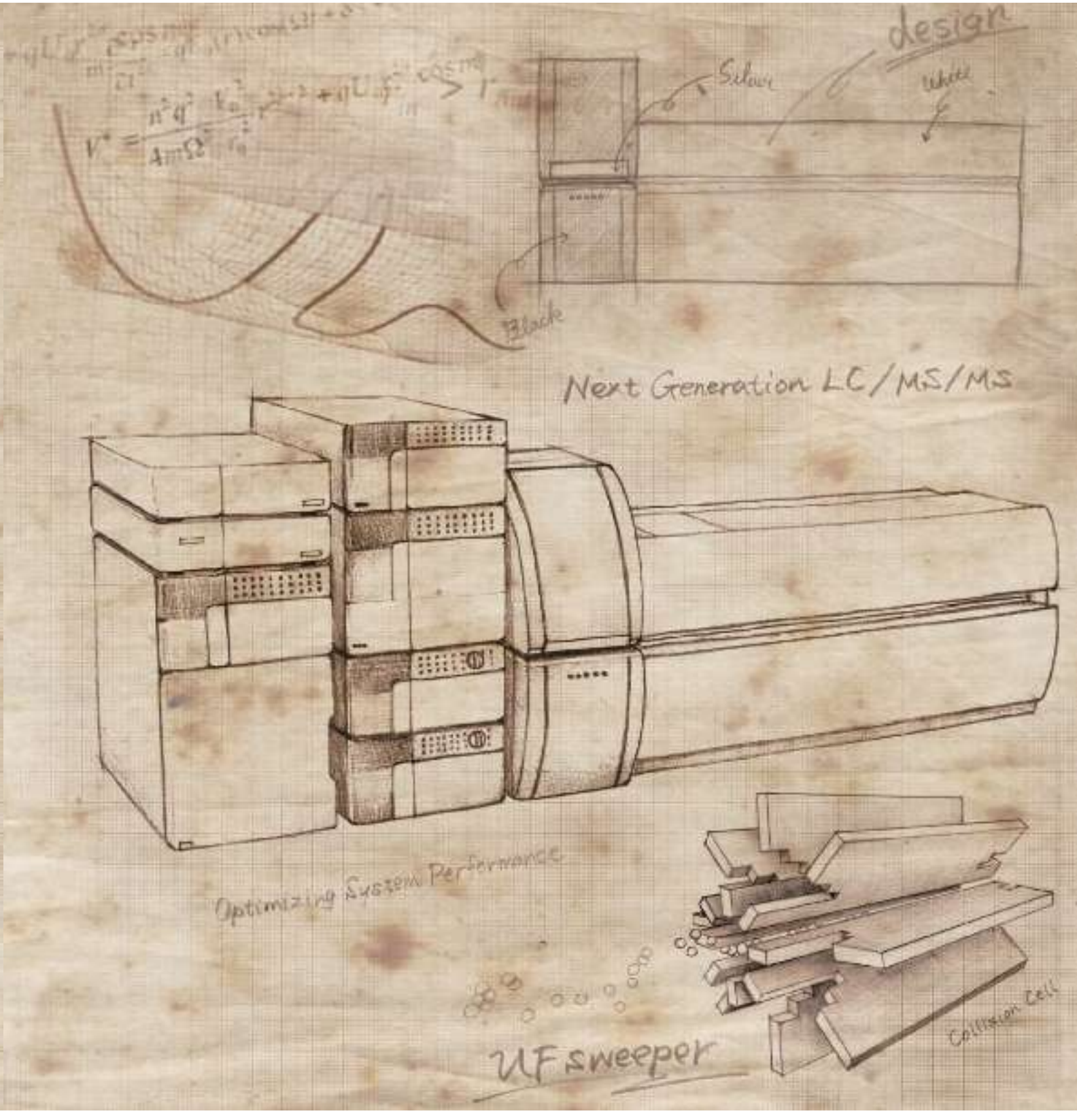

Shimadzu Scientific Instruments
North America

7102 Riverwood Drive Columbia, MD 21046 U.S.A.
Phone Number: 1-800-477-1227 Fax Number: 410-381-1222

Submission deadline August 1

Your name here.

The GE & Science Prize for Young Life Scientists. Because brilliant ideas build better realities.

Imagine standing on the podium at the Grand Hotel in Stockholm, making your acceptance speech for the GE & Science Prize for Young Life Scientists. Imagine having your essay read by your peers around the world. Imagine discussing your work in a seminar with other prize winners and Nobel Laureates. Imagine what you could do with the $25,000 prize money. Now stop imagining. If you were awarded your Ph.D. in molecular biology in 2010, then submit your 1000-word essay by August 1, and you can make it a reality.

Want to build a better reality? Go to www.gescienceprize.org

GE & Science Prize for Young Life Scientists

imagination at work

Science AAAS

* For the purpose of this prize, molecular biology is defined as "that part of biology which attempts to interpret biological events in terms of the physico-chemical properties of molecules in a cell".

(McGraw-Hill Dictionary of Scientific and Technical Terms, 4th Edition).

28-9402-06AB

One*Taq*™ DNA Polymerase

The ONE polymerase for your endpoint PCR needs

- Robust yield with minimal optimization
- Ideal for routine, AT- or GC-rich templates
- Hot start and master mix versions available

NEW ENGLAND BioLabs® Inc.
enabling technologies in the life sciences

Request a sample at
www.neb.com/OneTaq

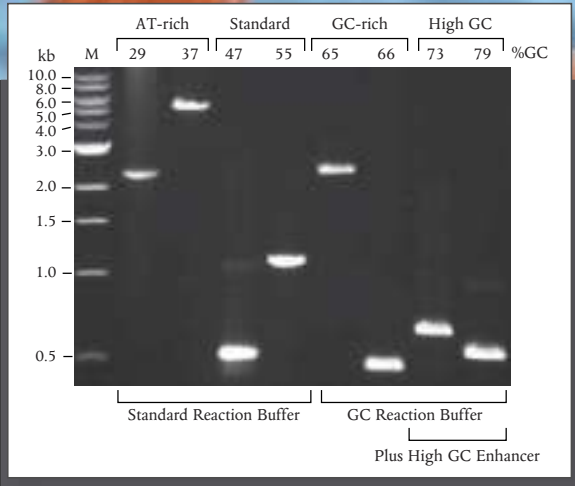

Amplification of a selection of sequences with varying AT and GC content from human and C. elegans genomic DNA, using OneTaq DNA Polymerase.

From DNA Sequence to Biological Relevance in RECORD TIME

Affordable, large-scale, complete human genome sequencing and analysis service that maximizes your discovery success

Complete Genomics has now delivered more than 1,000 complete human genomes to researchers like you, all over the world.

Our dedication to complete human genome sequencing and analysis enables scientists to conduct human disease research on large sample sets quickly and affordably—via a simple, outsourced service solution.

We produce the highest quality complete human genome datasets in the industry [1,2] including:

- Greater than 40x coverage (>50x on average)
- Over 90% of the genome and the exome confidently called (>95% on average)
- Comprehensive lists of annotated variants—including SNPs, indels, CNVs and SVs
- More than 400 genomes per month capacity

There are no expensive instruments to purchase, maintain and upgrade—and no complex laboratories to build and staff. You send us genomic DNA samples and receive research-ready sequencing results in record time.

Learn more at:
www.completegenomics.com/science

Complete genomics

Complete Genomics, Inc.
2071 Stierlin Court, Mountain View CA 94043 USA
Tel (650) 943-2800 | Email: info@completegenomics.com
Web: www.completegenomics.com

References:
1. Drmanac R, Sparks AB, Callow MJ, et al., *Science* **327**: 78-81. 2010.
2. Roach J, Glusman G, Smit AF, et al., *Science* **328**: 636-639. 2010.

Who's helping you get more for your retirement?

Take the Fidelity Challenge: Put your savings and current retirement savings provider to the test. We're already helping thousands of higher education professionals like you take a fresh look at their investments.

THE FIDELITY CHALLENGE

- ☐ **Start with a plan.** One that gives you the flexibility to make adjustments as your needs change.
- ☐ **Find the right mix.** Determine how to divide up your portfolio to help you meet your goals.
- ☐ **Compare investments.** Evaluate what you own now and explore other choices to consider.

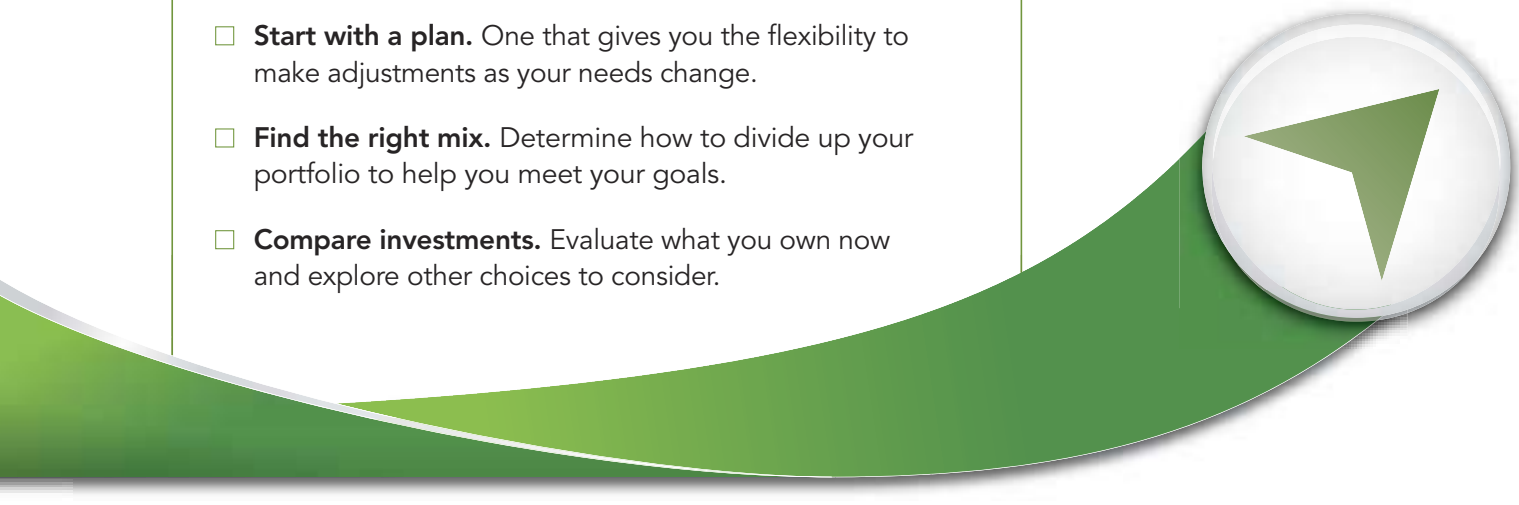

Take the Fidelity Challenge today

Schedule your one-on-one consultation with a Fidelity Planning and Guidance Consultant, and bring us your questions. You don't have to be a Fidelity client — and there's no cost or obligation. Let us help you feel more comfortable about your retirement.

Start now.

866.715.6111
Fidelity.com/challenge

Turn here®

Fidelity INVESTMENTS®

Keep in mind investing involves risk. The value of your investment will fluctuate over time and you may gain or lose money.

Although consultations are one on one, guidance provided by Fidelity is educational in nature, is not individualized, and is not intended to serve as the primary or sole basis for your investment or tax-planning decisions.

ATCGATCG

TruSeq™

The most accurate next-gen sequencing technology available.

Every Illumina sequencer is powered by TruSeq—the technology that delivers the most accurate human genome at any coverage. TruSeq produces the highest yield of error-free reads. The most bases over Q30. The greatest number of peer-reviewed publications—more than 1,000 in the past three years.

That's Tru data quality.

Get the proof. Go to
www.illumina.com/TruSeq

HiSeq™ 2000 | HiSeq™ 1000 | HiScan™ SQ | Genome Analyzer$_{IIx}$ | MiSeq™

illumina®

Eppendorf & *Science* Prize for

Neurobiology

Be the 10th winner!

2010 Winner
Christopher Gregg, Ph.D.
Postdoctoral Fellow
Harvard University

Kurstin Roe Photography

eppendorf & Science PRIZE FOR NEUROBIOLOGY

Get recognized!
US$ 25,000 Prize

Deadline for entries
June 15, 2011

It´s easy to apply! Learn more at
www.eppendorf.com/prize

Congratulations to Dr. Christopher Gregg on winning the 2010 Eppendorf & *Science* Prize for his studies on genes that alter their expression in the brains of offspring according to whether they were inherited from the father versus the mother. His findings suggest new pathways that may help to understand brain diseases such as autism, schizophrenia and eating disorders.

The annual international US$ 25,000 Eppendorf & *Science* Prize for Neurobiology honors young scientists for their outstanding contributions to neurobiological research based on methods of molecular and cell biology. The winner and finalists are selected by a committee of independent scientists, chaired by *Science's* Senior Editor, Dr. Peter Stern.

To be eligible, you must be 35 years of age or younger. If you're selected as this year's winner, you will receive US$ 25,000, have your work published in *Science* and be invited to visit Eppendorf in Hamburg, Germany. Past winners and finalists have come from as far a field as China, Chile, India and New Zealand. Yes, it *can* happen to you!

eppendorf
In touch with life

Science AAAS

MINIATURIZED CHROMATOGRAPHIC COLUMNS

PreDictor RoboColumn units are miniaturized chromatographic columns prepacked with GE Healthcare BioProcess chromatography media to enable high throughput process development (HTPD). PreDictor RoboColumn units support fully automated chromatographic separation workflows using robotic liquid handling workstations. The prepacked columns are available with a wide range of chromatography resins for ion exchange, affinity, multimodal, and hydrophobic interaction chromatography techniques. PreDictor RoboColumn units are designed for parallel screening of chromatographic conditions. Each row of eight columns is supplied with one chromatography media and individual columns can be easily arranged on a 96-position array plate. The columns are available in 50, 200, and 600 µl volumes and are compatible with solutions commonly used in the purification of biopharmaceuticals.

GE Healthcare

For info: 800-526-3593 | www.gelifesciences.com

CALIBRATION REAGENTS

Four Thermo Scientific Pierce Calibration Solutions are now offered for calibration of Thermo Scientific Mass Spectrometers, including the Thermo Scientific LTQ Orbitrap series and the Thermo Scientific TSQ Vantage series. The Pierce Calibration Solutions are ready-to-use liquid formulations that consist of highly purified ionizable molecules that produce strong peaks. The four reagents include Pierce ESI Negative Ion Calibration Solution, Pierce LTQ ESI Positive Ion Calibration Solution, Pierce LTQ Velos ESI Positive Ion Calibration Solution, and Pierce Triple Quadrupole Calibration Solution. All calibration solutions are manufactured in an ISO 9001 environment with strict specifications in quality-controlled lots and are provided in leak-proof, high-purity PTFE bottles for easy storage.

Thermo Fisher Scientific

For info: 800-874-3723 | www.thermoscientific.com/pierce

LIPID CHARACTERIZATION SOFTWARE

SimLipid analyzes lipid mass spectrometric data for characterizing lipids, greatly advancing lipidome data analysis. SimLipid can annotate mass spectra with identified lipid structures and abbreviations as well. SimLipid profiles lipids by matching the experimental MS spectra with its own comprehensive, robust, and annotated database, consisting of nine lipid classes and 1948 lipid species. It retrieves lipids that correspond with the observed m/z and user specified filter criteria. Alongside the probable lipid structure important information such as the lipid ID, lipid abbreviation, systematic name, lipid category, lipid mass, chemical formula, and other database links is also made available. In addition, users can look up the database using lipid abbreviation, mass, chemical composition, or lipid ID.

Premier Biosoft International

For info: 888-847-7494 | www.premierbiosoft.com

PROTEIN SAMPLE PREPARATION

The Perfinity Workstation is a multicolumn apparatus that automates protein separations and mass spectrometry (MS) sample preparation for more efficient liquid chromatography/mass spectrometry (LC/MS) analysis. The Perfinity Workstation uses Shimadzu hardware components in conjunction with five Perfinity Optimized columns that each perform a step of the MS sample-preparation process—affinity selection, buffer exchange, digestion, desalting, and reverse-phase separation. The automated integration of these steps enables users to start with serum and have peptides ready for LC/MS analysis in 10 minutes. The automated process removes much of the equipment and labor associated with MS analyses of proteins. The Perfinity Workstation combines the selectivity of antibodies with the resolving power of chromatography. Buffer exchange and desalting are performed online. The reduction in sample-processing time enables users to screen a variety of conditions rapidly.

Shimadzu Scientific Instruments

For info: 800-477-1227 | www.ssi.shimadzu.com

BENCHTOP MASS SPECTROMETER

The Waters Xevo G2 Tof (time-of-flight) mass spectrometer with UPLC/MS and QuanTof technology offers the most sensitive, exact mass quantitative and qualitative performance of any benchtop mass spectrometer system for scientists who need to confidently identify and quantify unknown compounds in complex samples. Powered by QuanTof technology, the Xevo G2 Tof brings SYNAPT G2 technology in an accessible, benchtop system for a new level of quantitative and qualitative performance. QuanTof technology combines an innovative high-field pusher and dual-stage reflectron with a novel ion detection system in an optimized time-of-flight geometry. Together these features provide a new dimension of high resolution, exact mass and quantitative performance uniquely available at acquisition rates that are compatible with UPLC separations.

Waters Corporation

For info: 800-252-4752 | www.waters.com

Electronically submit your new product description or product literature information! Go to **www.sciencemag.org/products/newproducts.dtl** for more information.

Newly offered instrumentation, apparatus, and laboratory materials of interest to researchers in all disciplines in academic, industrial, and governmental organizations are featured in this space. Emphasis is given to purpose, chief characteristics, and availability of products and materials. Endorsement by *Science* or AAAS of any products or materials mentioned is not implied. Additional information may be obtained from the manufacturer or supplier.

“A dream told me to do it.”

Dr. Carl Alving on his inspiration for inventing the vaccine patch.

Carl R. Alving, M.D.
Chief of the Department of Adjuvant & Antigen Research, Division of Retrovirology
at the Walter Reed Army Institute of Research
AAAS member

MemberCentral is the new website that looks at science through the eyes of AAAS members. It celebrates their achievements—like Dr. Alving’s vaccine patch—and their shared belief in the transformative power of science. Use **Member**Central to connect with other members, learn about work being done in other fields, and get fresh perspectives on issues ranging from speciation to STEM education.

Visit **Member**Central today and get to know the AAAS member community in a whole new way.

AAAS MEMBERCENTRAL

MemberCentral.aaas.org

Blogs | Videos | Webinars | Discounts | Downloads | Community

Profile Signaling Pathways

Biomarker Discovery

Explore Mechanism of Action

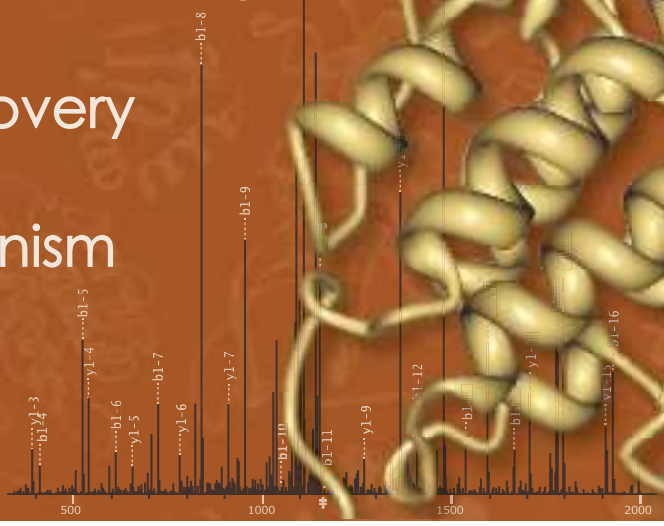

PTMScan®
Proteomics Services

from Cell Signaling Technology

PTMScan® Proteomics Services employ patented methodologies for antibody-based peptide enrichment combined with tandem mass spectrometry for quantitative profiling of post-translational modifications (PTMs).

Visit www.cellsignal.com/proteomics or contact ptmscan@cellsignal.com for more information.

PhosphoScan® Services provide a powerful strategy for kinome-wide phosphoproteomics employing phospho-motif antibodies to direct analysis to the relevant regions of the kinome.

UbiScan® Service is a sensitive method utilizing a unique ubiquitin-branch antibody for ubiquitinated sequence identification and the most comprehensive profiling analysis of cellular ubiquitin pathways.

AcetylScan® Service provides comprehensive qualitative and quantitative analysis of protein acetylation using proprietary acetylated-lysine antibodies optimized for AcetylScan®.

Register for a thought-provoking webinar on

The Proteomics of Post-translational Modifications

being broadcast live on June 8, 2011.

Sign up for free at www.sciencemag.org/webinar. Presented by the *Science*/AAAS Business Office and sponsored by Cell Signaling Technology.

for quality products you can trust...

www.cellsignal.com

Cell Signaling TECHNOLOGY®

UNIVERSITY OF MARYLAND

PROFESSOR AND DEPARTMENT CHAIR
Position Number 103682

The University of Maryland, one of the world's outstanding public research and teaching universities, invites nominations and applications for the position of Chair of the Department of Plant Science and Landscape Architecture in the College of Agriculture and Natural Resources.

The University of Maryland, located in College Park, is the Land Grant institution and flagship of the University System of Maryland. It is one of the nation's top 20 public research universities with over 2500 faculty members and a current enrollment of approximately 27,000 undergraduate and 11,000 graduate students. The 1300-acre campus has excellent research libraries and laboratories, as well as Metrorail access to national and international research institutions, archives, non-profit agencies, and significant cultural landmarks in the Baltimore-Washington, DC corridor.

The Department of Plant Science and Landscape Architecture includes 19 tenured faculty, 5 tenure-track faculty, and 2 non-tenure-track faculty. There are 27 graduate students in the Master of Science and PhD programs and 23 graduate students in the Master of Landscape Architecture program. There are 160 undergraduate students in three programs: Agricultural Science and Technology, Landscape Architecture, and Plant Science. The Department has a total state budget of nearly $3.3 million and over $16 million in extramural funding. Its primary offices, research laboratories, design studios and classrooms are centrally located in the Plant Sciences Building and H.J. Patterson Hall. The Department manages a state-of-the-art greenhouse on campus and has research and extension programs at centers throughout the state. Its proximity to Washington DC, Baltimore, and Annapolis provides excellent opportunities for collaborative activities with federal agencies and laboratories and national and international professional societies.

Responsibilities of the Department Chair include: 1. Vision, support and coordination in planning, development, and implementation of programs in teaching, research and extension, in accord with its Land Grant mission; 2. Leadership in recruiting and fostering academic growth, professional development, and diversity of faculty, staff, and students; 3. Administration of the Department's human, physical, and financial resources; 4. Leadership in promotion and marketing of the Department's national and international stature; and 5. Awareness and facilitation of external funding opportunities.

Required qualifications for Department Chair are an earned doctoral degree in agronomy, horticulture, landscape architecture, plant science, or a closely related discipline. The individual must have a record of outstanding achievement and professional activities related to teaching, research, extension, government, and/or industry that will qualify the individual to be a tenured full professor in the Department.

Applications must be completed online at jobs.umd.edu. A complete position announcement is available on the web site. Applicants must submit the following information:

- Statement that clearly explains the applicant's qualifications related to the position responsibilities and the applicant's vision for the Department's future;
- Statement of academic interests and administrative approach;
- Complete CV, signed and dated;
- Transcripts (copy acceptable); name, address, and contact information of four professional references;
- Examples of professional, scholarly and/or creative work.

For best consideration, material should be received by **August 15, 2011**. The search will continue until the position is filled. The effective start date is July 1, 2012. Inquiries may be directed to the PSLA Search Committee Chair Adel Shirmohammadi, PhD, Associate Dean, at **pslachair@umd.edu**.

The University Of Maryland Is An
Equal Opportunity And Affirmative Action Employer.
Women And Minorities Are Strongly Encouraged To Apply.

SOOCHOW UNIVERSITY

Faculty Positions in Neuroscience

The Soochow University, founded in 1900 in Suzhou, is a premier university in China. The University is committed to excellence in education, science and innovation. A complete listing of open positions is available at **http://rsc.suda.edu.cn/zpxx.asp?type=15**.

We seek distinguished professors and motivated individuals to join us in the **Institute of Neuroscience**. Successful candidates should have a Ph.D. and at least 3-year oversea research experience in neuroscience with particular emphasis in the area of Parkinson, Alzheimer, and cerebrovascular diseases.

Applicants should have high quality publications in top international journals, strong interests in translational research, and active research programs complementary to our existing strengths. Our institute is dedicated to build a state-of-the-art research platform. We provide an excellent environment for scientific pursuit and encourage close interactions between basic and clinical research. Competitive relocation and salary packages, generous start-up funds, and state-of-the-art lab facilities will be provided.

Interested individuals should send curriculum vitae, a summary of accomplishments, future research plans, and a list of three references to **Prof. Chunfeng Liu, Institute of Neuroscience, Soochow University, e-mail: liucf@suda.edu.cn, Dushuhu campus of Soochow University, 199 Ren-Ai Road, Suzhou, Jiangsu, 215123, China, http://neuroscience.suda.edu.cn/cn/**.

Call for Nomination for Next Director-General of KEK

KEK, High Energy Accelerator Research Organization, invites nominations for the next Director-General whose term will begin April 1, 2012.

The role of Director-General, therefore, is to promote with long-term vision and strong scientific leadership, the highly advanced, internationalized, and inter-disciplinary research activities of KEK by getting support from the public. The successful candidate is also expected to establish and carry out the medium-term goals and plans.

The term of appointment is three years. When reappointed, the term can be extended up to 9 years.
We widely accept the nomination of the candidates regardless of their nationalities.

We would like to ask you to recommend the best person who satisfies requirements for the position written above.

Nomination should be accompanied by: (1) letter of recommendation, (2) brief personal history of the candidate, and (3) list of major achievements (publications, academic papers, commendations and membership of councils, etc.). The nomination should be submitted to the following address **no later than July 8, 2011**:

Documents should be written either in English or in Japanese.

Inquiries concerning the nomination should be addressed to:

General Affairs Division
General Management Department
KEK, High Energy Accelerator Research Organization
1-1 Oho, Tsukuba, Japan 305-0801
Tel +81-29-864-5114
Fax +81-29-864-5560
Email: **shomu@mail.kek.jp**

DIRECTOR

Lawrence Livermore National Laboratory
Livermore, California

The University of California and Lawrence Livermore National Security, LLC (LLNS) invite nominations and applications for the position of Director of Lawrence Livermore National Laboratory (LLNL). LLNL is a national security laboratory managed by LLNS for the U.S. Department of Energy's (DOE) National Nuclear Security Administration (NNSA). It was established in 1952 and is located 49 miles southeast of San Francisco in Livermore, California.

LLNS is a limited liability company governed by a team that includes the University of California, Bechtel National, Inc., Babcock and Wilcox Company, Washington Division of URS Corporation, and Battelle Memorial Institute. The Laboratory Director is the President of the LLC, reports to the LLC Board of Governors (BOG), and is responsible for overall execution of DOE/NNSA's programs at LLNL.

The Director sets the strategic vision of the Laboratory and exercises broad delegated powers to ensure successful execution of Laboratory programs and operations and to maintain an outstanding workforce. The Director leads the development and implementation of the Laboratory's scientific vision, goals, and objectives. The position serves as the highest-level liaison with the DOE, NNSA, BOG, and other government, public, and private organizations. The Director exercises overall leadership and administration of the Laboratory's programs and operations, including the definition of their technical aspects, negotiation of their size and content, and execution of these programs with the highest quality. Special responsibilities include an integrated safety and security management program for high-hazard facilities ranging from nuclear materials, high explosives, to biological agents, and an integrated security program for many levels of highly sensitive information. A unique responsibility, shared with the Directors of Los Alamos and Sandia National Laboratories, is to annually provide the U.S. President, through the Secretaries of Energy and Defense, a personal assessment of the health of the nuclear weapons stockpile in terms of safety, security, and effectiveness, and whether confidence in the stockpile can be maintained without a nuclear test.

The Director is responsible for significant human, financial, equipment, and facility resources, including a workforce of approximately 7300 employees and an annual operating budget of approximately $1.6B. A particular responsibility is stewardship of the National Ignition Facility, the world's premier facility for the study of high-energy-density science. The Director must ensure that all LLNL user facilities are managed cost-efficiently and provide the level of service and scientific utility required by the world's leading researchers.

National security is the defining responsibility of the Laboratory, focusing on two of the nation's top priorities: ensuring the safety, security, and reliability of the U.S. nuclear stockpile, and preventing and countering the proliferation of weapons of mass destruction including nuclear, chemical, biological, and cyber threats. The Director must ensure that the Laboratory's programs anticipate and support national security needs and apply science and technology to the important problems of our time. The Director will be required to provide technical briefings on scientific and national security matters to policy leaders in Executive and Legislative branches of the Federal government. The Laboratory's primary mission and exceptional capabilities in high performance computing, high-energy-density science, and material science enable other programs in advanced defense technologies, energy, environment, biosciences and human health, and basic science. The Director must have a commitment and ability to lead cooperative integration of programs with Los Alamos and Sandia National Laboratories, and facilities and efforts across the NNSA national security complex.

Candidates should have demonstrated success in leading and managing large science-based programs and complex organizations, and should have a distinguished record of scientific and technical accomplishments. Strong leadership skills are required, including the ability to gain the confidence of key leaders, scientists, and operations staff, and the ability to develop strategic relationships and partnerships with key constituents. The ideal candidate should have demonstrated substantial management responsibility in a mission-oriented R&D institution. Significant management experience is needed to ensure that support and programmatic functions achieve compliance with all applicable Federal, State, and LLC policies and to operate as an effective member of the regional community. DOE Q security clearance will be required. Other required competencies and capabilities may be identified through the candidate selection process.

Nominations and applications accompanied by
current resumes may be sent to:
University of California, Office of the President
Attn: LLNL Director Search
1111 Broadway, Suite 1450 • Oakland, CA 94607-4081
Or email: llnldirectorsearch@ucop.edu

The position will remain Open Until Filled, but applicants are encouraged to submit a resume and statement of interest to the above address by no later than August 19, 2011, to be given full consideration. Salary is commensurate with experience. In conformance with applicable law and policy, the LLNS, LLC is an affirmative action/equal opportunity employer. A U.S. Department of Energy National Laboratory. Operated by Lawrence Livermore National Security, LLC

UNIVERSITY of HOUSTON
A CARNEGIE-DESIGNATED TIER ONE PUBLIC RESEARCH UNIVERSITY

Faculty Position in the Department of Biology and Biochemistry

Candidates for appointment at the Assistant, Associate or Full Professor level must show evidence of productive research accomplishments. A candidate for Associate or Full Professor must have a currently funded research program. All candidates are expected to develop/maintain a fully independent research program addressing fundamental questions in an area of modern biochemistry, participate in the teaching missions of the department and form productive interactions with colleagues and other scientists at the University of Houston. We are searching for an outstanding faculty in Proteomics with experience in the use cutting-edge mass spectrometric technologies and bioinformatics platform. Experience with high performance computing is a plus. The Department, of Biology and Biochemistry is also well equipped for performing functional follow-up studies by molecular biology and cell biology techniques and assays. In addition to developing an independent and extramurally funded research program, the successful individual will be expected to direct a newly established, institutional proteomic core facility that has a strong focus on drug discovery, 2D DIGE, protein-protein interactions, post-translational protein chemistry. The successful candidate will be responsible for developing and implementing protocols and data processing for state of the art LC/MS/MS, MALDI and 2D DIGE technologies. Preference will be given to applicants with evidence of excellence in research and teaching. This tenure-stream position offers outstanding scholarly and scientific resources and unique opportunities to interact with related departments and research centers throughout the University of Houston.

Interested applicants should submit a current CV, a clear statement of your specific research and teaching interests, and the names and contact information of at least three references to **rjschwartz@uh.edu**. For further details please visit **http://www.uh.edu/provostlfac/faculty-openings/**. Closing date for applications is **July 1, 2011**. We encourage applicants to combine PDF or MS WORD documents into one or two files. Salary to be commensurate with person's qualifications and experience.

UH is an Equal Opportunity/Affirmative Action Employer. Minorities, women, veterans, and persons with disabilities are encouraged to apply.

University of Cologne

The University of Cologne invites applications for a

Full Professorship (W3, tenured) in Systems Biology of Ageing

This is a joint appointment between the Faculty of Mathematics and Natural Sciences and the Medical Faculty, University of Cologne.

The successful applicant is expected to have an internationally recognized research programme in bioinformatics or computational biology with a focus on the molecular basis of biological function, and an interest in applying such approaches to the biology of ageing in the context of regulatory networks (prior experience in ageing research is not required). The integration of experimental and theoretical approaches and a close interaction with the Cologne Excellence Cluster on Cellular Stress Responses in Aging-Associated Diseases (CECAD), the Max Planck Institute for Biology of Ageing as well as with other relevant Collaborative Research Centers at the University of Cologne (e.g. CRC 635 and CRC 680) is expected. He/She should also contribute to teaching programmes in systems biology at the university.

The successful applicant will lead a research group located at the Cologne Center for Genomics and should establish collaborations with groups at the Max Planck Institutes and at the University of Cologne. The position is a full tenured professorship (W3).

The University of Cologne is an equal opportunity employer and encourages applications from women and from persons with a disability.

Applicants are requested to send a full CV including a complete list of publications, teaching experience, a statement of research interests and a selection of maximally five reprints by **June 30, 2011** to the Dean of the Mathematisch-Naturwissenschaftliche Fakultät of the University of Cologne, Albertus-Magnus-Platz, D-50923 Köln, Germany.

Nontraditional Careers: Opportunities Away From the Bench

Webinar

Want to learn more about exciting and rewarding careers outside of academic/industrial research? View a roundtable discussion that looks at the various career options open to scientists and strategies you can use to pursue a nonresearch career.

Now Available On Demand
www.sciencecareers.org/webinar

Produced by the *Science*/AAAS Business Office.

Science Careers
From the journal *Science* AAAS

POSITIONS OPEN

SENIOR AQUATIC SCIENTIST
Joseph W. Jones Ecological Research Center at Ichauway

The Joseph W. Jones Ecological Research Center at Ichauway invites nominations or letters of inquiry for a Senior Aquatic Scientist (**ASSOCIATE** or **FULL** level). The Center is interested in individuals with integrative skills willing to contribute to a field-oriented research program concerning environmental flows and their relationship to coastal plain riverine/reservoir/aquifer systems. Those studying altered flow regimes and their effects on the structure and function of large rivers, instream habitat, and water quality are encouraged to respond. Experience and inclination to apply basic ecological principles to regional conservation and management priorities are essential. Southeastern experience is desirable, but not required. The successful candidate is expected to have experience with extramural funding and will support their research, in part, from external sources. The Center is affiliated with several regional universities as well as numerous state and federal natural resource agencies. The position is a 12-month appointment, includes a permanent research technician (M.S. level, of the successful candidate's selection), graduate assistantship support, and internal research funds to support research related to the Jones Center mission. More information can be found at **website: http://www.jonesctr.org.**

Applicants must be U.S. citizen or permanent U.S. resident. Letters of nomination or inquiry should be sent electronically to **Dr. Lindsay Boring,** Director, J.W. Jones Ecological Research Center (**e-mail: aq_search@jonesctr.org**). All communications will be treated confidentially. Inquiries will be accepted until the position is filled. *Equal Employment Opportunity Employer.*

NIH-funded Immunology POSTDOCTORAL POSITION

Vaccine-induced T17 cells confer resistance to dimorphic fungi (*JCI* **121(2):** 554–68, 2011). The position will address the roles of the Syk-Card9 and TLR-Myd88 pathways and the PRRs and fungal ligands that drive differentiation of antifungal T17 cells. Candidates need to be motivated and experienced in cellular and molecular immunology. Direct resume, cover letter, and contact information for three references to: **Marcel Wüthrich, University of Wisconsin-Madison, Microbial Sciences Building, 1550 Linden Drive, Rm 4301, Madison, WI, 53711. E-mail: mwuethri@wisc.edu, telephone: 608-262-7703.**

Find your future here.

↓

Science Careers
From the journal *Science* AAAS
www.ScienceCareers.org

POSITIONS OPEN

ASU GRADUATE College
ARIZONA STATE UNIVERSITY

ARIZONA STATE UNIVERSITY BISGROVE POSTDOCTORAL SCHOLARS PROGRAM

Arizona State University Graduate College is now accepting Postdoctoral Applications for the Bisgrove Postdoctoral Scholars Program. The Award (sponsored by the Science Foundation Arizona) is designed to attract the nation's best early career scientists who exhibit the potential for outstanding competence and creativity in their research areas, strong communication skills, a passion for communicating the importance of their research to society, and a keen interest in educational science outreach to the community. *Individuals eligible to apply are U.S. citizens or permanent residents of the U.S.* Applicants should demonstrate research training in Health Initiatives, Sustainable Energy and the Environment, or Engineering. For application and submission procedures, go to **website: http://graduate.asu.edu/bisgrove.**

OPEN POSITION

The Physical Sciences Department, Faculty of General Studies at the University of Puerto Rico, Rio Piedras Campus, invites applications for a tenure-track position as **ASSISTANT PROFESSOR.** A Ph.D. degree in Physics-Chemistry is required as well as proficiency in scientific research in semiconductor and transition metals nanotechnology as evidenced by journal publications and funded research. The incumbent should demonstrate a potential for excellence in teaching for nonmajor in sciences undergraduate students, teach courses of Physical Sciences and Physics to undergraduate students, advice and mentor students attending his classes and prepare course materials, homework assignments, and grade students. Participate in curriculum revision and enhancement, seek funding for the research and teaching programs, supervise undergraduate research and creative work, and engage in professional development activities related to research, teaching, and advising. Keep abreast of field development, participate in professional organizations and conferences, publish in internationally renowned journals, and will seek funding for the research and teaching programs.

Applicants are requested to send a letter of application, curriculum vitae, research plan, list of publications, transcripts, teaching philosophy, and three reference letters by June 27th, 2011 to the following address:

Dr. Fernando J. Noriega
Physical Sciences Department
Faculty of General Studies
University of Puerto Rico
PO Box 23323
San Juan, PR 00931-3323

Equal Opportunity Employer.

MARKETPLACE